# Fundamentals of ultra scaled 3D magnetic tunnel junctions and integration routes for high density memory arrays

Nuno Caçoilo

THÈSE

Pour obtenir le grade de

**DOCTEUR DE L'UNIVERSITÉ GRENOBLE ALPES**

École doctorale : Electronique, Electrotechnique, Automatique, Traitement du Signal (EEATS)
Spécialité : Nano électronique et Nano technologies
Unité de recherche : Spintronique et Technologie Composants (SPINTEC)

# Fondamentaux des jonctions tunnel magnétiques 3D ultraminiaturisées et voies d'intégration ver les matrices mémoire à très haute densité. Fundamentals of ultra scaled 3D magnetic tunnel junctions and integration routes for high density memory arrays

Présentée par :


## Nuno CAÇOILO


Direction de thèse :

| | |
|---|---|
| **Ioan-Lucian PREJBEANU**<br>DIRECTEUR DE RECHERCHE, CEA | Directeur de thèse |
| **Olivier FRUCHART**<br>DIRECTEUR DE RECHERCHE, CNRS | Co-Directeur de thèse |
| **Ricardo SOUSA**<br>INGENIEUR CHERCHEUR, CEA | Co-Directeur de thèse |

Rapporteurs :

**Alexandra MOUGIN**
DIRECTRICE DE RECHERCHE, CNRS, Président de jury
**François MONTAIGNE**
PROFESSEUR DES UNIVERSITES, UNIVERSITÉ DE LORRAINE

Thèse soutenue publiquement le **13 Octobre 2023**, devant le jury composé de :

| | |
|---|---|
| **Alexandra MOUGIN**<br>DIRECTRICE DE RECHERCHE, CNRS, Président de jury | Rapporteure |
| **François MONTAIGNE**<br>PROFESSEUR DES UNIVERSITES, UNIVERSITÉ DE LORRAINE | Rapporteur |
| **Diana LEITÃO**<br>ASSISTANT PROFESSOR, EINDHOVEN UNIVERSITY OF TECHNOLOGY | Examinatrice |
| **Shunsuke FUKAMI**<br>PROFESSOR, TOHOKU UNIVERSITY | Examinateur |
| **Laurent RANNO**<br>MAITRE DE CONFERENCES, UNIVERSITÉ GRENOBLE ALPES | Examinateur |

# Resume

The perpendicular Spin Transfer Torque Magnetic Random Access Memory (p-STT-MRAM) is one of the most promising emerging non-volatile memory technologies. As these devices are limited by their thermal stability factor at technological nodes smaller than 20 nm, their downsize capability is compromised. A possible solution to this limitation relies in taking advantage of the shape anisotropy, by increasing substantially the thickness of the storage layer. Thanks to this now vertical aspect-ratio, the stability can be enhanced significantly to sub-10 nm nodes and this new memory element is named Perpendicular Shape Anisotropy MTJ (PSA-MTJ). Although a promising path to dense MTJ arrays, there are still several challenges that need to be addressed before adopting this technology. In this dissertation we address the bottlenecks of this novel memory element, namely the fabrication process and improvement of the reversal mechanism. Making use of micromagnetic simulations it is shown the different reversal mechanisms of the PSA-MTJ and a study on how to avoid a non-coherent reversal while keeping fast switching times at low switching voltages is realised. It is namely shown that it is necessary to finely tune the aspect-ratio of the memory cell to achieve faster switching times. This increase in switching speed comes, not only from the increase in anisotropy field (in a macrospin approximation, it increases to maintain the same stability at proportionally smaller magnetic volume), but also due to the stronger effect of the spin-transfer-torque. This idea is used as a baseline for fabricated sub-10 nm elements with vertical aspect-ratio, where switching is achieved through spin-transfer-torque. Usual p-MTJs are also fabricated using the same methodology and it is shown an increase in figure of merit ($\Delta/I_{c0}$) (a known parameter that relates the ratio between the stability and the critical current necessary to switch the device) as the diameter is reduced. In the limit of the dimension, devices as small as 5 nm in diameter show a stochastic behaviour (direction of magnetization fluctuates with the thermal noise), well controlled by the STT current. This opens the path to dense arrays of stochastic MTJs with ultra-small diameter and small switching current. However, to fabricate a dense MTJ array there are still several challenges that need to be solved, namely the stray field from neighbouring bits but also the shadow effect, which limits the pitch between devices. To tackle these constraints we make use of electrodeposition in pre-patterned nano-vias, either by electro-beam lithography (EBL) or direct self-assembly (DSA), to fabricate ultra-small MTJ. The nano-vias created by EBL show potential to achieve sub-10 nm thanks to the already small pre-defined diameter but also thanks to a more uniform ion beam etching of the pillar, avoiding tilted or fallen devices. STT-switching and very large TMR values were shown in single devices measurements using this approach for conventional pMTJ. The nano-vias created by DSA show promise for very small pitch ($\approx 50$ nm) and small node ($\approx 25$ nm) MTJ arrays. These can be adapted for CMOS integration, as the nano-via can be filled directly on top the already existing W via. A process flow that makes use of a common bottom electrode was devised and structural and magnetic characterization of the nano-vias was realised. A solution to the strong cross talk between magnetic devices was demonstrated analytically and micromagnetically through the use of a core-shell system for the storage layer. Thanks to the vertical aspect ratio of the magnetic layer, this system adds stability and reduced switching time without a penalty in the switching voltage. Additionally, the system can be adjusted so that there is no remnant stray field inside a magnetic array.

# Résumé

La Mémoire Magnétique à Accès Aléatoire et à Transfert de Spin perpendiculaire (p-STT-MRAM) est l'une des technologies émergentes les plus prometteuses pour les mémoire non volatile. Étant donné que le facteur de stabilité de ces dispositifs rencontre une limite fondamentale aux nœuds technologiques inférieurs à 20 nm, leur capacité de poursuite de réduction de taille. Une solution possible à cette limitation repose sur l'exploitation de l'anisotropie de forme magnétique, en augmentant considérablement l'épaisseur de la couche de stockage. Grâce à un rapport d'aspect vertical, la stabilité peut être significativement améliorée pour des nœuds inférieurs à 10 nm. Le nouvel élément de mémoire suivant ce concept est nommé Jonction Tunnel Magnétique à Anisotropie de Forme Perpendiculaire (PSA-MTJ). Bien que représentant une voie prometteuse vers des réseaux d'éléments MTJ denses, plusieurs défis doivent encore être relevés avant que cette technologie ne soit viable. Dans cette thèse, nous abordons les goulots d'étranglement de ce nouvel élément de mémoire, à savoir le processus de fabrication et l'amélioration du mécanisme de renversement d'aimantation. En utilisant des simulations micromagnétiques, nous montrons les différents mécanismes de renversement d'aimantation des PSA-MTJ, et réalisons une étude sur la manière d'éviter un renversement non cohérent, tout en maintenant des temps de commutation rapides à de faibles tensions de commutation. Il est notamment démontré qu'il est nécessaire d'ajuster finement le rapport d'aspect de la cellule mémoire pour obtenir des temps de commutation plus rapides. Cette augmentation de la vitesse de commutation est lié non seulement à l'augmentation du champ d'anisotropie (dans une approximation macrospin, ce champ doit être augmenté pour maintenir la même stabilité avec un volume magnétique proportionnellement plus petit), mais également à l'effet plus fort du couple de transfert de spin. Cette étude est utilisée comme base pour fabriquer des éléments de moins de 10 nm de diamètre avec un rapport d'aspect vertical, où la commutation est réalisée par transfert de spin. Des MTJ classiques sont également fabriquées en utilisant la même méthodologie, et une augmentation du facteur de mérite ($\Delta/I_{c0}$) est observée (un paramètre habituel qui compare le facteur de stabilité et le courant critique nécessaire pour commuter le dispositif) à mesure que le diamètre diminue. À mesure que les dimensions diminuent, pour des diamètres de l'ordre de 5 nm des dispositifs finissent par montrer un comportement stochastique (la direction de l'aimantation fluctue avec le bruit thermique) contrôlable par le courant STT. Cela ouvre la voie à des matrices d'éléments MTJ stochastiques à densité élevée avec un diamètre ultra-petit et un faible courant de commutation. Cependant, pour fabriquer une matrice d'éléments MTJ dense, plusieurs défis doivent encore être résolus, notamment le champ parasite induits pas les éléments voisins, mais aussi l'effet d'ombrage lors de la fabrication, qui limite l'espacement entre les bits voisins. Pour résoudre ces aspects, nous avons utilisé l'électrodépot dans des nano-vias prégavés, soit par lithographie par faisceau d'électrons (EBL) dasn une résine, soit par auto-assemblage direct (DSA) sur des substrats Si, pour fabriquer des MTJ ultra-petites. Les nano-vias créés par EBL montrent un potentiel pour atteindre des dimensions inférieures à 10 nm, grâce au diamètre déjà réduit défini par l'EBL, mais aussi grâce à la gravure uniforme par faisceau d'ions du pilier, évitant ainsi les piliers inclinés ou détachés issus du processus classique de fabrication des PSA. La commutation par STT et de très grandes valeurs de TMR ont été démontrées dans des mesures de dispositifs individuels en utilisant cette approche pour des MTJ conventionnels. Les nano-vias formés par DSA montrent des résultats prometteurs pour les piliers à espacement très réduit ($\approx 50$ nm) et les nœuds de petite taille ($\approx 25$ nm). Ils offrent des perspectives d'intégration CMOS, car le nano-via peut être directement rempli au-dessus d'un contact conducteur existant, dans le cas présent enW. Un procédé de contactage électrique utilisant une électrode inférieure commune a été mise au point et une caractérisation structurale et magnétique des nano-vias résultant a été réalisée. Enfin, l'utilisation d'un système cœur-coquille pour la couche de stockage est proposé comme une solution au problème de fort couplage entre dispositifs magnétiques voisins, comme démontrée analytiquement et micromagnétiquement. Grâce au rapport d'aspect vertical de la structure, ce système renforce la stabilité tout en réduisant le temps de commutation, sans pénalité en termes de tension de commutation. De plus, le système peut être optimisé de manière réduire drastiquement le champ magnétique parasite de couplage à l'intérieur d'un réseau magnétique dense.

*Not everyone who works hard is rewarded. But, all those who succeed have worked hard!*

はじめ

## Acknowledgements

Some people say that doing a PhD shows how mentally strong someone can be, through dedication and hard work. Although these are fundamental, I found out that, for me, it is not enough. The people we surround ourselves with have the biggest impact. The ones that stay and laugh with you when the fabrication process gets stuck multiple times in a row, or when a Japanese laboratory is 3 papers ahead of your research already in your first year. The ones that take the coffee break with you everyday or hear you complain to yourself in front of the computer. The ones that keep supporting you even if far away, as a simple text is enough to brighten even some of the worse days. I was lucky enough to be surrounded by these people during the years of my PhD.

Amongst them are obviously, my supervisors. Lucian and Olivier, to which I can't thank enough for allowing me to do the PhD with them. Although the beginning of this road was rocky, with COVID in the first months of my PhD and some rougher periods during the first two years, I am glad that in the end we were able to do so much and have such a strong connection. Lucian, I am thankful for all the insights you have given me, either pure research but also on some of the politics of research. I have grown a lot, as a researcher, thanks to our discussions. Olivier, thank you for all the scientific discussions in the laboratory. Thank you for always allowing me in your office with a smile, knowing that I would annoy you for 30 minutes straight about ideas of what we could do, I know that took a lot of strength. Even though both of you being are very busy, you always made time for me, and for that I am extremely grateful. I am happy that in the future we will keep on meeting, now as working colleagues. Where I can still, let us put it in a nice way, engage in an *enthusiastic* conversion about ideas and work that can still be done.

I also want to thank all of the permanent staff at SPINTEC. In special, Liliana, thank you for the help with the micromagnetic simulations. I know I burned 3 GPUs in my first year and that you had to spend money on getting newer ones. Which made me burn 2 other GPUs. But you never threw that at my face, and was happy to give me access to other, faster GPUs ... which I managed not to burn this time. Ricardo, thank you for all the discussions and help with the electrical measurements. I am sorry if I made the meetings less serious sometimes by making a joke or two. I am thankful for all of our discussions, every one of them made me more motivated to keep on digging deeper on the subject. Thanks to Stéphane and Jérôme for all the sample deposition. I am sorry if I used most of the Pt target, Alvaro was not happy with me. To Thomas a strong thanks for keeping the SENTECH and SCIA alive, I know they are moody machines. To Laurent, for his help at the start of my PhD in the clean room and the insightful conversations. A big shoutout to Florian, for all of his help and motivation in the cleanroom, it was amazing to work with you with the LETI samples and I know that the new arrivals will be in good hands with you there. I also want to thank all of the collaborators during this PhD. A big thanks to David and Trevor for the amazing TEM and Electron Holograhy measurements. They looked amazing on this thesis. To Maria, Guido, Khatia and Arnaud, for all the help and discussion about the wafers with the nano-vias. It was amazing to learn so much about a topic that I could not have worked on otherwise. To Laurent, an amazing thanks for all of the help with electrodeposition. I enjoyed our conversations and our coffees a lot.

To my SPINTEC family, the ones that left and the ones that still have a bit longer to go. I want to thank the MRAM team, starting with the older generation. Daniel, Marco, Alvaro, Steven and Aurélien. The start of the PhD with COVID was indeed quite rough, but I was lucky that I had you guys there. Daniel, thank you for all the conversations and motivation, I felt we were a bit in the same boat at some point and you were there to help me through it, I can't thank you enough for that. Marco, the PSA switched in the end, so joke's on you. Alvaro, Steven and Aurélien, thank you for all your help with the fabrication, who would have know that someone that was afraid to hold a wafer could spend so many hours inside the clean room and enjoy it so much. Ariam, although you are now a big shot in Germany, never forget that you can't win in FIFA against me anymore. David, I will still win a chess game eventually.

To my office friends. Louis, sorry for making so much noise, but you should have gotten better soundproof headphones. Libor, thank you for all of the jokes and listening to me ramble about work and random stuff. Ilaria, although you arrived only near the end of my contract, it was amazing having you there only if it was for a short time, I couldn't imagine that office any other way. I am pretty sure you will miss me being a drama queen there. To the Italian gang, Marco (thank you for all the Italian vocabulary), Salvatore (my duo Sion boy) and bello Paolo. It was amazing how many of you invaded spintec in the end, and I am so happy you did. Andrea, thank you for the leg day advice, I will keep them always in mind. Hasan, I will never forget the unicorn box, thank you for everything and the long talks my boy. Javi, my half-portuguese brother, thank you for making me more extrovert again, can't imagine not having met you. Capucine, thank you for allowing me to be a kid in the office with you. Laura, I am so happy I was able to have known you for the last 4 years, I will miss saying *ça va* to you everyday. Kamal, thank you for all the talks after 19:00. Loved saying see you tomorrow to you last in the office. Miina (*summa cum laude*) thank you for all the discussions, dinners and coffees we had. Hanna, I can't express how happy I am to have met you during the last year of my PhD. It was amazing hanging out with you. Pedro, my lek, brother, colleague and flatmate, thank you for everything during the last years. I am sure we will be making more anime nights in the future as a little distance will not affect our friendship.

I also want to thank, and not only, Leandro, Mateo, Anda, Sergi, Manuela, Thomas, Rodrigo, Lucile, Mario, Maxime, Quentin, David, Joseba, Aurélie, Theo, Philippe, Michael(s), Subham, Ryuhei, Rafael and Sambit.

Bruno, my research started with you during my bachelors. I never thought we would both come to France and keep working together. Like it or not, I will always see you as a mentor. Thank you for pushing me this far. To my long distance friends, thank you for all the long distance support. Jimena, Alejandra, Ana, JP, Martinho, Teixeira, Fábio, Maryam, Pietro, Daniel, Junta, Valentin, Elena, Raquel, Rita, Rui, Zé, Filipe and Maria. Pedro (opah), thank you for all the support during these years, every online call gave me energy to keep pushing further. Diogo, although we have different point of views regarding life in general, I am happy to know that we'll always be close independent of where it takes us. Looking forward for our trip in your corvette.

To my family, for supporting and understanding a son and a brother outside of home for so long. You were the ones that allowed me to take so many risks and supported me in my decisions. I will always be grateful to you and will never forget my roots.

Although my PhD journey finishes here, I am glad to look back and remember how all of you made it with me. The best word I can use to describe how I feel after this journey is that I will have *saudades* of all of you (will miss you all), and even on the other side of the world, I will keep annoying you.

Merci à tou.te.s et à bientôt.

# Contents

# 1 The need for emerging non-volatile memories

## 1.1 The memory hierarchy

The demand for an improvement in data handling has been growing exponentially during the last decades. Following the onset of high-performance computing and social networking, the memory market is tackling the needs for higher storage capacity, data treatment speed and energy consumption. Moreover, the constant miniaturization of the devices is pursued, and it is the latest complication regarding the Moore's law. Able to predict that the number of transistors would double about every 2 years, Moore's law now faces a downsize scalability limit. The microelectronics industry has been focusing efforts to tackle these current challenges for memory improvement, and a possible answer resides in the development of emerging non volatile memories (e-NVM) [1, 2].

In this section, a brief introduction into the evolution of the memory technology is presented, focusing on the successive improvements of write speed and endurance. The challenges facing the ubiquitous memories of nowadays, that ultimately lead to the emergence of new memories, will be explained with particular focus on the Magnetic Random Access Memory (MRAM), on the corresponding methods of writing information, from applied magnetic field to the use of the spin-transfer-torque (STT) effect and to the novel concept of Perpendicular Shape Anisotropy Spin Transfer Torque Magnetic Random Access Memory (PSA-STT-MRAM), which is the major focus of this thesis.

Memory devices can be divided in two major groups, regarding their applications. The first one is the stand-alone memory, which acts as an external component to the main unit and offers a high storage capacity. Its operation ranges from industry (*e.g.* automotive, sensor applications) to mass storage (*e.g.* USB sticks, Hard Disk Drives (HDD) and Solid State Drives (SSD)). The second group is the embedded memory which is a part of the main unit. Its storage capacity is smaller than that of the stand-alone and it finds application in mobile devices, cache and Micro-Controller units devices (*e.g.* smart cards). Within those fundamental groups we can find different memory types. The stand-alone group is dominated by the FLASH (NAND) technology and the embedded memory group by the Static RAM (SRAM) and Dynamic RAM (DRAM). The first one is termed as a non-volatile memory (NVM), as it retains information even when powered off, while the last two are labelled as volatile memories, as they lose information when turned off. In order to explain the differences in the intrinsic properties of these distinct devices, a hierarchic system can be adopted, as shown in Figure 1.1 (*a*). From this point we can divide the top- (SRAM and DRAM) and bottom-tier (FLASH, HDD, SDD) of the pyramid as hot-storage and cold-storage, respectively, depending on how often they are accessed. The hot-storage presents a very high writing speed and they are quite expensive. In contrast, the cold-storage does not possess a high writing speed but, being an external component, presents a larger storage capability at a lower cost [3, 4].

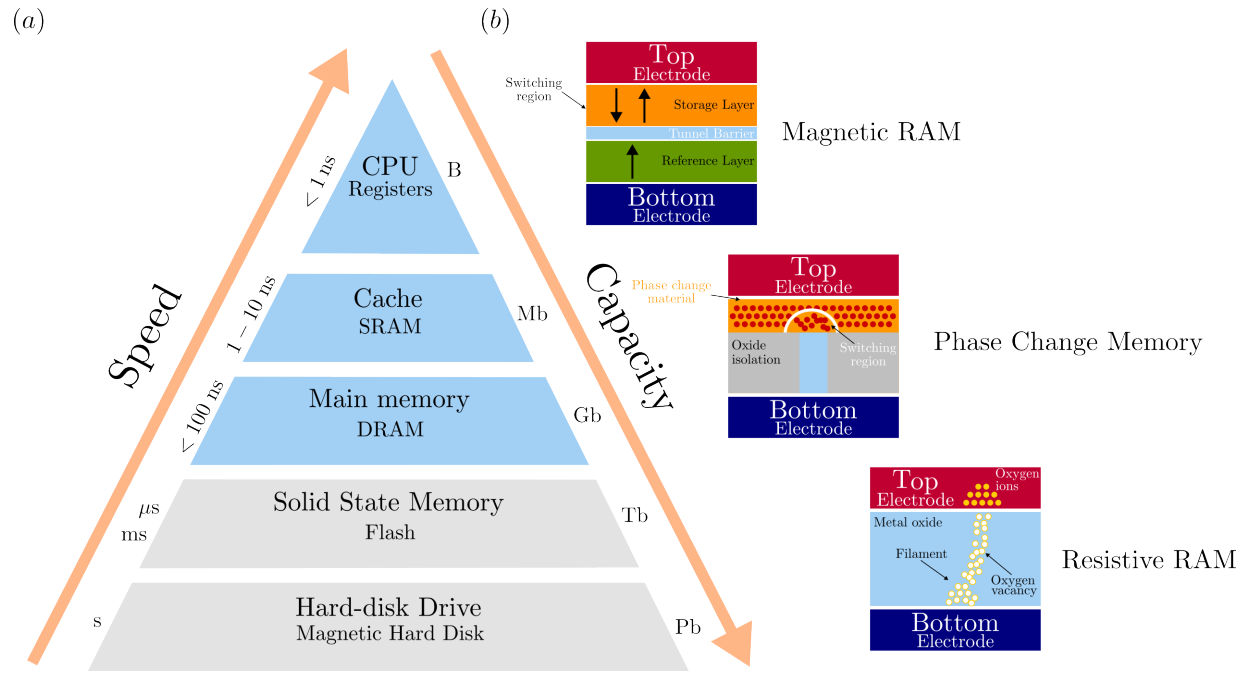


Figure 1.1: (*a*) Memory hierarchy with emphasis in the stand-alone (grey region) and embedded memory (blue region). Arrows represent increase in speed and density. (*b*) Schematics of some examples of e-NVM.

One vital parameter when describing a memory element is its endurance, which reflects the number of times the memory can be used before becoming defective. The top-tier memories offer higher endurance than the bottom-tier ones [5, 6]. Upon analysis of these different parameters, a gap between the top- and bottom-tier is found, which can be filled by the storage class memory (SCM). This gap is related to memories with writing speed and endurance near the ones of DRAM and SRAM, alongside the low cost and high density of the FLASH [4]. With the constant growth of data, the SCM market finds itself as the most suitable application-price range memory, estimating a revenue doubling every year [3]. Thus, the research of new memory types, adapted to this storage class, is of utmost importance. A possible answer to this memory demand are the novel e-NVM. In addition to being non-volatile, they offer higher density and endurance than the FLASH. Adding to this, the e-NVM memories offer a scalability advantage reaching below 20 nm nodes [7].

The volatile memory class comprises the usual DRAM and SRAM. The non-volatile class encompasses e-NVM and some standard memories, such as the FLASH and NVSRAM (non-volatile SRAM [8]). Inside the e-NVM the most promising technologies are the Ferroelectric RAM (FeRAM) [9, 10], Resistive RAM (RRAM) [11, 12], Phase-Change RAM (PCRAM) [13] and the Magnetic RAM (STT-MRAM), with schematics shown in Figure 1.1 (*b*). Although the mechanism driving these e-NVM technologies is different, they share a certain characteristic: after a certain external input, there is a measurable resistance change, allowing for the measure of a binary state 1 and 0. In these different technologies, there is a certain material, or materials, sandwiched between two metallic electrodes. For the RRAM this material is a metal oxide, such as $HfO_x$, $TaO_x$, $TiO_x$ and $AlO_x$. Through the use of an electric field, it is possible to induce the creation and motion of oxygen vacancies. This results in the formation of low resistance conductive filaments through the oxide.

Table 1: Performance indicators for several types of memory devices, from mature devices (SRAM, DRAM and FLASH) to e-NVM (PCM, RRAM and MRAM). The value F is taken as a the feature size, which refers to the minimum size of a single transistor gate width. Table redraw from [14]

| | FLASH | DRAM | SRAM | MRAM | PCM | RRAM |
|---|---|---|---|---|---|---|
| Non-volatile | Yes | No | No | Yes | Yes | Yes |
| Endurance | $10^5$ | $10^{16}$ | $10^{16}$ | $> 10^{15}$ | $10^8$ | $10^6$ |
| Read Speed (ns) | 50 | 30 | 1-100 | 2-20 | 20-50 | 10 |
| Write Speed (ns) | $10^4$ | 10 | 5-10 | 2-20 | 75 | 5-20 |
| Write power | Very High | Low | Low | Low to Medium | Medium | Low |
| Cell size ($F^2$) | 4 | 6-10 | 50-120 | 6-12 | 6-12 | 6-12 |
| Scalability | Yes | Limited | Limited | Yes | Yes | Yes |

By manipulating the electric field, one can create and destroy these filaments, bringing a change in resistance. The PCM, on the other hand, is based on the reversible transition between the crystalline and amorphous phase of a material (chalcogenide glass) through heating and cooling with different rates. This transformation, often triggered by the passage of current through the device (increase in temperature through Joule heating), results in different resistance levels. For the situation of the MRAM, there is not a single material placed between electrodes, but rather a multilayered structure. This can, in its core, be reduced to a magnetic tunnel junction (MTJ), *i.e.* two ferromagnetic layers spaced by a tunnel barrier. One of these layers has a fixed magnetization orientation (often labeled pinned layer or reference layer), while the other can be driven by an external stimuli. The relative orientation of the magnetization in these layers will result in different resistance states (high resistance if anti-parallel, and low resistance if parallel). The latter is the focus of this thesis and it will explored in detail during the remaining of the manuscript.

Even though none of these e-NVM shows an optimal set of parameters (table 1) (such as endurance, size and writing speed), depending on each application, they could replace some of the standard memories. For instance, the DRAM could be replaced by the STT-MRAM. Their speed is comparable, and the STT-MRAM is non-volatile. Compared with the FLASH memory, all the shown e-NVM show a competitive set of parameters. Nevertheless, the FLASH technology is quite inexpensive, being difficult to replace. At this moment, STT-MRAM finds its place for cache memory [15–17] and embedded MRAM for automotive applications [18, 19].

Nowadays we are witnessing an expansion of the MRAM memory market. Forbes [20] predicts that the market of the e-NVM will reach $20 Billion by 2029. One important point to be noticed is the drastic increase (compared with the other e-NVM types) in the MRAM revenues (expected to be dominated by the STT-MRAM) by 2029, with estimated revenues reaching around $4 billion, a 170× increase compared to 2018 [4, 20]. This prediction can be seen as a growth in the maturity of the technology and explains the companies entering in this highly competitive field. A diagram with the time-to-market perspective for each of these companies can be seen in Figure 1.2.

Even though the market viewpoint shows a promising future for this memory, the prospect for the long-term improvement of a technology is of high importance for its commercial uptake. Thus, it is important to revisit the first MRAM families and observe how they evolved and what can we

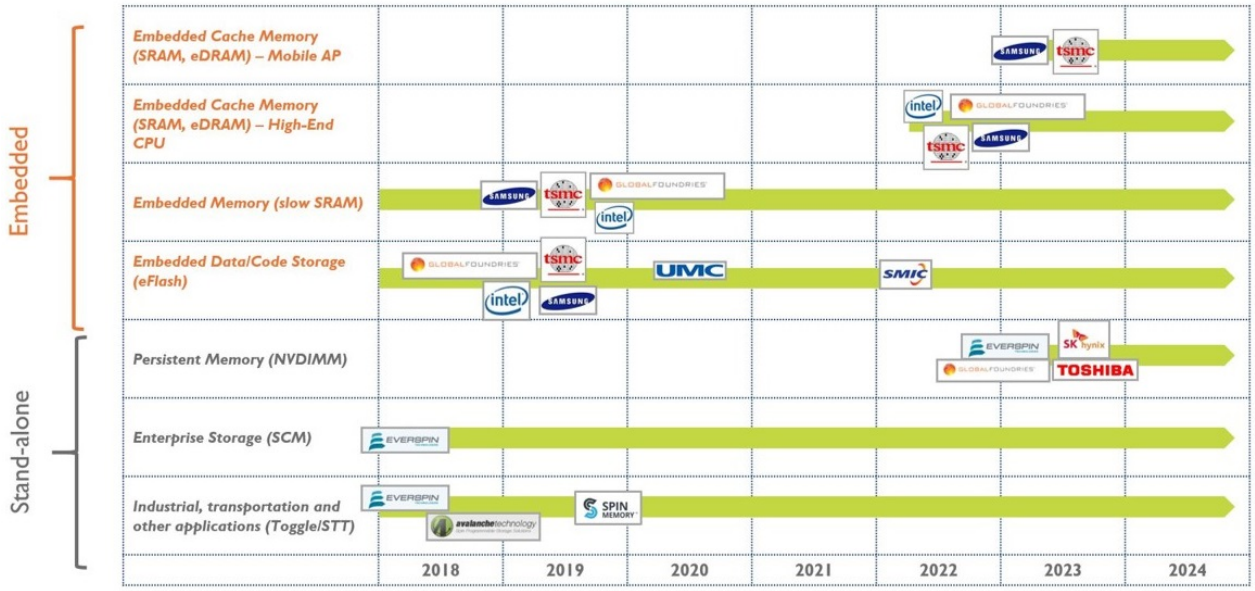


Figure 1.2: Time-To-Market for STT-MRAM actors, by applications, for stand-alone and embedded memory types. The time scale represents the entrance into the STT-MRAM market. An effort done by different companies in expected for the embedded market, mostly on possibly replacing SRAM and the embedded Flash Technology. Figure extracted and modified from [21].

expect from future engineered structures. For this purpose, a historical perspective of the road of the MRAM technology is shown and, lastly, the state of the art of the technology, exhibiting a competitive prospect for this research field.

## 1.2 The road towards the perpendicular STT-MRAM and beyond

The MRAM has, in its core, the MTJ, one of the most prevalent device in the field of spintronics, whose main characteristic is the combined manipulation of the spin and charge of the electrons [22]. This memory device defines bits 1 and 0 through the relative orientation of the magnetization in ferromagnetic layers, separated by an insulator layer, usually crystalline MgO. One of the magnetic layers has its magnetization pinned, behaving as a reference layer (RL). The other allows the manipulation of its magnetization, making possible the storage of information, being then denominated storage layer (SL) or free layer (FL). The insulator layer is called tunnel barrier (TB). When thin enough (typically less than 2 nm [23]), it enables the tunnelling of electrons. The resistance of the device is different depending on the relative orientation of the magnetization in the two ferromagnetic layers. The difference in resistance states defines the tunnel magnetoresistance (TMR),

$$\mathrm{TMR} = \frac{\mathrm{R_{AP}} - \mathrm{R_P}}{\mathrm{R_P}} \tag{1}$$

where $\mathrm{R_{AP}}$ is the resistance associated with the anti-parallel (AP) state of magnetizations and $\mathrm{R_P}$ the resistance state associated with the parallel (PP) state. The higher the difference in resistance, the easier it is to read the information in the device. Enhancing the crystallization of the layers promotes the tunnelling of spin polarized electrons, increasing the polarization efficiency.

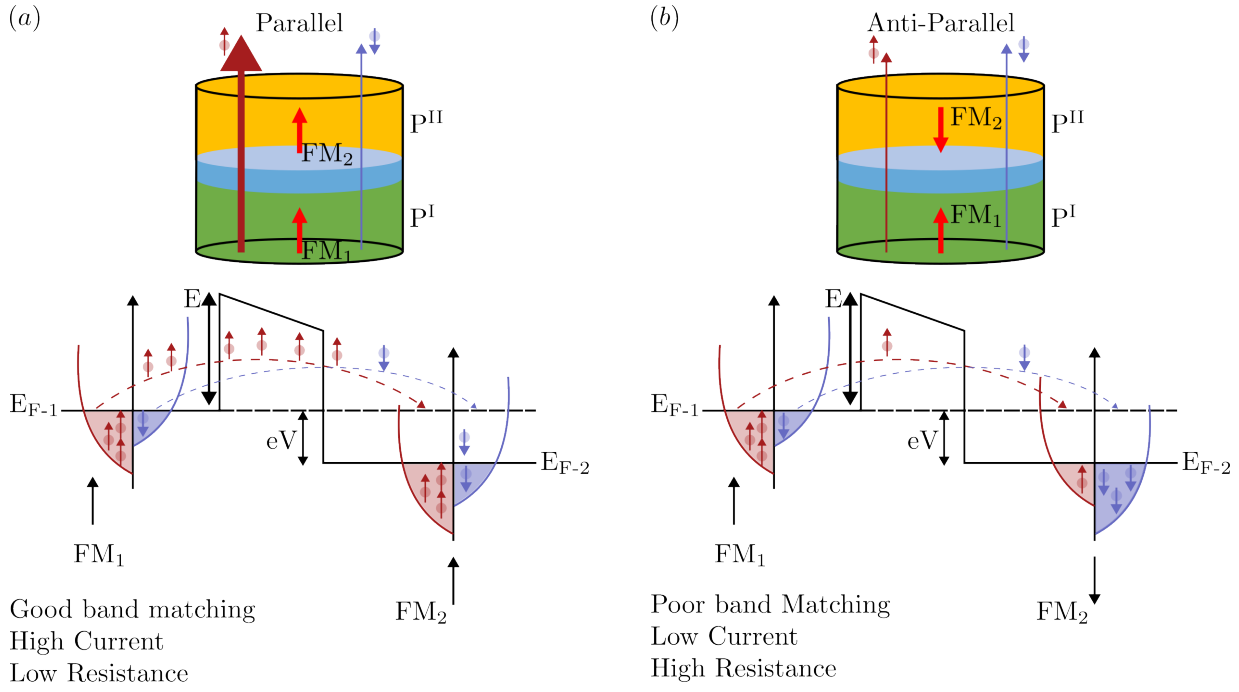


Figure 1.3: Schematics of the spin-tunnel transport for (*a*) parallel configuration and (*b*) anti-parallel configuration.

This phenomena can be understood considering the tunneling probability of the majority and minority spin-polarized currents between the parallel and anti-parallel alignments of the magnetization [24]. Figure 1.3 shows the basis of the spin-dependent tunneling transport for the situation of (*a*) a parallel alignment and (*b*) an anti-parallel alignment. When both magnetization are parallel, there is a good band matching, allowing a large number of conduction channels from majority bands to majority bands and from minority bands to minority bands. This results in a high current, linked with a low resistance. In contrast, for an anti-parallel magnetization state, the transport occurs from a majority band to a minority band and vice-versa, resulting in a low current passing through, associated with a high-resistance state. In this simplified approach, the tunneling probability is related with the density of states (DOS) and the number of occupied states at a given energy in the ferromagnetic metals in both sides of the tunnel barrier. By applying a bias voltage, the Fermi energy of one of the ferromagnets will decrease, causing a current flow from one ferromagnetic ($FM_1$) to the other ($FM_2$). The spin polarization of the conduction electrons contributing to the tunneling current can be expressed as:

$$P^i = \frac{DOS_\uparrow(E_{F-i}) - DOS_\downarrow(E_{F-i})}{DOS_\uparrow(E_{F-i}) + DOS_\downarrow(E_{F-i})}. \tag{2}$$

where $i$ is dependent on the ferromagnetic material (I or II).

Making use of the two-current model, which states that majority and minority currents will flow through parallel conduction channels, we can calculate the TMR making use of the polarization of each ferromagnetic layer (Jullière model, neglecting spin-flip scattering, magnon generation and

band structure effects)

$$\mathrm{TMR} = \frac{2\mathrm{P^I P^{II}}}{1 - \mathrm{P^I P^{II}}}. \tag{3}$$

The model of Jullière faces limitations when confronted with the high TMR values obtained in tunnel barriers consisting of crystalline MgO. This models disregarded the impact of Bloch states, which held validity only within amorphous barriers like $AlO_x$, where the coherency in these states is lost. However, in the case of a crystalline barrier, as it is the case for a MgO with bcc (001) crystalline texture, electrons can coherently tunnel between two ferromagnets exhibiting identical texture. A more complex model (labeled spin-filtering effect) was developed by Butler [25] and Mathon [26]. These account for the coupling between the wave function of the electrons in the ferromagnetic layer and the evanescent wave functions with similar symmetry in the tunnel barrier. This model shows that the polarization is different for the type of electron considered. Indeed, in a Fe|MgO system, it is found that the evanescent wave in the barrier decays much faster for some electronic bands ($\Delta_2$ and $\Delta_5$ ) than for others ($\Delta_1$). This means that the tunneling of $\Delta_1$ electrons is much more probable. In addition, for the $\Delta_1$ symmetry, there is only one spin population at the Fermi level, yielding a spin polarization of 100%. This is not the case for the $\Delta_2$ and $\Delta_5$ symmetries, as both majority and minority states coexist at the Fermi energy, making the polarization of these electrons neglegible. From these results, it was predicted TMR values above 1600% at room temperature [25, 26]. Unfortunately, these values have still not been reached, possibly due to imperfections in the crystalline structure and the possible contribution of $\Delta_5$ electrons as the thickness of the barrier is reduced. Nonetheless, values as high as 600% were reported in optimum conditions at room temperature [27].

This TMR value is one of the key requirements for a functional memory device, with values as high as TMR $>$ 200% necessary for a viable reading of the resistance state [28]. In addition to the high TMR necessary, we must be able to write information in our device and store it for a certain duration (retention time - application dependent, from a few seconds (SRAM-type) to around 10 years (DRAM-type)). Qualitatively, the information storage is dependent on the intrinsic magnetic properties of the storage layer, and is characterized by a thermal stability factor $\Delta$, which defines how long the memory chip can retain the information. This parameter is defined by the energy barrier ($\mathrm{E_B}$) that must be overcome for the magnetization in the storage layer to switch between two orientations (while turned off), divided by the thermal activation energy, defined as the product between the Boltzmann constant, $\mathrm{k_B}$, (of value $1.38 \times 10^{-23}$ $\mathrm{m^2\ kg\ s^{-2}\ K^{-1}}$) and the working temperature, T [23, 29]

$$\Delta = \frac{\mathrm{E_B}}{\mathrm{k_B T}}. \tag{4}$$

and, for a working device, should be $\Delta > 60$ for a 10 year retention in a 1 Gbit memory chip at room temperature.

During the last years, both academia and industry have sought to increase the stability of the device without increasing the current necessary to reverse the magnetization of the storage layer, while maintaining the desired scalability of the MRAM. Thus, different families of MRAM eventually evolved. In the first MRAM generation, the writing process requires an external applied magnetic

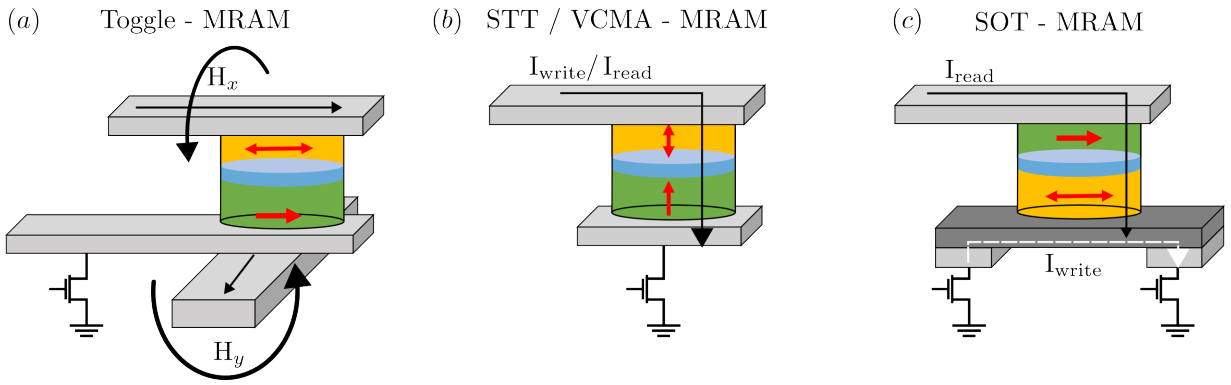


Figure 1.4: Schematics of different families of the STT family. In all situations the green layer is pinned and we are able to control the magnetization orientation of the yellow one

field to rotate the magnetization orientation in the storage layer (Toggle-MRAM, Figure 1.4 (*a*)). However, as the size of the memory cell decreases, a higher field is required to do the switching, resulting in a higher current through the selection lines and consequent increased power consumption [23]. These types of memories were the first in volume production [30], and still find their space from industrial automation to aerospace applications, thanks to their endurance and radiation tolerance [31]. An alternative method consists in the use of a spin-polarized current, relying on the STT effect (Figure 1.4 (*b*)). MRAMs based on this effect are called STT-MRAM and achieve a lower power consumption at increased bit densities as the current for the writing scales down with the device dimensions, bringing scalability alongside non-volatilily [32].

As the focus turns to STT based devices, different branches arise. In a first approach, the magnetization was oriented in the plane of the film (in-plane MTJ, ip-MTJ). A 64Mb DDR3 memory integrated on 90 nm CMOS based on this configuration was first introduced by Everspin [33]. However, it has been shown that a perpendicular orientation of the magnetization leads to an increase in thermal stability and reduction of the switching current. Additionally, these devices can be made circular, instead of ellipsoidal, making its fabrication easier and scalable. These devices are called perpendicular STT-MRAM (p-STT-MRAM) and use the interfacial perpendicular magnetic anisotropy (iPMA) originated from the interface between FeCoB layer and the MgO tunnel barrier [34]. These are now a somewhat mature technology, with several players on the market, such as Everspin (with its latest 22 nm node FDX pMTJ) and Samsung (at their 28 nm node ) [35]. Additionally, other memory architectures are under development. Attention is given to spin-orbit torque MRAM (SOT-MRAM) and voltage controlled magnetic anisotropy MRAM (VCMA-MRAM). The SOT-MRAM shows promise for high speed switching (relevant for SRAM replacement) and *virtual* unlimited endurance [36]. Contrary to the p-MTJ, the SOT-MTJ device has three terminals (2 transistors for 1 resistance, 2T1R), separating the reading from the writing path. This is crucial for high-speed applications, decreasing susceptibility to read disturbance and barrier degradation. The VCMA-MTJ, on the other hand, has a similar layout to the STT-MTJ (1 transistor per resistance, 1T1R) but instead of using a charge current, an electric field is used. This would allow for a much lower power dissipation, since there is a reduction of Joule heating. Recent studies have shown that it is possible to control, up to some degree, the iPMA of ferromagnet/oxide interfaces using

an applied voltage, and thus it would be possible to reduce the contribution of the iPMA to the stability of the system, up to the point where the magnetization of the storage layer would reverse. [23, 28, 37].

This thesis work is based in devices that are switched by STT. Thus, to fully explain their behaviour, it is necessary to provide some initial notions regarding magnetic anisotropy and STT reversal.

## 1.3 Physical background

### 1.3.1 Magnetic anisotropy

There are cases where, when describing magnetic properties of matter, no considerations are made regarding the relative orientation of the magnetization and particular orientations of the body. This case happens when the system is considered isotropic, *i.e.*, measurements of magnetic characteristics would yield the same value regardless of the chosen direction. However, in most real cases this is not true, and the material is said to posses magnetic anisotropy, being more easily magnetized to saturation when the magnetic field is applied along one direction (easy axis) than other directions (hard axis). The anisotropy energy ($E_{anisotropy}$) is an energy barrier which must be overcome to rotate the magnetization from the easy-axis to a hard-axis.

One of the possible anisotropy energies is the magnetocrystalline anisotropy, which is intrinsically related with the lattice throug spin-orbit coupling. This is a quantum relativistic effect which can be understood as a dipolar interaction between the spin of the electron and the magnetic field created by its own orbital motion [38]. Through this coupling, the spin is intrinsically coupled to the angular momentum of the hybridized orbitals of a crystal lattice. Thus, the magnetic moments have a predisposition to align along certain preferential crystallographic directions. Although quantum in nature, for the situation of unixial anisotropy, it can be defined as an energy per unit of volume ($J/m^3$)

$$\varepsilon_{uniaxial} = -K_u(\hat{n} \cdot \mathbf{m})^2, \tag{5}$$

where $K_u$ is an uniaxial anisotropy energy density constant, $\hat{n}$ is the unitary vector of the easy axis direction and $\mathbf{m}$ a unitary vector defining the magnetization, $\mathbf{M}$, direction [28].

Even though there are different anisotropy sources, a focus is made on the shape anisotropy, bulk anisotropy (for example, magnetocrystalline anisotropy) and interface-related anisotropy.

#### Shape anisotropy

The shape anisotropy results from magnetic dipolar anisotropy, when considered on a largely uniformely magnetized body. A magnetized body produces an intrinsic magnetic field, which is known for its long-range interaction [38]. This can be interpreted as if magnetic charges were left

at the surface of the ferromagnetic material (conceptual convenience), similar to the case of an accumulation of electric charges on the surface of the electrode of a capacitor, producing a magnetic field pointing in a direction opposite to that of the magnetization, known as the demagnetizing field $\mathbf{H_{demag}}$ [39]. This field is related with $\mathbf{M}$ through

$$\mathbf{H_{demag}} = -\mathcal{N} \cdot \mathbf{M}, \tag{6}$$

where $\mathcal{N}$ is a diagonal tensor, with a trace of 1.

When $\mathbf{M}$ is parallel to one of the axis of a ellipsoid, $\mathcal{N}$ is a number, characterized as the demagnetizing factor. Taking into consideration the demagnetizing field, we then obtain

$$\mathrm{E_{shape}} = -\frac{1}{2}\mu_0 \int_{\mathrm{V}} \mathbf{M} \cdot \mathbf{H}_{\mathrm{demag}} \quad \mathrm{dV}. \tag{7}$$

where $\mu_0$ is the vacuum permeability ($4\pi \times 10^{-7}$ H/m).

We rewrite the density of energy of the shape anisotropy as

$$\varepsilon_{\mathrm{shape}} = \frac{1}{2}\mu_0 \mathcal{N} (\hat{\mathrm{n}} \cdot \mathbf{M})^2 \tag{8}$$

### Anisotropy sources related to the coupling with the lattice

The source of anisotropy found in all materials and of bulk origin is the magnetocrystaline anisotropy (MCA).

$$\varepsilon^{\mathrm{bulk}} = -\mathrm{K_V} (\hat{\mathrm{n}} \cdot \mathbf{M})^2, \tag{9}$$

where $\mathrm{K_V}$ is a volume energy density (J/m$^3$). When this anisotropy is not purely uniaxial, additional terms must be considered. For instance, in an hexagonal structure, such as the case of Co, the MCA term can be written as

$$\varepsilon_{\mathrm{MCA}} = \mathrm{k}_1 \sin^2\theta + \mathrm{k}_2 \sin^4\theta, \tag{10}$$

where we define $\mathrm{k}_1$ and $\mathrm{k}_2$ as the first- and second-order anisotropy energy constants and $\theta$ the angle between the magnetization vector and the principal axis of symmetry. If we were to consider some anisotropy related with the basal plane, this description would require sixth order terms [38, 40]. Therefore, the symmetry of the MCA is closely linked to the symmetry of the crystalline structure.

Another source of anisotropy, highly relevant in thin films, and therefore important for MRAM, is of interfacial origin

$$\varepsilon^{\mathrm{interface}} = -\frac{\mathrm{k_s}}{\mathrm{L}} (\hat{\mathrm{n}} \cdot \mathbf{M})^2, \tag{11}$$

where $\mathrm{k_s}$ a surface anisotropy (J/m$^2$) and L the thickness of the magnetic layer [28]. This effect can occur at the interface of two different materials, where one of them is a ferromagnet. For certain combinations this anisotropy favours the alignment of the magnetization in a direction perpendicular to the plane. This possibility opened the doors to the p-STT-MRAM, being therefore heavily

researched [28, 38]. Combinations of Co/Pt and Co/Pd are known for having strong perpendicular magnetic anisotropy (PMA), related to an increase in the orbital momentum of the magnetic transition metal due to the strong hybridization between the 3d orbitals (of the transition metal) and the 5d orbitals (of the non-magnetic transition metal). This hybridization induces a charge transfer between the two layers which, combined with a strong spin-orbit coupling, leads to a PMA. The MRAM structure design was heavily impacted with the discovery of the iPMA arising from the overlap of the 3d orbitals of Fe and the 2p orbitals of O at the FeCoB/MgO interface [41, 42]. This allowed to bring the magnetization perpendicular (pMTJ), rather than in-plane, bringing scalability, higher stability and lower switching current.

It is quite straightforward that, by varying the different anisotropy sources, the magnetization in the material will align in the plane of the film or perpendicular to it, respectively, ip-MTJ and p-MTJ. This can be predicted from the effective perpendicular magnetic anisotropy of a thin film, considering the effect of iPMA, bulk anisotropy and shape anisotropy

$$\mathrm{K_{eff}} = \frac{\mathrm{k_s}}{\mathrm{L}} - \frac{\mu_0}{2} M_\mathrm{s}^2 + \mathrm{K_V}, \tag{12}$$

for the case of an infinitely long thin film. For a soft magnet, $\mathrm{K_V} \approx 0$, so the orientation of the magnetization depends on the strength of the surface anisotropy (which prefers a perpendicular alignment to the place) and the shape anisotropy (which, for an infinitely long thin film prefers a magnetization along the plane). In this situation the geometrical dependency of $\mathcal{N}$ is neglected, but for the situation of a MTJ will have a strong impact in the strength of the magnetostatic energy.

### Magnetic domains

When the magnetization is uniform according to some easy axis, as a result of the competition from the different anisotropies, it will create a dipolar field: stray field outside of the main ferromagnetic body and a demagnetising field inside of the ferromagnetic body. The magnetic material will try to reach the minimum energy state by reducing this dipolar field, as it makes some contribution to the magnetostatic energy. One way to do so is to break the material into magnetic domains, as proposed by Weiss [43]. For instance, if the material breaks into two domains the magnetostatic energy will be reduced because it will bring the magnetic poles closer to each other [44]. However, as we are considering that the magnetic domains appear inside the material as a result of short-range interaction, we must also account for the exchange energy which does not favour the appearance of domains at all, as it is minimized when neighbouring magnetic moments are parallel. This energy term is then written as

$$E_\mathrm{exchange} = -\mathcal{J} \sum_{\mathrm{i,j}} \mathbf{S}_\mathrm{i} \cdot \mathbf{S}_\mathrm{j}, \tag{13}$$

where $\mathcal{J}$ is the exchange integral (positive for a ferromagnetic coupling) and $\mathbf{S}_{\mathrm{i,j}}$ the spin of neighbouring magnetic moments. This means that the appearance of a magnetic domain wall, the region inside a magnetic body between domains with different orientations, comes with an energetic cost,

with the final result originating from the competition between magnetostatic and exchange energy. Considering different magnetic moments separated at the point where they do not interact with each other via exchange, the anisotropy energy (both uniaxial and magnetostatic) will overrule the exchange energy. For a Bloch wall, the bloch domain wall width $\gamma_B$ will depend on the competition between $K_u$ and $A_{ex}$

$$\gamma_B = \sqrt{\frac{A_{ex}}{K_u}}. \tag{14}$$

From this competition, the exchange interaction prefer a larger domain wall width, with incremental misalignment of the magnetization, while the uniaxial anisotropy prefers a thin wall [39, 43, 44]. Additionally, one can define the exchange length $\gamma_{ex}$ as the competition between the exchange interaction and the magnetostatic energy

$$\gamma_{ex} = \sqrt{\frac{2A_{ex}}{\mu_0 M_s^2}}, \tag{15}$$

which is indicative of a Neel domain-wall type, where the vector change is abrupt.

### 1.3.2 Spin transfer torque dynamics

The idea of the reversal of the magnetization of a magnetic layer using a spin-polarized current due to the STT effect was first predicted by Slonczewski [45] and Berger [46] in 1996. In 2004 this effect was first measured in a MTJ [47]. This idea of a spin polarized current interacting with the magnetization of the storage layer can be translated to an equation of motion, as additional terms to the conventional magnetization dynamics, which we introduce below.

As the storage layer is a ferromagnetic material, we must take into account the effective magnetic field $H_{eff}$, which includes a possible applied magnetic field $H_{app}$, anisotropy fields $H_K$, the demagnetization field $H_{demag}$ and stray fields arising from adjacent magnetic layers. As a first approach, we consider that all the magnetic moments inside the body rotate coherently towards a sufficiently strong external magnetic filed. This approximation receives the name macrospin, as the ferromagnetic body has as an uniform magnetization described by a direction and a magnitude (its saturation magnetization $M_s$). This model can be used in cases where the volume of the ferromagnetic material decreases down to the point where the formation of domain walls is energetically not favoured. In addition, the exchange energy term, equation (13) can be considered as a constant value in the total energy of the system, as long as the macrospin approximation remains valid.

The motion of a macrospin with respect to the effective magnetic field is conceptualized in the known Landau-Lifshitz (LL) equation

$$\frac{d\mathbf{m}}{dt} = \underbrace{[-\gamma\mu_0 \mathbf{m} \times \mathbf{H_{eff}}]}_{\Gamma_{precession}} + \underbrace{[-\alpha\gamma\mu_0 \mathbf{m} \times (\mathbf{m} \times \mathbf{H_{eff}})]}_{\Gamma_{damping}} \tag{16}$$

where $\mathbf{m}$ is the normalized magnetization vector, $\alpha$ is the total damping experienced by the magnetization, $\gamma$ the gyromagnetic ratio and $\mu_0$ the vacuum permeability [23, 48].

From the LL dynamics, Equation 16, we can realise that the first term, $\Gamma_{\text{precession}}$, acts as an undamped precession of $\mathbf{m}$ around $\mathbf{H_{eff}}$, with a frequency equal to the Larmor frequency, $\omega_{\text{Larmor}} = g\frac{2e}{2m_e}B$, where g is the g-factor of the electron, e is the electron charge and $m_e$ its mass [39]. The second term, $\Gamma_{\text{damping}}$, represents a damping of this precession (defined by $\alpha$), that will reduce $\mathbf{m}\times\mathbf{H}_{\text{eff}}$ until $\mathbf{m}$ aligns with $\mathbf{H_{eff}}$.

In a STT-MTJ the switching is achieved through a spin-polarized current [45, 46]. When a non-polarized current crosses the reference layer, it gains the direction of the magnetization in that layer. The polarized electrons are now transmitted throughout the tunnel barrier and exert a torque on the magnetization of the storage layer layer. This is the situation from antiparallel (AP) to parallel (PP) switching, visualized in the diagram of Figure 1.5 (*a*). If the two layers are aligned, there would be no torque that would bring the magnetization of the storage layer AP for this electron flow direction. Thus, the non-polarized current flows from the top of free layer, polarized by the magnetization in this layer. When crossing the tunnel barrier, the electrons with opposed spin to that of the reference layer are backscattered, exerting a torque in the magnetization of the free layer, as observed in the illustration of Figure 1.5 (b). Thus, through manipulating the current direction, it is possible to favor one of the states, AP or PP.

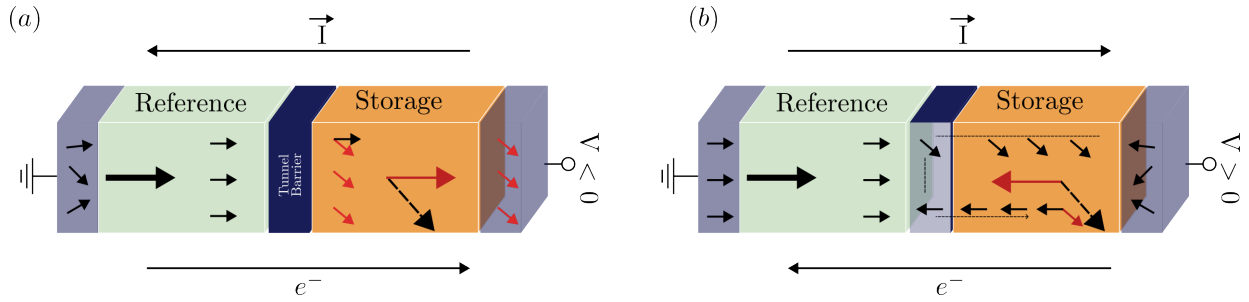


Figure 1.5: Schematics of the spin-transfer-torque effect in a MTJ for (*a*) AP-PP switching and (*b*) PP-AP switching.

This STT phenomenon is introduced in the LL equation as two additional torque terms, the IP torque (or damping-like torque), $\Gamma_{\text{STT}}^{\text{IP}}$, and the OOP torque (or field-like torque), $\Gamma_{\text{STT}}^{\text{OOP}}$. The resulting equation with added STT is called LLGS (LL Girlbert - Slonczewski) equation of motion and has the following representation

$$\frac{d\mathbf{m_{SL}}}{dt} = \Gamma_{\text{precession}} + \Gamma_{\text{damping}} + \Gamma_{\text{STT}}$$

with

$$\Gamma_{\text{STT}} = \underbrace{\left[-\gamma\mu_0\eta_{\text{STT}}\frac{\hbar J}{2e}\frac{1}{M_s L}\mathbf{m_{SL}}\times(\mathbf{m_{SL}}\times\mathbf{m_{RL}})\right]}_{\Gamma_{\text{STT}}^{\text{IP}}} + \underbrace{\left[\gamma\mu_0\eta'_{\text{STT}}\frac{\hbar J}{2e}\frac{1}{M_s L}\mathbf{m_{SL}}\times\mathbf{m_{RL}}\right]}_{\Gamma_{\text{STT}}^{\text{OOP}}}, \tag{17}$$

where J is the current density, L the storage layer (SL, for simplicity in the equation) thickness, $e$ the electron charge, $\eta_{\mathrm{STT}}$ the STT efficiency ($\sqrt{TMR(TMR+2)}/2(TMR+1)$ [49]), $\hbar$ the reduced Planck constant, $\mathbf{m_{RL}}$ the normalized vector defining the pinned magnetization in the reference layer and $\mathbf{m_{SL}}$ the normalized vector defining the magnetization in the storage layer.

Sometimes it is desirable to describe this effect taking into consideration an applied bias voltage $\mathrm{V_{Bias}}$. One can do so, resorting to some modification of the Equation 21 above

$$\frac{\mathrm{d}\mathbf{m_{SL}}}{\mathrm{dt}} = -\gamma\mu_0\mathbf{m_{SL}}\times\mathbf{H_{eff}} - \alpha\gamma\mu_0\mathbf{m_{SL}}\times(\mathbf{m_{SL}}\times\mathbf{H_{eff}}) - \gamma a_{\parallel}\mathrm{V_{Bias}}\mathbf{m_{SL}}\times(\mathbf{m_{SL}}\times\mathbf{m_{RL}}). \quad (18)$$

with

$$a_{\parallel} = \frac{\hbar}{2e}\frac{\eta_{\mathrm{STT}}}{\mathrm{RA}}\frac{1}{\mathrm{M_sL}} \quad (19)$$

defined as the STT pre-factor, using the following relation

$$\mathrm{J} = \frac{\mathrm{V_{Bias}}}{\mathrm{RA}}, \quad (20)$$

where RA is the resistance-area product of the storage layer. The latter is highly dependent on the materials adjacent to the MgO tunnel barrier, as well as the oxidation time of this insulator layer.

It is quite straightforward to realise certain similarities between the torques provided by the spin-polarized current and the usual torques from the LL equation. The first STT torque term, and the most relevant for STT-driven magnetization switching, is the so-called in-plane torque ($\Gamma^{\mathrm{IP}}_{\mathrm{STT}}$), since it lies in the plane defined by $\mathbf{m}_{\mathrm{SL}}$ and $\mathbf{m_{RL}}$. This term is frequently designated by damping-like torque, since it has the same term dependency ($\mathbf{a}\times(\mathbf{a}\times\mathbf{b})$) as the damping torque in the LL equation. The second STT torque term is labelled as field-like torque ($\Gamma^{\mathrm{OOP}}_{\mathrm{STT}}$), due to its similarities to the precessional term in the LLG equation ($\mathbf{a}\times\mathbf{b}$). This term is usually small when compared to the damping-like and, regularly, neglected when designing a STT-MRAM [28, 50–53]. Finally, it is possible to write the full LLGS equation, taking into account only the damping-like torque

$$\begin{aligned}\frac{\mathrm{d}\mathbf{m_{FL}}}{\mathrm{dt}} = &-\gamma\mu_0\mathbf{m_{FL}}\times\mathbf{H_{eff}} - \alpha\gamma\mu_0\mathbf{m_{FL}}\times(\mathbf{m_{FL}}\times\mathbf{H_{eff}}) \\ &-\gamma\mu_0\eta_{\mathrm{STT}}\frac{\hbar\mathrm{J}}{2\mathrm{eM_sL}}\mathbf{m_{FL}}\times(\mathbf{m_{FL}}\times\mathbf{m_{RL}}).\end{aligned} \quad (21)$$

Analysing Equation (21) it is possible to realise that the damping-like torque ($\Gamma^{\mathrm{IP}}_{\mathrm{STT}}$) can either reduce or enhance the effect of the damping torque, depending on the sign of the polarized-current. When $\Gamma^{\mathrm{IP}}_{\mathrm{STT}}$ opposes $\Gamma_{\mathrm{damping}}$, and overcomes its value in magnitude, the amplitude of precession increases to the point where magnetization switching can occur (as shown in the switching trajectory of Figure 1.6). The current at which this phenomena occurs is denominated by critical switching current $\mathrm{I_{c0}}$ written for the macrospin case and at 0 K (under no applied field $\mathrm{H_{eff}} = \mathrm{H_K^{eff}}$) [23, 28] as

$$\mathrm{I_{c0}} = \frac{2\mathrm{e}}{\hbar}\frac{\alpha}{\eta_{\mathrm{STT}}}\mu_0\mathrm{M_sALH_K^{eff}}. \quad (22)$$

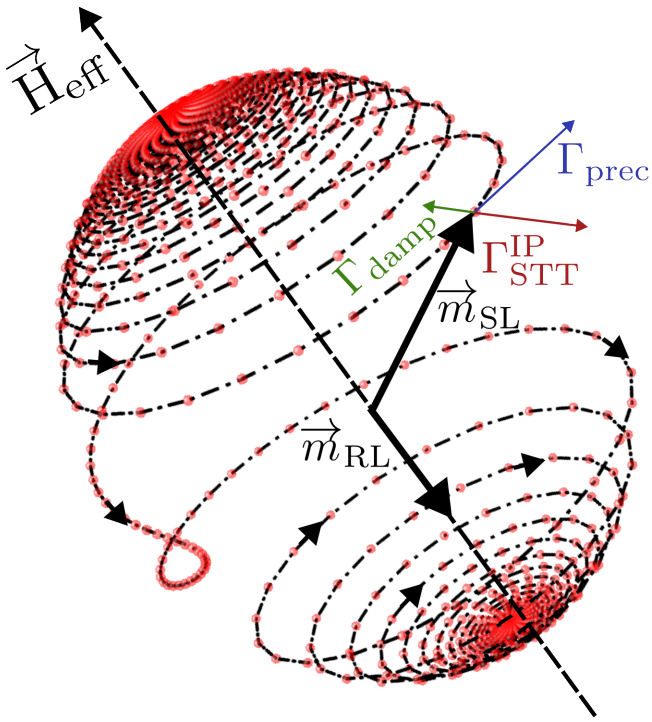


Figure 1.6: Trajectory of the magnetization switching induced by voltage described by the LLGS equation: the magnetization precession around the effective magnetic field ($\Gamma_{prec}$) term in blue, the precession damping ($\Gamma_{damp}$) in green and the damping-like torque $\Gamma^{IP}_{STT}$ in red which, in this situation, favour the alignment between $\vec{m}_{SL}$ and $\vec{m}_{RL}$.

It is important to realise that, in theory, if both magnetization in the storage and reference layer are perfectly collinear, there is no reversal driven by STT, as there can not be any torque exerted on the magnetization of the free layer, $\mathbf{m_{SL}} \times \mathbf{m}_{RL} = 0$. In real cases, thermal fluctuations introduce an initial misalignment of $\mathbf{m_{SL}}$ and $\mathbf{m_{RL}}$, promoting a sizable initial torque. Moreover, as it can be seen, $I_{c0}$ is proportional to the effective anisotropy field. Thus, an IP or OOP configuration of the magnetization will yield different values of critical current, as can be seen for an expanded equation

$$I_{c0} = \frac{2e}{\hbar}\frac{\alpha}{\eta_{STT}} M_s A L \mu_0 \left[H_{Ku} + H_{demag}\right], \tag{23}$$

where, for further simplification, and assuming that the switching only occurs due to the effect of the spin-polarized current, we neglect contributions from $H_{app}$. For the case of an IP magnetization, the dominating effect is the shape anisotropy, $H_{demag} >> H_{Ku}$. This happens because, during the STT-induced switching, the magnetization has to precess OOP, resulting in a huge increase of the shape anisotropy contribution to the magnetic energy.

On the other hand, by stabilizing the magnetization in an OOP direction through the use of perpendicular anisotropy fields that overcome the effect of the shape anisotropy ($H_{Ku} > H_{demag}$), the memory cells can be patterned as flat cylinders, allowing higher densities and a larger downsize scalability [28].

As already mentioned in section 1.2, this stability factor is dependent on the operation temperature (T), and on the energy barrier ($E_B$) one must overcome to reverse the orientation of the magnetization of the storage layer. Considering that this $E_B$ is the sum of anisotropy energies, we can establish an effective density of anisotropy energy ($K_{eff}$, similar to Equation 12) which is related to the effective anisotropy field :

$$\mu_0 H_K^{eff} = \frac{2K_{eff}}{M_s}. \tag{24}$$

Furthermore, knowing that the energy barrier is given by

$$E_B = K_{eff} V \tag{25}$$

we can rewrite

$$\Delta = \frac{\mu_0 M_s H_K^{eff} AL}{2k_B T}. \tag{26}$$

Finally, we are left with a proportional relation between $I_{c0}$ and $\Delta$

$$I_{c0} = \frac{4e}{\hbar}\frac{\alpha k_B T}{\eta_{STT}}\Delta \tag{27}$$

as long as the macrospin approximation remains valid.

As a conclusion, a relation between $\Delta$ and $I_{c0}$ can be extracted, as we are interested in memories with a high $\Delta$, promoting a high retention time, and a low switching current $I_{c0}$. This relation $\Delta/I_{c0}$ is usually used as a figure of merit, known as the switching efficiency of a MTJ [28, 54]

$$\frac{\Delta}{I_{c0}} = \frac{\hbar \eta_{STT}}{4e\alpha k_B T}. \tag{28}$$

For a p-STT-MRAM this ratio is larger than for an ip-STT-MRAM. However, this is only true as long as the damping does not grow larger, which is the case for perpendicular systems with FeCoB/MgO interface [28].

## 1.4 Motivation of the thesis

The STT-MRAM still faces some major challenges, predominately when the MTJ goes to sub-20 nm diameters. As the device lateral size shrinks, there is a decrease in $\Delta$ due to a decrease in the storage layer volume (see Equation 26, where $\mu_0 H_K^{eff}$ reduces with lateral size). This decrease significantly reduces the retention time of the memory. This limitation can be understood considering that at these small sizes the reversal of the magnetic volume is almost coherent, and so $\Delta$ is proportional to the storage layer volume. A proposal to counter this decrease is the use of a double FeCoB/MgO interface, by doubling the iPMA [55]. Still, it is challenging to keep $\Delta > 60$ at sub-20 nm diameters. A promising solution to this problem is a novel concept that takes advantage of the shape anisotropy of the storage layer by increasing its height to values of the order or larger than the device diameter. Thereby, the shape anisotropy no longer promotes an in-plane

orientation, but rather an out-of-plane, reinforcing the iPMA to further stabilize the magnetization in a perpendicular orientation. This concept of memory, named PSA-STT-MRAM, had been for the first time studied and experimentally developed simultaneously by SPINTEC [56–60] and Tohoku University [61, 62]. Promising as a viable candidate for DRAM replacement, this memory also holds significance in automotive applications due to its stability being primarily determined by the material's bulk magnetization, rather than surface anisotropy, making it resilient to high operating temperature [58, 59, 63–65].

Although this approach seems feasible to very high dense MRAM arrays, there are still several constraints that need to be addressed. The first and most dominant is the difficult fabrication of these very small nodes pillars. Due to the very high aspect-ratio and pillar shape, the wafer yield is small, with most of the pillars tilted or fallen. Moreover, the additional height of the storage layer promotes a larger shadow area during pillar etching, when compared with the usual p-MTJ. This limits the density of pillars one can attain. In addition, as the distance between devices gets shorter, there is an increasing stray field between different neighbours (affecting stability and also switching current). Apart from the fabrication point of view, the switching characteristics of the device itself is still not well understood due to the increased thickness of the storage layer. Indeed, since the STT has its effect mainly at the interface, it is necessary to understand how it will affect the switching of a thick layer. Moreover, a non-coherent reversal is expected as the layer grows thicker. In my dissertation work I address these different issues.

### Outline of the thesis

In an initial study (**chapter 2**) I make use of micromagnetic simulations (through a micro3D solver developed by Dr. Liliana Buda-Prejbeanu, SPINTEC) to understand the reversal mechanism of thick pillars under switching voltage [N. Caçoilo *et al.*, Physical Review Applied, **16** 024020 (2021)]. Additionally, I present possible improvements for switching speed and lower switching voltage, associated with a decrease in total thickness of the storage layer. To finish, a discussion regarding the limitation of scalability through the use of a single layer for the storage layer is done. In **section 3** I explore the scalability of the p-MTJ to sub-20 nm dimensions, through an optimization of the fabrication methodology done at PTA (*Plateforme de Technologie Amount*). I show that the device stability reduces with the diameter, as expected from the dependence of the surface anisotropy ($\propto D^2$). Although these devices would not be suitable for memory applications, I show that they have promise as stochastic devices, thanks to this superparamagnetic behaviour [N. Caçoilo *et al.*, under preparation (2023)]. By keeping the same stack composition, but increase the aspect-ratio of the storage layer, I show that we retrieve stability at diameters as low as 3.5 nm (for the sample explored in this document). In the end, a discussion is made regarding the need for lower R×A product of the tunnel barrier, showing STT switching in a device with an aspect-ratio larger than 1. In **section 4** I explore two alternative approaches for the fabrication of small node pillars, both making use of electrodeposition as the main piece for these approaches. In the first study, I make use of our collaboration with Dr. Laurent Cagnon (Néel Institute, Grenoble), to electrodeposit a metallic

material in pre-patterned holes defined by electron beam-lithography, on top of a MTJ at full sheet film. Starting with material as a hard-mask for the pillar definition, I show that it is possible to fabricate sub-20 nm (done at PTA) devices with a good shape, high TMR and STT switching [N. Caçoilo *et al.,* under preparation (2023)]. For the second study, a larger project, involving different colleagues at LETI (Dr. Maria Luisa, Dr. Guido Rademaker, Dr. Khatia Benotmane and Dr. Arnaud Cornélis), in Grenoble, and Fraunhofer (Dr. Lukas Gerlich and Dr. Maik Wagner-Reetz), in Dresden, Germany, is realized. In this approach, Co is deposited inside a matrix of nano-vias pre-patterned in $SiO_2$, from which I build the MTJ atop. This aims to show that the electrodeposition of Co in small nano-vias is a promising approach for high density PSA-MTJ [N. Caçoilo *et al.,* EP22204792.0, deposited: 31/10/2022]. Magnetic and structural characterization is realised at SPINTEC, with parallel imagining studies done at PFNC by Dr. Trevor Almeida and Dr. David Cooper (LETI, Grenoble). I developed a process flow for the integration of these nano-vias with the MTJ technology and validated it using conventional p-MTJ. To finish, in **section 5**, I develop an analytical and micromagnetic study along the possibility of using a core-shell structure to reduce the switching voltage of the PSA-MTJ. I show that this approach would give lower switching voltages and faster switching speeds, alongside a substantial reduction in cross-talk between magnetic devices [N. Caçoilo *et al.,* EP22204790.4, deposited: 31/10/2022, N. Caçoilo *et al.,*, under submission (2023)]. **Section 6** shows an overall conclusion of the work realised during my PhD studies, challenges faced and perspectives into future work that can be done using the knowledge acquired from this dissertation.

# 2 Improved switching dynamics in perpendicular shape anisotropy MTJ

As stated in the motivation of this dissertation, the behaviour governing the reversal of these small pillars is expected to deviate from the coherent regime because of the increased height and magnetic volume. Additionally, the effect of the STT is expected to occur mainly at the FeCo(B)|MgO interface. Both these facts make the use of macrospin simulations to describe the energy and reversal of the storage layer, rather limited. In this section we present a micromagnetic approach, which allows to better characterize the energetics and reversal dynamics of these thick pillars. Using this approach, we explore the physical phenomena happening during the switching of the magnetization of the storage layer under applied voltage, for different geometries. This groundwork allows us to optimize the storage layer for larger stability values and faster switching speeds, showing that there is a need to lower its height, which can be achieved by increasing the effective anisotropy field. This is the most effective to faster switching times, as it increases the effect of the STT along the height of the pillar.

This section is then divided in several subsections, evolving from the macrospin study of the energy barrier of the system, to the nature of the reversal dynamics under applied voltage. Based on these results, we study the main contributions for the switching time of the magnetization reversal and the limitations of the scalability of devices relying on a single thick storage layer. In each of these subsections a small conclusion is given, which sets up the next study.

## 2.1 Magnetostatic energy of a uniformly magnetized cylinder

To understand the benefits of the high aspect ratio storage layer compared to the usual thin storage layer used in conventional p-MTJ, it is necessary to first deepen the study of the magnetostatics of the storage layer. To do so, we employ a formalism based on the Fourier transform [66–68] that makes use of a shape amplitude function that defines the magnetization inside the magnetic body as $\overrightarrow{M}(\mathbf{r}) = M_\mathrm{s}\hat{\mathbf{m}}D(\mathbf{r})$, where $M_\mathrm{s}$ is the saturation magnetization, $\hat{\mathbf{m}}$ is the unitary orientation vector of the magnetization, and $\mathcal{D}(\mathbf{r})$ is the shape amplitude of the arbitrary magnetic volume (unitary inside the body and zero outside). For a magnetic cylinder with radius $R_0$ and height $L$ the shape amplitude in the k-space is given in cylindrical coordinates $(k_\perp, \theta, k_z)$ by [66]:

$$\mathcal{D}(k_\perp, k_z) = \frac{4\pi R_0}{k_\perp k_z}\mathcal{J}_1(k_\perp R)\sin(dk_z) \tag{29}$$

where $\mathcal{J}_1(x)$ is the Bessel function of the first kind, $k_\perp$ is $\sqrt{k_x^2 + k_y^2}$ and $d = L/2$ is defined for simplicity of the writing. Making use of the shape amplitude it is possible to calculate the demagnetising tensor as:

$$\mathcal{N}_{zz} = \frac{1}{8\pi^3 V}\int \frac{\mathrm{d}^3\mathbf{k}}{\mathbf{k}^2}|\mathcal{D}(\mathbf{k})|^2 k_z^2 \tag{30}$$

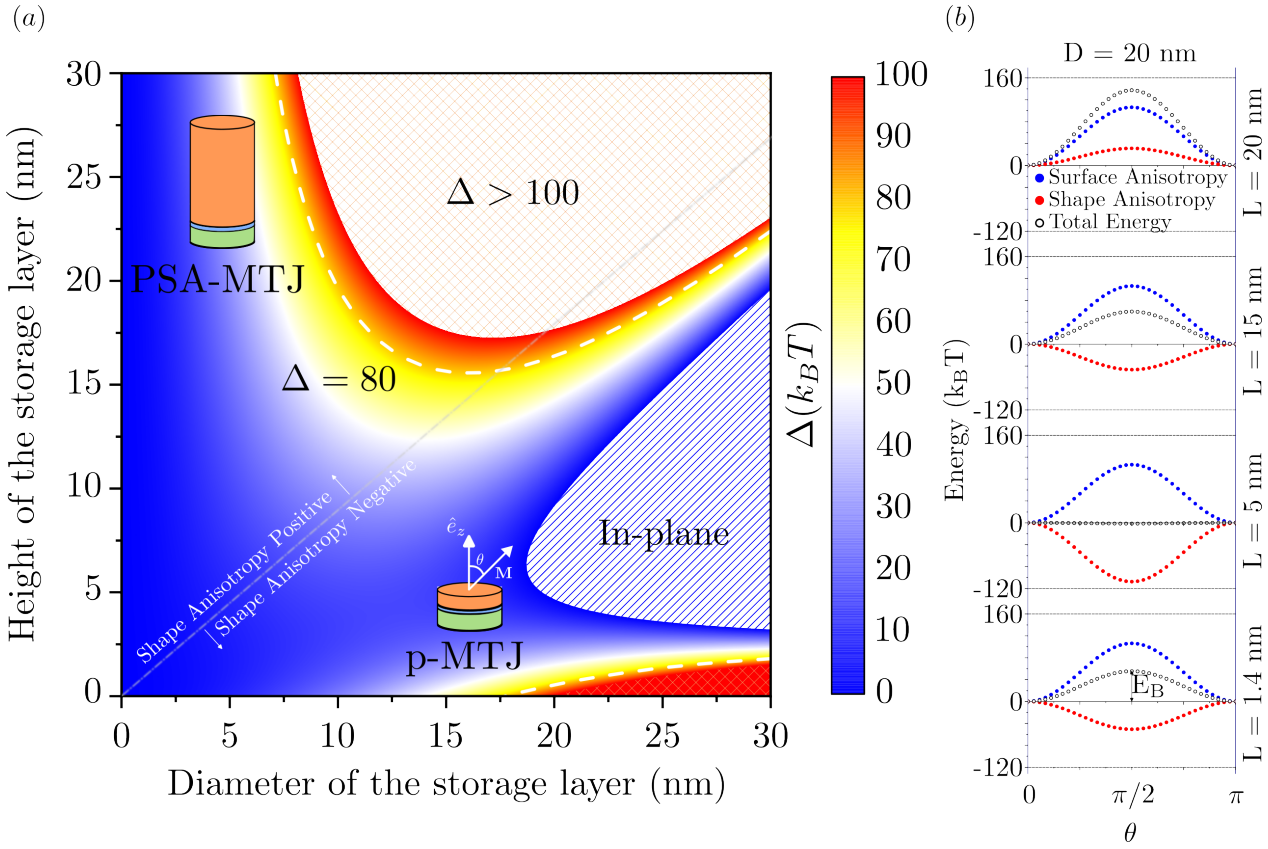


Figure 2.1: $(a)$ Stability diagram for different dimensions of the storage layer for a single FeCo(B)|MgO interface with a surface anisotropy of 1.4 mJ/m$^2$ for a interfacial thickness of 1.4 nm with a $M_s^{iSL} = 1$ MA/m. Increasing magnetic thickness is associated with $M_s^{tSL} = 1$ MA/m. The dashed gray line emphasizes the perpendicular and in-plane nature of the shape anisotropy, perpendicular for an aspect ratio above $\tau > 0.89$. The orange pattern shows a region with a stability greater than 100 $k_BT$ and the blue pattern shows the region where the magnetization has a preferential in-plane orientation. Orientation of magnetization shown for the case of the p-MTJ (perpendicular for $\theta = 0°$ and in-plane for $\theta = \pi/2$) $(b)$ Evolution of the different contributions to the total energy of the system for a 20 nm diameter and increasing thickness as a function of the angle between the magnetization and the normal to the plane: surface anisotropy (blue circles), shape anisotropy (red circles) and total energy (open black circles) for increasing thickness of 1.4 nm, 5 nm, 15 nm and 20 nm.

with $V$ the volume of the magnetic body defined by $\pi R_0^2 L$. After a series of integrations and transformations, it's possible to achieve a simpler notation for a single magnetised cylinder [67, 68]

$$\mathcal{N}_{zz}^{\text{cylinder}} = 1 + \frac{4}{3\pi\tau} - F_0\left(-\frac{1}{\tau^2}\right), \tag{31}$$

where $\tau$ is the aspect-ratio of the cylinder given by $L/2R_0$ and $F_0$ is a function shown for convenience, with ${}_2F^1$ a hypergeometric function (which can be related to elliptical integrals [69])

$$F_0(x) = {}_2F^1\left(-\frac{1}{2}, \frac{1}{2}, 2, x\right).$$

For the usual p-MTJ, due to the low aspect ratio of the storage layer (usually of the order of $L/2R_0 \approx 10^{-2}$, for a diameter of $20-80\,\text{nm}$ and a layer thickness of $0.8-2\,\text{nm}$) the magnetostatic energy is minimized for an in-plane alignment of the magnetization. Knowing that, since the trace of the demagnetizing tensor is unitary ( $N_{xx}+N_{yy}+N_{zz}=1$), to achieve a perpendicular orientation $N_{zz}$ must be $< 1/3$ ($N_{xx}=N_{yy}$ due to the cylindrical symmetry), which is attained at $\tau > 0.89$. The energy barrier can be expanded considering the different energies in the system (interfacial and magnetostatic) with their associated angular dependence

$$E(\theta) = V\left(-\frac{1}{2}\mu_0 M_s^2\left(\frac{3\mathcal{N}_{zz}-1}{2}\right)+\frac{k_s}{L}\right)\sin^2\theta, \tag{32}$$

where $\theta$ is the angle between the magnetisation and the normal to the plane of the magnetic cylinder. The selected normal vector ($\hat{n} \parallel \theta = 0°$) states that the energy is zero for a perpendicular magnetized cylinder and that it has its maximum (or minimum) energy state for an in-plane alignment of the magnetization.

Figure 2.1 shows a stability diagram for a cylinder geometry of the storage layer (height and diameter) for a FeCo(B) layer with saturation magnetization of $1\,\text{MA/m}$ and surface anisotropy $1.4\,\text{mJ/m}^2$ which are common values for MTJs. The separation between a preferred perpendicular orientation and a preferred in-plane orientation due to the effect of the shape anisotropy is shown with a dashed line. This diagram illustrates the limitation of the usual p-MTJ at small nodes, as the stability is reduced with diameter, decreasing below the required levels of 60-80 $k_BT$ at around 15 nm. It is possible to recover this stability by increasing the height of the pillar up to a point at which the magnitude of the negative contribution of the shape anisotropy no longer reduces the stability of the device, or by moving to a region in which the shape anisotropy prefers a perpendicular orientation of the magnetization (PSA) in which the stability increases steadily with an increased aspect ratio, leading to values larger than 100 $k_BT$ (shown with orange pattern). An illustration of the impact of the increase in aspect ratio for the different energy contributions for a fixed diameter value is shown in Figure 2.1 (*b*). For a height of 1.4 nm, it is seen that the shape anisotropy prefers an in-plane alignment of the magnetization, with a minimum of energy at $\theta = \pi/2$, but the surface anisotropy contribution is large enough to balance this preferential orientation and brings the magnetization perpendicular, leading to a total energy state that is minimized in a perpendicular configuration ($\theta = 0$ and $\theta = \pi$). As the height increases, there is a non-monotonous increase in the contribution of the total shape anisotropy $V(\mathcal{N}_{xx}-\mathcal{N}_{zz})$. For a height of 5 nm, the magnitude of the minimum of energy is much larger than that of the situation with a smaller height and is enough to overcome the competing surface anisotropy, bringing the magnetization in-plane. If the height is further increased, for instance to 15 nm, the magnitude of the minimum energy in the plane configuration is significantly reduced. Since the energy state brought by the surface anisotropy does not vary with height, this leads to a recovery of the perpendicular orientation with further stability enhancement. If we keep increasing the height and use an aspect ratio that allows for a preferential perpendicular orientation of the magnetization ($\tau > 0.89$), then we have an additional increase in the energy barrier, due to the now positive contribution of the shape anisotropy. The reduction of stability at low nodes can be compensated for by simply adjusting the height of the storage layer to

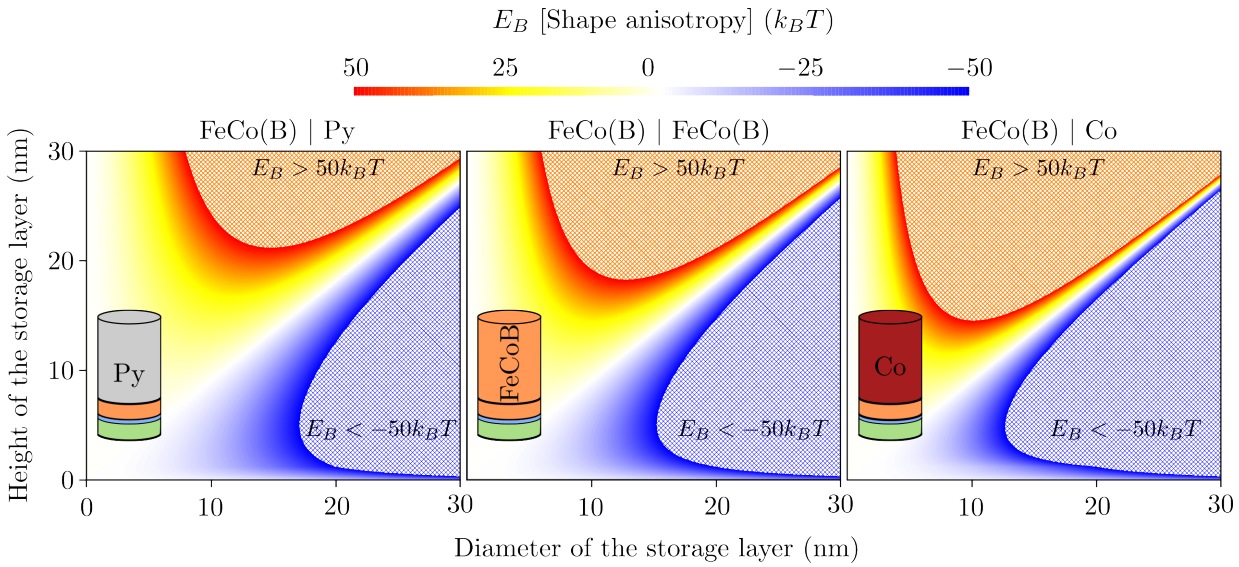


Figure 2.2: Contribution of the magnetostatic energy barrier to the energy barrier of the system for a thickness of interfacial FeCo(B) of 1.4 nm and increasing aspect ratio layer for different $M_s$: NiFe with $M_s = 0.789\,\mathrm{MA/m}$, FeCo(B) with $M_s = 1.0\,\mathrm{MA/m}$ and Co with $M_s = 1.446\,\mathrm{MA/m}$. The orange patterned region shows a region with $E_B > 50k_BT$ and the blue patterned region with $E_B < -50k_BT$, with a preferential in-plane orientation. Schematic of the storage layer in each diagram, with the FeCo(B) interfacial layer shown with an orange color, Py with a grey color and Co with a red color.

make use of the positive contribution of the shape anisotropy. Thus, below a certain diameter, for the situation of a cylinder, it is possible to maintain a perpendicular orientation with high stability up to a sub-5 nm diameter through an increase in height [56, 61].

Since magnetostatic energy is a key element in the thermal stability of the device, we show its individual contribution in Figure 2.2 for a FeCo(B) with a limiting interfacial thickness of 1.4 nm and for the increasing thickness of different magnetic materials with increasing $M_s$ ($M_s = 0.789\,\mathrm{MA/m}$ for NiFe (Py), $M_s = 1.0\,\mathrm{MA/m}$ for FeCo(B) and $M_s = 1.446\,\mathrm{MA/m}$ for Co). To maintain a valid macrospin model we assume that the magnetization of the magnetic body is the average of the magnetization along the height of the storage layer:

$$M_s^{SL} = \frac{M_s^{iFeCo(B)} L_{iSL} + M_s^{M_s(tSL)} L_{tSL}}{L_{iSL} + L_{tSL}}, \tag{33}$$

where iSL and tSL are related to interfacial storage layer and thick storage layer height, respectively. The most noticeable feature of these diagrams is the magnitude of the magnetostic energy barrier ($E_B^M$), associated with the minimum shown, for instance, in Figure 2.1 (*b*). Since the magnetostatic energy scales with $\propto M_s^2$, aspect ratios that show preferential alignments towards the in-plane orientation are heavily impacted by the increase $M_s$. Thus, there are different scenarios that need to be taken into account for the remainder of the section and the dissertation. If we want to fabricate a memory device with low aspect ratio ($\tau < 0.89$) in which the shape anisotropy promotes an in-plane orientation, it is more suitable to use a material with lower $M_s$ rather than the use of a material with

a high $M_s$, as the shape anisotropy will have a larger role in the stability of the magnetic system. Nonetheless, as long as we remain in a single layer regime, the higher stability will be given by the increased aspect ratio ($\tau > 0.89$), and thus a higher $M_s$ is preferred.

This memory shows a clear path for a high density memory array with high stability and a wide range of application temperature [58, 59, 63, 65]. However, there is a certain limit in which the macrospin model is no longer valid to represent the energy barrier and the reversal dynamics of this thick magnetic layer [62, 70]. To fully understand the limitations associated with this novel memory element, we use a micromagnetic formalism to explain the reversal mechanism of these small node pillars.

## 2.2 Micromagnetic model

The micromagnetic theory uses a continuum description of the magnetization of a ferromagnetic material (Figure 2.3):

$$\mathbf{M}(\mathbf{r}, t) = M_s \mathbf{m}(\mathbf{r}, t), \tag{34}$$

where $\mathbf{m}$ is the unitary vector defining the orientation of the magnetisation in each point in space $\mathbf{r}$. This first interpretation is the first step towards the micromagnetic description of a magnetic body and it was first described by Brown [71].

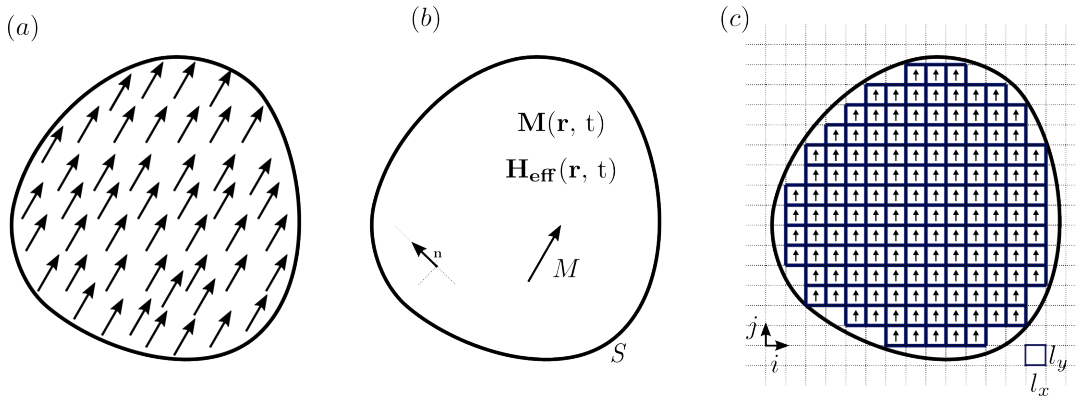


Figure 2.3: Micromagnetic description of a ferromagnetic material with surface $S$. $(a)$ Schematic of the magnetic moments of the ferromagnetic material $(b)$ continuous approximation of the magnetisation $\mathbf{M}$ in the space $\mathbf{r}$ of the ferromagnetic material with normal vector to the surface $\mathbf{n}$ and $(c)$ associated discrete approximation of the magnetic material in which each discretized cell has a 2D length of $l_x$ and $l_y$. Figure based from [72]

Moreover, the different interactions acting on the magnetic system will lead to different equilibrium magnetization arrangements. Taking these into consideration, the micromagnetic theory allows us to forecast the temporal evolution of the configuration of the magnetization of the magnetic body [71]. For this purpose, the different energy terms presented in the preceding section (1.3) are rewritten, taking into consideration the assumptions made before regarding the nature of the magnetization.

In this model, in contrast with the macrospin framework, the exchange energy ($E_{\text{ex}}$) is taken into account, as the different neighboring spins can be misaligned, being minimized for a parallel arrangement. As this interaction is short-range, only neighboring spins need to be accounted for. Making use of the continuous description, it is possible to express the exchange energy as

$$E_{\text{ex}} = \int_V A_{\text{ex}} \left( [\nabla m_x(\mathbf{r})]^2 + [\nabla m_y(\mathbf{r})]^2 + [\nabla m_z(\mathbf{r})]^2 \right) \mathrm{d}\mathbf{r}, \tag{35}$$

with $A_{\text{ex}}$ the exchange stiffness [J/m]. Still within this continuous approach, it is possible to extend the description of uniaxial anisotropies, such as PMA (MCA for instance) and interfacial (iPMA from the FeCo(B)|MgO interface):

$$E_{\text{uniaxial}} = \int_V K_{\text{u}} \left( 1 - [\mathbf{u_k} \cdot \mathbf{m}(\mathbf{r}, \mathbf{t})]^2 \right) \mathrm{d}\mathbf{r} \tag{36}$$

where $\mathbf{u_k}$ is the unit vector parallel to the easy axis of the material and $K_{\text{u}}$ is the unixial anisotropy constant $\left[\text{J/m}^3\right]$. The magnetostatic energy follows the same principle:

$$E_{\text{shape}} = -\frac{1}{2}\mu_0 M_{\text{s}} \int_V \mathbf{m}(\mathbf{r}, \mathbf{t}) \cdot \mathbf{H}_{\text{demag}}(\mathbf{r}, t) \mathrm{d}\mathbf{r}, \tag{37}$$

where $\mathbf{H}_{\text{demag}}(\mathbf{r}, t)$ is a time and position dependent demagnetizing field. As for the situation of the resulting energy from an interaction between the magnetisation of the magnetic body and an applied magnetic field $\mathbf{H}_{\text{applied}}$ (which can be time dependent), usually referred to as Zeeman energy:

$$E_{\text{Zeeman}} = -\mu_0 M_{\text{s}} \int_V \mathbf{m}(\mathbf{r}, \mathbf{t}) \cdot \mathbf{H}_{\text{applied}}(\mathbf{r}, t) \mathrm{d}\mathbf{r}. \tag{38}$$

It should be noted that these expressions allow for space dependence of the magnetization, while in the macrospin model $M_{\text{s}}$ is uniform throughout the entire volume.

Making use of these different energy contributions, it is possible to express the effective magnetic field $\mathbf{H}_{\text{eff}}$ as the variational derivative of the Gibbs free energy density $\varepsilon_{\text{tot}}$

$$\mathbf{H}_{\text{eff}} = -\frac{1}{\mu_0 M_{\text{s}}} \frac{\delta \varepsilon_{\text{tot}}}{\delta \mathbf{m}} \tag{39}$$

where $\varepsilon_{\text{tot}}$ encompasses the energy densities present in the magnetic system

$$\varepsilon_{\text{tot}} = \varepsilon_{\text{Zeeman}} + \varepsilon_{\text{shape}} + \varepsilon_{\text{uniaxial}} + \varepsilon_{\text{exchange}} \tag{40}$$

The variational principle states that, at equilibrium, the distribution of the magnetisation inside the magnetic body satisfies the energy relations:

$$\delta E_{\text{total}}(\mathbf{m}) = 0$$

$$\delta^2 E_{\text{total}}(\mathbf{m}) > 0$$

where $\delta E_{\text{total}}(\mathbf{m}) = E_{\text{total}}(\mathbf{m}+\delta\mathbf{m}) - E_{\text{total}}(\mathbf{m})$ is the infinitesimal variation of the energy induced by the small change in the function $\delta\mathbf{m}$. Making use of the equations shown before:

$$\delta E_{\text{total}}(\mathbf{m}) = \mu_0 M_{\text{s}} \int_V \left( \frac{2A_{\text{ex}}}{\mu_0 M_{\text{s}}} \nabla^2 \mathbf{m} + \frac{2K_u}{\mu_0 M_{\text{s}}} (\mathbf{u_k} \cdot \mathbf{u_k}) \mathbf{u_k} + \mathbf{H}_{\text{applied}} + \mathbf{H}_{\text{demag}} \right) \cdot \delta\mathbf{m} \mathrm{d}V + \oint_S 2A_{\text{ex}} \left( \mathbf{m} \times \frac{\partial \mathbf{m}}{\partial n} \right) \mathrm{d}S \quad (41)$$

The first quantity can be defined as an effective magnetic field

$$\mathbf{H}_{\text{eff}} = \frac{2A_{\text{ex}}}{\mu_0 M_{\text{s}}} \nabla^2 \mathbf{m} + \frac{2K_u}{\mu_0 M_{\text{s}}} (\mathbf{u_k} \cdot \mathbf{u_k}) \mathbf{u_k} + \mathbf{H}_{\text{applied}} + \mathbf{H}_{\text{demag}} \quad (42)$$

which comes from Equation 39 as long as:

$\frac{\partial \mathbf{m}}{\partial n} = 0$, for any point in space inside the defined magnetic surface $S$.

$\mathbf{m}(\mathbf{r}, t) \times \mathbf{H}_{\text{eff}}(\mathbf{r}, t) = 0$, for any point inside the specified magnetic volume $V$.

These two conditions are the basis of the Brown formalism and are thus defined as Brown's equations. They describe the equilibrium state of the magnetization; however, they do not describe the dynamics of the magnetization under under voltage or magnetic field. To understand the dynamical behaviour of the magnetization during the reversal process, the LLGS equation is implemented in this micromagnetic framework as

$$\partial_t \mathbf{m_{SL}} = -\gamma\mu_0 (\mathbf{m_{SL}} \times \mathbf{H}_{\text{eff}}) + \alpha (\mathbf{m_{SL}} \times \partial_t \mathbf{m_{SL}}) + \Gamma_{\text{STT}}^{\text{IP}}, \quad (43)$$

where $|\gamma|$ is the gyromagnetic ratio, $\mu_0$ the vacuum permeability and:

$$\Gamma_{\text{STT}}^{\text{IP}} = -|\gamma| a_{\parallel} V_{\text{applied}} \mathbf{m_{SL}} \times (\mathbf{m_{SL}} \times \mathbf{m}_{\text{RL}}) \quad (44)$$

where $a_{\parallel}$ is the pre-factor of the damping-like torque, $V_{\text{applied}}$ the applied voltage across the tunnel barrier, $\mathbf{m_{SL}}$ the normalized magnetization vector of the storage layer and $\mathbf{m}_{\text{RL}}$ the normalized magnetization vector of the reference layer. To solve numerically this equation of motion, it is necessary to subdivide the ferromagnetic body into different elementary units, either in surface, with size $l_x \times l_y$, or in volume, with size $l_x \times l_y \times l_z$. Moreover, as these are differential equations, the most direct method to solve them is to use the finite difference approximation. Thus, a prismatic grid is needed, as shown in the example of Figure 2.3 (*c*). Even though the use of the regular grid might bring about a constraint in the exact description of the geometry of the ferromagnetic body, it is quite powerful regarding computational time as it is possible to use the fast Fourier transform in the calculation of the magnetostatic contributions. Nevertheless, one can reduce the issue in the physical description by reducing the unitary cell size, although it is associated with a heavier computational burden. It is then important to know which is the maximum cell size that is suitable to our magnetic system. This is related with the typical scale at which the magnetization can vary,

and thus related with the exchange length $\gamma_{\text{ex}}$ and the Bloch length $\gamma_{\text{B}}$, defined in section 1.3.1. The selected cell size has to be smaller than both lengths for an accurate description of the effect of the neighboring magnetic moments [73].

Other important parameter to be taken into account is the integration step of the simulation $\Delta t_s$, which is computed considering that:

$$\Delta t_s \leq \frac{1}{2}\frac{\alpha}{|\gamma|(\mu_0 M_{\text{s}})}\frac{1}{\left(\frac{\gamma_{\text{ex}}}{l_x}\right)+\left(\frac{\gamma_{\text{ex}}}{l_y}\right)+\left(\frac{\gamma_{\text{ex}}}{l_z}\right)} \tag{45}$$

where $l_x, l_y$ and $l_z$ are the 3D cell size and $\alpha$ the damping used for the simulation [72]. For this work, a finite-difference 3D micromagnetic solver is used to simulate the magnetic system [74]. Within this framework, it is possible to achieve two different results: dynamical results based on the LLGS equation but also the calculation of the energy barrier making use of the Minimum Energy Path (MEP). To compute this minimum energy path using the micro 3D solver we need to compute the energy of the system in its initial orientation, for instance parallel (PP) and then its final energy state, anti-parallel (AP). This is done by relaxing the system with the LLG equation (without any external stimuli) with a large damping value (in this situation $\alpha = 1$) until there is no variation in the energy of the system. Because there is no consideration regarding interaction with the reference layer, the energy of the system is similar in both parallel and antiparallel configurations. Moving forward, a number of N micromagnetic state is generated and numbered from 1 to N, where 0 and N + 1 are the initial and final states. Following the relaxation, there is a linear extrapolation between the states (including the initial and final states) using the string method [75–80]. This redefines the values for the N intermediate steps until the energy between two consecutive iterations is below a certain defined threshold ($E^{i+1} - E^i < 1 \times 10^{-5}$ J/m$^3$ in this work).

In this study, we focus on pillars with a square base diameter of 20 nm and increasing pillar height, with $M_{\text{s}} = 1$ MA/m and $\text{A}_{\text{ex}}$ of 15 pJ/m. For the MEP calculation we use a high damping for fast relaxation ($\alpha = 1$) and no external stimuli ($\text{H}_{\text{applied}} = 0$, $\text{V}_{\text{applied}} = 0$). Due to the high aspect ratio of this system, in contrast with the usual p-MTJ, we implement an exponential decay of the interfacial effects [81, 82], such as surface anisotropy $k_s$ and spin-trasfer-torque efficiency $a_{\parallel}$. For the surface anisotropy, it is implemented as a volumic anisotropy (due to the 3D nature of the elementary cell) that decays through the height of the pillar as

$$K_u(z) = K_0 \exp\left(-\frac{z}{\lambda_{\text{Ku}}}\right), \tag{46}$$

where $\lambda_{\text{Ku}}$ defines the decay length of the interfacial perpendicular magnetic anisotropy (iPMA) throughout the height of the pillar. The value of the coefficient $K_0$ is then adjusted so that the incremental sum of the areal value of $K_{\text{u}}$ results in $k_{\text{s}}$, which is taken to be 1.4 mJ $\cdot$ m$^{-2}$:

$$k_{\text{s}} = K_0 \sum_{i=0}^{N_z-1} l_{\text{z}} \exp\left(-\frac{i l_{\text{z}}}{\lambda_{Ku}}\right) \tag{47}$$

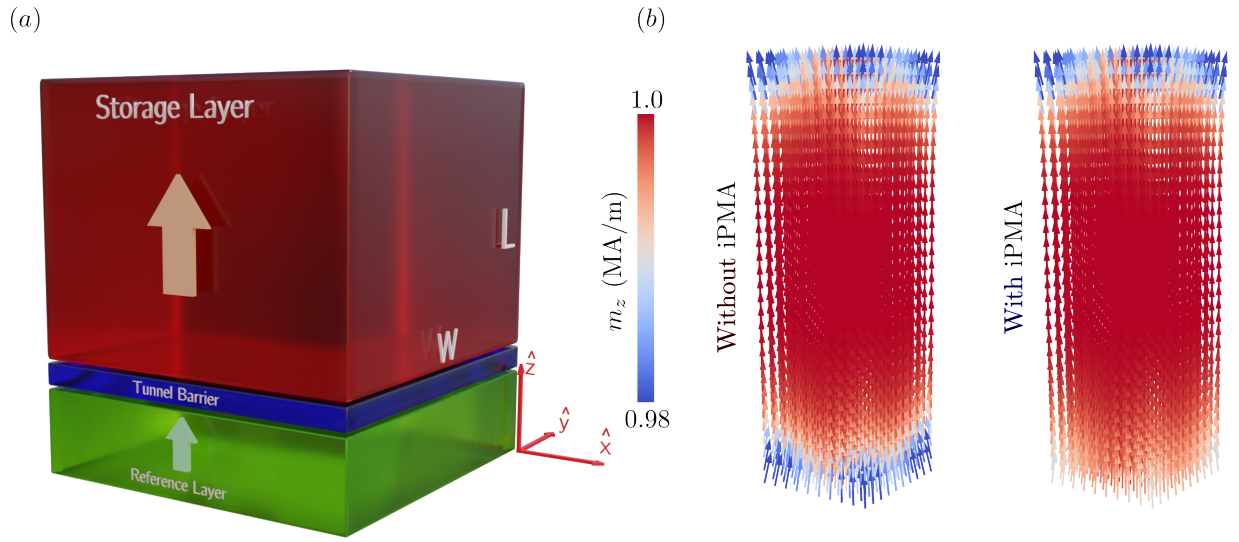


Figure 2.4: ($a$) 3D scheme of the studied FeCo(B) prism with height $L$ and base width $W$. The storage layer is shown with a red color, the tunnel barrier with a blue color and the reference layer with a green color. ($b$) 3D equilibrium initial state of a 60 nm-thick FeCo(B) layer without iPMA and with iPMA at the interface with the tunnel barrier. The color bar indicates the normalized magnitude of the magnetization along the defined z direction (along the square prism axis) in each computational cell.

with $N_z$ the number of computational cells layers along the defined evanescent orientation ($\hat{z}$).

As a first approximation, since the elementary cell is cubic, we use a square-shaped pillar, with a base width $W$ and height $L$ [Figure 2.4 ($a$)]. In this situation we have a strongly pinned reference layer with the magnetization pointing up along $+\hat{z}$, the tunnel barrier and a storage layer with magnetization pointing up $+\hat{z}$ (thus parallel to each other). The storage layer after the relaxation step is shown in Figure 2.4, for the case with ($b$) and without ($c$) the influence of the iPMA (surface anisotropy from the MgO | FeCo(B) interface). For the situation without surface anisotropy, a tilt of the magnetization (signature of the demagnetising interaction) at both top and bottom surfaces is observed along the pillar axis direction. This is commonly known as flower state [83], symmetrical as only the shape anisotropy induces the perpendicular orientation, being more pronounced because of the square shape. When a source of iPMA is introduced at the bottom surface, a sturdier perpendicular orientation is enforced. In addition, as the effect of the surface anisotropy is implemented only at the first interface, the magnetic display of the top surface is similar to that without $K_u$ due to the decay of the surface anisotropy.

## 2.3 Reversal dynamics of a single thick layer PSA-MTJ

After the magnetic state with iPMA is relaxed ($\alpha = 1$), a spin-polarized current is injected. Since the injection of this current physically occurs close to the FeCo(B)|MgO interface, it is expected that the spin polarization decays exponentially through the interaction with the magnetic moments

[81, 82]. We can model this behaviour considering that the magnitude of $a_{\parallel}$ decreases spatially as:

$$a_{\parallel} = a_0 \exp\left(-\frac{z}{\lambda_{\mathrm{STT}}}\right), \tag{48}$$

where $\lambda_{\mathrm{STT}}$ defines the length scale of the spin-transfer-torque decay. The value of the coefficient $a_0$ can be obtained knowing that the averaged sum of each plane of computational cells along the storage layer height will result in the macrospin value of $\langle a_{\parallel} \rangle$ in the first cell layer

$$\langle a_{\parallel} \rangle = \frac{\hbar}{2|e|} \frac{\eta_{\mathrm{STT}}}{\mathrm{R} \times \mathrm{A}} \frac{1}{M_{\mathrm{s}} l_z}.$$

From this value, it is possible to calculate the coefficient $a_0$ as follows:

$$\langle a_{\parallel} \rangle = \frac{a_0}{N} \sum_{i=0}^{N-1} \exp\left(-\frac{i l_{\mathrm{z}}}{\lambda_{\mathrm{STT}}}\right), \tag{49}$$

where $N$ is the number of elementary cells along the propagation direction ($\hat{z}$ in our specific situation), $l_z$ the cell size (which will vary for the different magnetic systems), the R × A product should be of the order of 1 to $2\,\Omega\cdot\mu\mathrm{m}^2$ to avoid excessive write voltages, which can otherwise cause dielectric breakdown of the tunnel barrier [84–86].

### 2.3.1 Increasing aspect ratio for prisms with similar base width

Through the use of the micromagnetic formalism and the description given for the interfacial effects, we study the nature of the magnetization reversal under applied voltage for magnetic pillars with different heights. We consider a set of magnetic prisms with 20 nm base width and different pillar height ($L = 16, 18, 20, 30, 40, 50$ and 60 nm). The increasing aspect ratio of the pillars will lead to a higher thermal stability as expected from the stability diagram of Figure 2.1. The role of the increase in aspect-ratio in (i) the time to reverse the magnetization in the layer (*i.e.* PP - AP) [60] (ii) the coherence of the magnetization reversal [62, 70] and (iii) in the switching voltage [87], has been investigated both by simulation and experimentally. To further understand this effect, we assume a cell size of $l_{x,y,z} = 2$ nm such that $N_{x,y,z} = L_{z,y,z}/2$ nm. These values are taken knowing that the critical lengths $\gamma_{\mathrm{ex}}$ and $\gamma_B$ are 4.9 nm and 3.3 nm, respectively. For the transport properties, we assume that we can achieve values of TMR of around 100% at low R× A products (leading to an STT efficiency $\eta_{\mathrm{STT}} = 0.43$). Making use of the description of $a_0$ presented in Equation 49 with a decay length of 1 nm (order of the cell size) we use a value at the interface of $a_0 = 60\,\mathrm{mT/V}$. In addition, the surface contribution from the FeCo(B)|MgO is assumed to be of $K_0 = 0.61\,\mathrm{MJ/m^3}$ with a decay length of 1 nm (order of the cell size). We assume that the initial state is PP so that the electrons are reflected near the FeCo(B)|MgO interface, a phenomenon that can be translated into a negative voltage across the MTJ in these simulations. A voltage of $-3$ V is applied to the different set of prisms. This is done neglecting critical voltage values, as it would not be possible to realize experimentally due to the dielectric breakdown of the MgO. During magnetization reversal

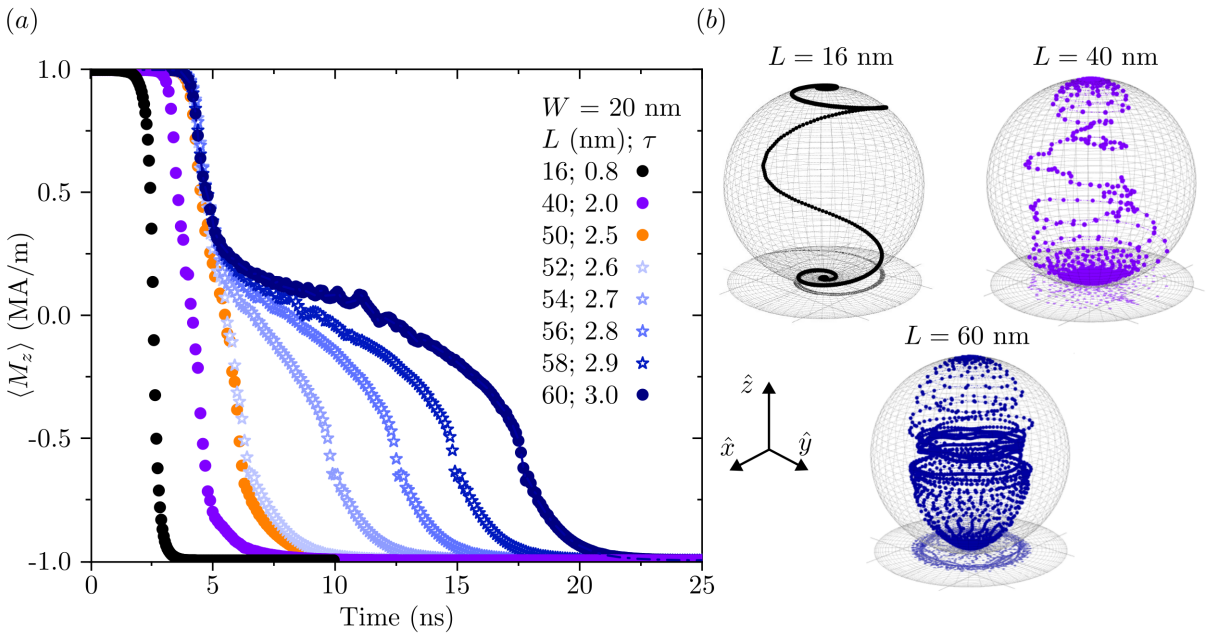


Figure 2.5: $(a)$ Time trace of the mean perpendicular magnetization $\langle m_z \rangle$ for a storage layer with fixed base width of 20 nm and increased aspect ratio for an applied voltage of $-3$ V and $(b)$ switching trajectories of the magnetization for different heights of 16 nm (black spheres), 40 nm (violet spheres) and 60 nm (blue spheres).

it is possible to extract the volume average of the different magnetization components $\langle m_{\mathrm{x,y,z}} \rangle$. These values are averaged through the magnetic volume so that, during the reversal, the quantity $\sqrt{\langle m_\mathrm{x} \rangle^2 + \langle m_\mathrm{y} \rangle^2 + \langle m_\mathrm{z} \rangle^2}$ is not necessarily 1, while for each individual cell $\sqrt{m_\mathrm{x}^2 + m_\mathrm{y}^2 + m_\mathrm{z}^2} = 1$ . Moreover, the damping value is taken as $\alpha = 0.01$ as commonly used in FeCo(B) based systems. With these parameters and an exchange length of $\lambda_\mathrm{ex} = 4.9$ nm, we use an integration step of $\Delta t_s = 0.5$ fs for this specific set of simulations.

Since the initial orientation of the magnetization is perpendicular, it is important to study how the magnetization along the vertical axis is changing over time. Figure 2.5 shows the average magnetization along the vertical axis of the storage layer for different heights at an applied DC voltage of $-3$ V. This voltage is not experimentally accessible, as it would break our barrier, and it is only used to study the qualitative nature of the magnetization dynamics. From these we observe that, for the same voltage, an increase in height results in an increase in the time it takes to start reversing the magnetic layer. Starting with the lower height of 16 nm, a sharp variation of the magnetization is observed during the reversal, while a slower relaxation is obtained for prisms with increasing height (see *e.g.* 40 and 50 nm). Further increasing the height of the prism leads to a change in the reversal profile. Around 54 nm the time trace of the magnetization reversal starts exhibiting a shoulder, an effect amplified as the layer height increases.

To understand the underlying mechanism of the magnetization reversal for the different heights we turn to the 3D trajectories described by the averaged magnetization vector inside the unitary sphere, shown in Figure 2.5 $(b)$. From these, a second confirmation that the mechanism of reversal is height dependent can be extracted. For the lower height of 16 nm height, a typical macrospin

switching trajectory is observed since the normalized magnetic moment conserves the length and it holds for the entire trajectory. For an increased height of 40 nm, the switching trajectory no longer lies on the unitary sphere, instead it lies inside of it with the magnitude of the magnetic moment being smaller than 1. This effect is more pronounced for a height of 60 nm, associated with slower magnetization dynamics. This slowing-down was already observed in Figure 2.5 (*a*), related with the shoulder near $\langle m_z \rangle \approx 0$. Moreover, it is observed that, for increasing height, there is no significant variation in the start of the reversal. This is due to the similar size of the domain wall nucleated at the interface, which increases for larger height and takes longer to be expelled by STT.

We can further observe this behaviour from the 3D snapshots of the magnetization, shown in Figure 2.6 at different time steps, for three different heights, 16 nm, 40 nm and 60 nm. These snapshots are seconded with the respective temporal dependencies of the magnetization (in both $\hat{x}$, $\hat{y}$ and $\hat{z}$ orientations) and the different system energies, such as demagnetizing ($E_{\text{demag}}$), from the surface anisotropy ($E_{\text{iPMA}}$), exchange ($E_{\text{exchange}}$) and the total system energy ($E_{\text{total}}$). Starting with the smaller height 16 nm, oscillations in $\langle m_{x,y} \rangle$ are observed associated with the precession of the magnetic moments with the applied STT, whose magnitude becomes stronger during half of the reversal where the average magnetization is in-plane. This behavior is characteristic of a coherent-like reversal, as observed by the coherent rotation of the magnetic moments in the time frames shown in Figure 2.6 (*d*). In addition, the dependencies of the energies in Figure 2.6 (*a*) show that there is a small variation in $E_{\text{exchange}}$ most likely due to the sharp corners of the simulation and decaying value in the effective anisotropy field through the thickness of the layer (since the surface anisotropy is interfacial). Moreover, the different preferential orientations of the magnetization for each energy term can also be seen in this dependence. The demagnetizing energy has a minimum energy when magnetization is in-plane, which follows the preferential alignment for in-plane orientation of the magnetostatic energy since $\tau < 0.89$. For the height of 40 nm, the magnetization reversal follows a buckling-like mechanism since the whole magnetic prism reacts simultaneously during the reversal but in a nonuniform way [88–90]. This is observed in both 3D snapshots (2.6 (*e*)) but also in the dependence of the magnetization components and energies. Opposite to the situation with a height of 16 nm, there are now strong oscillations in the $xy$ plane since the early reversal. Additionally, we observe an increase in the exchange energy during the reversal, which is not expected in a macrospin-like reversal. Moreover, strong oscillations in the energy associated with the surface anisotropy are indication of the oscillation of the moments near the interface, so that the whole system reacts during the reversal. For the larger height of 60 nm, the nucleation of a domain wall starts at the bottom interface (where the STT is maximal). Two magnetic domains, in a tail-to-tail domain wall configuration, are observed in the frame at 11.5 ns. The domain wall then propagates along the vertical direction of the magnetic prism, while it rotates azimuthally in the transverse plane. This reversal mechanism is identified as the propagation of a transverse domain wall [91]. From the temporal dependency of the different energies in the system we can see that for both cases of 40 and 60 nm the demagnetizing energy is maximal when the magnetization processes in-plane, due to the strong perpendicular shape anisotropy. Moreover, for the case of 60 nm the surface anisotropy energy is maximum at the beginning of the reversal since, after nucleation of the tail-to-tail domain-wall,

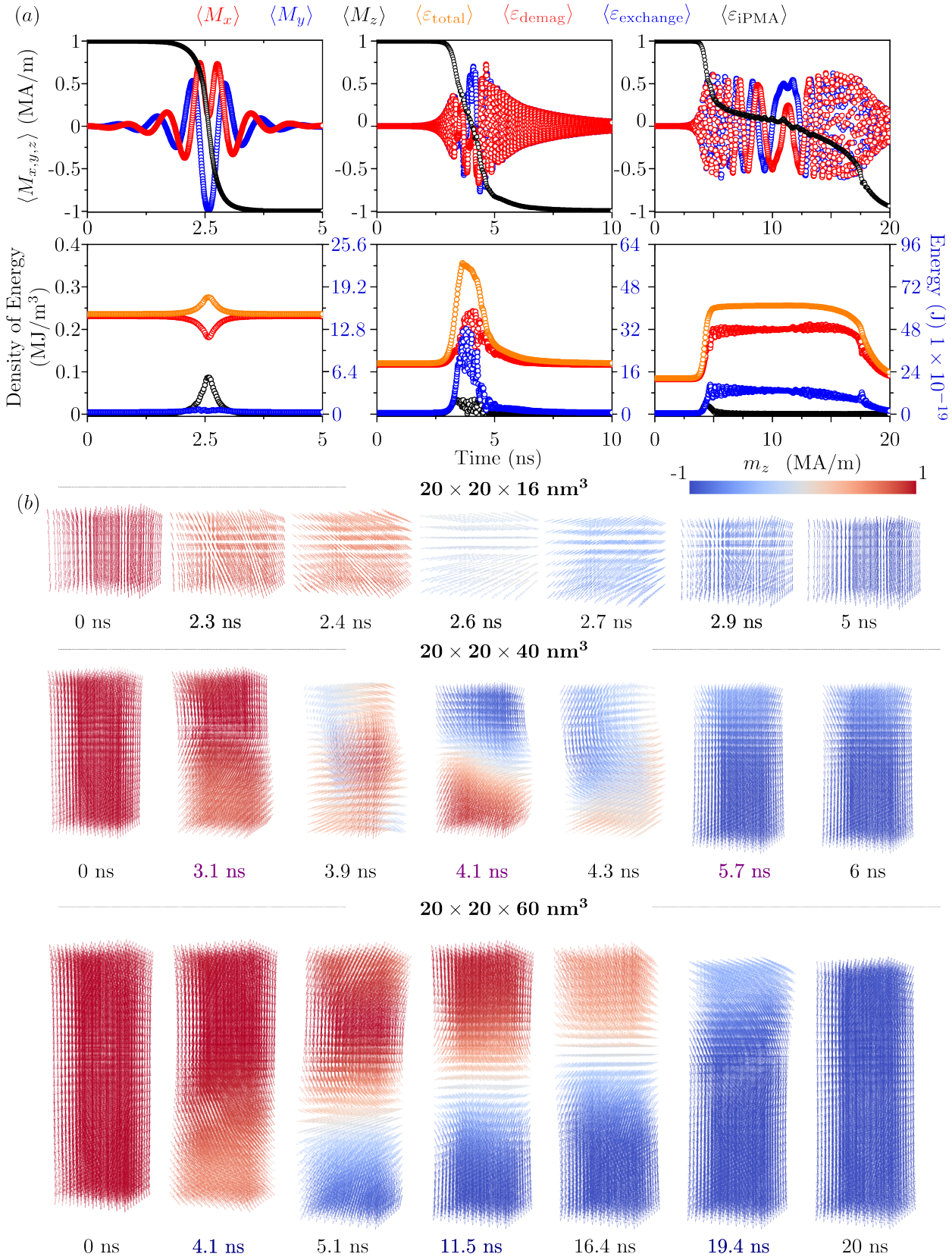


Figure 2.6: (a) Time traces of the different magnetization components $\langle m_x \rangle$ (represented with blue open circles), $\langle m_y \rangle$ (represented with red open circles) and $\langle m_z \rangle$ (represented with black open circles) and dependence of the different energies ($E$) and density of energy ($\varepsilon$) in the system: $E_{\text{total}}$, with orange open circles, $E_{\text{shape}}$, with red open circles, $E_{\text{exchange}}$, with blue open circles and $E_{\text{surface}}$ with black open circles, for different heights of $L = 16\,\text{nm}$, $40\,\text{nm}$ and $60\,\text{nm}$ ($b$) 3D snapshots of the magnetization at different time steps of the magnetization reversal. The colorbar is linked to the $m_z$. value

there is only a movement of the domain-wall and not from the magnetic moment at the interface. It is important to mention that, for this specific case, there is no consideration for repolarization effects that might occur for domain-wall driven dynamics [82].

From the curves shown in Figure 2.5 (*a*) it is possible to extract an important feature of the STT-driven magnetization reversal: the dependence of the switching time on the applied voltage. We define this switching time $\tau_{\text{switch}}$ as the time it takes to reverse half of the magnetic volume. In a macrospin regime, this means that the magnetization lies perpendicularly to its initial orientation, *i.e.* $\langle m_z \rangle = 0$. This is shown in the inset of Figure 2.7 (*a*). Additionally, it is important to define an incubation time - $\tau_{10\%}$ - (the time it takes until 10% of the magnetic layer reverses), the near reversal time $\tau_{90\%}$ (the time it takes until 90% of the magnetic layer reverses) and the transition time $\tau_{\text{Transition}}$ $(\tau_{90\%} - \tau_{10\%})$. The latter is meaningfull since it dictates the time it takes for the magnetic layer to reverse from the point it nucleates. From this relationship, it is possible to extract the critical switching voltage $V_{c0}$ as the minimum necessary voltage for STT switching with an infinite long pulse. Usually measured as a function of the pulse width $\tau_P$, results in the ballistic regime provide a linear dependency between $\tau_P^{-1}$ and the applied voltage, predicted by the conservation of angular momentum [92–97]

$$\frac{1}{\tau_P} = A(V - V_{c0}), \tag{50}$$

where $A$ is a constant that expresses the angular momentum conservation. It is possible to achieve a more direct equation to the material parameters and device properties through [97, 98]

$$V = V_{c0}\left(1 + \frac{\tau_D}{\tau_P}\right) \tag{51}$$

where $\tau_D$ is a characteristic time for switching, and $\theta_0$ an initial average angle of tilt that is usually related to the thermal fluctuations and can be related to the energy barrier through $\theta_0 \approx 1/\left(2\sqrt{\pi\Delta}\right)$. Both $V_{c0}$ and $\tau_D$ are related to the materials parameters through

$$\tau_D = \frac{1+\alpha^2}{\alpha\gamma\mu_0 \mathrm{H_K^{eff}}} \ln\left(\frac{2}{\theta_0}\right) \tag{52}$$

and

$$V_{c0} = \frac{\alpha\mu_0 \mathrm{H_K^{eff}}}{a_{\parallel}}, \tag{53}$$

showing that these values are height independent for macrospin reversal for similar values of $\mu_0 \mathrm{H_{eff}^K}$ and $a_{\parallel}$. This value is taken as the necessary voltage to reverse the magnetic layer under an infinitely long pulse ($\tau_{\mathrm{P}} \to \infty$). For small voltage pulses, this value will grow larger, as dependent of the value of $\tau_{\mathrm{D}}$.

From Figure 2.7 (*b*) it is observed that the relationship is indeed linear, although for larger heights it moves away from the macrospin approximation (as observed in Figure 2.5 and 2.6). From this linearity, it is possible to extract $V_{c0}$ as the intercept and $\tau_{\mathrm{D}}$ proportional to the slope of the linear fit. Focusing only on the macrospin-like situations (16 and 18 nm), we observe that $V_{c0}$ increases for larger thickness, which can be associated with an increase in anisotropy field $\mu_0 \mathrm{H_{eff}^K}$ due to the

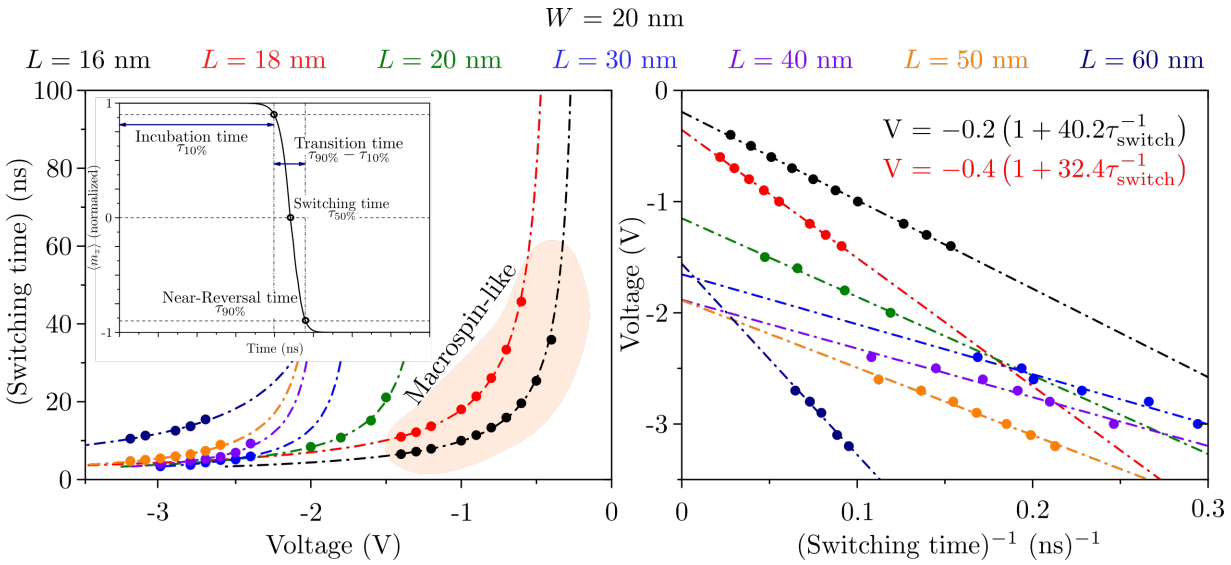


Figure 2.7: (*a*) Dependence of the switching time on the applied voltage for different heights of the storage layer for a fixed width of 20 nm, the coherent reversal is highlighted with an orange region. The inset represents the typical event times considered during magnetization switching. (*b*) Dependency of the inverse of the switching time on the applied voltage.

impact of the increased aspect ratio in the magnetostatic energy. Similarly, the increase in $\mu_0 H_{eff}^{K}$ is associated with a smaller $\tau_D$, and thus a smaller variation of the switching time on the applied voltage is expected.

### 2.3.2 Switching dynamics at lower diameters with fixed stability value

At this moment, it is still not fully understood if the nonuniform dynamics is solely given by the increase in the energy barrier of the magnetic layer, which scales steeply with increasing height. To further confirm this behavior, we analyze the reversal dynamics of prisms with different aspect ratios and decreasing widths. The geometry is defined so that for a given lateral size, the stability of the prisms is $\approx 80\,k_BT$. To address this, the mesh is reduced to 1 nm for a more flexible size dependence. By reducing $l_{x,y,z}$ new values for $K_0$ and $a_0$ need to be provided, respectively $0.89\,MA/m^3$ and $120\,mT/V$. In addition, the time step is adapted to $\Delta t_s = 0.2\,fs$. It should be noticed that, due to change in mesh size and integration step, the different simulations should not be quantitatively compared, and only comparisons within the same transport and mesh parameters are realized.

To understand the dependency of the switching time and reversal mechanism at smaller base width, we use a different set of prisms geometries (base width of 10, 12, 14, 16 and 18 nm) with different heights (respectively, 18, 16, 16, 16 and 16 nm). To maintain a similar stability as we reduce the diameter, it is necessary to eventually start increasing the height of the prisms, due to the reduction in iPMA energy and reduction in total magnetic volume. In addition, it is interesting to point out the similar thickness of 16 nm for different widths up to 10 nm, showing that variations in width where the shape anisotropy has a substantial contribution do not translate to strong variations

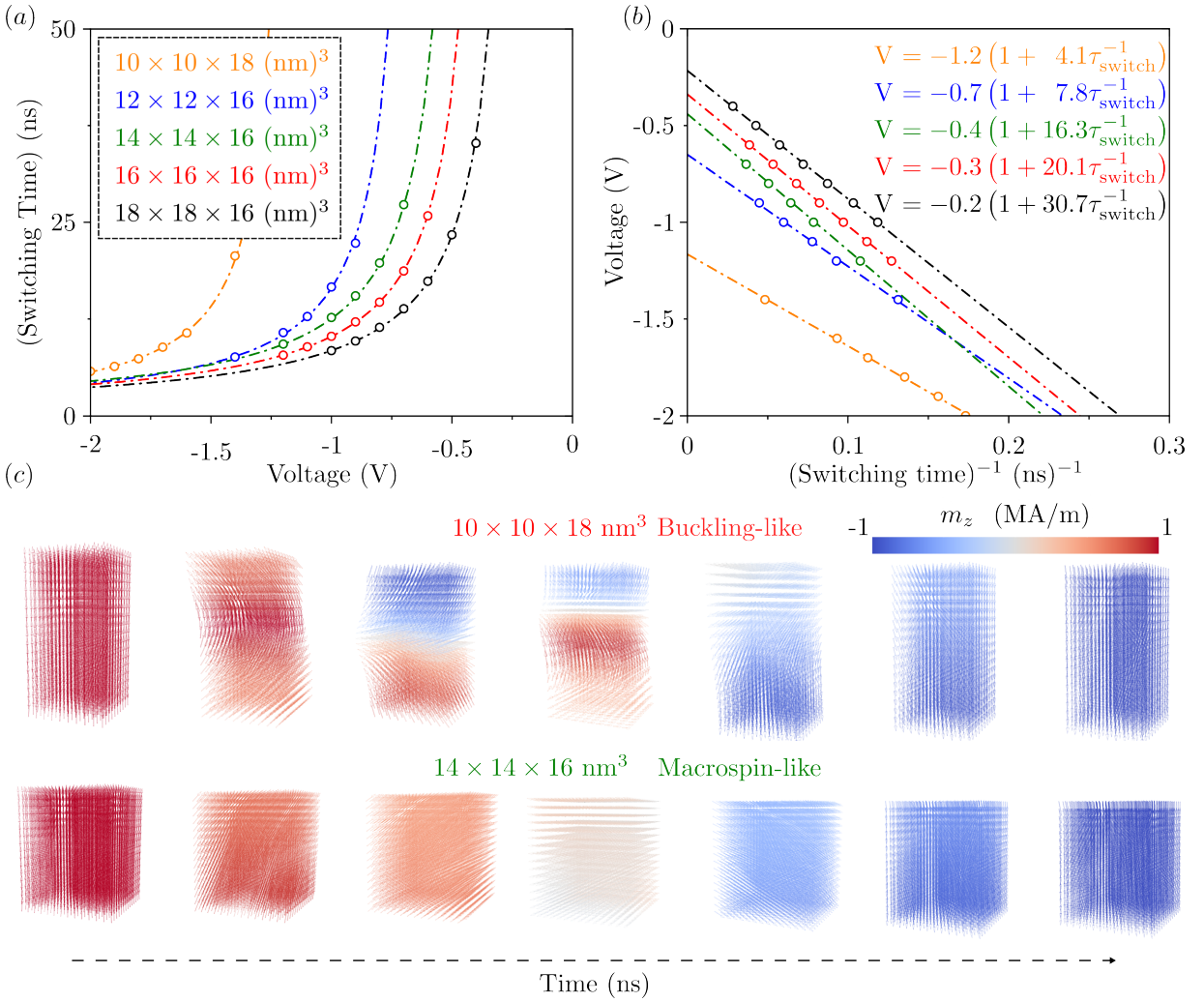


Figure 2.8: (*a*) Switching time of a set os prisms with different base widths depending on the applied voltage and (*b*) associated linear dependence of the voltage on the inverse of the switching time. (c) Associated frames of a buckling like reversal for the larger aspect ratio and macrospin-like reversal for limiting aspect-ratio.

in stability, as would be the situation for a stability given solely by surface anisotropy [56]. Indeed, at this height we are in the isoline ($\Delta \approx 80$) of Figure 2.1 where withing a certain diameter range $\delta\Delta/\delta D \approx 0$. Figure 2.7 (*a*) shows the dependence of the switching time on the applied voltage for the different sets of prisms. It is observed that for a width of 10 nm, there is a much stronger variation in the switching voltage compared to the remaining prisms. Although an increase in $V_{c0}$ was expected with increasing $\mu_0 H_{eff}^K$, as observed in the linear dependence of Figure 2.7 (*b*), the variation in $\mu_0 H_{eff}^K$ is not enough to justify this sharp increase. This is attributed to the nonuniform reversal occurring for this geometry, as observed in Figure 2.7 (*c*). In this situation, we observe a buckling-like reversal, similar to the one shown before for an aspect ratio of 2, but for a larger base width of 20 nm. This similar aspect ratio is a hint of the nature of the nonuniform mechanism in aspect ratios that promote a perpendicular shape anisotropy. Moreover, from the linearity, we can observe that there is also a discrepancy for the situation of 12 nm, especially in $\tau_D$, further revealing a nonuniform mechanism in this aspect ratio.

Thus, to avoid excessive writing voltages and long switching times, it is necessary to avoid this non-uniform reversal by lowering the aspect ratio of the storage layer to values closer to the threshold between in-plane and perpendicular shape anisotropy ($\tau \approx 0.89$). This can be done through an increase in $M_s$, as long as we keep the height at a value for which the aspect ratio promotes a perpendicular shape anisotropy [60]. Additionally, by making use of additional FeCo(B)|MgO interfaces, it is possible to further reduce the height of the storage layer. However, before studying possible solutions, it is important to disentangle the contribution of the decay of the STT throughout the magnetic stack, which can be different for different materials on top of the necessary interfacial FeCo(B) layer. Thus, in the next subsection we explore the role of the nature of the STT and how much it would affect the qualitative nature of the micromagnetic results.

### 2.3.3 Interfacial nature of the STT and impact in the switching time for a cylindrical shape

We now analyze the situation where we have a somewhat circular cylinder. Due to the effect of the finite difference in the nature of our micromagnetic solver, there is a staircase side effect that might lead to some pinning sites alongside the edges of the cylinder. To decrease this, we use a cell size of $l_{x,y} = 1\,\text{nm}$ which seems reasonable for the selected diameter of 20 nm. Moreover, to avoid large computational time we use a micromagnetic cell size of $l_z = 1.5\,\text{nm}$. Keeping a damping value of $\alpha = 0.01$ for the dynamics after an initial relaxation step at $\alpha = 1$, we use a timestep of $\Delta t_s = 0.35\,\text{fs}$. Moreover, the effect of the surface anisotropy is added only at the interface so that $K_0 = k_s/l_z$, for this specific $l_z$ we use a value of $\text{K}_\text{u} = 0.93\,\text{MJ/m}^3$. For the effect of the STT we assume that $a_\parallel$ is decaying with $\lambda_\text{STT} = 1\,\text{nm}$, so that $a_0 = 73\,\text{mT/V}$. In contrast, we assume that the entire contribution of the STT is allocated only in the first cell layer as

$$a_0 = \frac{\hbar}{2e}\frac{\eta_\text{STT}}{\text{R}\times\text{A}}\frac{1}{M_s l_z}. \tag{54}$$

with a value of 94 mT/V for the parameters used beforehand.

Figure 2.9 (*b*) shows a representation of this effect, where the STT that was decaying through the thickness of the pillar is now concentrated at the interface with the equivalent contribution throughout the layer. From Figure 2.9 (*a*) we can observe the dependency of the perpendicular component of the magnetization as a function of time for different applied voltages for both decaying STT and pure interfacial STT. It is observed that in the situation with decaying STT, the incubation is faster than the case with interfacial STT due to its interaction with the remaining plane of cells. Nevertheless, although the switching is faster for the decaying STT (as observed in Figure 2.9 (*c*)), the transition time is not significantly different. This shows that the STT triggers the onset of the reversal but it does not affect the reversal itself. Moreover, we can argue that the magnitude of the decay of the STT is more important for the situation in which there is no thermal fluctuations, which is not the case for real device applications.

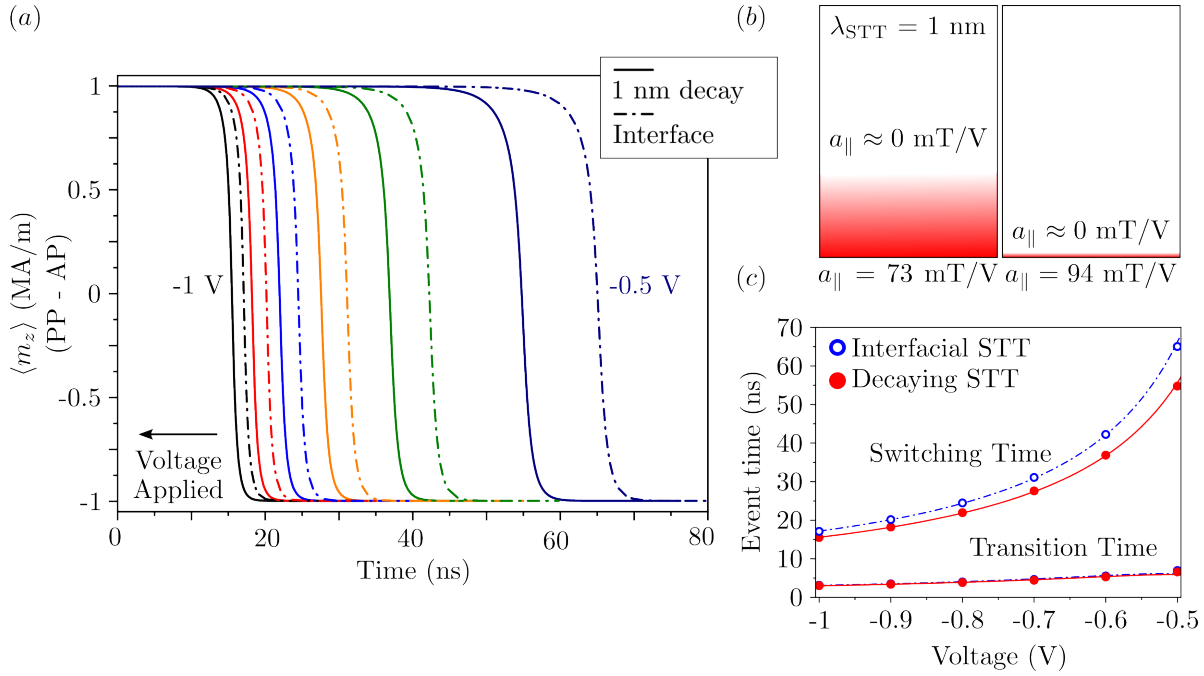


Figure 2.9: ($a$) Time trace of the perpendicular component of the magnetization $\langle m_z \rangle$ as a function of the applied voltage (from $-0.5$ V to $-1$ V) for a magnetic cylinder with diameter 20 nm and height 16.5 nm for two different situations of applied STT: with a 1 nm decay (solid lines) and applied only in the first cell layer (dash dotted lines) ($b$) Illustration of the decay of the STT through the height of the pillar and (c) dependence of the switching and transition time with the applied voltage for both nature of the STT (interfacial with open blue circles and decaying with red circles).

The incubation time can be drastically affected (reduced) by the effect of thermal fluctuations. We implement these fluctuations in the simulations by assuming that the magnetization is in contact with a heat bath with a temperature $T$. These dynamics are correctly described by the Langevin equation in the form of a stochastic relation:

$$\frac{dX}{dt} = a(X,t) + b(X,t)\eta(t) \tag{55}$$

where X is the variable under study, in this situation the magnetisation, $\eta(t)$ a noise term and $a(X,t)$ and $b(X,t)$ are, respectively, the drift and diffusion term. This thermal noise is implemented by taking into consideration the Brown theory, being translated as a random field $H_{th}$ described as a Gaussian distribution with a mean value given by $\langle H_{th}(r_1,t_1) \cdot H_{\mathrm{th}}(r_2,t_1)\rangle = D\delta(r_1 - r_2)\delta(t_1 - t_2)$ where $D$ is a variance expressed as [99]

$$D = \frac{2\alpha k_B T}{\mu_0^2 M_{\mathrm{s}} V \gamma}. \tag{56}$$

This thermal field is then taken into consideration as a perturbation to the effective magnetic field in each cell element (Equation 42). Since this field is random, it takes into account stochastic processes. Therefore, the following simulations are performed several times, obtaining a statistical result. Since this effect occurs in each elementary cell, the length of each individual magnetization is the same. However, the average amongst the magnetic system will be reduced because of the

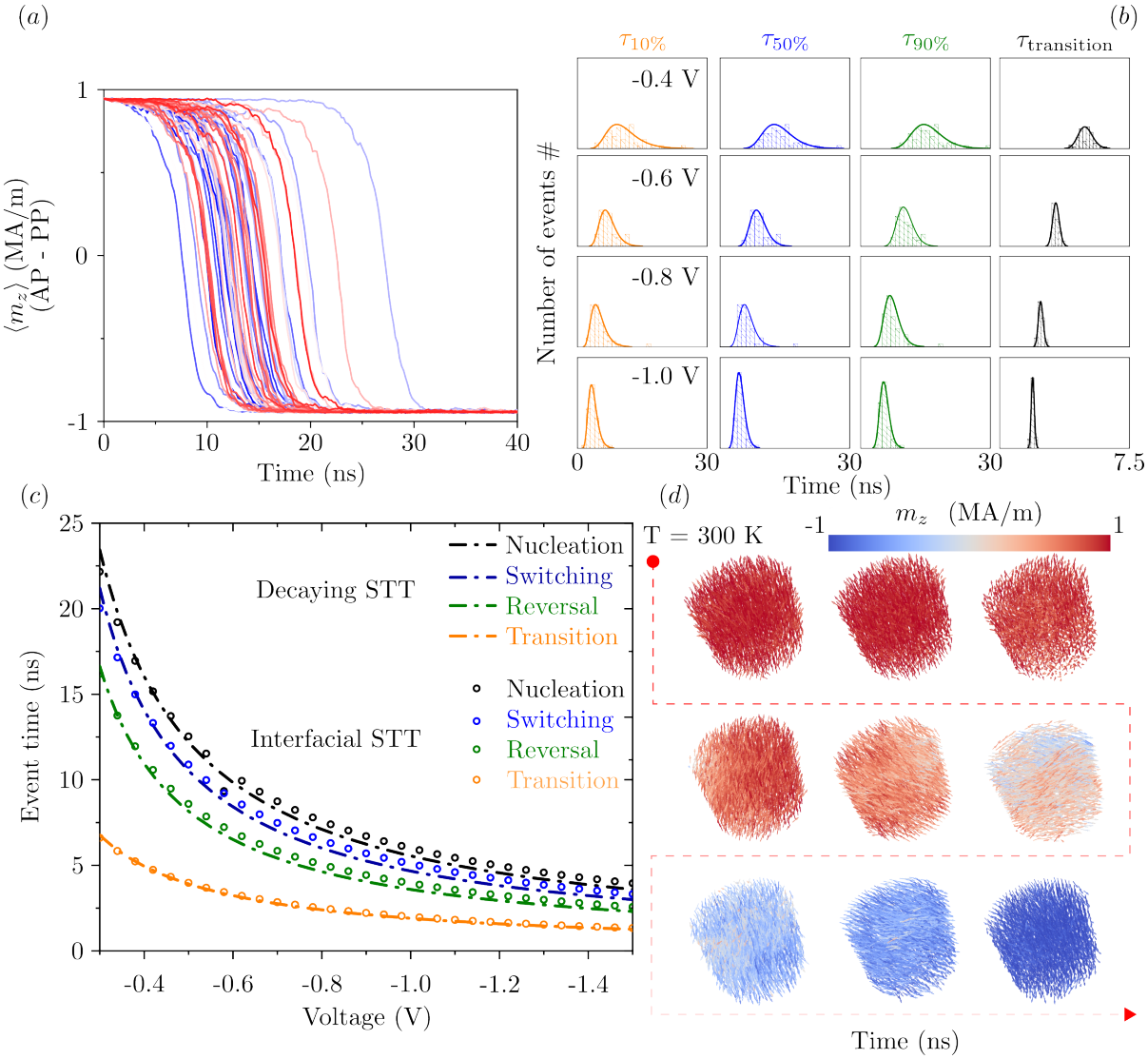


Figure 2.10: $(a)$ Time trace of $\langle m_z \rangle$ for 50 events at the same applied voltage of $-0.4\,\mathrm{V}$ (b) Distribution of the different time events for the different applied voltages. The bins are enveloped with a lognormal distribution curve. $(c)$ Dependence of the event time with the applied voltage for both decaying and interfacial STT and $(d)$ 3D snapshots of magnetization reversal under applied voltage with thermal fluctuations. Results obtained for a temperature of $300\,\mathrm{K}$ and $\Delta t_s = 0.35\,\mathrm{fs}$.

increased randomness. In the previous sections, the simulations were performed considering that the system had no thermal fluctuations, however, the considered material parameters were those at $300\,\mathrm{K}$. Thus, these results cannot be directly compared to those without thermal fluctuations, but only amongst those with the same properties. For a complete quantitative study with temperature, it is necessary to use the values at $0\,\mathrm{K}$ and explore their dependence on temperature.

In the following simulations, we use same transport properties as used for the situation without thermal fluctuations shown in Figure 2.9. As explained before, since the results have a stochastic nature, it is necessary to perform, for the same transport situation, several events to obtain a statistically significant result. Figure 2.10 $(a)$ shows a number of events for an applied voltage of $-0.4\,\mathrm{V}$. In Figure 2.10 $(b)$ we observe that there is a dispersion of time traces that occurs due to the

low applied voltage, being reduced at increasing voltage. A fitting based on a lognormal distribution is performed for the different voltages, and the mean switching time is shown as a function of the applied voltage for the case of a decaying STT and interfacial STT in Figure 2.10 (*c*). It is observed that, in contrast to what is shown in Figure 2.9 (*a*), there is no significant variation in the different temporal quantities for both STT cases, showing that implementing STT only in the first cell layer is enough to qualitatively model the reversal of an high aspect ratio pillar. Moreover, the quasi-coherency of the reversal is shown in Figure 2.10 (*d*) as 3D snapshots illustrating the inherent randomness of the magnetic moments in the storage layer. Moreover, with the assistance of the thermal fluctuations, the nucleation is expected to start sooner due to the random misalignment of the magnetic moments near the interface, providing a sizable torque in the first cell layer. Thus, although the nucleation time seems quite large for the simulations done up to this point, in reality the reversal would be faster due to the random thermal fluctuations acting in the device.

From this point on, we will separate the layers into the first layer providing iPMA and where maximal torque is exerted, and subsequent layers that might be simple bulk magnetization ($K_\mathrm{u} \approx 0$) or addition of spacer layers that might have some additive surface anisotropy term ($k_\mathrm{si}$).

### 2.3.4 Comparison between single layer PSA-MTJ and p-MTJ

Now that the STT is being exerted in a single plane, we can do a comparison with the usual p-MTJ, since we can give them the same transport properties and observe how the addition of the thick magnetic layer has an effect on the switching dynamics. For this purpose, we model the device so that it has the same thermal stability factor $\approx 80 \mathrm{k_B T}$ using a capping MgO layer for the p-MTJ. In this situation the surface anisotropy and STT are applied throughout the entire magnetic body. For the p-MTJ a total uniaxial anisotropy value of $1.27\,\mathrm{MJ/m^3}$ is taken for a cell size of $l_{x,y} = 1\,\mathrm{nm}$ and $l_z = 0.5\,\mathrm{nm}$ for a full height of $1.5\,\mathrm{nm}$. Due to the smaller $l_z$, a time step of $\Delta t_s = 0.15\,\mathrm{fs}$ is used for the p-MTJ. The transport properties are the same as for the thick layer, so a value of $a_\parallel = 90\,\mathrm{mT/V}$ is used along the entire height of the cylinder for an initial tilt angle of the magnetization of $\theta_0 = 0.1°$. From this point on, the STT is considered purely interfacial for the PSA-MTJ, so the geometry of this layer can be thought of as an initial layer that has the same properties as the p-MTJ (except the higher volume anisotropy) with a thicker storage layer added on top of it with, in this situation, the same material FeCo(B) ($\mathrm{M_s} = 1\,\mathrm{MA/m}$ and $\mathrm{A_{ex}} = 15\,\mathrm{pJ/m}$). After relaxation at $\alpha = 1$, different DC voltages are applied for $\alpha = 0.01$ and the time trace of the perpendicular magnetization is extracted and shown in Figure 2.11 (*a*) for both geometries. Here we can observe that the switching of the p-MTJ is significantly faster than that of the PSA-MTJ, although the range of voltages is similar (Figure 2.11 (*b*)). Keeping the same linearity between the applied voltage and the inverse of the switching time, we can see that there is a variation regarding the critical switching voltage. Since we are using the same transport properties, from Equation 53, we would expect that the thicker layer would have a smaller $V_{c0}$ due to its lower $\mu_0 \mathrm{H}^\mathrm{K}_\mathrm{eff}$.

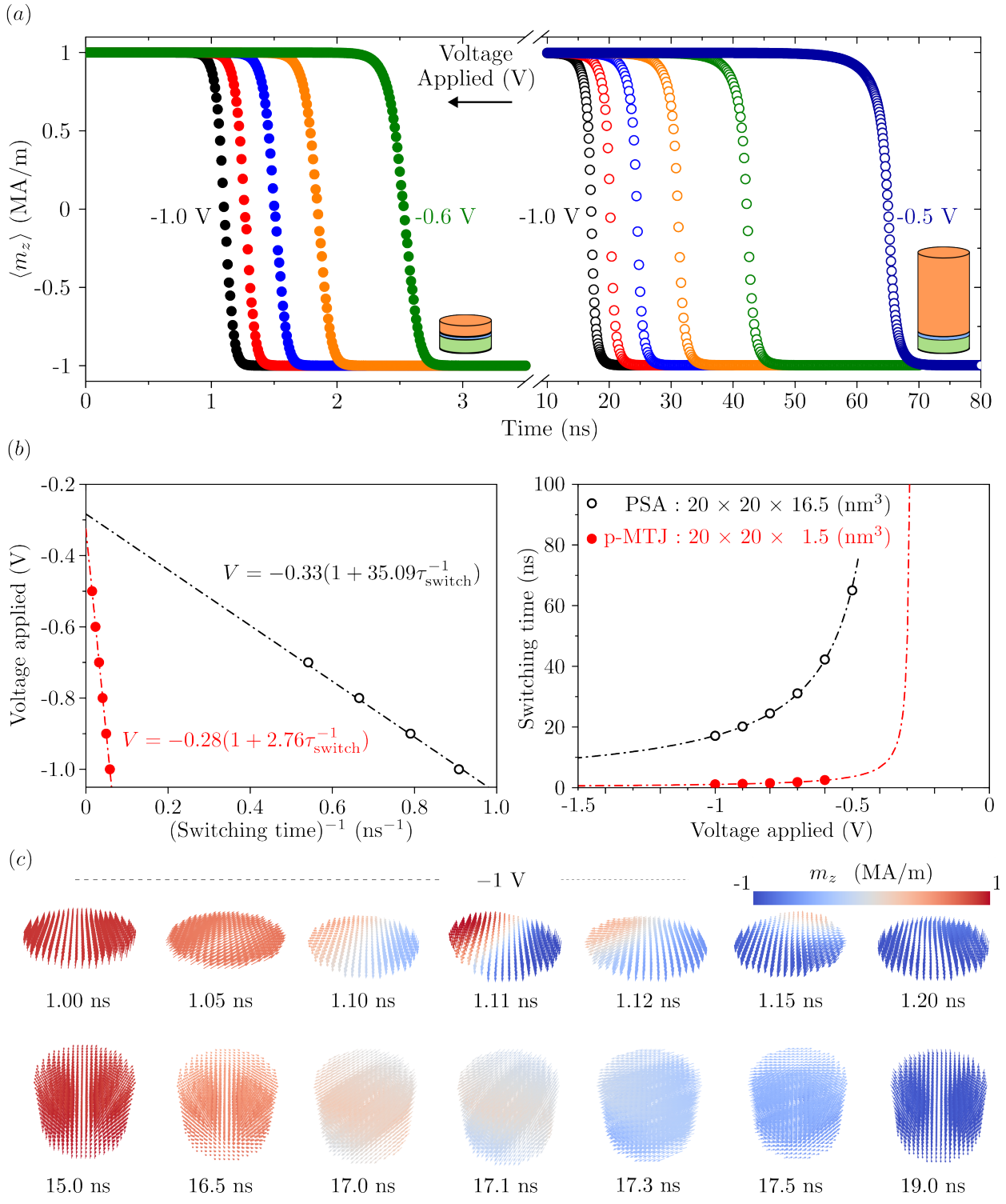


Figure 2.11: ($a$)) Time traces of $\langle m_z \rangle$ for different applied voltages, for the situation of the p-MTJ (filled cirles) and PSA-MTJ (open circles). ($b$) Associated dependence with the switching time on the voltage applied for the p-MTJ (closed red circles) and PSA-MTJ (open black circles) and ($c$) 3D snapshots of the magnetization reversal for the p-MTJ and PSA-MTJ for an applied voltage of $-1$ V. Results obtained for an initial tilt angle of 0.1° and $\Delta t_s = 0.35$ fs for the PSA-MTJ and $\Delta t_s = 0.15$ fs for the p-MTJ.

This provides a hint that the height of the storage layer is playing a critical role in the transport properties, since the STT needs to be able to start the nucleation of a much thicker layer during the coherent reversal. A striking difference is also obtained for $\tau_D$, ascribed to the lower $\mu_0 H_{eff}^K$. This results is large switching voltages for smaller voltage pulses. Indeed, for this situation, at a pulse length of 100 ns, a switching voltage of $-0.45$ V is necessary for the PSA-MTJ, while for the p-MTJ only $-0.28$ V is needed. Moving to lower pulse length increases this difference, as for a pulse of 10 ns a switching voltage of $-1.5$ V is necessary for the PSA-MTJ, while for the p-MTJ $-0.36$ V are enough. This shows that, in addition to lower $V_{c0}$, it is also necessary to maintain a low $\tau_D$, avoiding excessive writing voltages at smaller voltage pulse. Regarding the switching mechanism, 3D snapshots of the magnetization reversal are shown in Figure 2.11 (*c*) for the situation of both p-MTJ and PSA-MTJ. It is seen that for the p-MTJ, for these material parameters, there is a lateral domain-wall nucleation, even at this smaller diameter. This is expected due to the much larger surface anisotropy and thus smaller critical diameter, which for p-MTJ is given by [100]

$$d_c = \frac{16}{\pi}\sqrt{\frac{2A_{ex}}{\mu_0 M_s}}\frac{\sqrt{H_K - M_s}}{H_K - (\mathcal{N}_{zz} - \mathcal{N}_{xx})M_s}. \tag{57}$$

Even though it seems that, in terms of the switching time, it is difficult for the PSA-MTJ to compete with the p-MTJ, it is important to note that this comparison is made at a diameter for which the p-MTJ is still operable. The PSA-MTJ proves superior at lower nodes (even if the switching time is not particularly fast) and for applications operating in a wide range of temperatures, as showcased beforehand. Thus, it is necessary to associate each of the devices with its application domain, which would be DRAM and automotive for the PSA-MTJ in which switching times below 20 ns are acceptable. Nevertheless, it is still possible to reduce the switching time of the PSA-MTJ by optimizing the height of the magnetic layer, as will be shown in the following subsection.

## 2.4 Assets of increased $\mu_0 H_{eff}^K$ in PSA-MTJ

As already mentioned, an increasing aspect ratio leads to a transverse domain-wall nucleation and further propagation, which has a negative impact on the switching voltage, but also on the time required to fully reverse the magnetic layer. A way to address this issue is by increasing $\mu_0 H_{eff}^K$ and thus lowering the necessary magnetic volume. As a reminder, the stability factor for a macrospin can be written considering $\mu_0 H_{eff}^K$ through

$$\Delta = \frac{M_s \mu_0 H_{eff}^K V}{2k_B T}$$

and thus, for the same diameter, an increase in $\mu_0 H_{eff}^K$ leads to a decrease in $L$ for a given stability value. For this specific design problem, we can increase the value of $M_s$, and thus decrease the total height necessary for a certain stability value. However, this limits the height to values similar to that of the diameter.

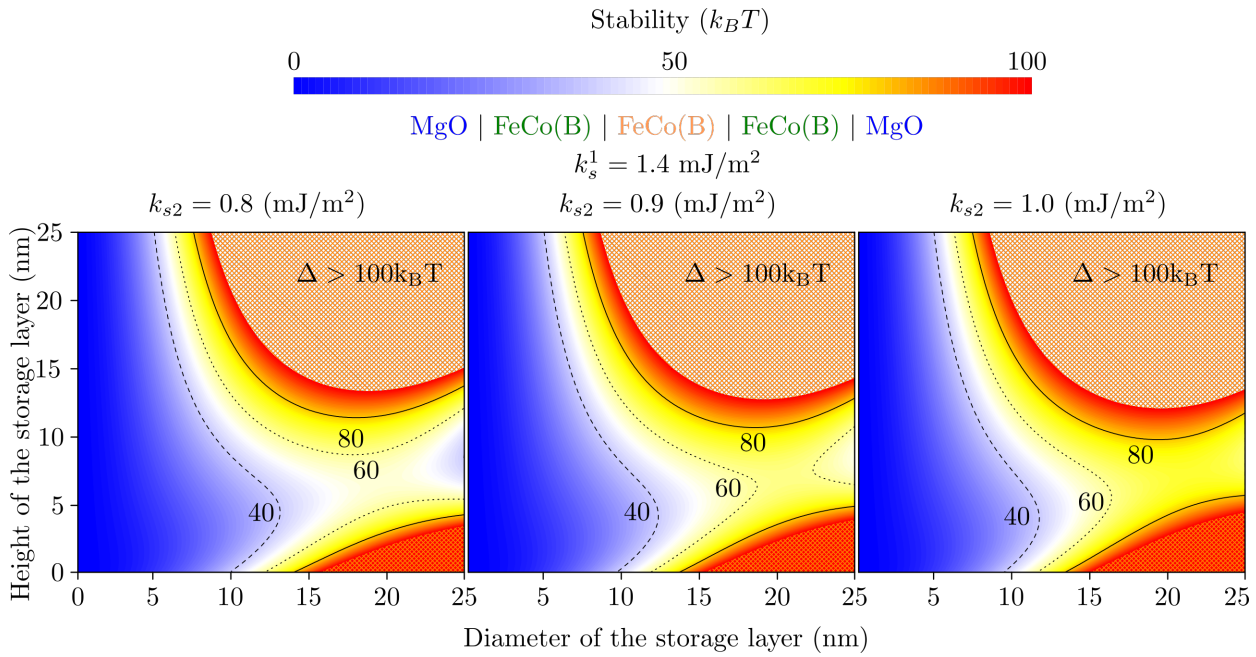


Figure 2.12: Stability factor for different thick layers with an additional FeCo(B)|MgO capping layer with values of $k_{s2} = 0.8$, 0.9 and 1.0 mJ/m$^2$ and fixed $k_{s1} = 1.4$ mJ/m$^2$. The colorscale is linked to the colorbar in energy values of $k_BT$ and the patterned orange region is shown for values $\Delta > 100\,k_BT$

Another viable approach is to continue using the effect of the surface anisotropy through additional FeCo(B)|MgO interfaces, namely by using a capping MgO [61, 62, 87]. To mimic this effect, we consider that there is a second interfacial layer in the last plane of cells with a specific value of surface anisotropy ($k_{s2}$). It is important to mention that this additional barrier increases the resistance of the device. Even though this does not bring an increase in critical switching current (or critical current density) since it is only related to the spin polarization of the first tunnel barrier, the critical voltage will increase until a point where it might be high enough to break the MgO tunnel barrier. In these simulations, this increase in resistance is not considered, since the comparison is made within the same transport properties.

With this idea in mind, we first analyze the beneficial increase in surface anisotropy in the stability of the storage layer for the first interfacial surface anisotropy of $k_{s1} = 1.4$ mJ/m$^2$ and different surface anisotropies in the second FeCo(B)|MgO interface $k_{s2} = 0.8$, 0.9 and 1 mJ/m$^2$. The stability diagram for these different parameters is shown in Figure 2.12 for an interfacial FeCo(B) and thick layer with a $M_s = 1$ MA/m for different aspect ratios, with isolines at $\Delta = 80$, 60 and 40 $k_BT$. As expected, an increase in overall stability is observed due to the larger $\mu_0 H_{eff}^K$ for somewhat larger diameters ($D > 10$ nm), while for lower diameters this effect is not as significant. To study how this would affect the switching speed for the PSA layer, we kept a diameter of 20 nm in the simulations, where the incremental surface anisotropy still plays a considerable role. We use a cell size of $l_{x,y,z} = 1$ nm and different heights that, for the damping value of 0.01, make it necessary to use an integration step of $\Delta t_s = 0.35$ fs. Due to the size of the elementary cell, we use a volume anisotropy value of 1.4 MJ/m$^3$ in the first plane of cells and different volume anisotropy values (0.8,

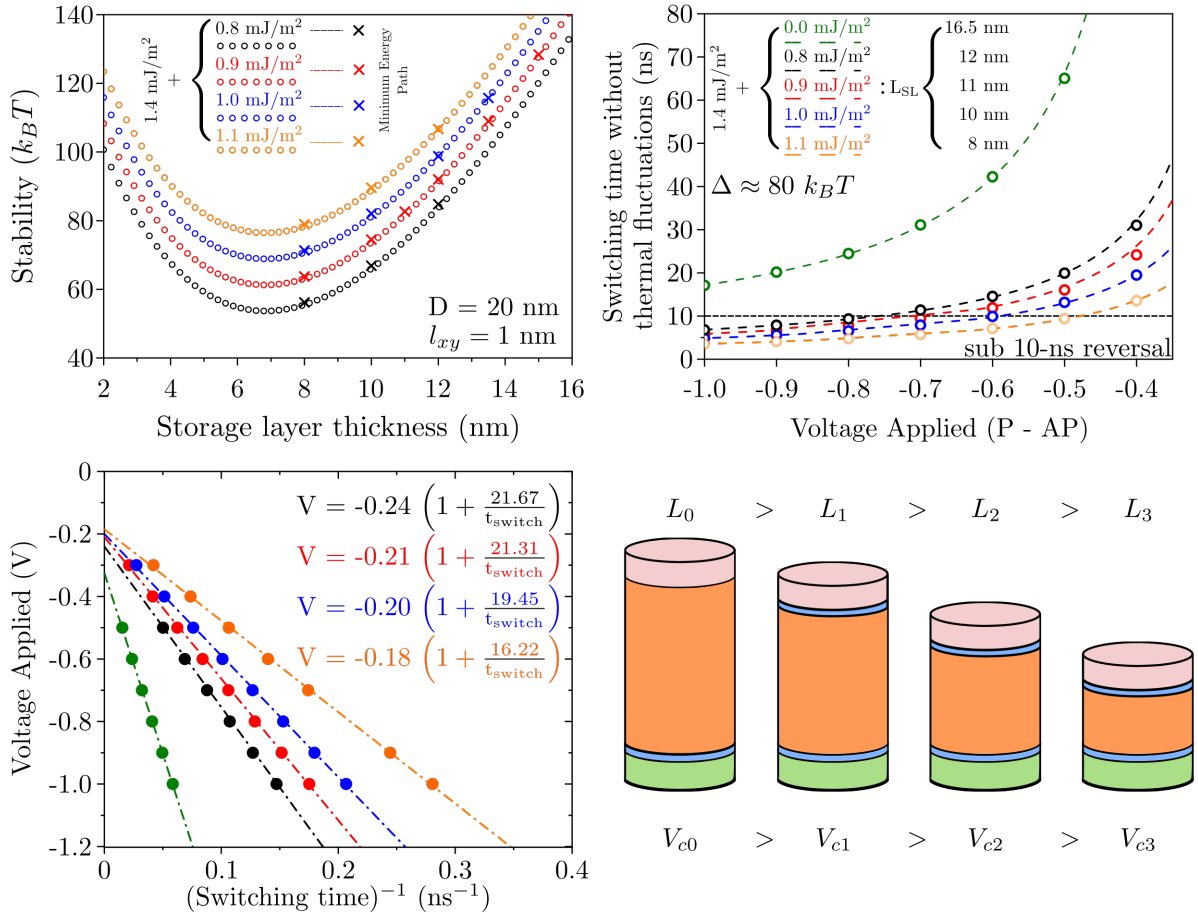


Figure 2.13: ($a$) Values of the stability for an iso-line of 80 $k_BT$ for a macrospin model, overimposed with micromagnetic minimum energy path results for a fixed diameter of 20 nm and increasing layer height for different values of increasing capping surface anisotropy. ($b$) Associated dependence of the switching time on the applied voltage ($c$) linear dependency of the inverse of the swtiching time with the applied voltage and ($d$) illustration of the reduction of the critical voltage $V_c$ with the reduced layer height.

0.9, 1.0 and 1.1 MJ/m$^3$) for the last plane of cells. To maintain coherency throughout the results, we use the same stability $\approx 80\,k_BT$ for the different capping anisotropies. To calculate at which height the same stability value is attained, minimum energy path simulations are performed for different heights. Figure 2.13 ($a$) shows the macrospin iso-line of 80 $k_BT$ for the different capping conditions for a diameter of 20 nm with micromagnetic MEP results superimposed, showing a good conformity with the macrospin results. This shows that even though there is the staircase effect owing to the finite-difference method, there is no loss of generality at these dimensions. This might, however, not hold for smaller diameters where the edge effects become more prominent. Using heights that correspond to the stability of 80 $k_BT$ we study the dependence of the switching time with the applied voltage for an interfacial STT effect with $a_0 = 140$ mT/V (R × A product of 1 $\Omega \cdot \mu$m$^2$ and 100% TMR), as shown in Figure 2.13 ($b$). Clearly, an improvement in the switching time is observed when the layer height is reduced, even though the stability is the same for the different layers. Moreover, by linearity of the inverse of the switching time with the applied voltage [Figure 2.13 ($c$)] we can extract the critical switching voltage that decreases with lower aspect ratio (for the fixed stability

situation, with higher $\mu_0 H_{eff}^K$), a situation that is not expected considering equation53. The height reduction is further accompanied by a reduction of $\tau_D$, which is expected through the increase in $\mu_0 H_{eff}^K$.

Up to this point we know that, by reducing the height of the layer there is an improvement of switching time and switching voltage. However, it can be hypothesized that this improvement is not only due to the increase in $\mu_0 H_{eff}^K$ because the switching voltage decreases with increasing $\mu_0 H_{eff}^K$ through reduction in the height of the storage layer.

To understand the critical elements for fast switching and low switching voltage, it is necessary to dissociate the different parameters that could have an impact on the dynamics of the system, such as $\mu_0 H_{eff}^K$, height $L$ and stability $\Delta$. To understand the impact of each of these parameters, we need to keep one constant at all times while varying the remaining. This is shown in Figure 2.14 for a fixed stability value of 80 $k_B T$, fixed height of $L = 12$ nm and fixed effective anisotropy field of $\mu_0 H_{eff}^K$= 61 mT. For the first situation, if we keep the stability the same, then there is an increase in $\mu_0 H_{eff}^K$ as the height is reduced for the same diameter. If we look at the switching characteristics for the same transport parameters given in the example above, we observe a similar trend, decreasing the height leads to a lower switching voltage and lower $\tau_D$. Moreover, there is a significant variation in the transition time between the different heights, where the situation with a larger $\mu_0 H_{eff}^K$ gives the smallest transition time, a result expected from a macrospin regime. If we now keep the height the same ($L = 12$ nm) and increase $\mu_0 H_{eff}^K$, we increase proportionally $\Delta$. For this situation, it is observed that above a certain voltage threshold there is no significant variation in the nucleation time, and, below this threshold, the layer with the smaller $\mu_0 H_{eff}^K$ (and thus smaller stability) starts its reversal faster. If we look at the transition time, we observe once again that there is no significant variation, although for the larger $\mu_0 H_{eff}^K$ the transition is faster, which follows previous analytical studies [101].

This shows that the main actor for reduced switching time and switching voltage is the height of the storage layer, while $\mu_0 H_{eff}^K$, for these dimensions and transport properties, has a marginal effect, being more relevant for the transition time. To further confirm this statement, we fix the value of $\mu_0 H_{eff}^K$ and increase the height value. As a result of the increase in volume, this also increases the stability of the layer. It is observed to have a behavior similar to that of the fixed stability. Although volume has no direct implication in the macrospin result for $V_{c0}$ it does have a strong micromagnetic variation. This can be associated with the effect of the STT through the thick layer. As the height of the storage layer decreases, the critical voltage should increase, near the one expected from the macrospin regime. Moreover, the smaller the layer, the faster it would be to reverse it through a strong interaction between the neighboring magnetic moments.

Thus, for a fast memory device, it is important to reduce the thickness of the storage layer so that the effect of the STT is maximized through the magnetic layer. Additional improvements in STT efficiency can be achieved by making use of concepts that result in additive STT, such as the implementation of a top-pinned reference layer or through the use of an assistance layer coupled through dipolar coupling with the thick storage layer [102, 103]

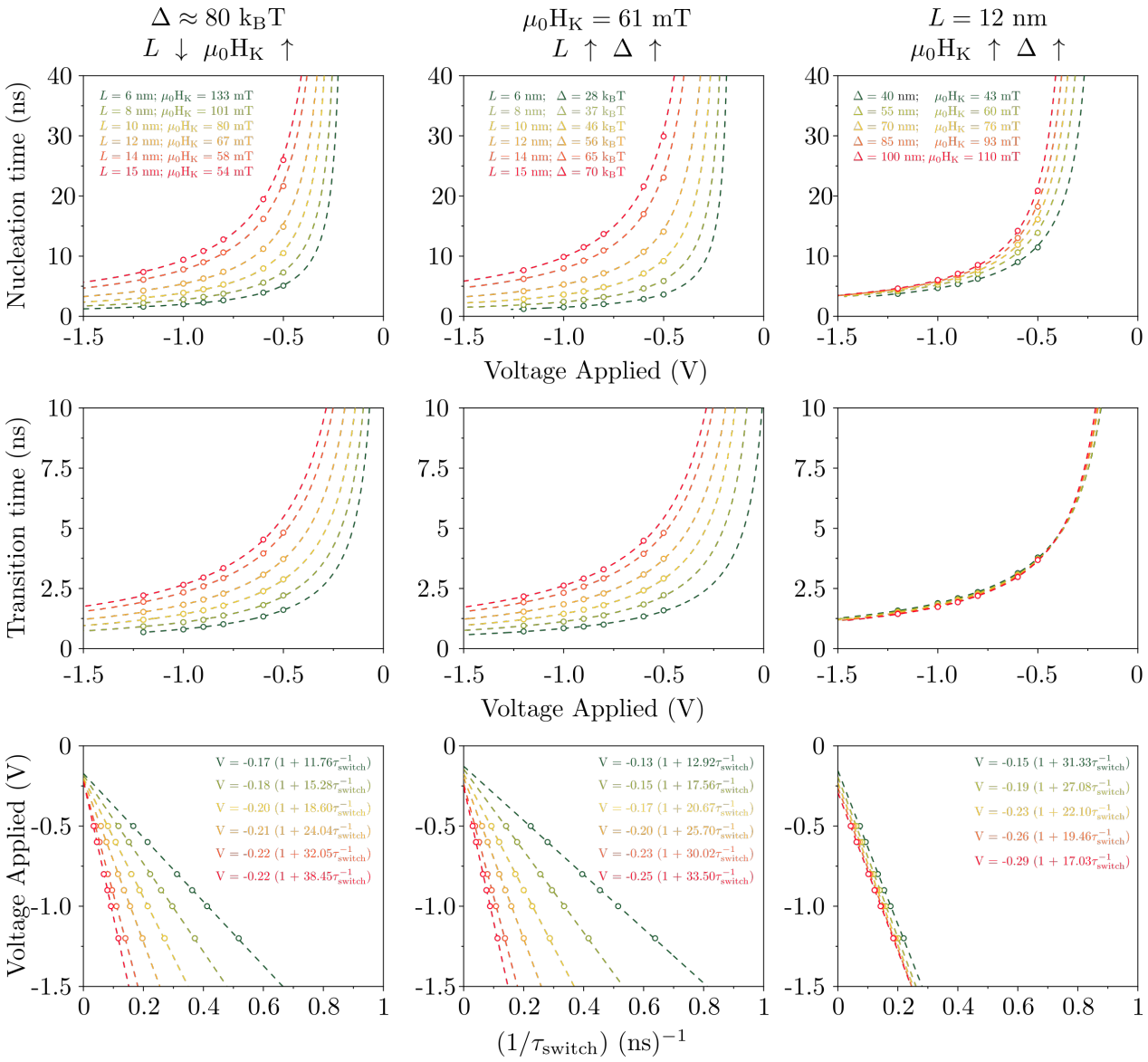


Figure 2.14: Dependence of the nucleation time (ns), transition time (ns) and the inverse of the switching time on the applied voltage, for a situation of a fixed $\Delta$, fixed $L$ and fixed $\mu_0 H_{eff}^K$.

## 2.5 Capping in scalability using a single PSA-layer

At this point, several conclusions have been drawn, with the impact of the height of the pillar on the switching time and on the switching voltage being the most noticeable. It has been shown that the use of a capping MgO, to promote additional surface anisotropy, allows to reduce the height of the storage layer. However, the downsize scalability of the storage layer design is limited. First, the increase in stability due to surface anisotropy is limited when scaling down the device. This was already noticed in Figure 2.12, where even though the surface anisotropy was increased there was no significant increase in stability below 10 nm. Secondly, a small dispersion of diameters will translate into a larger inter-device dispersion of $\mu_0 H_{eff}^K$ and $V_{c0}$. This was not the case for a single layer that relied only on shape anisotropy at smaller nodes. In addition, the advantage of the wide range of temperature applications is lost, since $k_s$ scales down much faster than $M_s$ with temperature [58,

59, 63, 64]. Nonetheless, relying only in the shape anisotropy is also not trivial, as it is necessary to increase the thickness of the layer to compensate for the $\mu_0 H_{eff}^{K}$. This brings a limit to $\Delta$ since at, at a certain point, there is a domain-wall inside the storage layer. Thus, the stability of the device is associated with the energy barrier of the domain wall itself. As already observed [56], this upper limit can be determined considering a tail-to-tail domain-wall formed along the height of the pillar [Figure 2.15 (*a*)], which is dependent on $A_{ex}$ and $M_s$

$$\Delta^{DW} = \frac{\mu_0 M_s^2}{2k_B T}\frac{\pi D^2}{4}\left(\frac{D}{2} + L_{DW} + \frac{2(L_{DW}^2)}{D + 2L_{DW}}\right), \tag{58}$$

where $L_{DW}$ is the width of the domain wall, with a usual value of $\sqrt{\frac{4A_{ex}}{\mu_0 M_s^2}}$. This limitation in stability is shown in Figure 2.15 (*b*) for a pillar with 5 nm diameter for the case of NiFe (Py) ($M_s$ = 0.789 MA/m, $A_{ex}$ = 8 pJ/m), FeCo(B) ($M_s$ = 1 MA/m, $A_{ex}$ = 15 pJ/m) and Co ($M_s$ = 1.446 MA/m, $A_{ex}$ = 30 pJ/m) for a macrospin approximation (dashed line) and the domain-wall limit (dotted line $\Delta^{\infty}$) followed by micromagnetic MEP calculations (open circles). It is observed that an increase in $M_s$ will shift the capping limit. Nevertheless, to maintain a lower height, namely to aspect ratios closer to and below 1, even for the material with largest $M_s$, the stability is still below 30 $k_B$T.

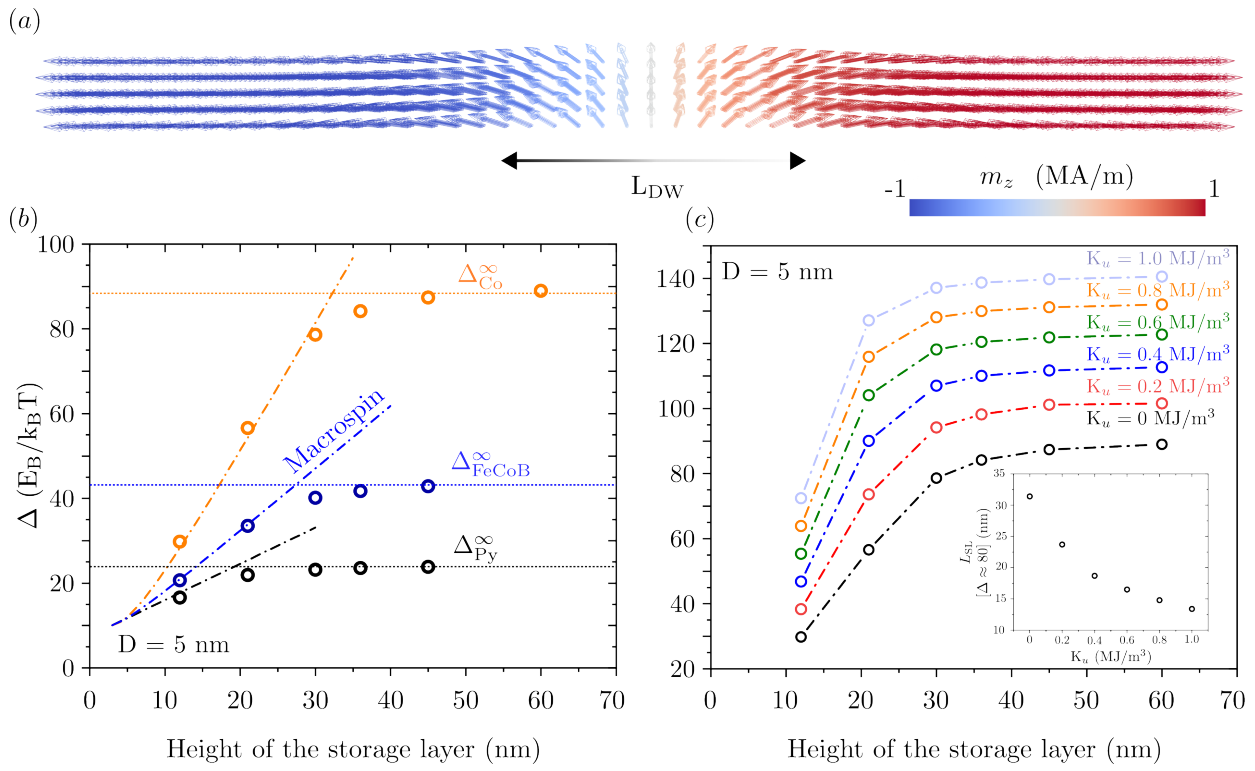


Figure 2.15: (*a*)) Example of a transverse domain-wall switching in PSA-MTJ with domain-wall width $L_{DW}$ with magnitude of $m_z$ linked to the colorbar. (*b*) Thermal Stability factor of a 5 nm diameter PSA-MTJ with different storage layers, Py (in black), FeCo(B) (in blue) and Co (in orange). The macrospin limit $\Delta^{\infty}$ is shown with a dotted line, conventional macrospin results shown with a dashed line and micromagnetic MEP results shown with open circles. (c) Thermal stability factor for a Co pillar with increasing uniaxial anisotropy. The height at which a thermal stability of 80 $k_B$T is attained for each value of $K_u$ is shown in the inset of this figure.

Although the use of materials with larger $M_s$ is to be considered (for instance, CoFe alloys), one still needs to maintain an aspect ratio above 0.89 to retain perpendicular magnetization. A viable option to further reduce the aspect ratio of the magnetic stack is to make use of additional sources of uniaxial anisotropy, such as magnetocrystaline. Figure 2.15 (*c*) shows that, for a thick layer of Co we can shift the stability capping to larger heights, which would allow larger stability at a lower height, as observed in the inset for a fixed stability of $80\,k_BT$ for different values of uniaxial anisotropy. This could be the example of alloys such as FePd or MnAl alloy [104]. The later has a small $M_s$, so that the negative impact of the shape anisotropy is reduced. Additional approaches rely in the use of multiple MgO interfaces throughout the layer. This approach has already been shown to be viable for the usual p-MTJ technologies with increased stability and is adapted for lower diameters with multiple insertions [87, 105, 106]. Although there are different possibilities to continue the scaling of the STT-MTJ, the layer with vertical aspect-ratio has the additional benefit, compared with the remaining approaches, of tolerating high operating temperature. Moreover, similar to the layers with unixial anisotropy, small variations in diameter do not translate to large variations in stability or switching voltage. These benefits keep the PSA-MTJ attractive for applications, even for DRAM applications, where the switching time is of around 20 ns.

# 3 Ultimate sub 10-nm scalability for MTJ: from high stability to stochastic applications

In this section we explore the magnetic stack design for the optimized conditions of our low R × A memory devices. It is shown that, to achieve the necessary lower R × A with a naturally oxidized MgO tunnel barrier we must resort to extremely low oxidation conditions which can lead to a strong coupling between the reference and the storage layer. To avoid this constraint, a trade-off between a lower value of coupling and R × A is needed. We then fabricate a standard p-MTJ with MgO capping and explore its viability at lower diameters. It is observed an overall increase in the figure of merit $\Delta/I_{c0}$ with decreasing device diameter, with magnitude larger than that of a single interface p-MTJ. Interestingly, as the device diameter is reduced, we enter in a low stability region, pertinent for stochastic MTJs. Experimental studies validate the control of the dwell time with applied DC voltage at electrical diameters as low as 8 nm. To regain $\Delta$ at low diameter, we increase the aspect-ratio of the storage layer. It is shown that, although we are able to achieve perpendicular orientation with reasonably high TMR values, STT switching is still limited by the R × A of our tunnel barrier. It is shown that, by reducing this R × A one step further we are able to reverse this thick layer by STT , urging the need for optimized and reliable low R × A conditions.

## 3.1 Optimization of the magnetic stack for low diameter applications

The main core of the samples studied along this thesis work is based on samples in which the materials are deposited by DC magnetron sputtering technique onto thermally oxidized silicon wafers. This is a physical vapor deposition (PVD) system, adopted in industry and research due to a combination of high deposition rates and good material quality [107]. This system allows for deposition of several target materials, oxidation treatments and surface etchings.

Our tunnel barrier is naturally oxidized, and thus an natural oxidation step is necessary during deposition. For this, a first metallic Mg layer is deposited, followed by a natural oxidation step for a pre-determined time under a certain pressure followed by a second Mg deposition. The conditions at which the natural oxidation is done are critical for the values of TMR and the values of iPMA, as it will affect the interface between the FeCo(B) and MgO. To improve the reliability of the MgO tunnel barrier, it is imperative to avoid moisture in the chamber during deposition, so a base pressure of $10^{-9}$ bar is used. The latter is important since Mg is hydrophilic [108], so this would introduce impurities at the oxide interface, diminishing both spin polarization and TMR. An alternative to a naturally oxidized MgO is to use RF sputtered MgO. This provides a better quality interface, reaching very low R × A products with larger TMR values [109, 110]. However, from a more fundamental point of view, it is interesting to vary the material parameters and engineer the interface quality to adapt it to our research. Making use of this naturally oxidized MgO we can then vary the thickness of the total MgO layer and the degree of oxidation of the layer. This allows a control of the value of iPMA at the interface and TMR. Previous studies have shown that these parameters appear to have

Table 2: Values of R × A product and TMR for full sheet film multilayers with different pressure and oxidation conditions in Mg (7.5) | Ox. (x) Pressure (y)| Mg (5.0) (in blue, values for 2022) and Mg (7) | Ox. (x) Pressure (y) | Mg (5.0) (in white, values obtained before this work). Values represented are nominal values.

| Pressure (mbar) | Time (s) | $R \times A$ ($\Omega\mu m^2$) | TMR (%) |
|---|---|---|---|
| $3 \times 10^{-2}$ | 30 | 10 | 80 |
| $3 \times 10^{-2}$ | 10 | 5.4 | 37 |
| $3 \times 10^{-2}$ | 5 | 4.8 | 65 |
| $1 \times 10^{-2}$ | 10 | 2.5 | 59 |
| $3 \times 10^{-3}$ | 30 | 2.4 | 64 |
| $3 \times 10^{-3}$ | 10 | 1.8 | 51 |
| $3 \times 10^{-3}$ | 1 | 1.2 | 27 |
| $1 \times 10^{-3}$ | 30 | 1.9 | 19.6 |
| $1 \times 10^{-3}$ | 10 | 1.2 | 14.5 |
| $1 \times 10^{-3}$ | 1 | 1.1 | 12.4 |

a peak at around the same value of thickness of MgO for the same conditions of oxidatation and base pressure [111]. Moreover, by varying the oxidation time and base pressure it is possible to vary the R × A and the TMR values. This is explored to achieve small R × A products for small MTJ diameters. Preliminary data from current-in-plane tunneling (CIPT) measurements at full sheet film realised for different oxidation conditions of the layer are shown in table 2 for different multilayered stacks after annealing at 300° for 10 min.

It is seen that, with decreasing pressure, there is a reduction of the R × A at thin film level. This is directly related to the amount of oxygen in the chamber, limiting the amount of oxidation of the Mg layer. A similar correlation is observed for the oxidation time where, for the same base pressure, lower oxidation time leads to lower R × A values. In both situations, the common factor is the degree of oxidation of the Mg layer. When pressure and oxidation time are elevated, then the Mg layer will be fully oxidized, leading to a larger resistance and proportionally increased R × A value. On the other side, if the base pressure and oxidation time are low, then the thickness of the oxide formed is smaller, and conductive Mg is still present. This lowers the resistance of the barrier, and thus proportionally the R × A. Moreover, the thickness of the Mg also makes a difference in the R × A of the barrier. Although not illustrated here, the reasoning behind it is straightforward. If the thickness of the Mg is reduced, then, even for lower oxidation time, the layer is more likely to be fully oxidized, leading to higher R × A. On the other hand, if we increase the thickness of this layer, then the oxidation will only be partial, lowering R × A. Although the latter seems the most interesting for our situation, the thickness of this layer will also have a strong effect on the iPMA and TMR. To explore this dependence we use Magneto-optical Kerr effect (MOKE) microscopy in double wedged 4 inch samples. Here, we vary the thickness of both the FeCo(B) storage layer and Mg. This is possible using our deposition system through an off-axis deposition. In this situation it is possible to create a gradient in the thickness of the deposited layer that is dependent on the coordinates on the wafer.

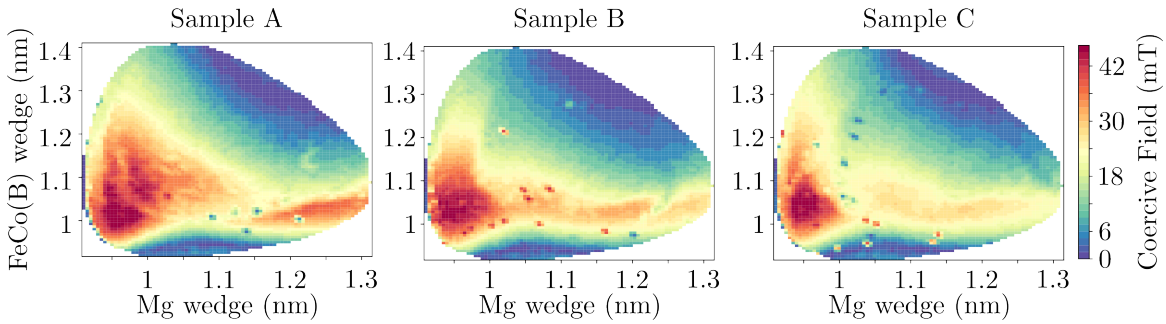


Figure 3.1: Coercivity mapping of a sample with 10 seconds oxidation at a base pressure of $3\times10^{-2}$ mbar (sample A), 10 seconds oxidation at a base pressure of $1\times10^{-2}$ mbar (sample B) and 10 seconds oxidation at a base pressure of $3\times10^{-3}$ mbar (sample C). Samples annealed at 300 °C for 10 minutes.

In this study, we use a conventional stack Ta (220)| FeCo(B) (8) | Pt (80) | (Co (5) / Pt (3))$_{\times6}$ | Co (5) | Ru (9) | (Co (5) / Pt (3))$_{\times2}$ | Co(5) | W (2) | FeCo(B) (9) | **Mg** (4.1 - 11) | (Ox., Press.) | **FeCo(B)** (10.6 - 15.5) | W (20) | Pt (50) (nominal thickness in Angstroms), annealed at 300 °C for 10 minutes. The Ta|FeCo(B)|Pt serves as a seed layer for the good structural growth of the Co|Pt multilayers. Later on, the Ta is used as a bottom electrode for our device. The next structure is composed of a synthetic antiferromagnetic (SyAF), a multilayer composed of two ferromagnetic layers, antiferromagnetically coupled across a Ru spacer by the Ruderman-Kittel-Kasuya-Yoshida (RKKY) coupling [112, 113]. This configuration allows for a reduction of the resultant dipolar field from the reference layer in the storage layer (through otimisation of thicknesses and number of multilayers). Afterwards, we deposit an amorphous interfacial FeCo(B) layer (B is an amorphising element), spaced from the last Co|Pt multilayers by a small W layer. This spacer is thin enough so that the FeCo(B) layer is coupled to the Co|Pt multilayers, increasing its stability as a reference layer. The W, just as the Ta, acts as a texture breaker and boron-getter [114–116]. This layer allows a structural transition from the threefold symmetry fcc (111) of the Co|Pt multilayers to the fourfold crystallographic symmetry bcc (001) of the MgO tunnel barrier. Additionally, during the annealing, the boron atoms diffuse out of the FeCo(B) alloy and get absorbed by this non-magnetic spacer. Then, the already textured MgO further crystallizes and acts as a seed layer for the crystallization of the interfacial FeCo. On top of this, a second W layer is deposited, acting as a boron-getter for the storage layer. Notice that the placement of these W layers allow for a B-free region near the MgO - FeCo interface, improving TMR and surface anisotropy. A Pt metallic capping is then deposited for oxidation protection.

Here we have a strongly pinned reference layer, which can be pointing up or down, as there is no field applied during annealing, and we expect magnetic switching only from the case of the FeCo(B) storage layer wedge. The coercivity mapping for samples with different natural oxidation conditions is shown in Figure 3.1 for the case of **Sample A** (10 seconds oxidation at a base pressure of $3\times10^{-2}$ mbar), **Sample B** (10 seconds oxidation at a base pressure of $1\times10^{-2}$ mbar) and **Sample C** (10 seconds oxidation at a base pressure of $3\times10^{-3}$ mbar). It is observed, qualitatively, the same behaviour in the three situations with a slight drop of coercivity for case of with lower base pressure, as expected from the least amount of oxidation and proportional decrease in iPMA.

It can also be seen that, if we fix, for instance, the thickness of FeCo(B) at around 1.2 nm and increase the thickness of Mg, there is a drop of coercivity (for reference, the loops are shown in Figure 3.2 (*a*)). This can be explained the same way as for the situation with the drop in R × A. Since the oxidation is small compared with the total thickness of the Mg, there is less oxygen arriving at the interface with the FeCo(B), which lowers iPMA, and thus coercivity. It is interesting to state that, for longer oxidation time or higher base pressures, this trend would shift to thicker values of Mg. Indeed, if the oxidation is larger then, for a smaller thickness of Mg, there can be oxidation of the magnetic electrode, which lowers the coercivity of the storage layer as well. In this situation, thanks to the lower oxidation, this is not observed. If we now fix the value of Mg at around 1.1 nm, and increase the thickness of FeCo(B) ((for reference, the loops are shown in Figure 3.2 (*b*))) we can observe a first increase in coercivity, followed by a decrease after a certain threshold thickness. If the thickness of the FeCo(B) is small, then during annealing, there might be diffusion of some of the W in the capping layer to the interface between MgO|FeCo(B), lowering coercivity. As the thickness of FeCo(B) is increased, the separation between the interface and the W layer is larger, reducing the impact of diffusion at the interface, increasing coercivity. However, if we keep on increasing the thickness of the layer, then there is a certain point at which the demagnetising energy is enough to bring the magnetization in-plane, and thus we lower the perpendicular component of the magnetisation. A striking feature in the loops of figure 3.2 is the existing coupling field. Indeed, since we are in the thin film limit, there should be no contribution to this offset, which usually comes from dipolar coupling with the reference layer once the device is patterned. In our situation, however, this is related to a possible direct-coupling through the tunnel barrier. Indeed, as these layers are grown using sputtering, it is expected a certain degree of roughness at the different interfaces. This roughness, present in the tunnel barrier as well, can lead to a so called Néel coupling or *orange peel coupling* between the reference layer and the storage layer [117, 118]. This can be expected from our samples for the lower thickness of Mg and, adding to the fact that the oxidation is limited, there are most possibly pinholes through the tunnel barrier. Works on coupling at thin film level between the reference and storage layer spaced by a naturally oxidized MgO spacing layer were already reported [119]. There, it was observed an oscillatory coupling, that would prefer a parallel or antiparallel alignment depending on the thickness of both tunnel barrier and magnetic electrodes. This was not, at this point observed in our thin film devices, due to our possibly lower oxidation conditions. This brings negative implications for the lower R × A MgO but also offers interesting opportunities for future works (possible use for Quad-MgO PSA-MTJ, thanks to the direct coupling given between adjacent ferromagnetic layers [106, 120]). Regarding the use of lower R × A, at this moment, we are limited to oxidation times of 10 seconds due to the non reproducible oxidation of the Mg layer, *i.e.* there might be regions in the wafer that are oxidized and others in which there is no oxidation or it is underoxidized. This can bring issues in the electrical characterization of the devices due to possible shorts (conductive Mg), different TMR values but also different coupling fields. In a process flow in which the fabrication is divided in multiple steps, each one critical to the yield of the wafer, added constraints should be avoided. For this purpose, we use for our limit in R × A oxidation conditions of the main barrier 10 seconds at a base pressure of $1\times10^{-2}$ mbar, as reducing the base pressure brings limitations regarding variability throughout the wafer.

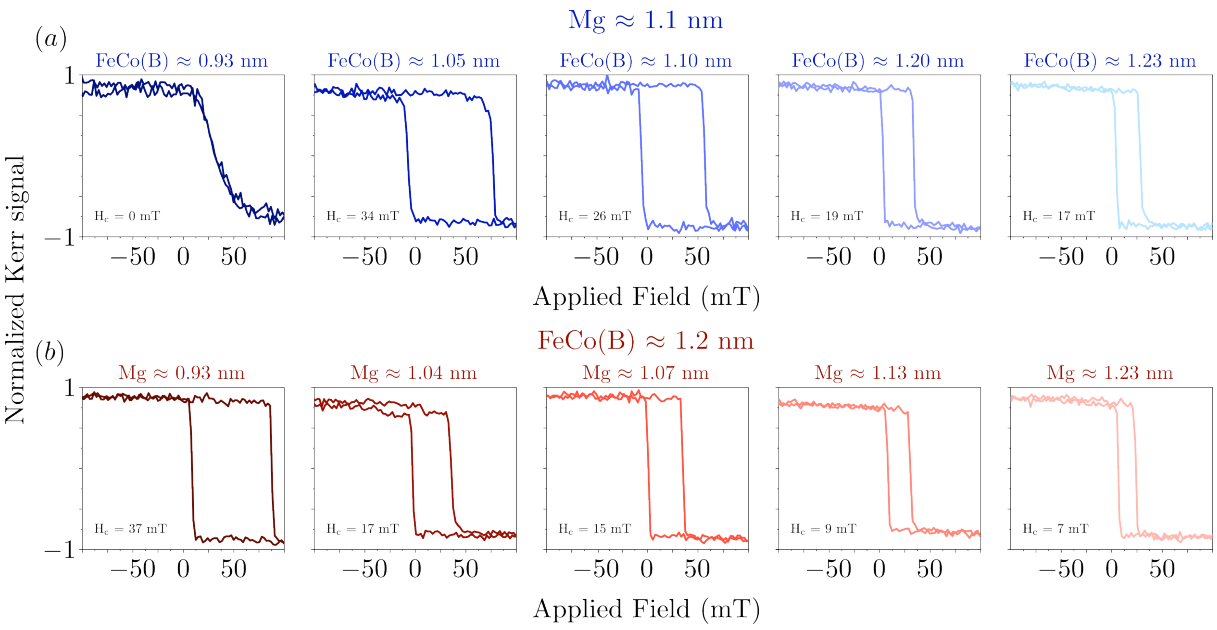


Figure 3.2: Evolution of the coercivity through moke measurements along two different wedges in sample C. In a first wedge measurement the thickness of the Mg is fixed at 1.1 nm and, in the second wedge measurement, the FeCo(B) is fixed at 1.2 nm.

After the optimization of the magnetic layers is done, we process the wafer to achieve several individual patterned pillars. In the next subsection we detail the process flow with examples and schematics of each of the important critical steps.

## 3.2 MTJ fabrication

To fabricate our magnetic devices we need to consider several steps along the fabrication process, from chemical etching to physical etching and the use of UV lithography to define some of the layers of the electrical device. The different process steps are shown sequentially.

As already explained, after multilayered deposition, there is an annealing step at 300 °C for 10 minutes. In some situations, this step can be done at a later stage. Nonetheless, we choose to do it before hard mask deposition. This prevents any deterioration of the hard mask, which could potentially compromise its etching. After this step we can choose to do MOKE measurements, especially to compare with post-processed samples. Afterwards, we deposit a 3 nm Ru stop layer and a 150 nm Ta hard mask that will be used to define the magnetic pillar.

At this point, we have the entirety of the magnetic layers, shown in 3.3 (*a*). For convenience and simplicity, the colours represent different layers in the stack. From bottom to top, we have in grey the $SiO_2$ base wafer, at white a Ta layer of 22 nm and in green a multilayer composed of FeCo(B) (8) | Pt (80) | (Co (5) / Pt (3))$_{\times 6}$ | Co (5) | Ru (9) | (Co (5) / Pt (3))$_{\times 2}$ | Co(5) | W (2) | FeCo(B) (9) |. Blue represents the single tunnel barrier Mg (7.5) | (Ox. Press. Time.) | Mg (5.0). In red it is shown the layers above the MgO, such as FeCo(B) and the capping layers composed of | W (20) | Ta (20) | Pt (50). These are examples of possible layers, but the structure is generalized

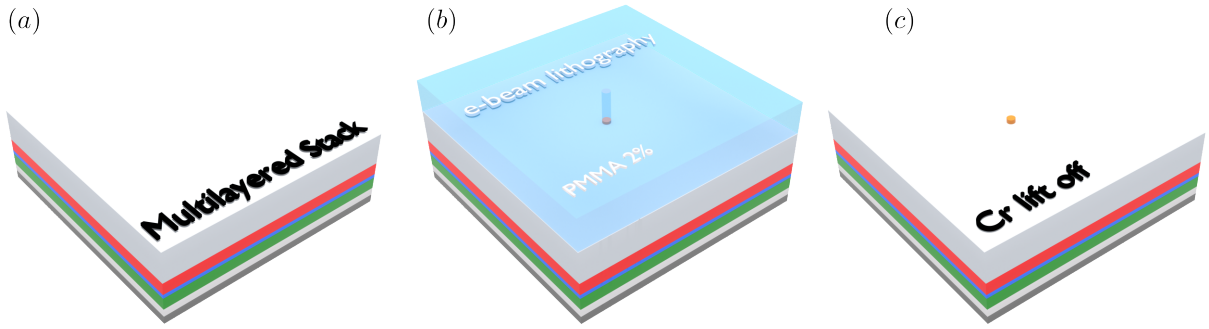


Figure 3.3: (*a*) Multilayered stack after Hard-Mask deposition (*b*) Cr deposition inside a nano-hole defined by electron beam lithography in a PMMA spin coated layer (*c*) Lift off of the Cr, leaving a first definition of the pillar.

as the bottom electrode, reference layer, tunnel barrier, storage layer and capping layers. It is then possible to modify the red layer by using other capping layers, such as an additional MgO, as it will be one of the samples given as an example in the next subsection.

After deposition of the hard-mask a polymer (poly methyl methacrylate - PMMA - 2%) is spin-coated onto the wafer. This polymer is commonly used for electron beam lithography (e-beam lithography, or EBL) due to to its high resolution [121]. Although this method can create dense arrays, the pillars need to be sufficiently spaced enough to do single device measurements, making it possible to cover an entire 4 inch wafer in a reasonable time. Through variations of the beam dose and exposure time, it is possible to write different diameters into the PMMA. Assuming that a single diameter is considered to be circular, it can be represented by the illustration of Figure 3.3 (*b*). After exposure and development (this step removes the part of the PMMA that was exposed) a 20 nm Cr layer is deposited by evaporation onto the wafer. Here, it is expected the Cr to cover the PMMA but also the depth of the hole formed by EBL. This is represented in Figure 3.3 (*b*), without the Cr on top of the PMMA for simplicity. Afterwards it is necessary to remove the PMMA along with the remaining Cr layer, done through a lift-off (combination of ultra sounds, isopropanol (IPA) and acetone). Afterwards, we are left with a clean wafer with Cr dots (3.3 (*c*)). These can have different geometries with varied thicknesses and shapes throughout the sample, as it is dependent on the lift off process and the quality of the deposition by evaporation. Thus, it is usual to get a diameter larger than the nominal diameter expected from EBL. We now have an initial definition of the device and it remains necessary to etch the hard-mask.

The etching of the hard mask is done using Reactive Ion Etching (RIE). This vertical etching is selective to Ta, so all the material that is not protected with the Cr dot will be etched. For a vertical pillar it is necessary to have an optimal etching time and the correct concentration of the gases in the chamber. In our process we use $SF_6$ (reactive agent) and $CH_2F_2$ (passivator). The ratio between these two gases will give us the straighter walls of the pillar, optimal for the further etching of the magnetic layers. It is important to realize that in this step there is no redeposition of Ta as the highly volatile Ta will bond to the reactive species and will be pumped out of the chamber. Thus, the shape and dimension of the pillar at this step, are related to the EBL, Cr deposition and further

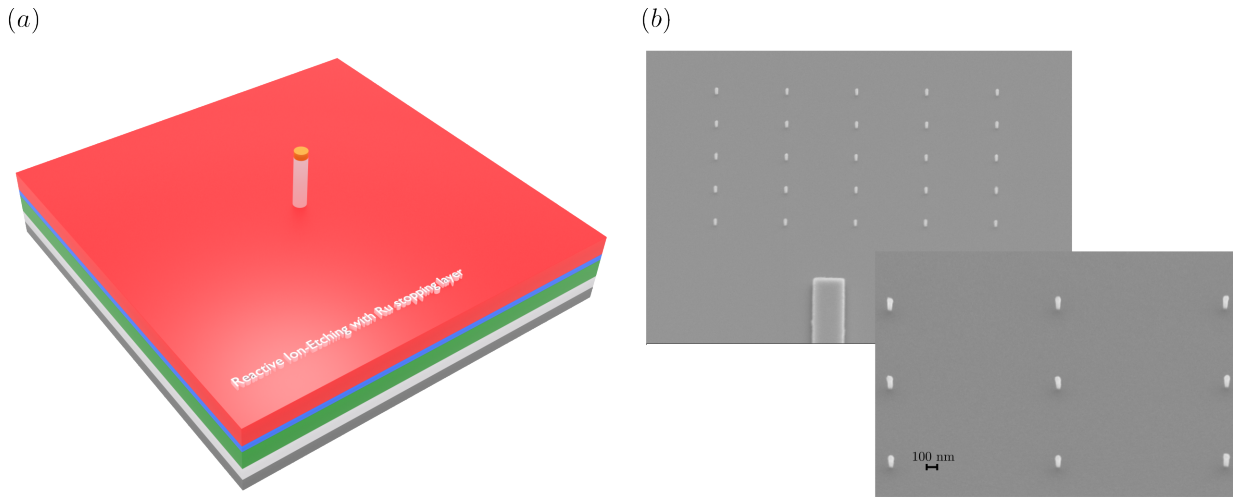


Figure 3.4: (*a*) Schematics of the magnetic pillar after Ta selective reactive ion etching and (*b*) scanning electron microscopy imaging of an array of pillars with nominal diameter of 35 nm after reactive ion-etching.

lift off, and possible imbalance between the gases in the chamber (impact in the RIE). A schematic of the fabrication process at this stage is shown in Figure 3.4 (*a*). Figure 3.4 (*b*) shows scanning electron microscopy (SEM) images of an array of pillars after RIE, with base diameter smaller than 50 nm.

After the pillar is defined, it is necessary to etch the remaining of the layers. At this stage, there is no RIE recipe that can etch the individual magnetic layers, so we proceed with Ion Beam-Etching (IBE). Contrary to RIE, there is a strong redeposition at this step, so the final diameter of the device is larger than the one obtained by RIE (Figure 3.5 (*c*)). To avoid most of this redeposition, the IBE is done at an angle of $\theta = 55°$, leading to a sufficient etching, while avoiding excessive increase in diameter. This is followed *in-situ* through a Secondary Ion Mass Spectrometer (SIMS) and shown for reference for a sample with capping MgO (Figure 3.3 (*b*)). In this example we show only 5 different materials (Fe, Co, Mg, Ru and Pt) which exemplifies the etching profile through the layers. In the first step we observe etch of Ru (1), followed by Pt (2). These correspond to the capping layers defined before. Afterwards, there is etching of FeCo (there is a small dead layer before the Mg) (3), followed by the etching of the capping MgO layer (4). Afterwards, the storage layer is etched composed of Fe and a small amount of Co (5). The main tunnel barrier is then etched (6) followed by the FeCo reference layer (7) and the start of the Co|Pt multilayers (8). Afterwards we reach the Ru layer (9) followed by the second set of Co|Pt multilayers (10), it should be noted that the magnitude of this is larger than the first set of multilayers due to the increased number of repetitions. To finish we reach the thick Pt layer (11) that promotes the growth of the Co|Pt, followed by what we define is the stopping layer before the bottom electrode, made of FeCo (12). The stop layer is defined to be the Ta bottom electrode right after the peak of the last FeCo layer. For usual MTJ diameters (above 50 nm, usually with a resistance of around kΩ), etching deep in the bottom electrode might lead to a series resistance, reducing the value of TMR of the electrical device. However, this variation in resistance will be insignificant compared with the already large resistance of the fabricated small diameters (usually above tens of kΩ).

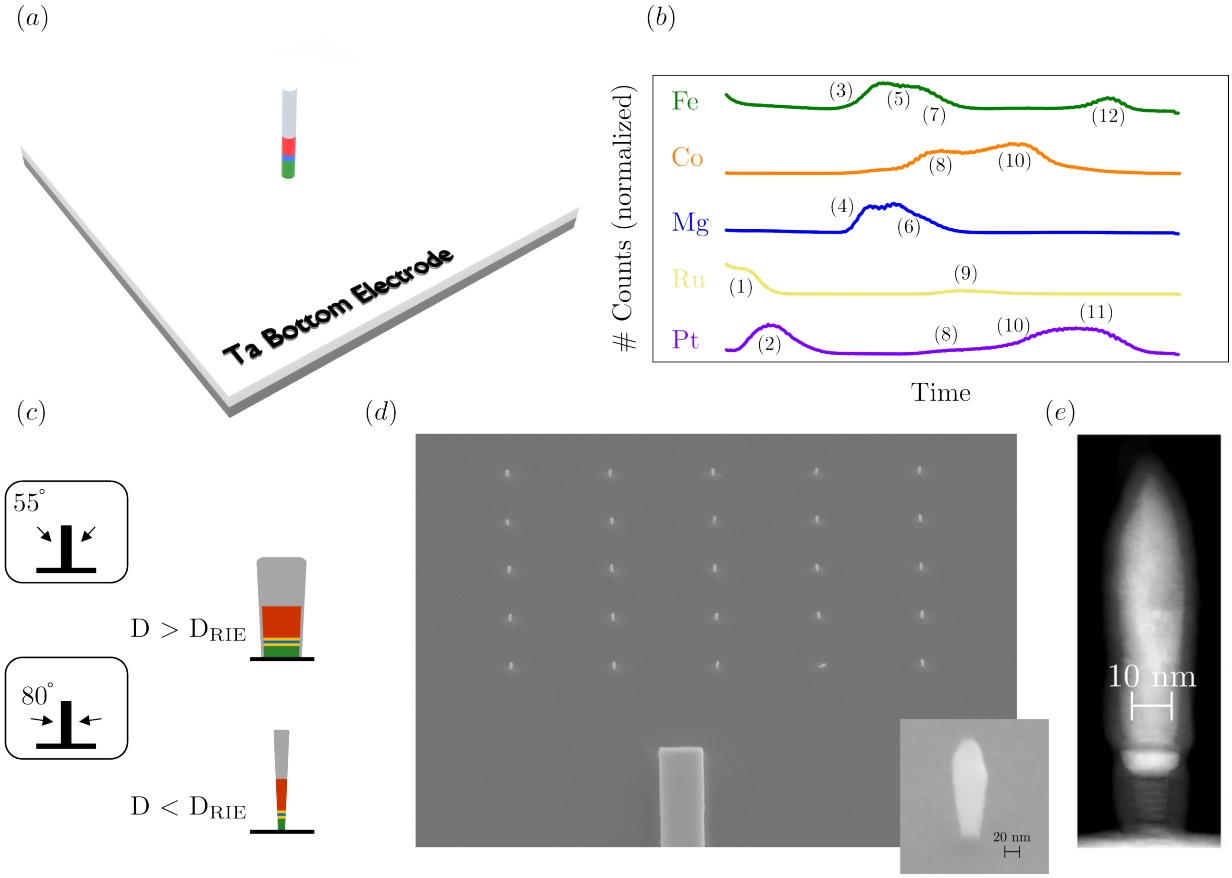


Figure 3.5: (*a*) Schematics of the magnetic pillar after ion-beam etching of the magnetic tunnel junction (*b*) SIMS profile of an usual perpendicular MTJ with capping MgO layer, representation of 5 different elements (Fe, Co, Mg, Ru and Pt) for simplicity (*c*) Schematics of the ion beam-etching process, with an initial etching angle of 55° with Ta redeposition (grey element) and associated trimming at a grazing angle of 80° (Angles taken considering the normal to the plane of the schematics) (*d*) Scanning electron microscopy imagining of an array of pillars with nominal diameter of 35 nm after the trimming step (close up in a pillar with diameter of around 20 nm) (*e*) High-angle annular dark-field scanning transmission electron microscopy imaging of a processed pillar showing a diameter smaller than 10 nm (figure also shown in [122]).

After the etching is done, it is necessary to clean the sidewalls of the pillars. Indeed, the Ta atoms removed from the hard mask will redeposit around the magnetic pillar, which will create shunts (shorts through the tunnel barrier as the current would prefer to pass through the metallic sidewall), shown in the schematic of figure 3.5 (*c*). This is done through an additional etching at a grazing angle of $\theta = 80°$ (completary angle of 10°, schematic of Figure 3.5 (*c*)). In conventional MTJ this step might be short, as only a small cleaning is required. However, to reduce substantially the diameter of the pillar it is necessary to trim more than in usual MTJs. This leads to several constraints, mainly fallen pillars, which lowers the yield of the wafer. Some of these can be observed in Figure 3.5 (*d*). An array of pillars after excessive trimming is shown in Figure 3.5 (*d*) with a closeup of a single pillar with an apparent diameter of 20 nm. It is important to notice the shape of this pillar. Indeed, through high-angle annular dark-field scanning transmission electron microscopy (STEM-HAADF) we observe the same shape of the pillar as in the SEM. However, we observe that the real non-oxidized diameter of the pillar is smaller than the one expected, which correlates with the

electrical diameter measured being smaller than the one measured by scanning electron microscopy (SEM). This shape needs to be already achieved from the RIE step, as present in the pillars shown before in Figure 3.4 (*b*). Indeed, if the pillar has an initial truncated shape, in which the base is larger than the top of the pillar, it will be impossible to reduce the MTJ to small diameters without damaging substantially the hard mask. As the latter will be our contact with the top electrode, a damaged hard mask (for instance triangular due to the overtrimming) will not allow for a proper electrical contact. If we are able to get a base diameter smaller than the top of the pillar, but the lateral dimension of the pillar is large, then there is a certain point in which the pillar will fall. This can happen due to two reasons: the first is that, during the trimming process, since the Ta hard mask is not etched at the same rate as the MTJ, there is a moment where the diameter of the MTJ is much smaller than that of the thick hard mask, tilting the pillar or making it fall: the second reason is the high aspect-ratio of the pillar and hard-mask. Considering the situation before, if the hard mask thickness was, for instance, half of its value, then the pillar could withstand its base diameter without tilting or falling. Since the thickness of the hard-mask cannot be substantially reduced without exhaustive optimization processes in both RIE and further contact with the top electrode, we use a ratio of $SF_6$ and $CH_2F_2$ that creates a slight overetch of the base of the hard mask. This will create a base diameter that is lower than the top of the Ta hard-mask. This effect avoids the creation of the enhanced foot in the MTJ, which leads to the typical truncated shape. However, for this step to be viable, it is necessary to start with a reduced diameter of the hard mask pillar. For this purpose we use nominal diameters of 35 nm and 50 nm for our devices, with test pillars at 80 nm. After the pillars are etched to the desired diameters, a photoresist is spin-coated onto the

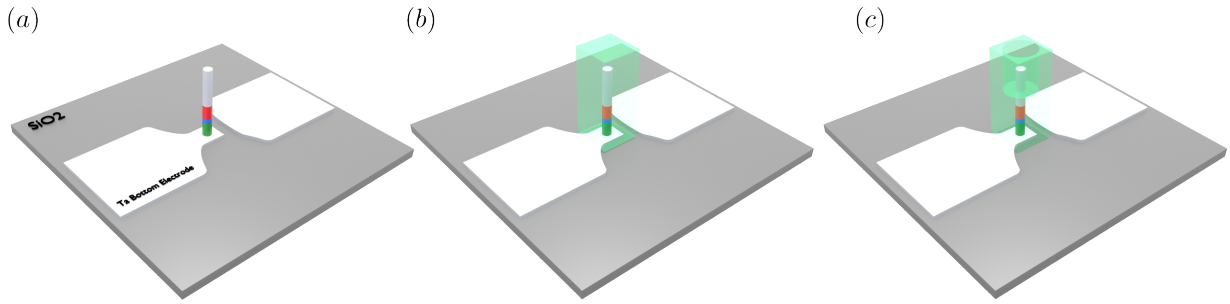


Figure 3.6: Schematics of (*a*) the Ta bottom electrode and magnetic pillar after RIE (*b*) the definition of the encapsulation of the pillar with ACCUFLO (green material) after RIE and (c) opening of the window in the ACCUFLO, exposing the hard-mask of the pillar.

wafer. This allows to define the bottom electrode through UV lithography. As the bottom electrode is made of Ta, the same RIE used for the hard mask is used to etch the layer. This lithography step disconnects the pillars from their neighbours [Figure 3.6 (*a*)], making possible single device measurements. It is then necessary to create a top electrode, isolated from the bottom electrode. To isolate these two electrodes, an organic polymer (ACCUFLO) is used for pillar encapsulation. This polymer has the advantage of planarization after spin-coated, so that its thickness along the wafer is roughly uniform. At this stage this polymer is deposited everywhere throughout the wafer but afterwards, by making use of UV lithography, it is confined to the surroundings of the pillar [Figure 3.6 (*b*)], followed by an etching by RIE. At this point the contact with the pillar is gone, so it is necessary to uncover the metallic hard-mask to realize the electrical contact with the MTJ. This is

done through an opening in the polymer, using UV lithography [Figure 3.6 (*c*)]. The depth at which we should etch into the ACCUFLO is critical as, if not enough to uncover a substantial part of the hard-mask there is no contact with the device and thus the magnetic element will read as open and, if we overetch and cross the tunnel barrier, it will read as short. Thus, the correct measurement of the etching time and etching speed of the ACCUFLO is crucial for the correct electrical contact with the device. After the ACCUFLO opening is correctly etched we deposit the top electrode, made of

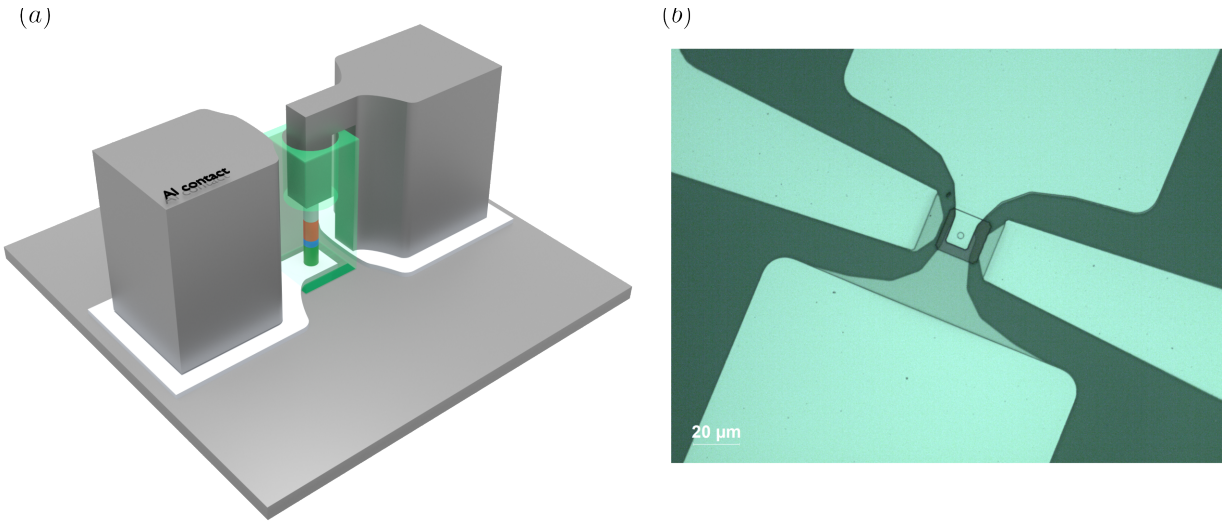


Figure 3.7: (*a*) Shematics of the final electrical device after deposition of the top electrode and (*b*) associated SEM image showing the top and bottom electrodes with a hole representing the ACCUFLO window. The extra metal pads are used in RF measurents.

10 nm Cr and 300 nm Al. The definition of the top electrode is realised in a two step UV lithography using a positive photoresist. Before deposition by evaporation of the metallic contact layers a small pre-etch is performed to clean any TaOx that might be present around the Ta hard mask. This step is minimized for small diameters as the hard mask is already very small and might damage further the contact. A schematic of the final device after lift-off is shown in Figure 3.7 (*a*) and a SEM image in Figure 3.7 (*b*). Now, it is possible to realize single-device measurements. This will be shown in the next subsection for the situation of a simple p-MTJ and afterwards for the situation of increasingly lower diameter.

### 3.2.1 Fundamentals of the electrical measurements under applied field

As a reference sample for the electrical and magnetic characterization, a standard perpendicular MTJ with single MgO and standard oxidation conditions (30 seconds at $3 \times 10^{-2}$ mbar)[a] was fabricated with a nominal diameter of 50 nm on a 100 mm wafer and annealed at 300 °C for 10 minutes prior to hard mask deposition. After patterning, we use an automatic prober station to measure the electrical properties of the devices in wafer. This is done through the extraction of the magnetoresistance of each individual device as a function of the applied field (resistance × field **RH** loops), as

[a] Ta(30)| | Pt (250) | (Co (5) / Pt (2.5))$_{\times 6}$ | Co (5) | Ru (9) | (Co (5) / Pt (2.5))$_{\times 3}$ | Co(5) | W (2) | FeCo(B) (9) | Mg (7.5) | (30 sec, $3 \times 10^{-2}$ mbar) | Mg (5) | FeCo(B) (15) | W (30) | Pt (50) (nominal thickness in Angstroms), reference sample named AV16_11

a function of the voltage applied (either DC or pulsed, leading to resistance-voltage **RV** loops) or as a function of both field and voltage (from which it is possible to construct phase diagrams). Each one of these measurements leads to different sets of results. Regarding field measurements, these are done by sweeping the field generated by an electromagnet placed directly on top of the measured device, reaching values as large as $|300\,\mathrm{mT}|$.

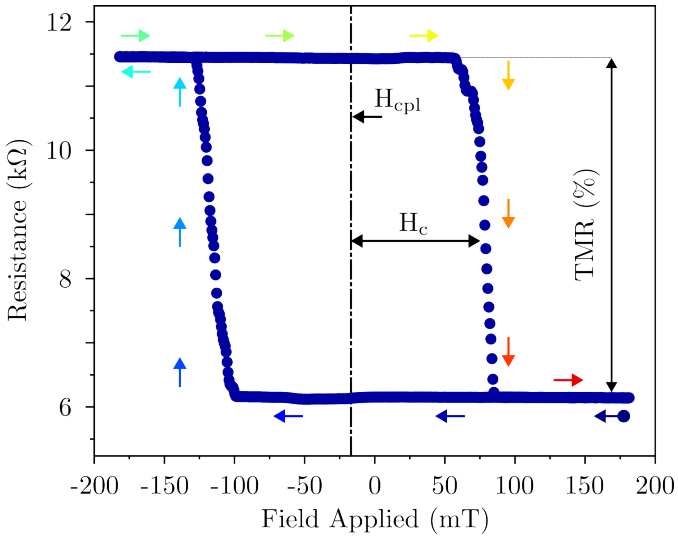


Figure 3.8: Example of a RH loop with coercivity $H_c$ and a coupling field $H_{cpl}$ for a device with a nominal diameter of 50 nm and uniform FeCo(B) storage layer thickness of 1.5 nm. The arrows show the direction of the sweep of the magnetic field applied, from blue to red.

To measure the resistance of the device a RF probe is used to connect the electrical pads. A low bias voltage is constantly applied (usually around 30 mV) to measure the resistance variation during the field sweep. A typical RH loop obtained from this type of measurement is observed in Figure 3.8. The field sweeps starts with a full saturation at positive values, at around 200 mT, which then starts reducing towards negative values. In this case, if the reference layer is pinned along $+\hat{z}$ then we are in the minimum resistance state $R_{PP}$, as long as the field applied is larger than the switching field $H^{switch}$ of the layer. When reducing the field up to a critical value ($-H^{switch}$) then the storage layer will reverse anti-parallel to the reference layer and thus leading to an increase in resistance $R_{AP}$. The ratio of the resistance states will give us the TMR of our device. When sweeping the field towards the other polarity, from negative to positive, a resistance change will occur when the field applied is larger than $H^{switch}$. This would be the situation in which there is no interaction from the reference layer in the storage layer, which is rarely the case. Indeed, for the SyAF fabricated in this stack, there is still some remnant uncompensated dipolar field acting on the storage layer. This is observed as a shift in field needed to start the field reversal, which usually favours the parallel configuration. The effect of the interaction between the reference layer and the storage layer can then be described as a shift in the switching field of the device for a certain value of coupling field ($H_{cpl}$):

$$H^{shift}_{switch} = \pm H_c + H_{cpl}, \tag{59}$$

the latter being negative if the reference layer is pointing up and positive if the reference layer is pointing down, which means that it is needed less field to orient the layer PP, than it would be the situation for AP.

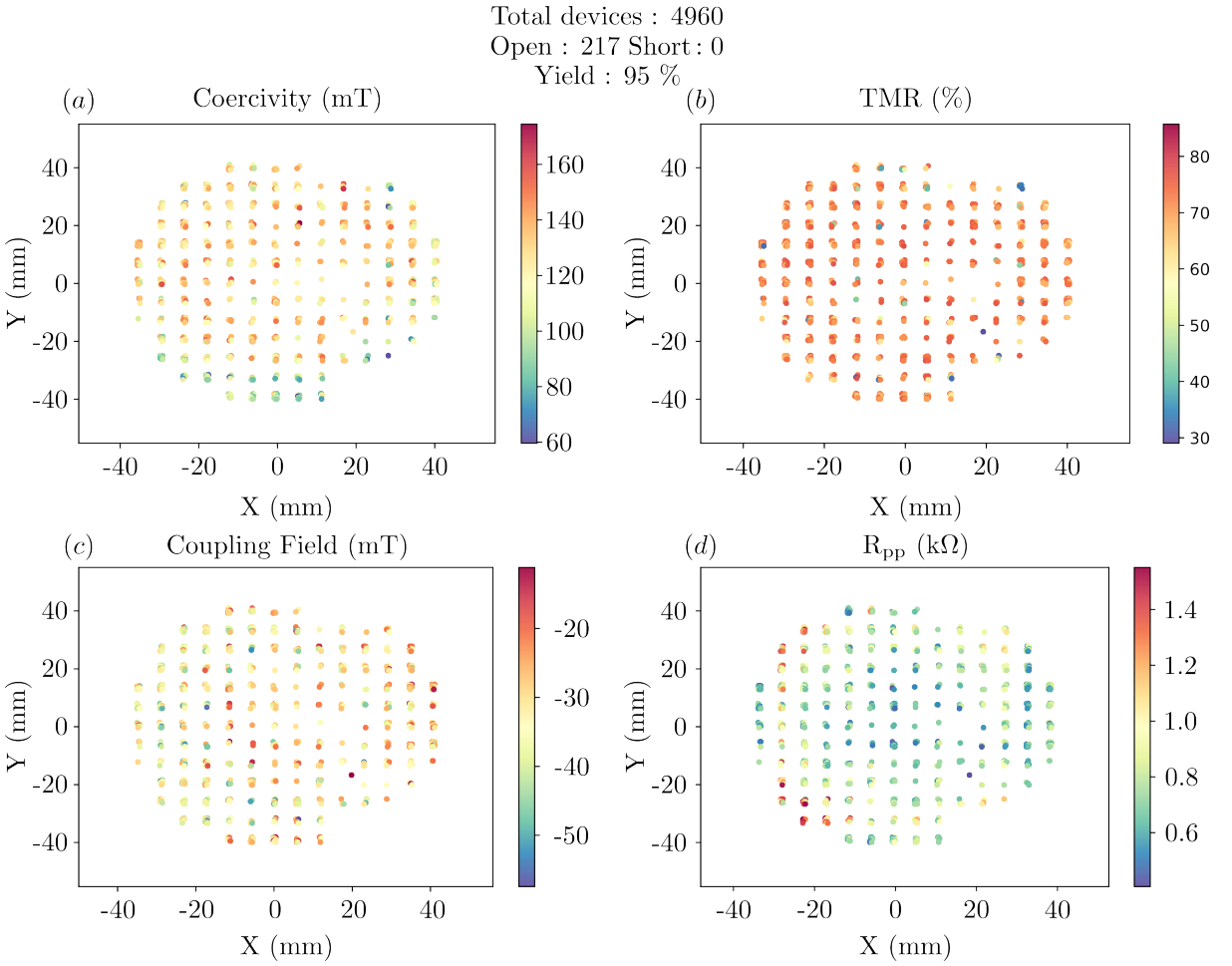


Figure 3.9: Mapping of ($a$) the coercivity of the devices along the wafer ($b$) the TMR of the devices along the wafer, ($c$) the coupling field of the devices along the wafer and the ($d$) minimum resistance state ($R_{PP}$) of the devices along the wafer. Mapping obtained for the nominal diameter of 50 nm. Electrical measurement considered for the conditions in which $R_{PP} > 20\,k\Omega$ and $R_{PP} < 500\,\Omega$.

The advantage of using an automated prober is that we can get each of these RH curves for each device in the wafer. This allows a statistical study if we are using wedges in the multilayers, but also for an analysis of the fabrication process. In Figure 3.9 we show the mapping of the ($a$) coercivity of the device, ($b$) the TMR, ($c$) coupling field and ($d$) the minimum resistance state ($R_{PP}$), for measurements of devices with a nominal diameter of 50 nm. The results are filtered considering that, for the $R \times A$ product of our tunnel barrier around ($10\,\Omega\mu m^2$, from table 2), the devices should not have $R_{PP} > 20\,k\Omega$ and $R_{PP} < 500\,\Omega$. Analysing the mapping, we see that the coercivity values are larger around the center of the wafer, although the nominal thickness of the storage layer is similar. This happens due to the different etching steps that occur during the fabrication. After the step of the RIE the devices at the border of the sample have a different wall profile than the ones in the central region. Usually, if the center pillar has a foot after RIE it will look straighter in the edge of the sample. This is what will be used afterwards for lower diameter and it is what is

happening at larger device diameter as well. Regarding TMR, it is seen that it is not varying largely throughout the wafer, although is gets reduced outside of the center region. This is most likely cause due to edge effect in the tunnel barrier during the trimming step. Regarding the coupling field it is seen that it increases, as well, when moving away from the wafer center. Although this difference in field is not substantial throughout the wafer, it can be expected due to the shape of the pillar after patterning and due to the smaller diameter. To corroborate the dependency with the diameter of the device, it is shown that, by moving away from the central part of the wafer, there is an increase in $R_{PP}$. This can happen thanks to (1) decrease in total diameter of the tunnel barrier, since the R × A product should be constant, or (2) increase in contact resistance, either from the bottom electrode or through oxidation in the hard mask before deposition of the top electrode. However, parasitic resistance values usually have an impact in the TMR of the device, which is seems hard to relate with the low distribution of data in this sample.

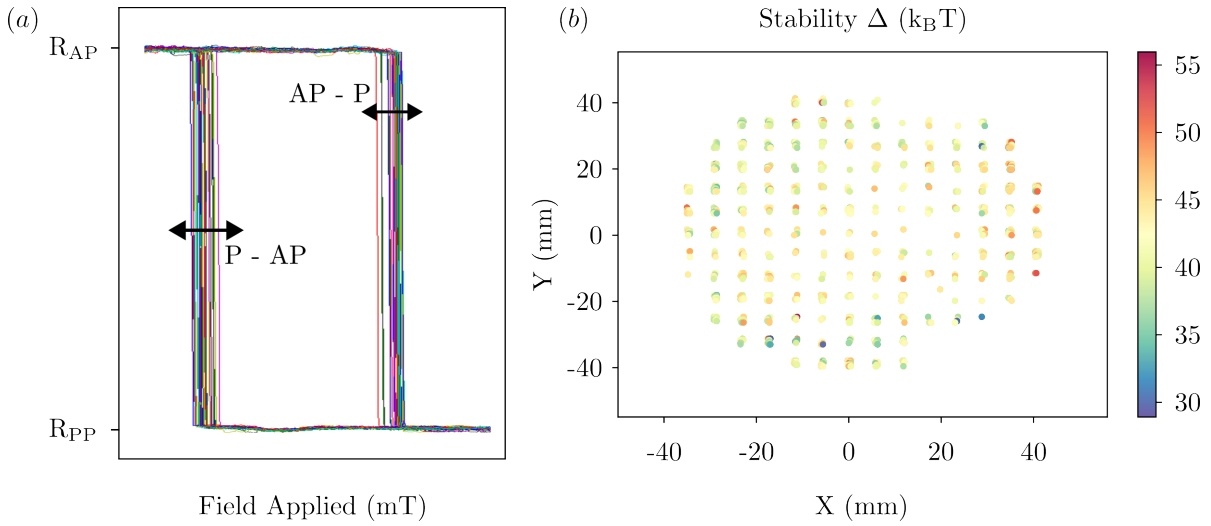


Figure 3.10: (*a*) Several RH measurements for extraction of the distribution of coercivity values PP-AP and PP-AP switching. (*b*) Mapping of the average value of the stability measured through the distribution of coercivity for each measured device.

This type of measurement allows to extract the value of the stability factor ($\Delta$) through the use of a perpendicular applied magnetic field. This method is based in the switching field distribution (SFD), originally based on the probability of switching a magnetic nanoparticle under an applied field [123]

$$P(t) = 1 - \exp\left\{-\left|\frac{H_K}{2t_0 R_s}\right|\sqrt{\frac{\pi}{\Delta_0}}\,\mathrm{erfc}\left(\left|\sqrt{\Delta_0}\right|\left(1-\frac{H(t)}{H_K}\right)\right)\right\} \tag{60}$$

where $\mathrm{erfc}(x)$ is an error function, $t_0$ is the switching attemp time set at 1 ns and $R_s$ the sweeping rate of the magnetic field, which is our setup can vary from $1\,T\cdot s^{-1}$ (commonly used for high resistance devices) or $5\,T\cdot s^{-1}$ for low resistance devices [124]. This method can be applied to the statistical distribution of coercive fields for a typical RH measurement. Indeed, Figure 3.8 shows the situation of a single RH measurement, however working at room temperature brings a need for a statistical distribution of the results and, for that, different RH loops are necessary to extract important values such as $\Delta$ and the anisotropy field $H_K$. From Figure 3.10 we can see in (*a*) the distribution of the coercivity values from PP-AP and from AP-PP, these will give us an associate value for $\Delta_{AP}$ and

$\Delta_{PP}$. In Figure 3.10 we can observe the mapping of the average value of the stability from both situations. It is observed, as expected, a similar trend to the distribution of the average coercivity throughout the wafer, in which the values associated with larger $R_{PP}$ show lower stability, as it scales with the device surface $\Delta \propto D^2$.

### 3.2.2 Fundamentals of the electrical measurements under applied voltage

For a functional device we want to be able to control the magnetization reversal without applied magnetic field, and thus the knowledge of the voltage-driven measurements is necessary. With these, we can extract important values, such as the critical switching voltage $V_{c0}$. This can be done similarly to the method employed for the field switching distribution as:

$$P(V) = 1 - \exp\left\{\frac{t_P}{t_0}\exp\left\{\Delta\left(1 - \frac{V}{V_{c0}}\right)\right\}\right\}, \tag{61}$$

where V is the applied voltage and $t_P$ the pulse length (usually our measurements are done with 100 ns pulses). Prior to the measurements with voltage, RH measurements are done on the device. This allows to calculate the intrinsic coupling field which, if not cancelled, will favour one of the states rather than other. For this purpose, during the voltage measurement, there is constantly

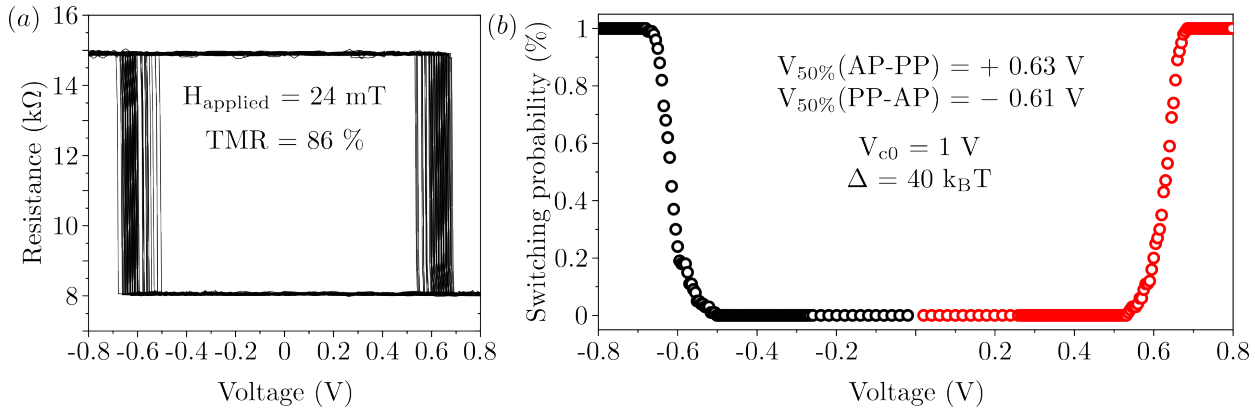


Figure 3.11: (*a*) 100 Resistance × Voltage loops under a constant applied field of 24 mT, device selected with a TMR of 86 % and $R_{PP} \approx 8\,k\Omega$ and (*b*) associated switching probability for extraction of critical switching voltage $V_{c0}$ and stability factor $\Delta$. For convenience, the switching voltages at half height (50%) are shown for both negative (black symbols) and positive (red symbols) voltage.

applied a magnetic field with opposite sign to that of the device coupling field. In Figure 3.11 (**a**) it is shown different events of voltage sweep from −0.8 V to 0.8 V, confirming first and foremost, the switching by STT. From the distribution of the switching voltages, similarly to the distributions in coercive field shown before, it is possible to assign a switching probability to each applied voltage (Figure 3.11 (**b**)). From here, one can use Equation 61 to extract parameters such as the $V_{c0}$ and the stability factor $\Delta$ (both these results are taken as the average from AP-PP and PP-AP). In the situation of 100 ns pulse measurements, as it is often our situation, it is also important to extract the quantities $V_{50\%}$ for both AP-PP and PP-AP. These, should be similar under the assumption that the switching characteristics of the STT are similar (*i.e.* there are no different transport properties

between states) and the coupling field is perfectly compensated, as it is roughly in this situation. Additionally, this is implemented in the mapping of the wafer, and we can observe how the critical voltage is changing through the wafer, as shown in Figure 3.12 (*a*). There are different methods

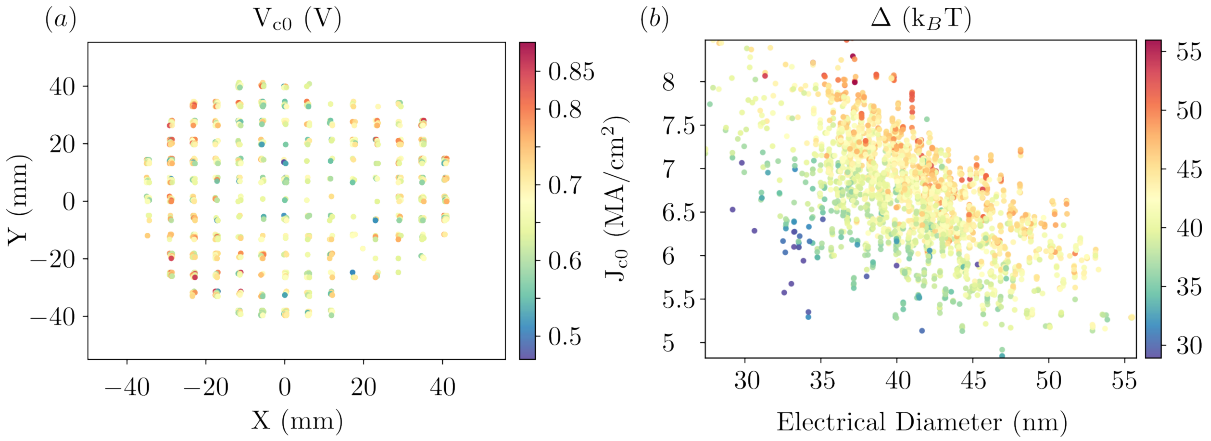


Figure 3.12: (*a*) Mapping of the critical switching voltage ($V_{c0}$) throughout the 100 mm wafer and (*b*) dependency of the switching density of current ($J_{c0}$) with the electrical diameter. Colorscale linked with the magnitude of the stability factor calculated through the RV loops.

and models proposed so comparisons between critical values such as $V_{c0}$ and $\Delta$ are realised within the same extraction method, which allows for a consistent study. Here, aligned with the results of coercivity, it is shown that there is a minimum of critical switching voltage $V_{c0}$ in the center portion of the wafer, which increases when moving towards the edge. Since there is no significant variation in $\Delta$ throughout the wafer, this variation in voltage is due to an increase in resistance of the device, thanks to a decrease in the surface area. This can be related to the critical switching density ($J_{c0}$)

$$J_{c0} = \frac{V_{c0}}{R \times A}, \tag{62}$$

assuming that the $R \times A$ product of our MgO is constant after patterning of the pillar, which might not be the case due to edge effect in the MgO. However, as this is hard to estimate, an initial assumption that it is constant is valid for the remaining of the study. It is shown that, firstly, as the electrical diameter reduces, there is an increase in $J_{c0}$. This is related to an increase in $V_{c0}$ due to the increase in $R_{PP}$. Nonetheless, it is also observed that, for the lower electrical diameter of around 30 nm, there are lower values of $J_{c0}$, associated with the lower value of $\Delta$.

Other important factor to consider is the critical switching current $I_{c0}$, knowing that this is simply given by the ratio $V_{c0}/R_{PP}$. From this relation we expect for $I_{c0}$ to depend roughly on $R_{PP}^{-1}$, which can be observed in Figure 3.13 (*b*). This can be further related with the electrical diameter of the device knowing that the $R \times A$ is related with the electrical diameter and $R_{PP}$ as,

$$D_{elec} = 2\sqrt{\frac{(R \times A)}{\pi R_{PP}}} \tag{63}$$

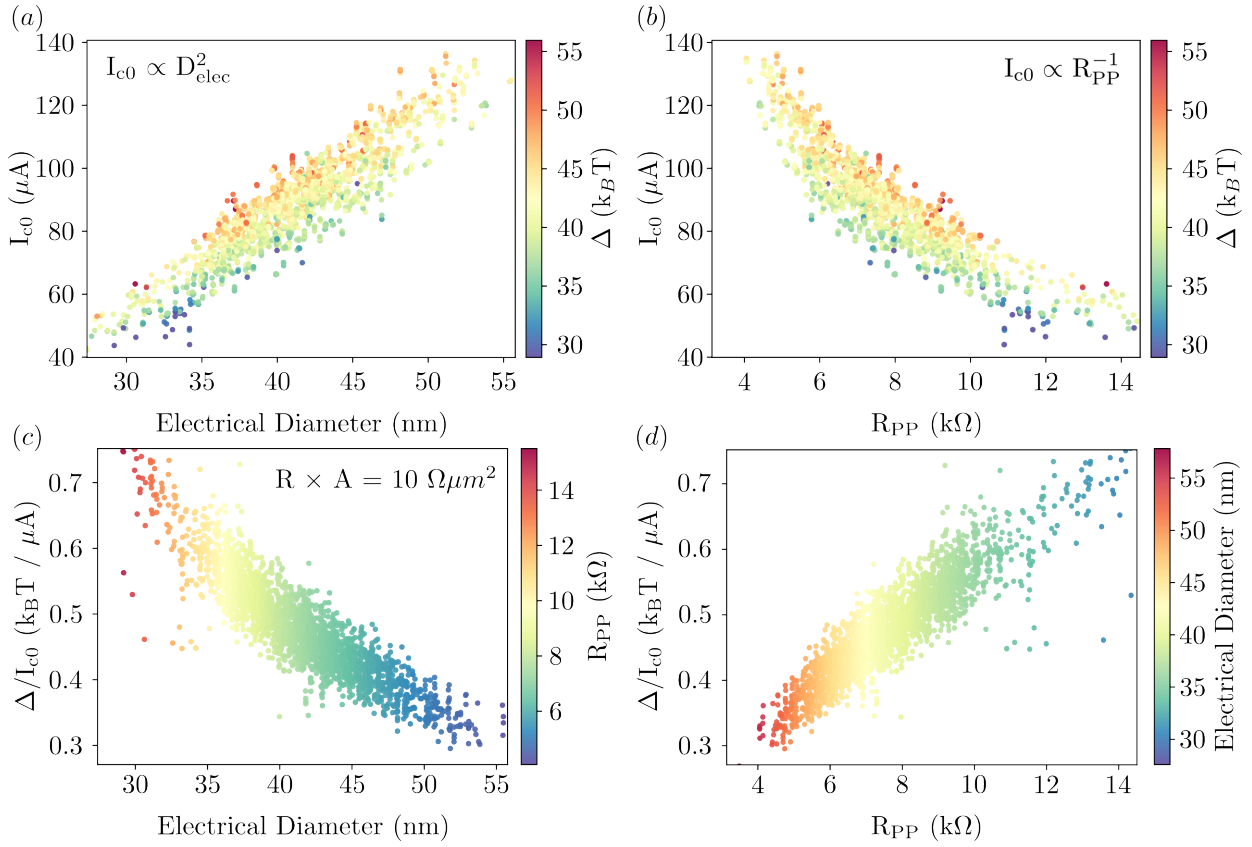


Figure 3.13: (*a*) Dependence of the critical switching current with the electrical diameter ($I_{c0} \propto D^2_{elec}$), with the colormap linked to the individual stability of the device, (*b*) Dependence of the critical switching current with the minimum resistance state ($I_{c0} \propto R^{-1}_{PP}$), with the colormap linked to the individual stability of the device, (*c*) Dependence of the figure of merit FOM ($\Delta/I_{c0}$) with the electrical diameter (FOM $\propto 1/D^2_{elec}$) with colormap linked to the value of $R_{PP}$ and (*d*) Dependence of the figure of merit FOM ($\Delta/I_{c0}$) with the minimum resistance (FOM $\propto\approx R_{PP}$) with colormap linked to the value of $D_{elec}$.

and thus, we expect a somewhat linear relation with $I_{c0}$, as observed in Figure 3.13 (*a*). From the relation between $\Delta$ and $I_{c0}$, it is possible to extract a relevant quantity for an MRAM device, its figure of merit (FOM) ($\Delta$ / $I_{c0}$). In Figure 3.13 (*c*) we observe that this FOM increases as the resistance increases (or the electrical diameter is reduced, as long as the R × A product is kept constant after patterning). This happens since there is no significant variation in stability factor in this range of diameters and the main effect is the increase in resistance and thus an increase in $V_{c0}$. Moreover, this increase can be somewhat linear with the increase in $R_{PP}$ (since $I_{c0} \propto R^{-1}_{PP}$) or increase with the inverse of the diameter, where for smaller diameter there is the largest FOM ($I_{c0} \propto D^2_{elec}$).

### 3.2.3 Fundamentals of the electrical measurements under applied voltage and applied field

There are also different characteristics that we can extract from voltage-field stability phase diagrams, such as the influence of the STT and heating effects. These can be extracted through the shape of the diagram. This is done by a succession of RH loops at different applied voltages. First, a field is swept at a certain frequency (in usual situations it is used a sweep rate of $5\,\mathrm{T}\cdot\mathrm{s}^{-1}$) in which at each field point there is a voltage with a certain amplitude V applied for a pulse length of 100 ns, with further measurement of the resistance state of the device with a voltage of 30 mV.

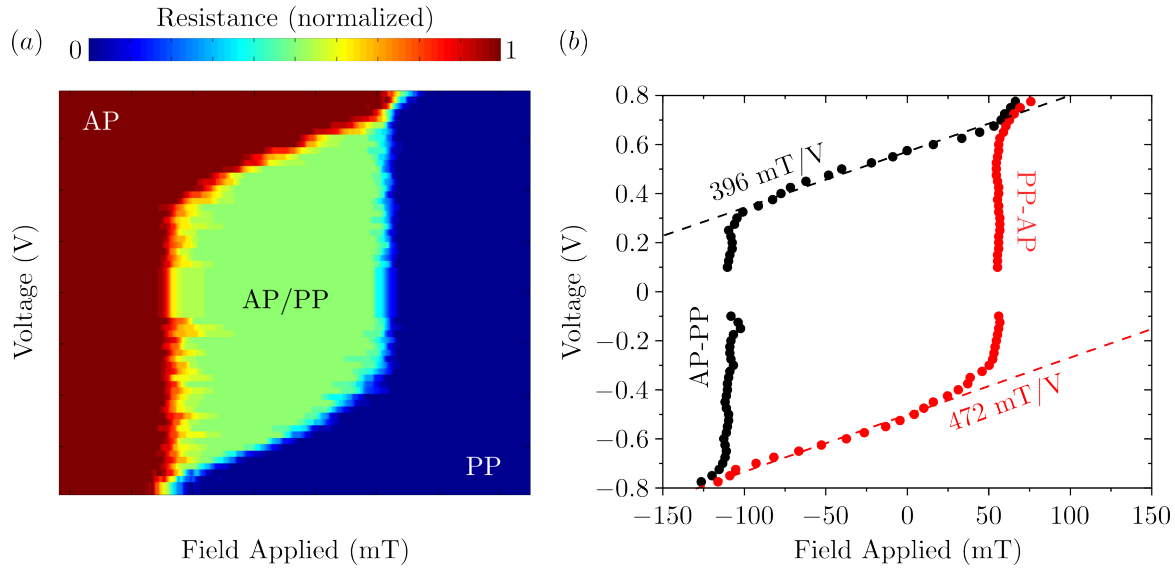


Figure 3.14: ($a$) Phase diagram of a generic perpendicular MTJ device with red color the AP region (high resistance state) green color the transition region from AP/PP and blue color the PP region with the lowest resistance state and associated ($b$) boundaries of the phase diagram for AP/PP and PP/PP as well as the associated slopes. Values obtained for a sample with 70 % TMR and an extracted $\Delta = 82\,\mathrm{k_B T}$.

In Figure 3.14 ($a$) we can observe an example of a 100 ns pulsed phase diagram as a function of the voltage and applied field. As the resistance is measured at each data point for each applied voltage, there are three different regions. A fully AP region (in red) with maximum resistance state. This can be given for regions in which the field applied is larger than the switching field for the anti-parallel configuration. An intermediate region, in which it is either AP or PP. At no applied pulsed voltage, the width of this region is related to the coercivity of the device measured by a single R-H measurement. After a positive field larger than the PP switching field we are met with the minimum resistance state, as this field saturates the layer fully PP. As we apply the voltage in the system we distort this relation and the switching occurs also through voltage. The effect of the STT, and thus its efficiency, is given by both slopes in the phase diagram, associated with the boundaries shown in Figure 3.14 ($b$). From these, it is possible to extract a value proportional to the STT switching efficiency $a_{\parallel}/\alpha$, for both the AP-PP and PP-AP transitions, as shown from the linear fit [52, 125]. Here, we can observe that there is a discrepancy between the two switching values. From

the relation

$$\frac{dH}{dV} = \frac{a_{\parallel}}{\alpha} = \frac{2e}{\hbar}\frac{\eta}{\alpha(R \times A)M_s t}, \tag{64}$$

we would expect that symmetrical switching would correspond to the same slope, which is not the case in this situation.

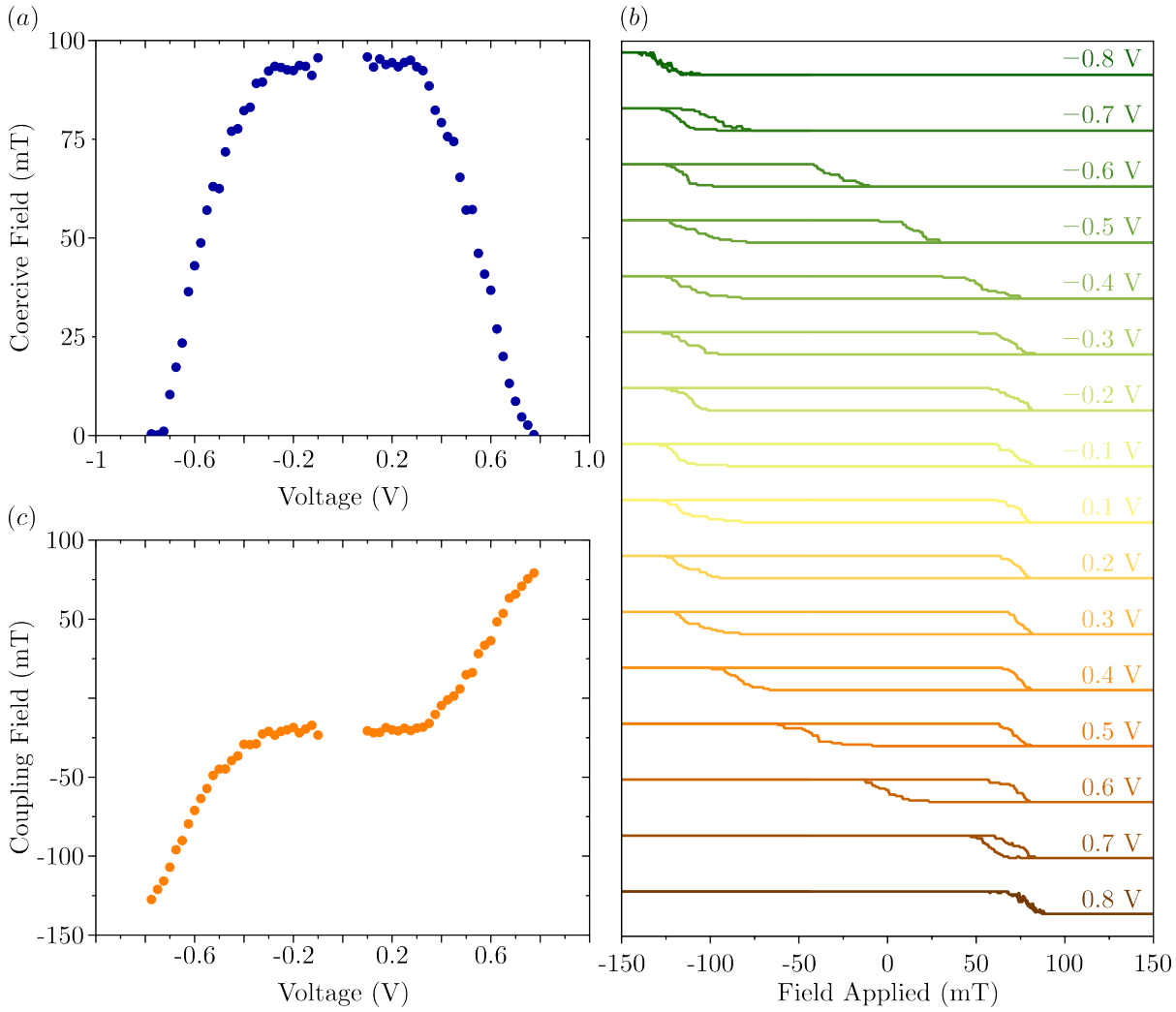


Figure 3.15: Dependence of ($a$) the coercive field and ($b$) the coupling field on the pulsed applied voltage. ($c$) RH loops for different applied pulse voltage. Dependencies obtained for a sample with 70% TMR and an extracted $\Delta = 82\,k_BT$.

A better understanding on how the STT is affecting the magnetic layer can be observed in the variation in coercivity of Figure 3.15 ($a$) as a function of the applied voltage. Indeed, in the range of voltages where there is no slope $dH/dV = 0$ there is no difference in coercivity and neither in coupling field (3.15 ($b$)). The representation of each device RH curve for each voltage point is shown in Figure 3.15 ($c$). As we increase the voltage, either in positive or negative polarity, we observe a reduction of the coercivity. However, there is only one branch moving, and thus there is an increase in coupling field. As we increase the voltage to positive values at which the STT starts acting in the device it will start favour the AP state. In this case, even if the voltage is positive, the flow of electrons is opposite to the current applied. Now, this will not vary the AP switching field, but the

field necessary to reverse the magnetic layer for an AP state is much smaller than before, because of the effect of the STT. The same happens symmetrically for the PP state where now the branch that favours the AP transition shifts to larger negative fields.

## 3.3 Enhanced stability and performance through MgO capping

The electrical characterization methods described in the last section are now used for a p-MTJ with MgO capping. Indeed, as explained before, one of the possible routes to reduce the total height of the PSA-MTJ is to make use of an additional MgO capping layer. As the yield of a wafer with PSA-MTJ pillars is quite low, it is difficult to extract relevant significant statistic information from wedges at the interface. Thus, we make a wedge along an usual p-MTJ layer with MgO capping. Here, we start with nominal diameters of 35, 50 and 80 nm. The reason for this is twofold. With the lower diameter we can test the viability of the small R × A, namely as a function of the $R_{PP}$ of the device. Additionally, at 80 nm nominal diameter we can test this wafer for usual MTJ applications, thanks to the enhanced stability. We then fabricate a wafer[b] with low offset field and with Ta bottom electrode, as explained beforehand, with Ta (220)| FeCo(B) (8) | Pt (80) | (Co (5) / Pt (3))$_{\times 6}$ | Co (5) | Ru (9) | (Co (5) / Pt (3))$_{\times 2}$ | Co(5) | W (2) | FeCo(B) (10) | Mg (7.5) | (10 s and $1 \times 10^{-2}$ mbar) | Mg (5) | **FeCo(B)** (6.5 - 11.5) | W (2) | **FeCo(B)** (5.5-9.1) | Mg (8) | (10 s and $3 \times 10^{-3}$ mbar | Mg (5) | FeCo(B) (4) | W (20) | Ta (20) | Pt (50) (nominal thickness in Angstroms). This stack is different from the one shown before because of the top MgO capping. Now, we need to use a W spacer layer in between both FeCo(B) layers, so that there is also crystallization in the capping MgO. For simplicity, we call the FeCo(B) in contact with the main MgO bottom FeCoB and the one in contact with the capping MgO, Top FeCo(B). The MOKE mapping of this sample is shown in figure (3.16) for the coercive field and remanence. It is shown that the maximum coercivity is

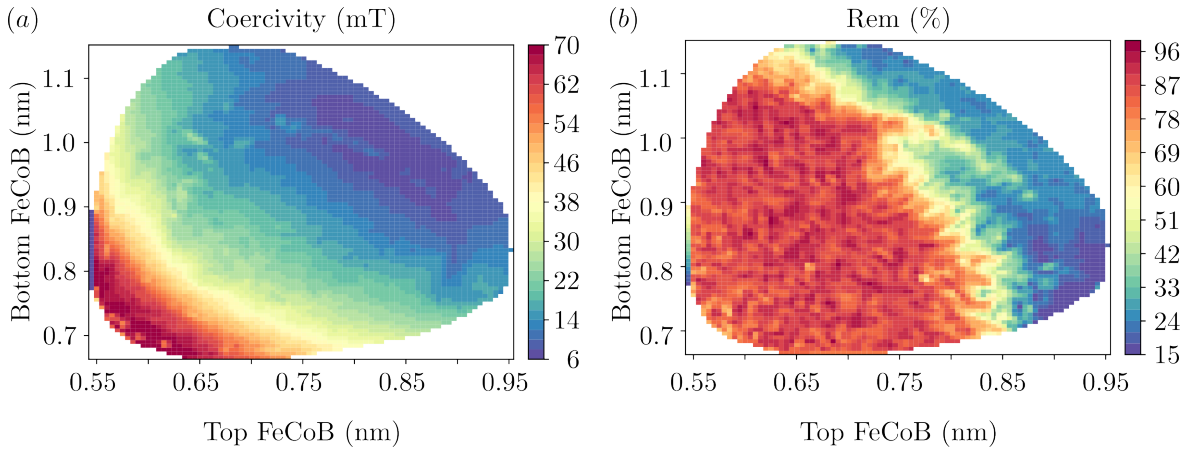


Figure 3.16: Mapping at thin film level of (*a*) Coercivity and (*b*) remanence as a function of the wedge in the bottom and top FeCo(B) layers.

obtained for the lower thicknesses of both wedges, with a total thickness of around 1.4 nm. This value is quite similar to the one used for usual FeCo(B) layers with a single MgO interface. However,

[b]Reference sample name AX37_15

for patterned devices we expect a shift in this maximum of coercivity due to the geometrical factor coming from the shape anisotropy. In this stack we also use a barrier with lower pressure for the top MgO interface so that there is less resistance associated with it, as it will impact the voltage necessary to reverse the layer. Indeed, as observed in table 2, the total R× A product of this composite layer is of around $4.5\,\Omega\mu m^2$. We can also expect that the top MgO barrier is growing on top of a rougher surface, so that its R × A might be slightly lower than the one expected from CIPT measurements at thin film level as a main barrier.

Following the description of the fabrication at lower diameter in the beginning of the section, we fabricate and measure the electrical results of the sample making use of the capping MgO layer. In Figure 3.16 are shown the results of the minimum resistance state $R_{PP}$ measured throughout the wafer. We observe a low yield for devices with larger $R_{PP}$ (lower diameter), and a higher yield for larger pillars (lower $R_{PP}$). Moreover, the yield of the nominally smaller diameter devices (those

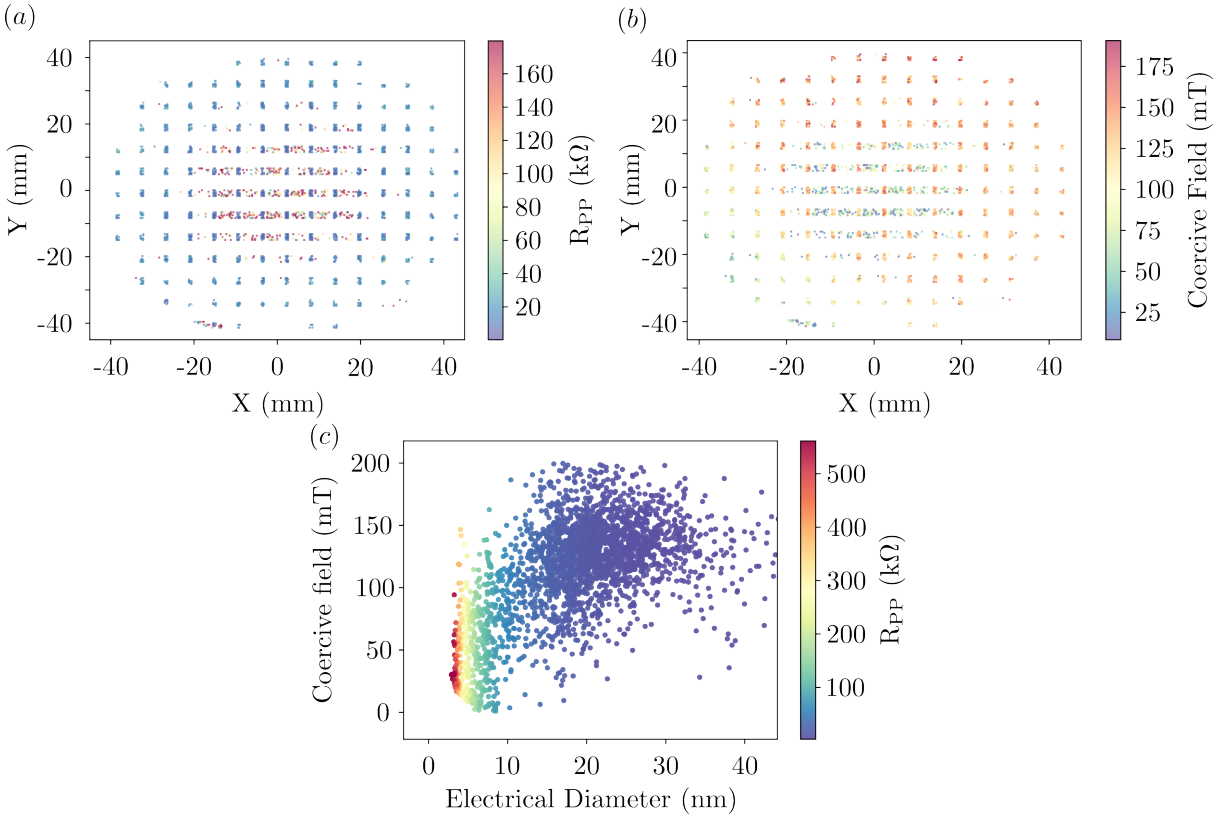


Figure 3.17: Patterned devices mapping of (*a*) the minimum resistance ($R_{PP}$) value and (*b*) the coercive field. (*c*) Dependence of the coercive field with the electrical diameter of each measured device. Colormap linked to the minimum resistance measured for each individual pillar.

smaller after RIE) is larger in the wafer center. Indeed, around the edges of the wafer, the trimming was so exhaustive that the pillars collapsed or disappeared due to their ultra-small dimension. This can also be observed through the mapping of the coercivity in Figure 3.17 (*b*), in which the coercivity is significantly reduced for the larger resistance (associated smaller diameter) devices. This is better seen through the dependence of the coercive field with the electrical diameter (Figure 3.17 (*c*)). There we observe a substantial decrease of the coercivity as the diameter reduces. Although there

might be some parasitic resistance associated with $R_{PP}$, overestimating the value of $D_{elec}$, these would account for some kΩs and, even though non-negligible for large diameters ($R_{PP} \approx k\Omega$), when in the range of tens or hundreds of kΩs becomes insignificant.

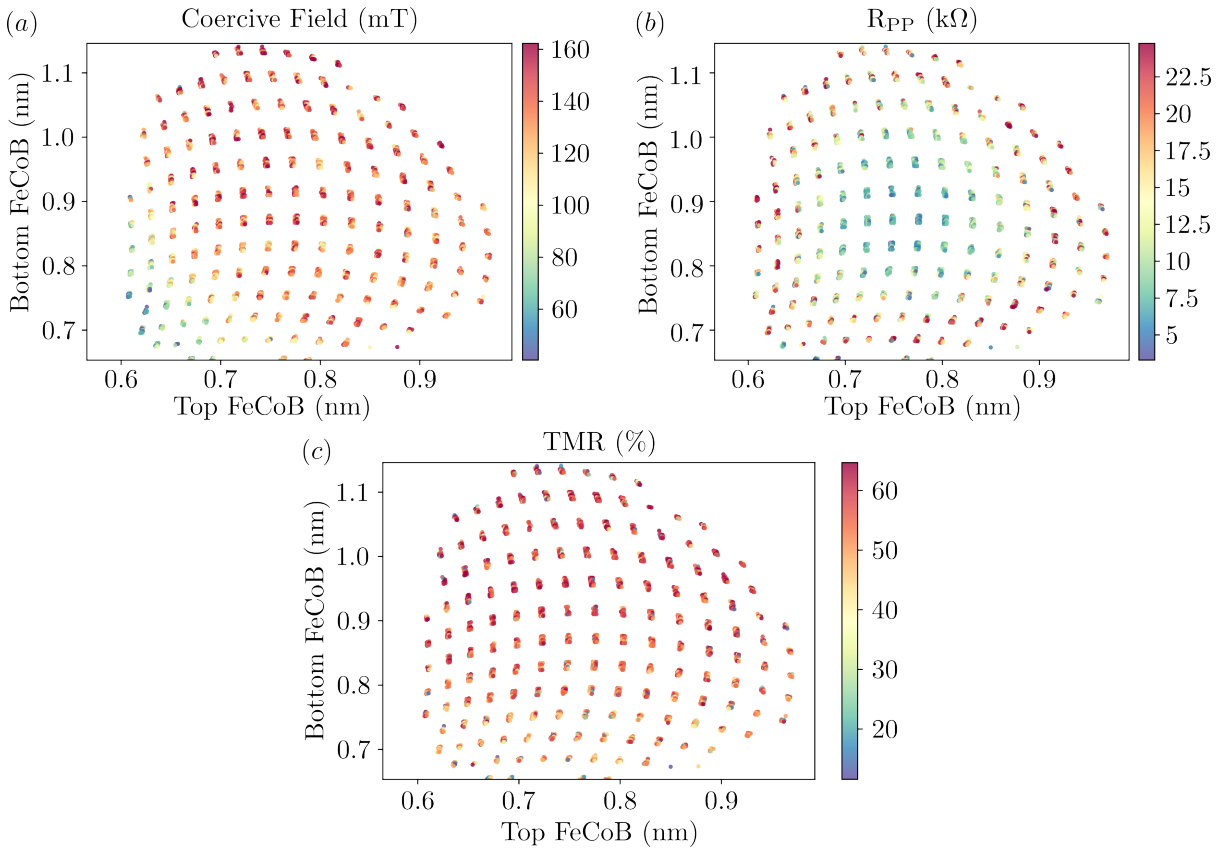


Figure 3.18: Mapping of the (*a*) coercive field, (*b*) minimum resistance state $R_{PP}$ and (*c*) TMR as a function of the different wedge thickness.

To further optimize the interfacial layers, it is enough to observe the devices with the initially largest nominal diameters, as after processing they reach electrical diameters around 20 to 40 nm. For this, we translate the coordiante mapping of the devices on the processed wafer to their corresponding thickness value on the wedges, as shown in Figure 3.18. Regarding coercive field, we observe that the region that had the highest PMA at thin film level has the lower coercivity at device level. This can be related to the shape factor of the shape anisotropy, but also thanks to the lower diameter around the region in which the coercivity was maximal. Overall, we allow for an increase in thickness thanks to the capping MgO layer. The reduction in diameter is clearly observed in Figure 3.17 (*b*), as the different etchings are stronger around the edges of the wafer. Moreover, there are not strong variations in TMR, showing that small variations in thickness of the interfacial FeCo(B) is not varying significantly the TMR of the devices. The next step is to study the STT switching of the devices and, as shown before, we make use of a 100 ns pulse voltage with constant field applied (to compensate for the offset field). With this we observe that (Figure 3.19 (*a*)), the lower switching voltages are obtained for the devices with lower coercivity, although $R_{PP}$ is larger in these devices. From these results it is possible to analyze the FOM of the pMTJ with capping MgO and, thanks

to a weak variation in Δ, we observe a similar trend to the usual pMTJ (Figure 3.19 (*b*)). This, however, is shown to have much higher FOM values, thanks to the substantial increase in $R_{PP}$ and, thus, reduction in diameter.

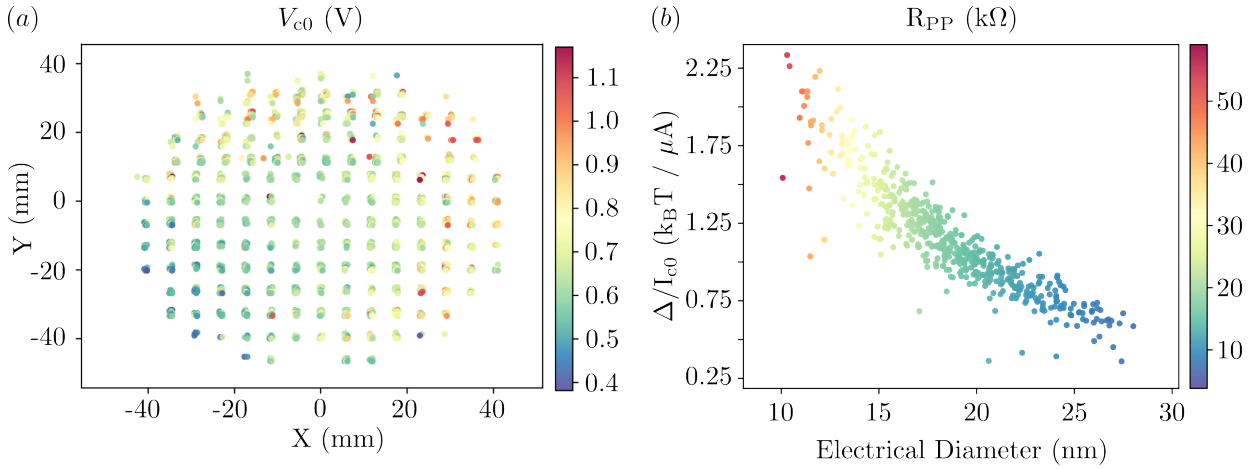


Figure 3.19: (*a*) Mapping of the critical switching voltage $V_{c0}$ as a function of the position of the device in the wafer and (*b*) dependence of the figure of merit ($\Delta/I_{c0}$) with the electrical diameter of the device. Colorbar linked with the minimum resistance ($R_{PP}$) of each device.

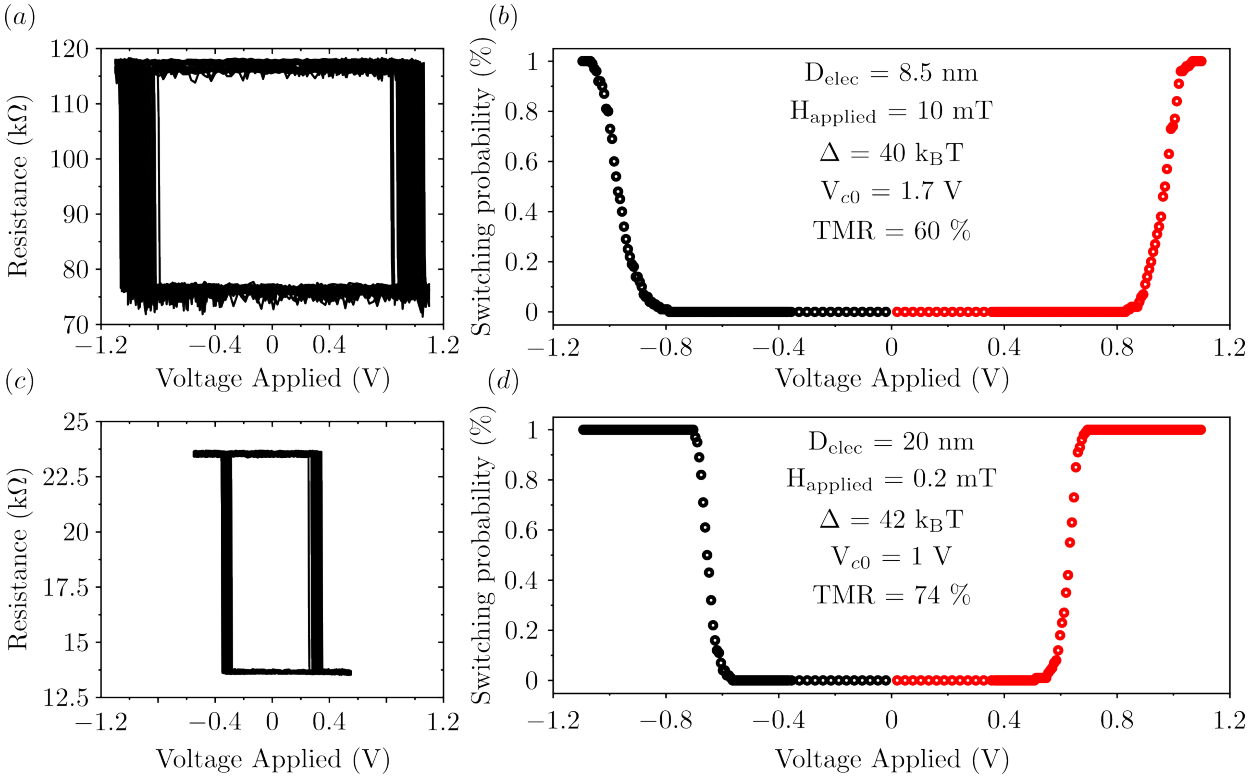


Figure 3.20: (*a*) 100 Voltage - Resistance loops and associated switching probability diagram for a device with an electrical diameter of 8.5 nm and (*b*) 100 Voltage - Resistance loops and associated switching probability diagram for a device with an electrical diameter of 20 nm. Electrical diameter values calculated for a total R × A value of 4.5 $\Omega\mu m^2$.

The determination of the critical switching voltage is shown in Figure 3.20 for the situation of very small diameter (*a*) and larger diameter (*b*). For these situations the average stability obtained from switching probability is similar. Nonetheless, we observe that there is a small variation in TMR,

which might be hint to damages to the MgO at lower diameters. It is still observed a switching at around 1.1 V for the case of larger $R_{PP}$. For the situation of smaller $R_{PP}$ the switching happens at around 0.7 V. The latter would still be, in principle, reversible for lower voltage pulses, since $V_{c0}$ is still below the MgO breakdown voltage of around 1.2 -1.3 V in our fabricated devices. For the lower diameter however, the critical switching voltage of 1.7 V shows that for shorter voltage pulses this device would not reverse by STT, and lower R × A values are necessary. This also forecasts that the thick layer, with these $R_{PP}$ values, will not reverse by STT since the switching voltage necessary for switch is much larger than that of the p-MTJ (as discussed in section 2.3.4).

Although the use of the capping MgO can lead to increased stability and increased FOM, this stability eventually starts falling at around 10 nm. By keeping the idea of the use of additional MgO layers for increased PMA, reports on four or more MgO interfaces have been published [87, 105, 106, 120]. This approach, associated with the development for low R × A barriers, leads to switching voltages below the breakdown limit at lower nodes, and thus further increasing the figure of merit at lower dimensions.

## 3.4 Ultra scaled perpendicular superparamagnetic MTJ

In the previous subsection, it was shown that, through the use of a MgO capping layer, one could increase the stability of the device at lower nodes, a result that brings an increase in FOM as the current necessary to reverse smaller node pillars is reduced. However, below a certain diameter, the coercivity of the device is reduced, as expected from the dependency of the interfacial PMA with the device area. This brings a constraint to lower nodes for applications that require some level of storage ($\Delta \gtrapprox 60 k_B T$). However, devices with reduced thermal stability open new opportunities that go beyond the traditional non-volatile memory schemes, bringing MTJs to a different set of applications where information is no longer encoded in deterministic physical variables.

Such new paradigms are of particular interest for unconventional computing [126], where less energy-hungry computing hardware is envisioned. In this context, exploring information encodings that are not perfectly deterministic but carry non-idealities or that are entirely noise-dominant forms an exciting new avenue leveraging the stochastic properties of the hardware. This strategy resonates with stochastic features observed in biological systems, such as neural assemblies in the brain [127], which could be useful for low-energy neuromorphic computing schemes. Furthermore, this approach avoids energy-consuming error correction overheads that are essential in deterministic schemes. One such strategy is probabilistic computing [128] which employs randomness in information encoding. This approach can yield energy consumption gains in specific applications, like solving combinatorial optimization problems [129], as well as cognitive tasks such as image recognition using stochastic neural networks [130]. In this paradigm, emulated stochastic bits that offer such properties are referred to probabilistic bits or p-bits, as they fluctuate between the two deterministic states 0 and 1

within a certain probability. Although reproduced by field programmed gate arrays (FPGA), MTJs that have this stochastic behaviour have shown promise regarding lower currents, higher density, and faster operation speed [131, 132].

When the energy barrier of the MTJ is sufficiently small, the room temperature thermal fluctuations are enough to make the magnetization of the storage layer fluctuate randomly between the PP and AP configurations. These unstable MTJs are called superparamagnetic MTJ (S-MTJ) and several hardware proof of concepts based on them were already demonstrated [127, 129], using in-plane and perpendicular magnetic tunnel junctions respectively. In recent works, the in-plane magnetization tunnel junctions attracted a lot of attention due to fast magnetization fluctuations, especially if the MTJ has an elliptical shape, bringing a uniaxial in-plane anisotropy [101, 133–138]. In these studies, the reduction of the energy barrier is trivial through the increase of storage layer thickness, where the shape anisotropy will dominate, bringing the magnetization in-plane. However, its scalability is limited, due to the elliptical shape and edge sensibility during the etching process. In this section, we offer another approach to reach low energy barriers while retaining scalability. Here, we reduce the diameter of the device while maintaining a strong anisotropy field $\mu_0 H_{eff}^{K}$. Thus, the reduction in energy barrier comes from the decrease in volume rather than the decrease in the anisotropy field, as commonly done. This brings several advantages. First and foremost, by showing that we can have a stochastic behaviour at sub-10 nm diameter, we have promise for a dense array of S-MTJ. Moreover, thanks to the lower diameter, smaller currents are necessary for STT to play a role in this device. To show this promise, we make use of the devices with smaller diameters fabricated in the last sample described with a capping MgO layer.

### 3.4.1 Resistance × Voltage phase diagrams of ultra-scaled Superparamagnetic Magnetic Tunnel Junctions

As already observed in the last section, we are able to reverse the magnetization in the storage layer using STT at large $R_{PP}$ (several tens of kΩ). However, to do so, large voltages are required, close to the breakdown voltage of the MgO. These can be reduced through lowering the stability of the device. This is the situation for devices with a diameter so small that they become superparamagnetic. In this situation, it is not interesting to perform only **RV** loops. Since after the voltage pulse is applied there is a certain delay in the acquisition of the resistance state of the device, a delay that might be longer than the lifetime of the state in the MTJ, and a correct resistance state would not be measured. It is then more interesting to do phase diagrams (Resistance as a function of the voltage and applied field, as shown in the sections before). In Figure 3.21 shows the situation for a magnetic device with $R_{PP}$ of 160 kΩ, corresponding to an electrical diameter of around 6 nm at a field sweep of 1 $T{\cdot}s^{-1}$. It is observed a multitude of different coercive fields for sequential measurements, indicate the inherent randomness of the device. When a pulsed phase diagram is realized, we observe that there is no evident STT effect (Figure 3.21 (*b*)), as there is no noticeable slope. However, since the resistance acquisition is made without voltage applied, the magnetization might revert back to its original state, thanks to the low coercivity of the device. To be sure that

there is STT in the system, it is necessary to apply a constant DC voltage and acquire the resistance state continuously. This is shown in Figure 3.21 (*c*) where we observe a slope around the offset field between $|V| = \pm 0.35\,V$.

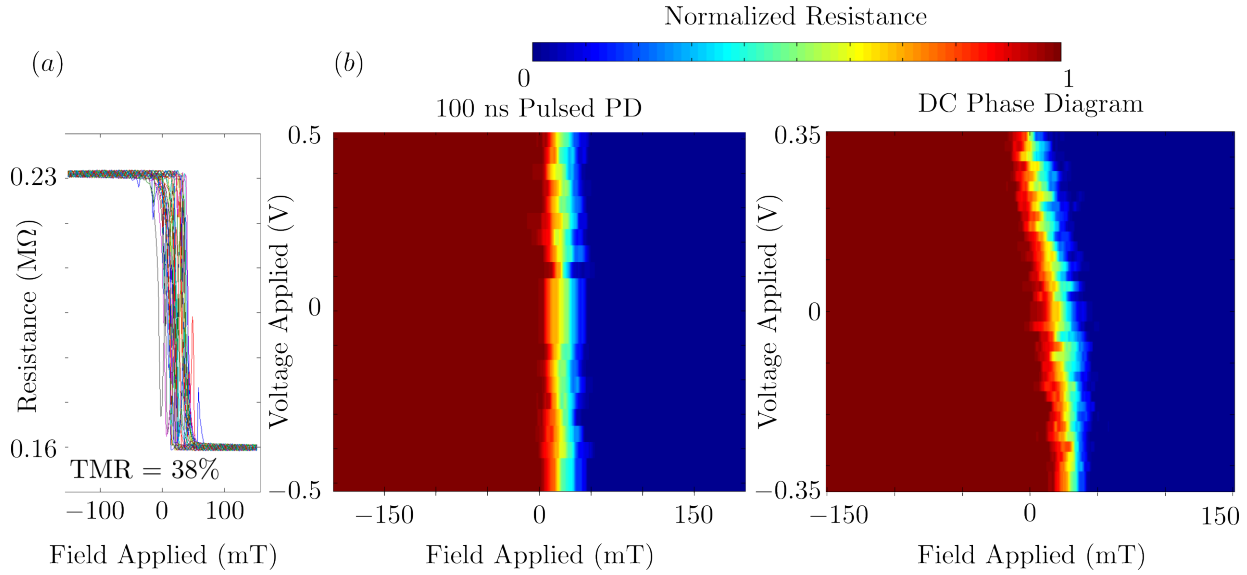


Figure 3.21: (*a*) Sequential RH measurements in a device with $R_{PP} = 160\,k\Omega$ and TMR = 38% (*b*) 100 ns pulsed phase diagram and (*c*) DC phase diagram for the similar device. The color scale is related to the normalized resistance (red is the AP state, and blue is the PP state) and is associated with the color bar.

Usually, DC phase diagrams are avoided, and pulsed are preferred due to the effect of the Joule heating in the system. Indeed, the breakdown voltage of the MgO occurs at much lower voltages for a DC pulse (at around 0.6-0.8 V for our fabricated devices) rather than for pulsed voltage, since the MTJ will start to heat up. Nonetheless, this is an adequate technique as most of the use of S-MTJ is to be realized through DC voltage. From here, it is also possible to observe a decrease in the resistance state of the device as a function of the applied DC voltage (Figure 3.22 (*a*)). Here, we still observe the two different regions from the DC phase diagram shown before; however, there is a strong variation in the resistance state of the device, namely for the situation in which the layers are anti-parallel. Indeed, this is already expected thanks to the asymmetric decay behaviour of the TMR under applied bias voltage [139]. This can be further observed for three different situations in Figure 3.22 (*b*), for the situation of an applied voltage bias of 40 mV (similar to the one applied to read the device in the voltage pulse measurements), in which we have maximal TMR value and two opposed bias voltages, for the situation of 300 mV and −300 mV. It is shown that, although the bias applied is symmetrical, the reduction in TMR is much larger for a negative bias.

In the next subsection, we select a device that has similar qualitative behaviour, but smaller $R_{PP}$. This allows us to reduce substantially the voltage required for STT switching, avoiding possible MgO breakdown (which can happen at around 0.6 V for DC current for an usual MgO tunnel barrier).

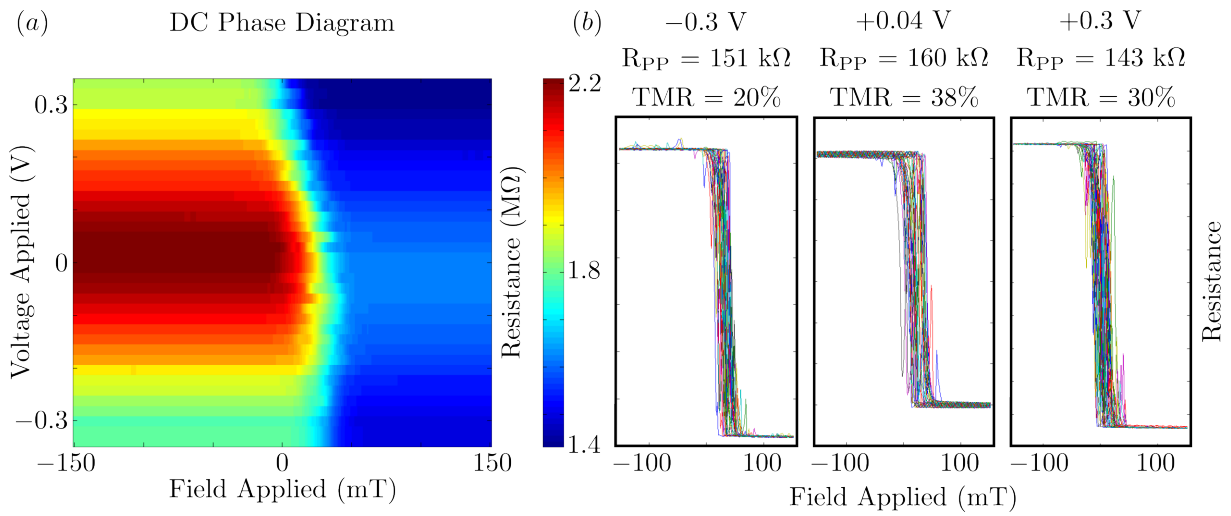


Figure 3.22: (*a*) Evolution of the resistance value in the DC phase diagram as a function of the applied field and DC voltage applied with (*b*) associated **RH** loops for different bias voltages applied (−300 mV, 40 mV and 300 mV). The color scale of the phase diagram is linked to the resistance state value.)

### 3.4.2 Real-time measurements of ultra-scaled S-MTJ

To remain within the regime of low coercivity, we select a device with $R_{PP}$ = 82 kΩ, with translated to an electrical diameter of around 8.5 nm. Several RH loops of this device are shown in Figure 3.23 (*a*), showing a small coercivity and a relatively small offset (of around 6 mT). This allows us to perform real-time measurements without an applied magnetic field compensation. If there was a strong offset field, there would be a shift in the switching voltages towards more or less positive values, as one of the states would be favoured. In some situations, this shift would be large enough for the dielectric breakdown along one of the polarities (emphasis that the favoured one would switch at a much lower voltage). This does not occur in our situation. The electrical measurements were carried out at room temperature using the setup shown as a schematic in Figure 3.23 (*b*). Here, the S-MTJ is placed in series with a shunt resistor of 10 kΩ. The resulting circuit corresponds to a voltage divider where the oscilloscope measures the voltage across the S-MTJs in a DC configuration (the internal impedance of the oscilloscope was set to 1 MΩ) which allows monitoring SMTJs magnetization fluctuations occurring at timescales larger than 1$\mu$s. This timescale limitation is imposed by the electrical RC delay of the circuit, which is around 300 ns.

An example of a voltage-time trace recorded for this device without external applied magnetic at an applied source voltage of 130 mV is shown in Figure 3.23 (*c*). From here, it is possible to observe two well-established resistance levels. At this voltage, the PP state is favoured (lower resistance state), showing the stochastic behaviour as well as the positive effect of the STT in the system. This is also observed in the associated voltage histogram, showing a larger count for the PP state, than for the AP state. The signal is digitized in order to properly extract the timescale of the fluctuations in each state, fluctuating between the two deterministic states, 1 and 0 (shown in red).

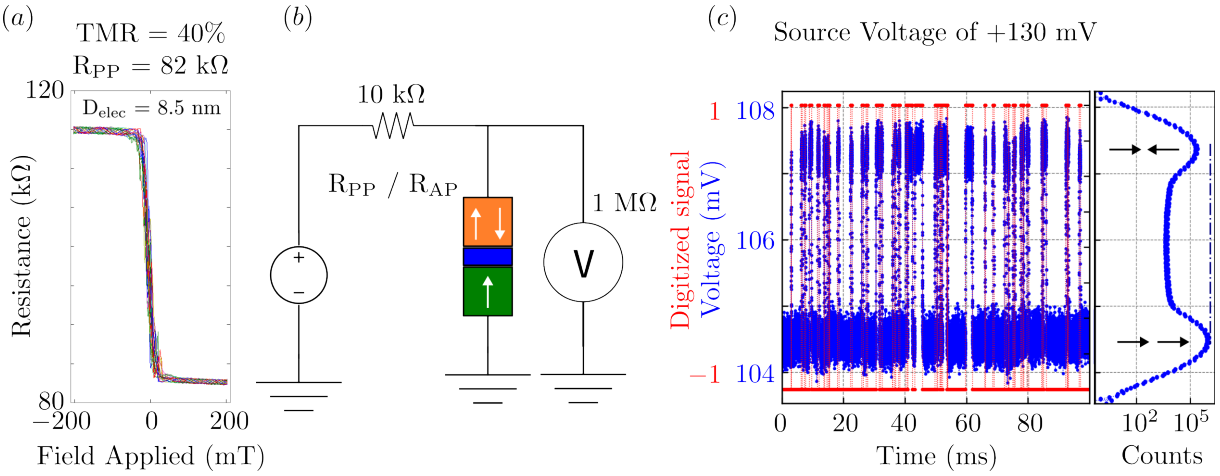


Figure 3.23: (*a*) 100 **RH** loops of a pMTJ with $R_{PP} = 82\,k\Omega$ and small offset field of around 6 mT. (*b*) Schematics of the electrical circuit to measure, in real-time, the resistance of the device as a function of an applied source voltage with (*c*) example of the real-time measurement for an applied source voltage of 130 mV and the associated voltage histogram.

Figure 3.24 (*c*) shows the evolution of the voltage-time trace of the resistance for different applied voltages: from the positive voltage (green) in which the state stays most of the time in the PP configuration to a negative voltage (brown color) in which the state stays mostly AP. This represents the clear influence of the STT in the system where it is possible to control the proportion of time the magnetization stays in the AP or the PP state. Moreover, it is seen that between |50 mV|, both PP and PP state are occupied at roughly equal time proportions.

From these, it is possible to extract one of the main features of the S-MTJs, the mean dwell times. These are obtained by making use of histograms where the dwell times are computed from a single applied source voltage. In Figure 3.24 (*a*) this is shown for an applied source voltage of 170 mV. Making use of the cumulative distribution function (CDF), one obtains the mean dwell time for this particular PP configuration and applied source voltage through an exponential fitting. This is shown in Figure 3.24 (*b*), where it is observed good agreement with the exponential distribution. This method allows us to obtain the mean dwell times for the different configurations AP or PP, representing the average time spent in one of the states. Depending on the operation voltage, the extracted mean dwell times drastically change from 200 $\mu$s to more than 5 ms. As shown in 3.25 (*b*) the PP mean dwell time increases with voltage. For instance, for 200 mV it is observed that $\tau_{PP}^{dwell} > \tau_{AP}^{dwell}$, while the opposite occurs for a voltage of −200 mV.

The average of the dwell time for both PP and AP as a function of the applied source voltage is calculated considering that there are two different distinct states and that, above a certain threshold, we are in one state or the other. Events that do not evolve above this specific threshold are not considered. The ratio of the mean dwell times will give us the probability in which the magnetization will be in a certain direction

$$P\ (AP\ /\ PP) = \frac{< \tau_{AP\ /\ PP}^{dwell} >}{< \tau_{PP}^{dwell} > + < \tau_{AP}^{dwell} >}. \tag{65}$$

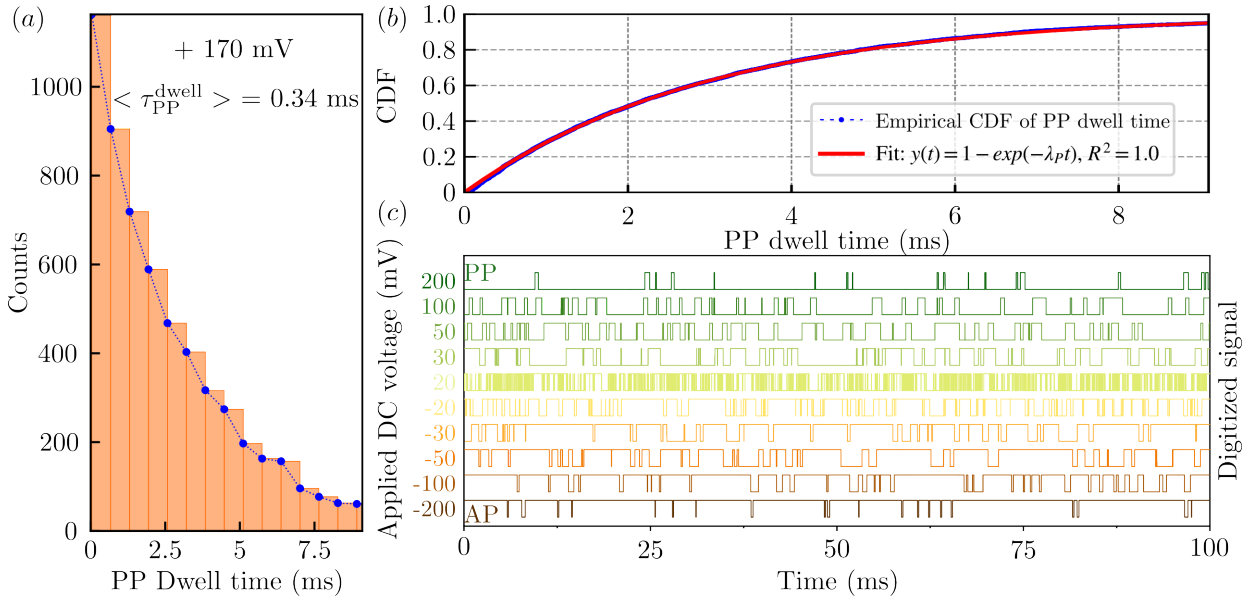


Figure 3.24: (*a*) Histogram of dwell times for the PP state (*b*) Fitting of the CDF for the associated PP dwell times and (*c*) digitized time-traces as a function of an applied source voltage during a time interval of 100 ms. Results obtained for a device with electrical diameter of 8.5 nm and 40% TMR.

This probability is seen, as a function of the applied source voltage, for the situation of the PP state in Figure 3.25. The shape we obtain is the typical sigmoidal relation observed in S-MTJ where the probability of a certain state is well tuned by a DC bias voltage. The average dwell times, from which these probabilities were extracted are shown in Figure 3.25 (*b*), for both AP and PP situations, showing an exponential behaviour with respect to the voltage. Overall, it is seen that these are in the order of ms. These mean dwell times are similar to the ones reported in perpendicular S-MTJ [129]. The latter however needs larger current values when compared with devices with lower diameter.

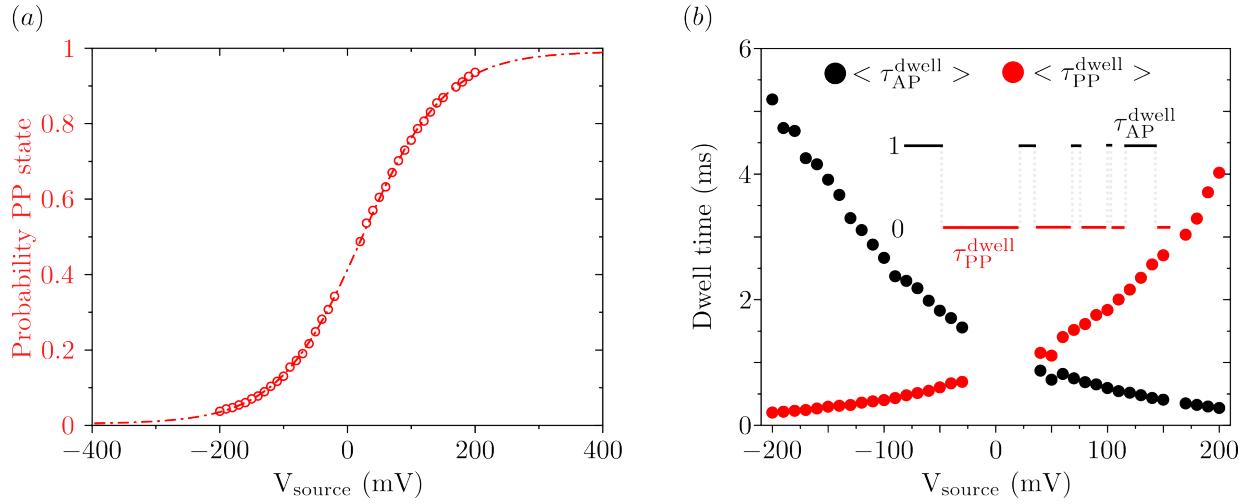


Figure 3.25: (*a*) Probability of the PP state as a function of the applied source voltage and (*b*) mean dwell time for both PP and AP state as a function of the applied source voltage. Inset shows a representation of the calculation of the AP and PP dwell times.

Our work shows that it is possible to extend the scalability of S-MTJ towards sub-10 nm nodes, which is not viable in making use of elliptical in-plane S-MTJ. The state of the fabricated device shows a well controlled state probability under a small applied current (orders of $\mu A$ or below). In a future work, it is necessary to make the fluctuations of this device even faster. Indeed, thanks to the lower magnetic volume, it is expected a faster switching mechanism and devices below 5 nm have shown sub-10 ns switching with a large stability factor. It is expected that decreasing this stability factor will also decrease the switching time. For this, it is necessary lower R × A values and larger TMR in our devices. This will make our STT switching more efficient and, faster. Nonetheless, intensive simulation work is necessary to correlate different material properties and engineer a magnetic stack that makes use of the very small diameter to increase its magnetization fluctuation speed.

## 3.5 PSA storage layer for high stability

In the last subsection we have shown that, by drastically decreasing the diameter, it is possible for the MTJ storage layer to become superparamagnetic and the device becomes stochastic, with practically no coercivity. However, if we take those low diameter pillars and substantially increase the storage layer thickness, we retrieve the lost stability. For this purpose we make use of the structure obtained by the optimising of the pMTJ with capping MgO. Here, we use thicknesses values associated with high values of stability that required low switching voltages for switching. The structure of this thick layer is then similar to the one presented for the sample with capping MgO with an additional FeCo(B) thick layer in between these two interfacial layers with thickness between 14.4 nm and 16.6 nm. The interfacial portion of the storage layer, *i.e.* the one in between the MgO tunnel barrier and the W spacer, was 0.95 nm thick, while the top portion, in between another W spacer and the top MgO capping, had a thickness of 0.8 nm. Both these layers are spaced from the thick layer* by a 0.2 nm W layer to promote crystalization of the interfaces. Here, we don't expect for the entire (B) to be extracted from the thicker FeCo(B) storage layer, only near the interfaces with the thin W layers.

In Figure 3.26 it is observed a set of **RH** measurements of devices from this multilayer after the patterning described for ultra small MTJ, with increasing value of $R_{PP}$. To this, there is an associated decrease in electrical diameter, as can be further confirmed by the increase in coupling field at lower nodes [140]. It is further observed that, as the diameter is reduced, the coercivity of the device increases. As the devices were extracted from the same region of the wafer (no significant variation in the wedge of FeCo(B)), this increase in coercivity is ascribed to the effect of the perpendicular shape anisotropy. Indeed, for a certain total thickness value, the aspect-ratio of the storage layer increases with decreasing diameter. For this geometry, at a certain point the aspect-ratio is larger than 1. Nevertheless, there seems to be a limited gain in coercivity below 5 nm. This was already

*Ta(220)| FeCo(B) (8) | Pt (80) | (Co (5) / Pt (3))$_{\times 6}$ | Co (5) | Ru (9) | (Co (5) / Pt (3))$_{\times 2}$ | Co(5) | W (2) | FeCo(B) (10) | Mg (7.5) | (10 sec, $1 \times 10^{-2}$ mbar) | Mg (5) | FeCo(B) (9.5) | W (2) | FeCo(B) (144 - 166) | W (2) | FeCo(B) (8.5) | Mg (8) | (10 sec, $3 \times 10^{-3}$ mbar) | Mg (3) | FeCo(B) (4) | W (30) | Ta (30) | Pt (50) (nominal thickness in Angstroms

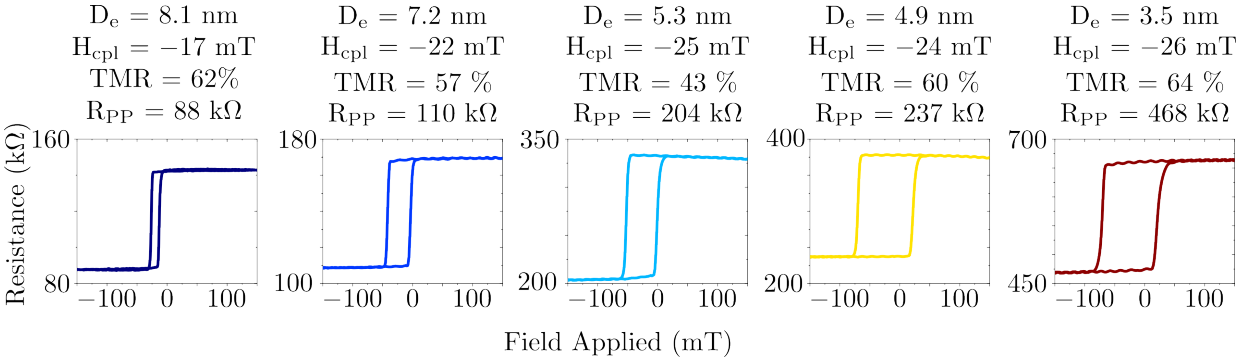


Figure 3.26: **RH** curves for a different set of devices with decreasing (increasing) electrical diameter (parallel resistance) for the case of a layer further stabilized by perpendicular shape anisotropy.

expected from the stability diagram shown in section 2 in Figure 2.1, due to a decrease in magnetic volume. Moreover, for the device with lower TMR value, it is observed that it does not follow the trend of the increase in coupling field. Indeed, since there are larger TMR values scattered through the wafer and there are no variations in Mg wedge, theoretically all the devices should have the same TMR. Edge effects from fabrication might reduce this value and, assuming that the increase in $H_{cpl}$ remains, this device should be associated with a smaller diameter.

If we analyse the device with larger electrical diameter (at around 8 nm) we notice similarities with the small pMTJ wich we were able to switch with STT at large $R_{PP}$ in Figure 3.20 (*a*). Here, we have similar values of $R_{PP}$, TMR and $\Delta$ (extracted from the **RH** measurement). The latter reversed with 100% probability at around 1.2 V. From our simulation results we are aware that, as the thickness of the storage layer is reduced, so is the critical switching voltage and, in proportion, the critical switching current. In this situation, as $R_{PP}$ is similar but the thickness of the storage layer is now around 10 times larger, we expect a much larger $V_{c0}$ than it would be for the situation with the pMTJ, as the STT is purely interfacial. Indeed, for these values of $R \times A$, it is not possible for us to reverse sub-10 nm pillars, as the required voltage is increasingly closer to the breakdown voltage. Nonetheless, if there is a small contribution from the STT, it would be observed in a pulsed phase diagram, in the form of a small slope along the boundaries. In Figure 3.27 we show the phase diagram for the case of a device with $R_{PP}$ of (*a*) 110 kΩ and (*b*) 237 kΩ. These show no variation in the boundaries, making it clear that there is no STT effect up to 1.2 V.

One of the solutions to reduce the switching current is to use thinner layers. We can make use of several MgO insertions to maintain higher stability [87, 105, 106] at lower nodes but, in this work, we decide to maintain in the regime of the perpendicular shape anisotropy (increased vertical aspect-ratio). To reduce the switching voltage it is then necessary to reduce the $R \times A$ of the device. This will enable us to switch by STT sub-10 nm devices. Other approach is to simply increase the diameter of the device, lowering the value of $R_{PP}$. In Figure 3.28 (*a*) we report a pulsed phase diagram of a MTJ with $R_{PP} = 50\,k\Omega$. This device has a $R \times A$ value of $7\,\Omega\mu m^2$, with an electrical diameter of 13 nm, for a total FeCo(B) thickness of 17 nm. It is seen that, even for the small TMR of the device (which is artifact from the fabrication process but will have an impact in the switching voltage of the device), we are able to reverse this thick magnetic layer using STT at an applied

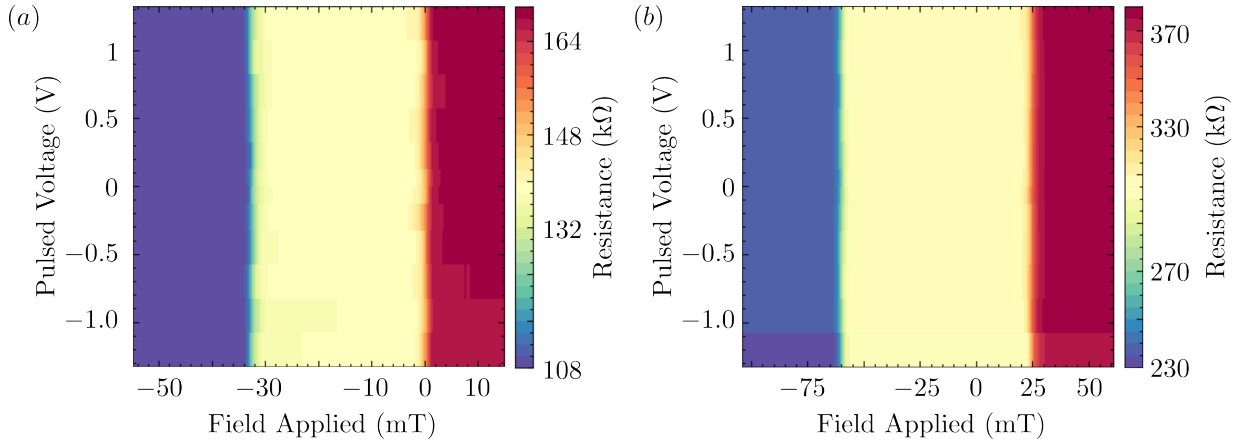


Figure 3.27: Pulsed Voltage Phase diagram for the situation of a device with (a) 110 kΩ and (*b*) 237 kΩ. The colorscale is given by the associated colorbar.

voltage of around 1.2 V from AP - P. From Figure 3.28 (*c*) we observe that the same decrease in coercivity does not happen for the PP - AP reversal, assumed to be due to the inherent coupling field to the reference layer. Indeed, it will be observed in the next section that the impact of coupling field is more important in MTJ with a vertical aspect-ratio than for usual flat MTJ. Due to the use of very large voltages we observe the effect of Joule heating in these devices, given by the increase in coupling field, as observed in figure 3.28 (*b*) for positive voltage.

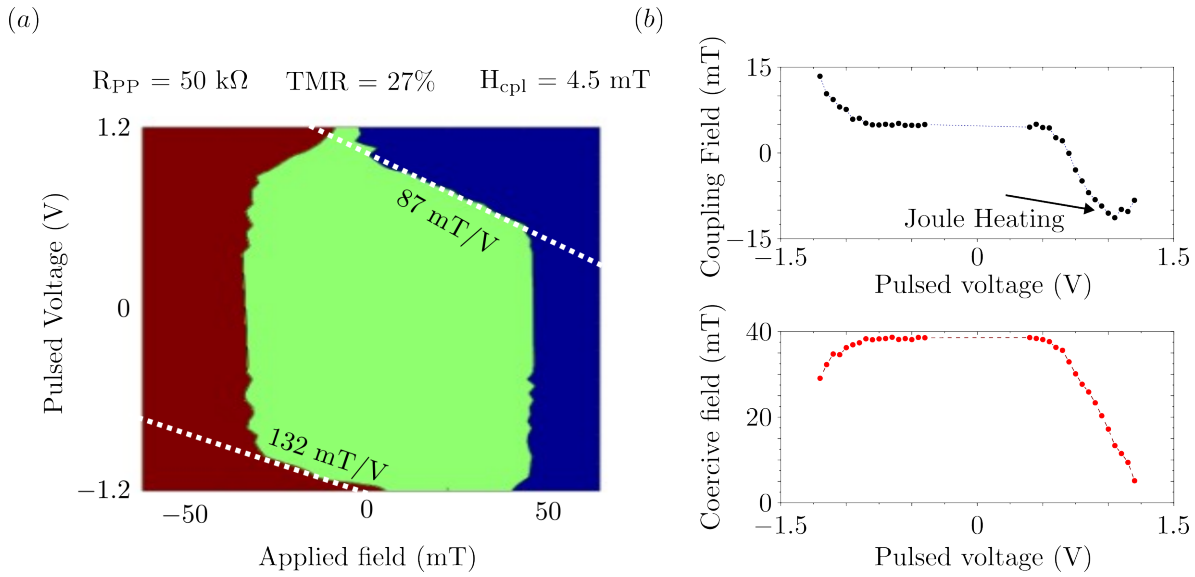


Figure 3.28: (*a*) Pulsed Voltage Phase Diagram for a device with $R_{PP}$ = 50 kΩ (*b*) Dependence of the coupling field as a function of the applied voltage and (*c*) dependence of the coercive field as a function of the applied voltage. Results obtained for 100 ns pulses.

As future work in regards to the switching of the PSA-MTJ, it is necessary to reduce substantially the R × A of the tunnel barrier. It is then important to move to RF deposited MgO which will enable us to achieve smaller R × A products with smaller wafer-wafer dispersion. Up to this point, it has been shown switching of ultra-scaled devices that make use of MgO insertions. This is to be also done in our side through a natural oxidized MgO barrier, where the coupling between the two magnetic layers is large. Although several studies are still ongoing or planned, it is all for nought

if we are not able to achieve a high yield in a wafer with ultra-scaled MTJs. As the main goal of these devices is to replace DRAM in terms of density, it is then necessary to engineer a solution that tackles the remaining challenges. These are the pitch at which the pillars can be defined and the magnetic cross-talk between magnetic neighbours. In the next section we will address the latter, in which the study of the interactions in an array of MTJ with vertical aspect-ratio is realised and a method of avoiding high stray fields is envisioned.

# 4 Integration routes for high density ultra-small MTJ

### 4.0.1 Motivation for the use of nano-vias for high density MTJ

In the previous sections, we addressed the fundamental aspects of individual ultra-scaled magnetic tunnel junctions (with critical dimension **CD** below sub-20 nm). However, these devices need to be manufactured in arrays, and for DRAM replacement, the pitch (defined as the distance between the center of two neighbouring devices) between the neighboring magnetic element needs to be very small $\approx 1\times$CD. As spintronics stacks require the use of IBE for patterning, there is always an additional trimming step, at a grazing angle, that helps to remove redeposited matter off the sidewalls (shunt prevention) and to reach the intended small CD. However, due to the thickness of the magnetic stack (namelly if it has a PSA layer) and, mainly, of the hard mask necessary for the fabrication process, there is a region in which the trimming is not effective (shadow area). This is illustrated in Figure 4.1 (*a*), for two adjacent MTJ (simplified structure) pillars with a diameter CD and a certain thickness, separated by a certain pitch. Indeed, at small pitches $2\times$CD with a CD of 28 nm a significant redeposition has been shown to exist around the sidewalls of the pillars [141]. For this integration, a full etching flow based on RIE would prove useful for high density MTJ arrays [142]. Although different etchless approaches have been tested, for instance, with the use of pre-patterned Ta posts [143], at this moment the use of IBE is standardized.

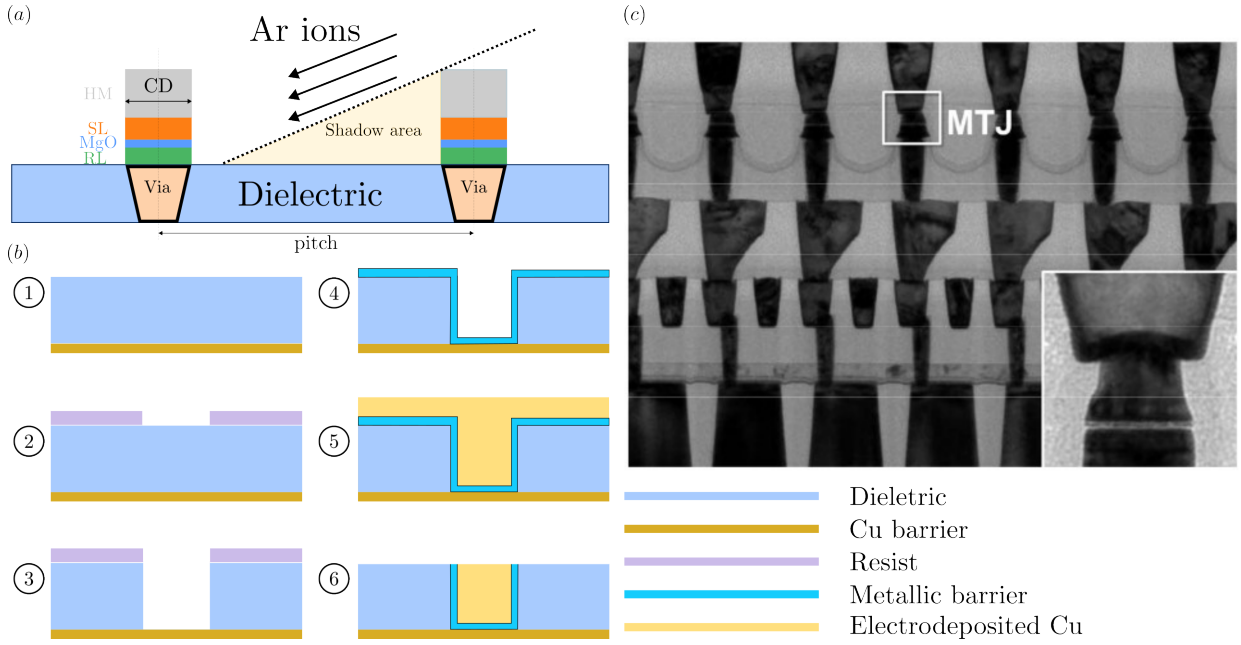


Figure 4.1: Schematics of the (*a*) trimming at a grazing angle with associated shadow area and (*b*) single damascene process flow for the via underneath the magnetic tunnel junction. The different steps are described along the text and the different layers are labelled by color. (*c*) Cross-sectional TEM image of the full process flow with the different Cu interconnects and 28 nm MRAM, figure extracted from [144].

Assuming that the use of IBE remains a necessity, we explored in our study possible routes to reduce the shadow area associated with high vertical-aspect ratio MTJ at low pitch. For this, we explore the use of electrochemical deposition (**ECD**) to deposit specific layers of our stack. The use of this technique in the microelectronic industry is well known and documented, namely for the deposition of metallic interconnects (vias and trenches). Today, these are made of Cu [145], which is deposited in pre-patterned vias created through a damascene process [figure 4.1 (*b*)]. In this technique, there is a (1) first deposition of a dielectric on top of a metallic barrier, which can already be some pre-deposited Cu followed by resist deposition and photolithography (2). Next, there is an anisotropic etch of the dielectric (here, a perfect rectangular shape is shown, but in reality there is a certain slope along the sidewalls) (3). After photoresist removal, it is necessary to deposit a metallic barrier (4). For the case of Cu, this is made of an initial layer of TaN or TiN (usually deposited by PVD), which protects against Cu diffusion into the dielectric layer, followed by deposition of an adherent layer, usually Ta. Afterwards, to initiate the growth of Cu by ECD, a Cu seed layer is deposited by PVD. After the deposition of these layers (which cover a considerable portion of the via, around 20 nm), ECD Cu is deposited inside the vias (5). Since now we have Cu on top of all the vias, it is necessary to planarize it, which is done by using a step of chemical mechanical polishing (**CMP**) (6). This is a simplified process flow, whereas the microelectronics industry makes use of dual-demascence patterning of a via followed by a metallic lead [146]. For simplicity, we will stay with the idea of the single damascene flow for the remainder of the chapter, as there is no concept of lead in our fabrication process. Moreover, as the dimensions of the vias continue to shrink, the scaling of these Cu based interconnects will lead to dimensions where performance deterioration is observed [147]. For narrower vias, there is an increase in resistivity and resistance, and most importantly, the metallic barrier thickness does not scale with CD, reducing the total amount of Cu in the via [146, 148, 149]. Solutions that make use of W or Co for smaller nodes have been heavily investigated [150–156].

This brings several opportunities to MRAM technology. As the use of ECD at very small nodes is mastered in the CMOS back end of line (BEOL), if we were to add non-conventional steps in the MRAM design and fabrication, it would be without heavy implementational constraints. Moreover, the added value of exploring knowledge about a wide variety of materials (either magnetic or non-magnetic [157]) deposited inside different types of templates (from porous alumina to different porous polycarbonates [158, 159]) by electrochemical processes from different fields, brings a multitude of possibilities regarding materials for our MTJ stack.

In a first section of the chapter, we will tackle the constraint of tilted or fallen pillars due to the small CD. Here, we will make use of ECD to deposit our metallic hard mask inside nano vias written by EBL onto the unpatterned MTJ thin film. This will prove to be useful due to the initial smaller CD and vertical sidewalls of the created standing pillars. In the second section, we will tackle both the low yield, but also the shadow effect given by the vertical aspect-ratio pillars. Here we create embedded nano-vias filled with Co. Using this approach we target very small pitches ($\approx 1.5\times$CD), adapted for the existing BEOL process flow. We further explore the use of these vias for either a reference layer or storage layer of our MTJ.

## 4.1 Electrodeposition as a viable tool for ultra-small MTJ

As described in section 3.2, the need for a hard mask with smaller CD and smaller height is vital for the larger yield of sub-10 nm MTJ. For this we took inspiration from by the high reliability of the ECD filling, which is at the backbone of BEOL interconnects. Since the deposition of metals is well understood [160], integration of ECD with the usual MTJ technology could be straightforward. To investigate the viability of this approach, electrochemical depositions in both thin film and pre-patterned vias are realised at Néel institute, under the supervision of Dr. Laurent Cagnon.

We first prepare two different electrolytic baths. These were used to deposit, individually, Co ([40 g/L] $CoSO_2$ + [40 g/L]$H_3BO_3$) and Pt ([3.3 g/L] $K_2PtCl_6$ + [40 g/L]$H_3BO_3$) onto a wafer of Au [161]. To study the electrochemical behavior of these electrolytes, we make use of a three-electrode setup [162], as shown in the schematics of Figure 4.2 (*a*). Here, there are three different electrodes placed inside the same electrolyte (orange solution with free ions represented as red spheres). The reference electrode (**RE**) is an unpolarized electrode that is used to measure the potential applied to the substrate where we want to deposit our material (in this configuration, the working electrode). In our setup, the RE consists of a saturated Ag/AgCl electrode, which is placed between the working electrode and the counter electrode. The counter electrode (**CE**) enables the current to flow in the circuit and, in our situation, is made of Pt. The working electrode (**WE**) is the substrate on which we will deposit our material. This is typically made of a noble metal such as Au, Cu, or Ag. In this initial analysis of the electrolytes, we make use of a bilayer of Ta(15 nm)|Au (100 nm) WE, prepared by PVD. The use of Ta served as an adhesion layer to the Si wafer; Ti could also be used for a similar effect.

To study the electrochemical behavior of these baths, we make use of the potentiostatic mode. This means, we fix the voltage and monitor the evolution of the current over time. We first consider cyclic voltammetry (**CV**), in which we vary the voltage while measuring the current. This approach allows us to identify specific reactions that occur at the interface of our WE [162]. In Figure 4.2 (*b*) it is shown the CV of the two different electrolytes, whose potential is measured against a Ag/AgCl RE. This measure starts at the open circuit potential (**OCP**), a potential at which there is no net current in the system (the cathodic current is the same as the anodic current), and then the voltage is swept to more negative values, increasing the contribution of the cathodic current. For the case of the Co electrolyte, it is seen that there is no increase in cathodic current up to around $-0.8$ V (point A). This increase in current is associated with the reduction of $Co^{2+}$ ions in solution and the deposition on the surface of the working electrode, which follows the reduction process:

$$Co^{2+} + 2e^- \rightarrow Co.$$

If we move to increasingly lower potentials, the deposition rate increases; however, this would make the deposition difficult to control for very small thicknesses. If we now increase the voltage towards positive values we see a crossover $I > 0$ around $-0.5$ V. This marks the transition from the cathodic to the anodic region. If we continue to increase the voltage, we observe a large increase in the anodic

current. This is associated with the oxidation of the material deposited during the cathodic scan. Complete dissolution of this material occurs with the drop in the anodic current (point B). Therefore, the CV allows us to determine two important values: the potential at which Co is deposited and the potential at which Co is removed from the substrate. If we apply the same technique to Pt, we realize that the anodic region is now much smaller than the one for Co. Thus, once Pt is deposited on the surface, it is not possible to strip it using CV unless we move to much higher voltages.

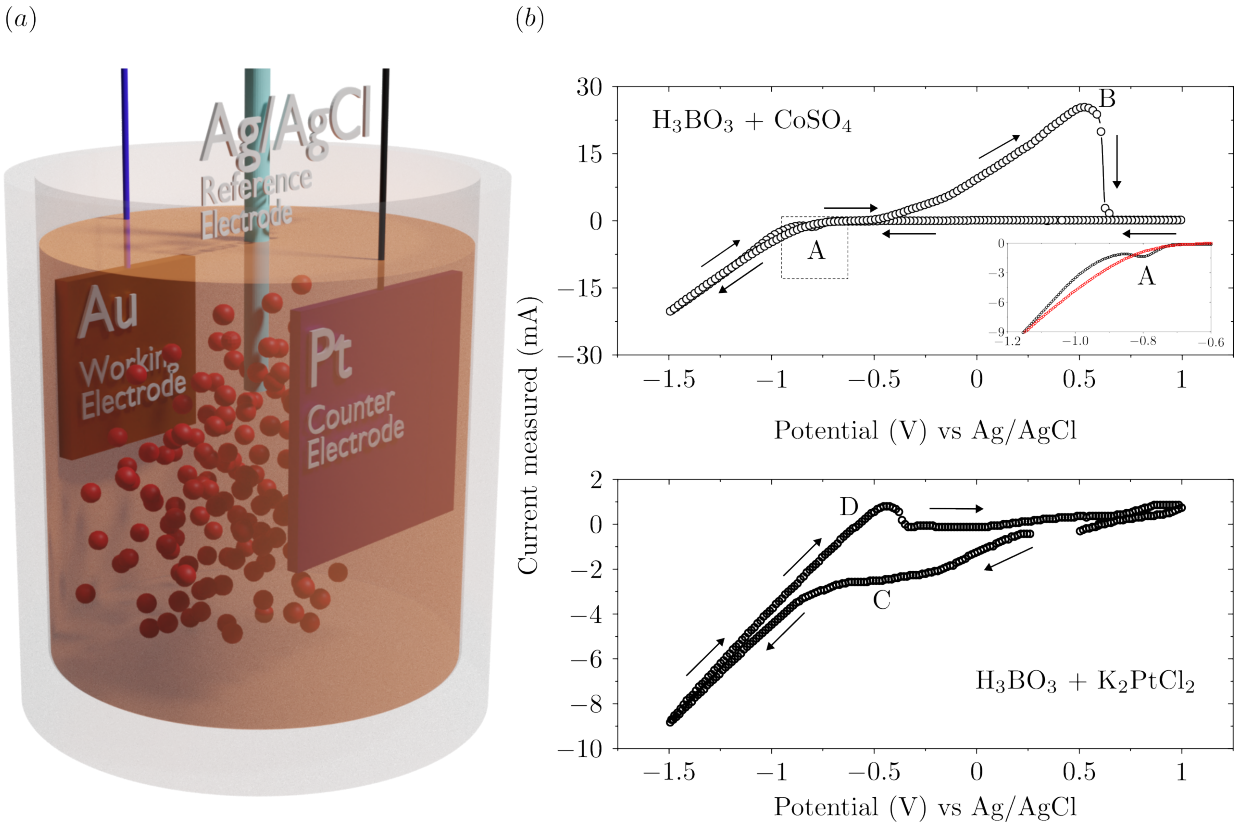


Figure 4.2: (*a*) Schematic of the three electrode setup where the Au working electrode, Pt counter electrode and Ag/AgCl reference electrode are immersed in a certain electrolyte. These are connected to a potentiostat. (*b*) Cyclic voltamogram curves for the Co and Pt electrolyte. The CV associated with the Co electrolyte shows an inset for the specific A region.

From this CV, it is possible to see that the Pt begins to deposit around $-0.4\,\mathrm{V}$ (C), a region close to the removal of the Co in the previous CV. Additionally, there seems to be a peak at around the same region when the voltage is swept the other way. This is often associated with hydrogen evolution [163]. Although this effect is important, it is beyond the scope of this thesis and emphasis is given only to the deposition potential of Pt. The latter is deposited in two different steps [164]

$$\mathrm{PtCl_6^{2-}} + 2e^- \rightarrow \mathrm{PtCl_4^{2-}} + 2\mathrm{Cl^{2-}}$$

$$\mathrm{PtCl_4^{2-}} + 2e^- \rightarrow \mathrm{Pt} + 4\mathrm{Cl^-}.$$

The choice of these two electrolytes is not arbitrary. Indeed, a combination of these can lead to an MTJ with a significant number of advantages. First, the sequential deposition of Co and Pt is mastered and there are a number of research studies that make use of these [165–170]. If we are able

to grow sequentially Co and Pt inside a pre-patterned structure with small CD, most of the stack thickness would be pre-defined. This is most relevant for MTJ with a vertical aspect ratio. In this case, as the thickness of the storage layer is thicker than the usual perpendicular MTJ, the etching of the magnetic stack is considerably longer. Consequently, the redeposition around the pillar is larger. By avoiding this longer etch time, we also avoid the lateral size enlargement of the pillar, which allows for shorter trimming times and less damage to the hard-mask and to tunnel barrier. Additionally, by using a hard mask that is etched at around the same rate as the pillar, we avoid diameter variations (between the height of the entire pillar) that can lead to a tilted or fallen device. However, there are several steps that need to be addressed before moving on to this more complex approach. In this section, we will focus on addressing the integration of the ECD as a working hard mask for the MTJ. This allows us to confirm the viability of ECD in filling vias written by EBL and to assess the value of ECD for MTJ with sub-20 nm dimensions.

### 4.1.1 Optimization of the PMMA thickness

Before moving to the direct deposition on top of our MTJ, it is necessary to confirm if the metal is effectively deposited inside vias written by EBL. Contrary to the situation of filling of the vias using a damascene process, here there is no seed layer to initiate the deposition. Thus, the bottom of the via needs to be conductive, without remains of polymer or oxidation. To ensure this, we first use a Ta | Au bilayer to carry out initial deposition trials (commonly used for nanowire deposition in polycarbonate or alumina templates of pores [158, 159]).

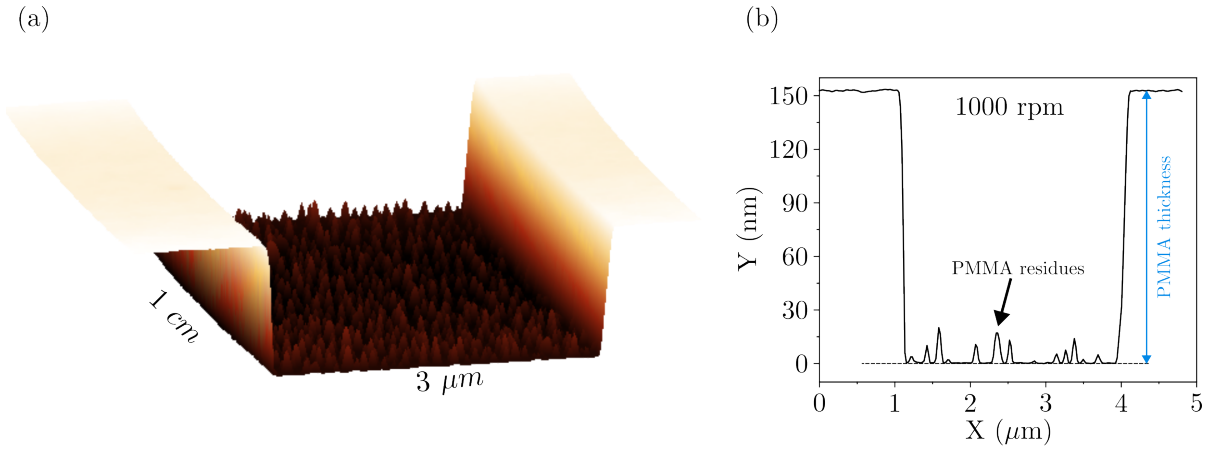


Figure 4.3: ($a$) 3D topography profile of a trench formed by EBL in PMMA and ($b$) associated depth profile for a PMMA spin-coating of 1000 rpm. Data retrieved making use of atomic force microscopy.

For these series of tests, we use an EBL mask composed of trenches with 1 cm length and 3 3 µm wide [profile shown in the 3D topography of 4.3 ($a$)] and vias of different nominal CD (in the examples below the CD displayed is 30 nm nominal). The depth of these structures is the same as the thickness of the deposited PMMA (which is reduced as we move from the center of the wafer). The thickness of this PMMA layer is critical for our sub-20 nm dimensions. As the Pt is to be used as a hard-mask, its thickness needs to be large enough to be able to connect electrically, but not so

large so that the pillar becomes tilted or fallen due to the increased aspect-ratio of the structure. Thus, it is necessary to optimize the thickness of this PMMA layer, to accommodate a certain range of deposits inside the vias.

In our usual process flow, the PMMA is coated at 4000 rpm, which gives a thickness of around 70 nm. Although this is enough for the evaporated 20 nm Cr layer, it is not enough for a hard mask. Indeed, as we now expect the hard mask to be etched roughly at the same rate as the remaining metallic layers, the loss in thickness of the hard mask is roughly proportional to the thickness of the entire MTJ stack. To increase the thickness of the polymer, we can simply apply some modifications in the spin-coating step (by decreasing the rpm). The height of the PMMA trenches after development is measured using atomic force microscopy (AFM). An example of a height profile is shown in Figure 4.3 (*b*), for the situation of a 1000 rpm coating. It is seen that in addition to the increase in PMMA thickness, there are also some PMMA residues at the bottom of the trench (also observed through the 3D profile of the trench, which is also expected for other PMMA thicknesses. Although not detrimental to our measurements, it hints at a possible obstacle at the bottom of the vias, in which some of them might not be completely cleaned. This would reduce the nanofabrication yield of the wafer as well as impact the shape of the ECD metal.

Table 3: Thickness of the deposited PMMA 2% as a function of different rpm values. Values taken for the situation of a single deposition (5 minute baking) or double deposition (1 minute baking followed by a 5 minute baking).

| PMMA 2% spin-coating rpm × depth (nm) (1 min + ) 5 min baking | | | | | |
|---|---|---|---|---|---|
| 1000 | 2000 | 4000 | 4000 + 4000 | 2000 + 4000 | 1000 + 4000 |
| 150 | 100 | 70 | 140 | 170 | 220 |

Although a thickness of 150 nm can be reached with a single PMMA deposition, this would still not be enough for the hard mask, since the electrochemical deposition rate could become unstable or might be difficult to control. Thus, it is better to further increase the thickness of the PMMA, allowing a larger range of thicknesses inside the vias. For this purpose, we made use of a double baking technique, in which a first layer of PMMA is spin-coated (thick portion of the PMMA) and baked. Usually done for 5 minutes, we restrict ourselves to 1 minute baking in the first step. This allows for polymerization and a solid interface for the next PMMA deposition. Now, we spin-coat the smaller portion of the PMMA and proceed with the usual 5 minute baking. If we were to do the same baking time of 5 minutes twice, the first layer might be burned and the EBL writing would not be efficient. In Table 3, the different values of the PMMA thickness are shown for different rpms used (extracted by AFM characterization).

We then make a first trial for an initial PMMA thickness of 70 nm. Making use of the described Pt electrolyte, we apply a voltage of $-0.55$ V after a 10 seconds OCP measurement. The dependence of the measured current as a function of the time is observed in figure 4.4. After the OCP measurement, the potential is stepped to the deposition potential value, and a sharp increase of the

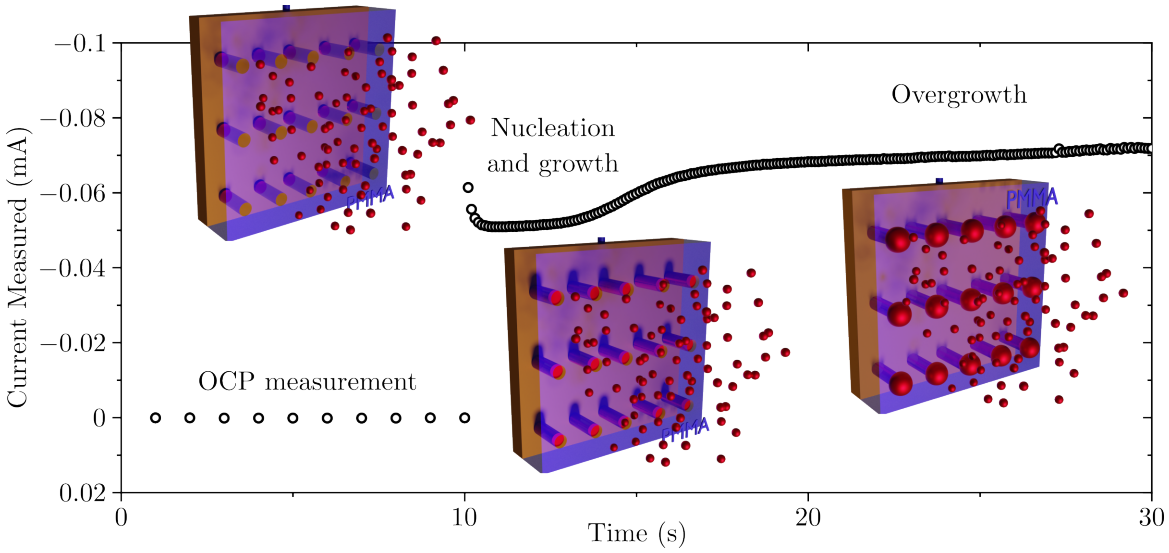


Figure 4.4: Measured current as a function of the deposition time for a Pt electrolyte at a voltage applied of −0.55 V. Deposition start after a 10 second OCP step, followed by growth, deposition and overgrowth (each of these associated with a schematic in the graph).

cathodic current value. After a short drop, there is a constant value observed which corresponds to the filling of the vias. Starting around 13 s we see an increase in absolute current, indicative of a larger contact area. This can be associated with the growth of structures that were not grown before (for instance due to the state of the bottom of the via) and most likely, associated with the overgrowth of these structures. These can be observed in the schematics shown alongside the deposition curve. Within a PMMA thickness of 70 nm, we proceed to two different deposition times, 6 and 60 s, after a 10 second OCP measure. According to the deposition curve of Figure 4.4 both these situations will lead to a situation of overgrowth. Both these situations are shown in Figure 4.5 for (*a*) a 60 s deposition and (*b*) a 6 sec deposition, without PMMA stripping. In both situations it is observed a clear filling of the rectangular trenches, even if there were some PMMA residues prior to deposition. For the situation of 60 s, there is a clear overfilling of the vias, although not uniform throughout the array, which might point to the non-uniform kick-start of deposition. Although the overgrowth size are very different, it should be noted that the overgrowth speed is much faster than the growth inside the via. This means that, even if the filling inside the vias was not very far apart, the first one overgrowing would do so much faster than the other. Thus, we can expect a certain degree of deposition in most of the vias, as long as there is enough time for it to kick-start. The same situation is observed for the smaller time scale of 6 s. Nonetheless, there still seems to be a clear deposition inside most of the vias, even if the overgrowth is different.

### 4.1.2 Platinum electrodeposition on top of a full sheet MTJ stack

At this point, we now know that if the bottom of the via is conductive, we can deposit inside of them, although not totally controlled due to possible PMMA remains (as observed in Figure 4.3). To ensure that there are no larger variations in height (avoiding overgrowth), it is necessary to further increase the height of the PMMA. We then increase this height to 220 nm by double baking

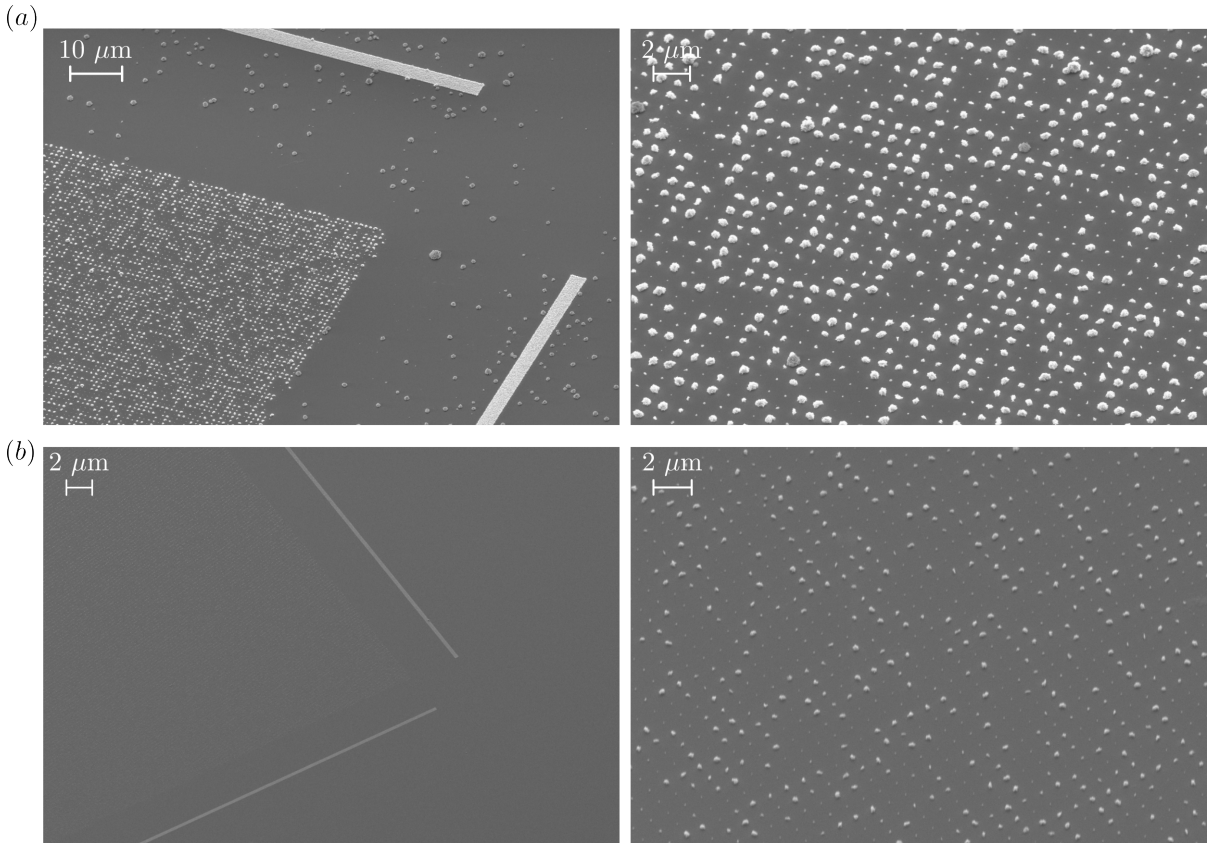


Figure 4.5: Scanning electron microscopy images of vias and trenches written by electron beam lithography on a Au working electrode with 70 nm PMMA for (*a*) 60 second and (*b*) 6 second deposition in a Pt electrolyte at −0.55 V after 10 second open circuit potential.

at 1000 rpm and 4000 rpm in a classical single MgO MTJ composed of Ta (220)| FeCo(B) (8) | Pt (80) | (Co (5) / Pt (2.5))$_{\times 6}$ | Co (5) | Ru (9) | (Co (5) / Pt (2.5))$_{\times 3}$ | Co(5) | W (2) | FeCo(B) (10) | Mg (7.5) | (30 s and $3 \times 10^{-2}$ mbar) | Mg (5) | FeCo(B) (15) | W (2) | Ta (20) | Pt (50) (nominal thickness in Angstroms). The capping layers of the stack are conductive and do not oxidize, so we expect good deposition on top of them. Moreover, even though there is an MgO in the stack, as we are at the thin film limit, for certain R×A, its resistance is negligible (A $\rightarrow \infty$). Thus, no voltage drop or breakdown is expected to happen, which would not be the situation if we were doing ECD on top of pre-patterned MTJ. In this experiment, we use 2 inch samples with the appropriate mask for further processing and measurements with a single device. Figure 4.6 shows SEM images, after PMMA removal (overnight with acetone, without the use of ultra-sounds, to not damage the fragile deposited pillars), for 5, 6 and 7 second deposition of Pt at a voltage of −0.55 V after 10 seconds of OCP. It is observed that, for the situation of 5 seconds, there is barely any deposition along some existing marks in the wafer (for reference, the figure for 6 seconds deposition shows the same patterned marks). There is also no significant deposition inside the vias, although there is one surviving pillar, showing a different nucleation in that specific via. If we move to 6 second deposition, we observe a good filling of the vias, which leaves behind straight pillars. Although the yield along the wafer of these pillars seems viable, the thickness of the pillars is below 100 nm, which would prove difficult to connect electrically afterwards. For the 7 seconds deposition it is seen that, although some pillars survive, most did overgrow.

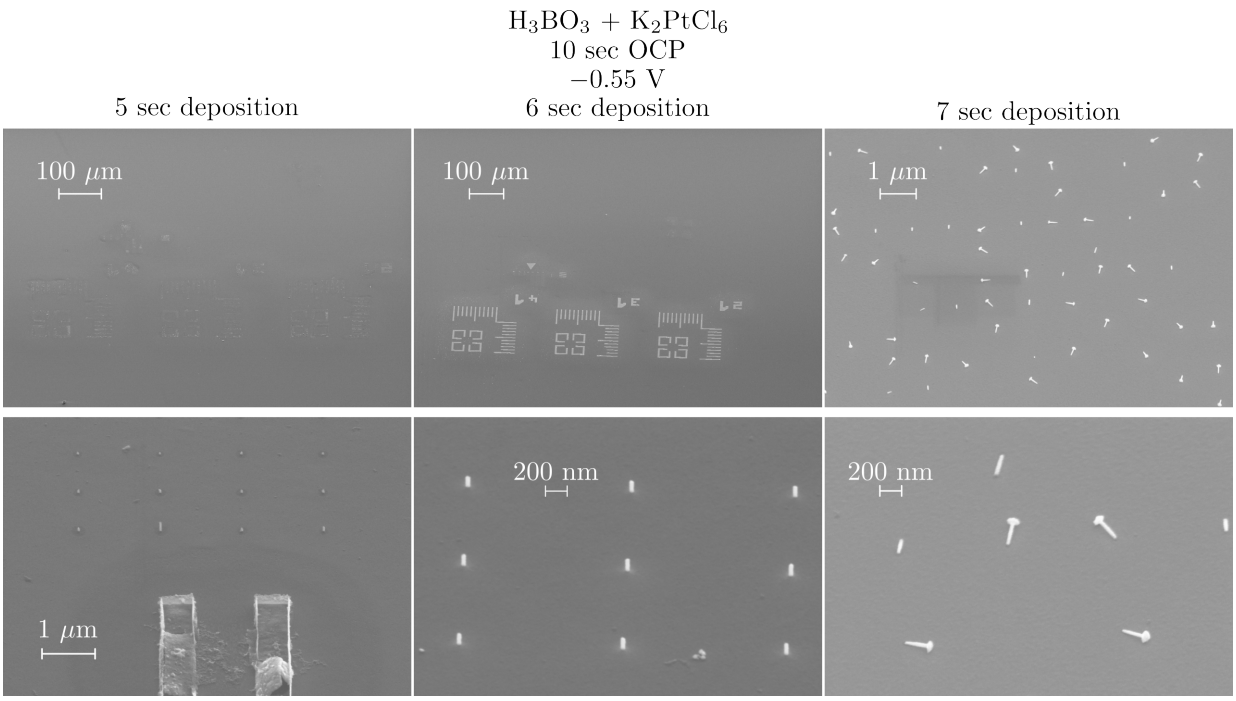


Figure 4.6: Scanning electron microscopy images of the deposition of Pt inside holes written by electron beam lithography on a MTJ working electrode with 5 nm Pt capping layer. Imaging performed after PMMA stripping with overnight acetone. Situations for 5, 6 and 7 seconds deposition after a 10 seconds OCP step.

In the end, we make use of the 7 seconds deposition time for the Pt ECD making use of EBL defined nominal diameters of 28, 30, 32 and 34 nm. Although the risk of overgrown pillars and consequently open devices is large, the surviving ones will have a suitable thickness for electrical connection. In Figure 4.7 we observe the situation of the Pt ECD at a EBL size of 34 nm. It is observed that there is no overgrowth in this situation, and some of the pillars are thinner than the average of the observed matrix. However, an increase in the absolute current density is observed after around 2 sec, whichhints at an overgrowth in other places of the wafer, but also at a possible growth start of different vias, since there are different thicknesses in the same matrix. To test the stability of the pillars against IBE, we follow the fabrication procedure described in Section 3.2. It is seen that, after etching the multilayer stack and a small trimming (around 2 minutes) at a grazing angle of 10°, the pillars are still standing, with no measurable tilt and a sub-20 nm diameter.

We then fabricate single electrical devices with these pillars. The process flow remains the same as before, except for the hard mask deposition and etching. After fabrication a mapping is done on the 2 inch wafer, as shown in Section 3.2 for the characterization of the single and double MgO 4 inch wafers. A yield of 18% working devices was measured, with a 1% short ($R_{PP} < 500\,\Omega$) throughout the wafer. The TMR characterization of individual devices are shown in Figure 4.8 (*a*) associated with the variation of the measured electrical diameter (R × A product of 8 $\Omega\mu m^2$ from table 2) as a function of the EBL nominal CD. It is observed that there is a larger variation of electrical diameters for larger EBL CD, which is associated with a higher yield for this CD. Indeed, we can assume that the larger diameter allows for better PMMA removal from the bottom of the via. Nonetheless, most of the measured devices have an electrical diameter of 10 nm, with a marginal

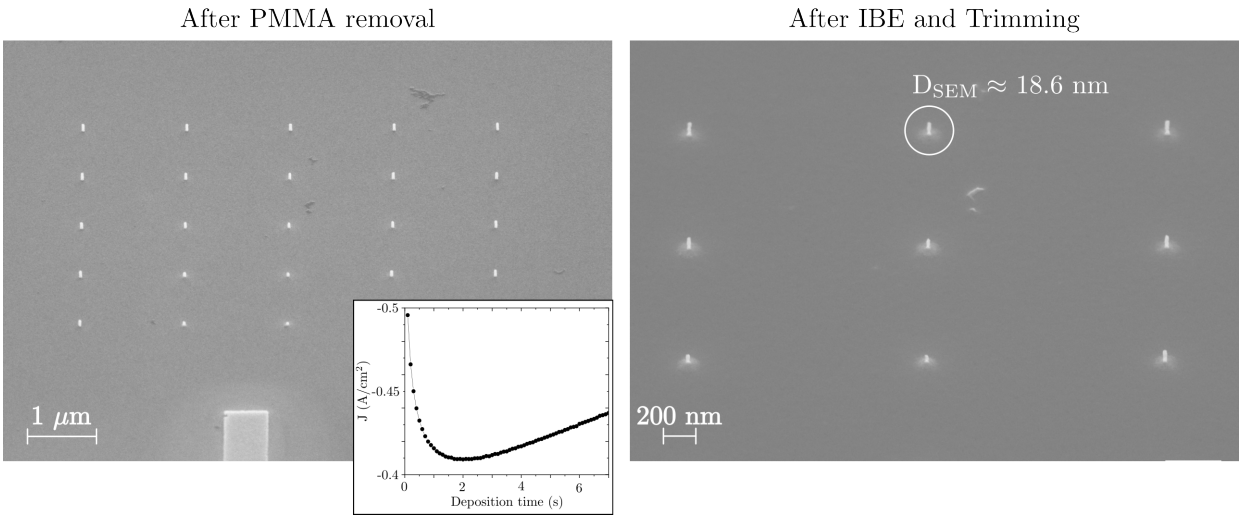


Figure 4.7: Scanning electron microscopy imaging of a 7 seconds Pt deposition after a 10 seconds OCP step in vias written by electron beam lithography after PMMA stripping and after ion beam etching and trimming. The inset shows the density of current measured as a function of the deposition time.

increase with increasing EBL nominal CD. It is also observed that the TMR appears to decrease at these small CD values, although still above 50%. This can be due to the poor connection between the hard mask and the top electrode due to the thinning step of the accuflo, but also due to the strong edge effect around the tunnel barrier coming from the small lateral dimensions. Regarding

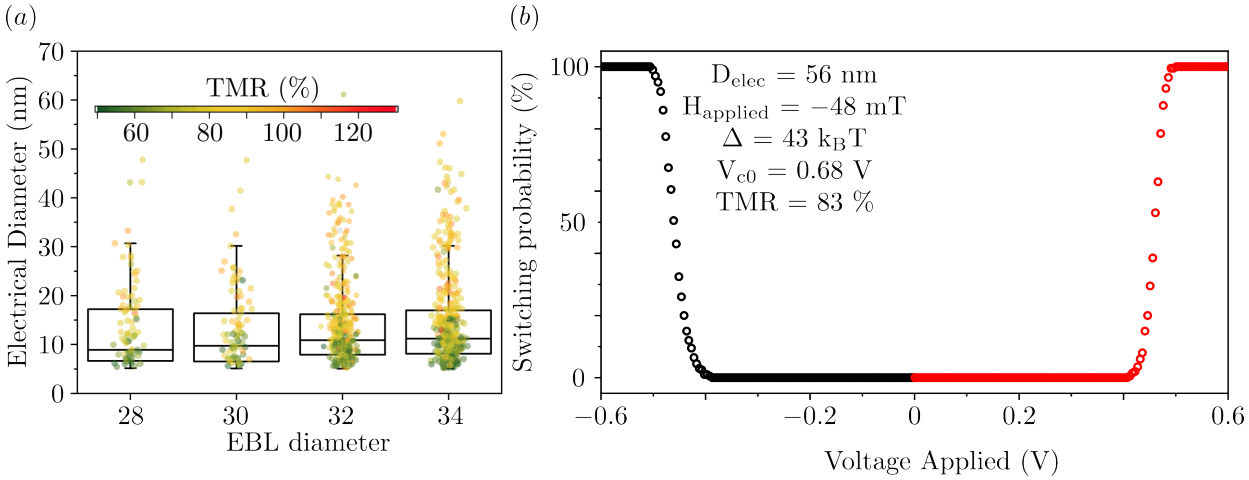


Figure 4.8: Results from single device measurements. (*a*) Electrical diameter variation for each nominal diameter written by electron beam lithography. Associated colormap with the TMR of the device, shorten above 50%. (*b*) Switching probability of a MTJ device with 56 nm electrical diameter and 83 % TMR.

the open devices in this wafer, one of the most plausible explanations is the spread of thicknesses of the hard-mask. If the pillar is not tall enough, there will be no electrical connection, and if it overgrew during Pt deposition, then it collapsed after PMMA removal. Then, it is important to get a clear grasp of the deposition rate of the material. However, good control of the deposition will only be reliable if the vias are properly clean. For this, further developments at the level of the

EBL are still necessary. However, even with these constraints, the connected pillars show high TMR values and are capable of switching by STT, as shown in the switching probability as a function of the pulsed applied voltage of Figure 4.8 (*b*). This is made for a device with larger $D_{elec}$ since devices with low diameter show low coercivity in the superparamagnetic regime, as is the case for the sample with double MgO measured in Section 3.3.

From these studies, it is shown that ECD is a viable tool to achieve sub-20 nm dimensions. Alongside with high TMR values and STT-switching, the ECD of Pt as a hard mask shows a good approach to move towards smaller diameters. This can be used for conventional perpendicular MTJ but also for MTJ with vertical aspect ratio. The latter is rather interesting. As stated above, the use of Co in vias is typical in the microelectronics industry, so there would be no added need for new materials. Moreover, if this patterning is done before IBE, most the largest portion of the stack is already defined. This allows to etch less material, having less redeposition around the pillar. Although the trimming step would still be required, it would not be as agressive, avoiding pillar collapse. This would enable us to achieve larger yield. Studies are underway to integrate this bilayer into the MTJ using a double bath technique, in which a first deposition of Co is realized followed by the deposition of Pt. As this Co is to be grown on top of a magnetic layer and not the capping, it is necessary to take into account the possible oxidation of the MTJ stack. Moreover, the deposition voltage of these electrolytes needs to be controlled as usually the voltage at which the Pt is deposited is similar to the one that etches the Co layer.

## 4.2 Promise of direct self-assembly for high density MTJ

Although in the last approach we can reach lower diameter, increasing wafer yield, there would still not be a direct integration with a high dense process flow, as the trimming step is still necessary to clean some of the redeposits. Moreover, although we start with a smaller diameter, the thickness of the stack is still quite large, namely if we make use of a layer with vertical aspect-ratio. Thus, in this next approach we move a portion of the MTJ to an embedded nano-via, which would not be accounted for the shadow effect. This approach allows us to reach very small pitch with smaller CD, in addition to the versatility of the ECD. To form these nano-vias we make use of direct self-assembled (DSA) block-copolymers (BCP). This approach resembles the damascene process shown on the subsection 4.0.1, where Co is deposited inside the nano-via. This work is part of a large collaborative work, between SPINTEC, LETI (Grenoble, France) and Fraunhofer (Dresden, Germany). Different steps of the process flow are done at each institute, and will be mentioned alongside the process description.

Starting with the electrodeposited material prior to the deposition of the MTJ avoids the constraint of deposition onto an exposed FeCo(B)|MgO interface. Additionally, this approach brings several advantages, such as:

- The deposition of Co in pre-patterned vias at low CD is standard in BEOL (replacing Cu at lower nodes), as discussed in section 4.0.1.

- The shape of the deposited material is given by the shape of the via and, as they are embedded, the high aspect-ratio of the stack does not cause tilted or fallen pillars.
- By embedding a significant height of the magnetic stack, there is less shadow effect during trimming and less redeposition during ion beam etching.
- The already existing conductive via in the BEOL can be adapted to be part of our integrated MTJ.

In this section, we realize a structural and magnetic characterization of the embedded Co vias. An initial study is realized on a non-conductive substrate (bulk Si), while the subsequent one is performed using a conductive substrate (W) to allow for transport measurements. Following this, we address the viability of a process flow adapted for a common bottom electrode. This is initially validated using a MTJ with a Ta bottom electrode and later used as a basis for samples with Co vias. For these cases, we outline integration strategies for electrical connection and possible stack functionalities.

### 4.2.1 Structural and magnetic characterization of self-assembled nano-vias with Co filling

The vias fabricated for this study are produced through DSA of BCL. This approach has received a lot of attention in recent years due to the possibility of small pitch between structures, reproducibility, low CD and relatively lower costs compared to other UV technologies with similar resolution. The most commonly used BCPs are PS-PMMA [polysterine-poly(methyl methacrylate)]. These are deposited in solution and spin coated onto our desired surface (process performed by Dr. Guide Rademaker). Afterwards, thermal annealing is used to speed up the formation of periodic structures. These structures vary in shape, size, and spacing, and can be controlled by modifying the different phases of the copolymer. For example, it is possible to achieve cylinders with dimensions as small as 5 nm [171–173], with a pitch defined by the intrinsic period of the BCL $L_0$ (related to the degree of polymer polarization). After the formation of these structures, it is possible to transfer this pattern to an underneath layer ($SiO_2$ in our specific situation).

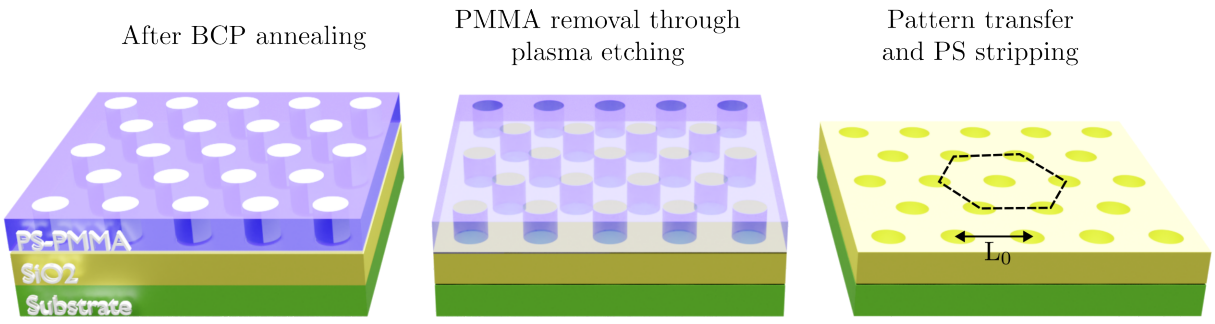


Figure 4.9: Schematic of the process flow used in the formation of the nano-vias through the use of direct self-assembly of block-copolymers.

This process is performed at LETI (Grenoble) and is illustrated in the schematics of Figure 4.9. The first drawing shows three different layers, substrate (Si bulk), a layer of $SiO_2$ (where the pattern will be engraved) with a selected height for the via and the spin-coated PS-PMMA after thermal annealing. The separation of PS and PMMA is shown using different colors, with the PMMA structures shown as white cylinders in a hexagonal array. The PMMA phase is selectively removed by plasma etching, leaving only the PS phase. Subsequently, a physical vertical etching is performed. This will etch the material that is not protected with the PS layer and thus transfer the pattern to the layer below. The PS layer is stripped from the film, leaving the pattern in $SiO_2$(process performed by Dr. Khatia Benotmane). In our situation, the properties of the BCP are selected such that the pitch between the structures ($L_0$) is around 43 nm. For an initial batch of wafers, the height of $SiO_2$ is selected to be 20, 30 and 40 nm. The transferred patterned is observed using SEM in

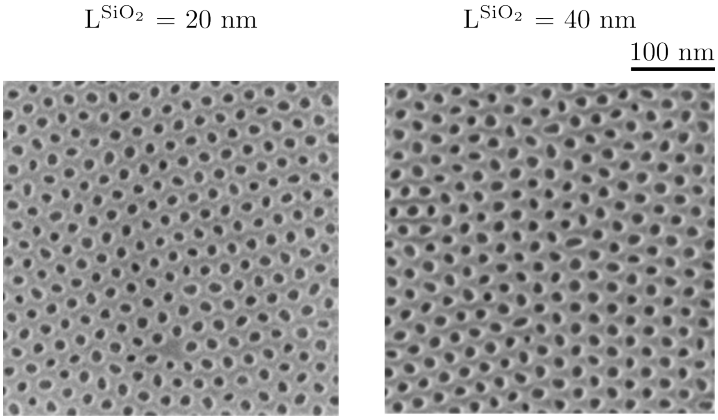


Figure 4.10: Scanning electron microscopy imaging of the transferred patterned with 20 and 40 nm height after PS stripping. Average CD of 20 nm. Characterization done at LETI, France.

Figure 4.10, for a $SiO_2$ height of 20 and 40 nm. The CD of these structures is approximately 20 nm in the center of the wafer, which tends to enlarge as we move towards the edge of the wafer (around $2-3$ nm). The average measured pitch is around 43 nm, confirming the good reproducibility of this technique.

At this point, it is possible to start filling these structures. This is done in two different steps. The first is done at Fraunhofer facilities, in Dresden, Germany, under the supervision of Dr. Lukas Gerlich and Dr. Maik Wagner-Reetz. Here, the initial metallic layer shown in the damascene process is deposited. This is made of a first PVD TaN, used to prevent the diffusion of Co to $SiO_2$, with a height of 3 nm, and a consequent Co layer, deposited by metallic-organic CVD (MOVCD), with a height of 6 nm. This layer is used as the seed layer for Co deposition by ECD. The deposition of ECD Co is done back at LETI by Dr. Maria Luisa, using an electrolyte and electrode provided by the company AVENI [174]. The 300 mm wafer is immersed in this electrolyte and a current density of 7.6 $mA \cdot cm^{-2}$ is applied to deposit a 300 nm thick Co layer.

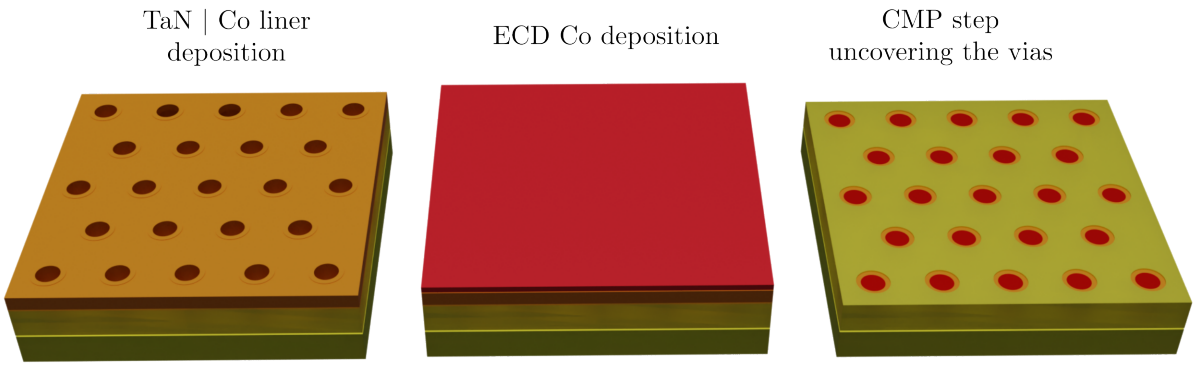


Figure 4.11: Schematic of the process flow used in the formation of the vias through the use of direct self-assembly of block-copolymers after the deposition of the metalic liner, Co ECD and CMP to uncover the magnetic vias.

Following the deposition of ECD Co, it is necessary to remove the excess metal (both metallic spacer [TaN|Co] and ECD Co) from the top of the matrix between the vias. This is done through CMP (perfomed at LETI, by Dr. Arnaud Cornélis) until the filled vias are reached, as observed in in the schematic of Figure 4.11. At this point, there might be some dishing on top of the via, so that the uncovered surface of the via is somewhat larger than previously.

This is observed more in detail in Figure 4.12 through TEM images of the wafer with (*a*) 20 nm and (*b*) 40 nm $SiO_2$ height. This dishing can be as large as 5 nm, causing deformation in the cylindrical shape, leading to a more trapezoidal one. However, this is anticipated from the CMP process, as the vias usually have this shape. In our situation this effect seems stronger when compared with standard contact vias in BEOL because here our height is substantially smaller.

From the SEM images in the same figure, we can clearly observe the $SiO_2$ layer, the inner deposited Ta spacer layer and the Co filling. Additionally, element dispersive x-ray (EDX) mappings of Co (yellow), O (red), Ta (blue) and W (pink) are shown for comparison with the TEM images. In the bottom of the vias, mostly Ta is observed from the PVD deposition. On top, the Co filling is observed. This is divided into metallic Co and $CoO_x$. The latter occurs because of the natural oxidation after CMP. Although this $CoO_x$ layer might potentially introduce some additional resistance within the via, we anticipate that it will not critically compromise the functionality of our integrated device (it will however play a role in its electrical and magnetic properties). However, this brings obstacles for vias with a lower height. Considering the height of Ta, $CoO_x$ and also some height reduction from CMP, we move from an expected 20 nm of Co to around 5 nm. This can also be seen in the taller vias, with an effective Co thickness of around 25 nm.

Other important parameter is the roughness of the post-CMP surface where we will deposit the remaining of our magnetic stack. Since the MTJ needs to grow on top of these vias, the starting surface cannot be rough, otherwise the tunnel barrier will be shorted. For the sample with a height 40 nm, this roughness is measured by AFM, with a value of 0.7 nm outside of the via and 1.1 nm inside the via. It is important to note that the size of the tip greatly influences these measurements. Although enough for structural observation, conclusions regarding the step height between $SiO_2$ and

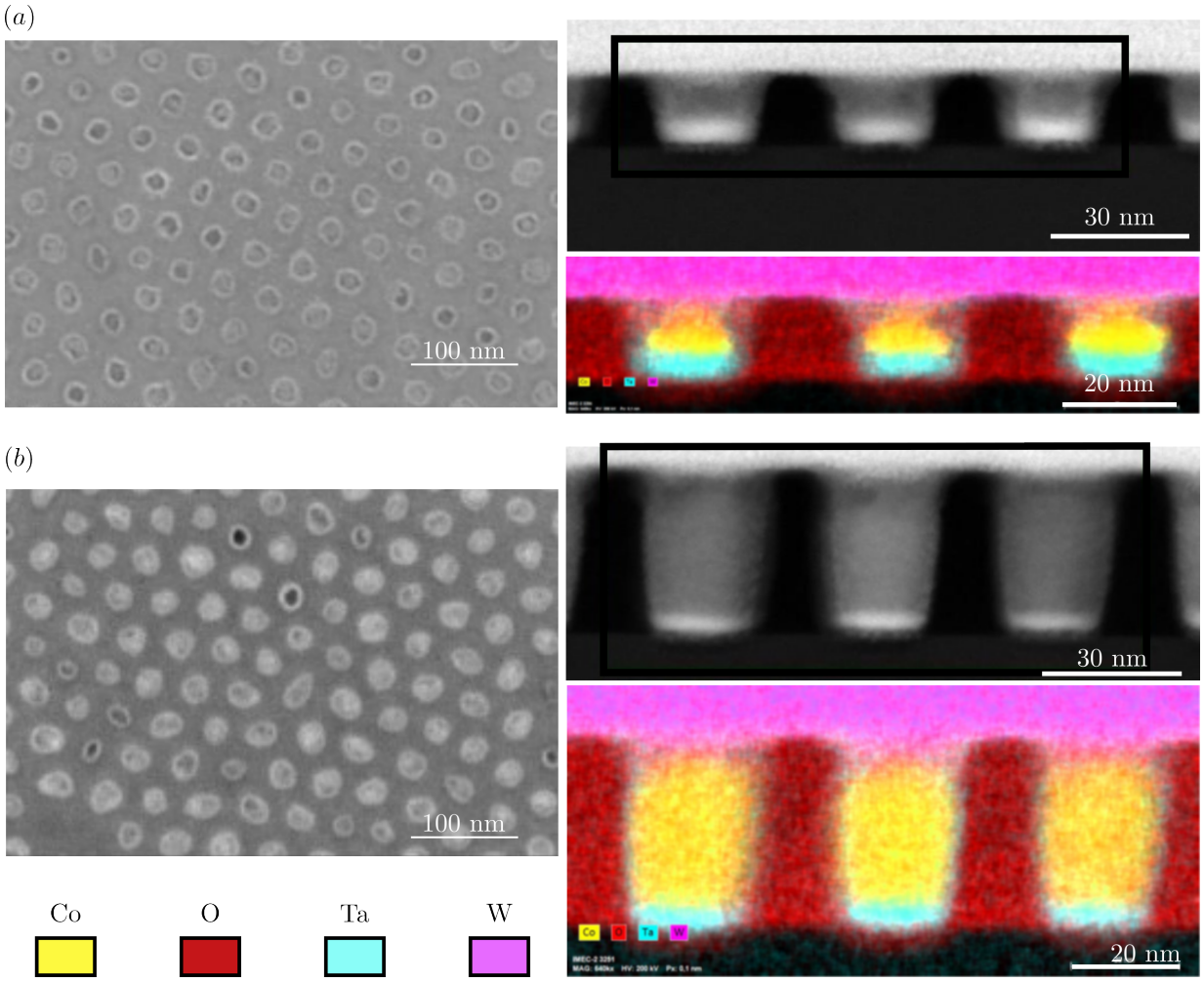


Figure 4.12: Scanning and transmission electron microscopy imaging with associated energy dispersive X-ray mapping of ($a$) vias with 20 nm height and ($b$) vias with 40 nm height after chemical mechanical polishing.

the via should be taken with care. Notably, for further analysis, we tentatively adopted a value around the via roughness, recognizing the need for more precise studies into this step height in the future.

Magnetic measurements are performed in squares of 5 mm samples for the three different heights, and shown in Figure 4.13 for perpendicular and in-plane applied magnetic field. Focusing in the VSM for the perpendicular orientation, we observe that the magnetic moment is reduced as the height is reduced, as expected from the reduced magnetic volume of the vias. Furthermore, an easy axis behavior is not observed, typical of arrays of tightly packed structures, related to a dispersion in coercivities from the magnetic vias and the dipolar coupling between them [175, 176]. Additionally, these curves show harder-axis behavior as the height of the via is reduced. This is expected and related with the aspect ratio of the via after CMP. Indeed, for the thinner via situation, this aspect ratio ($< 0.89$) promotes an in-plane shape anisotropy. Thus, the magnetization prefers to orient in-plane, an energy state that is further minimized by dipolar coupling. For the intermediate height, although an in-plane alignment seems preferred, there is still some perpendicular component, which

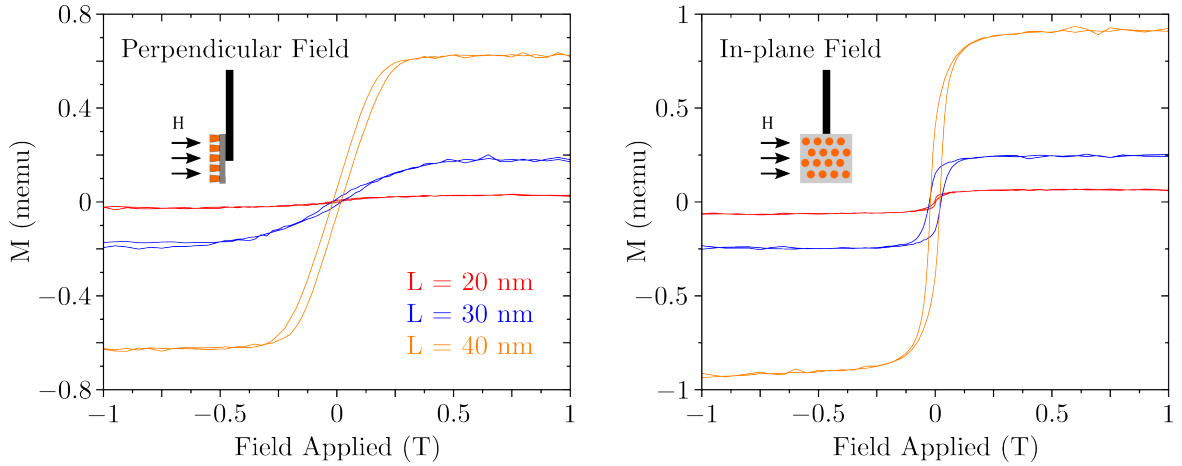


Figure 4.13: Vibrating sample magnetometry in perpendicular and in-plane configuration for a sample with magnetic vias with a height of 20, 30 and 40 nm.

might hint at the different shape of the vias along the wafer, leading to complex configurations stabilized by dipolar coupling. These results are further confirmed by the in-plane field measurements. Indeed, there is also no easy axis behaviour for the in-plane measurements, although, as the height is reduced, there is an in-plane field alignment. This is the case for instance for a thickness of 30 nm, as the coercivity is larger than for its perpendicular counterpart, and for the thinner via 20 nm, where we observe now some magnetic signal, contrary to the perpendicular measurement, thanks to the preferred in-plane alignment of the magnetization in the via.

In parallel to these measurements, an off-axis electron holography is performed by Dr. Trevor Almeida, at PFNC, Grenoble. In this technique, an electron biprism is used to interfere with an electron wave passing through the material with a second wave that passes in a field-free environment. From this interaction, we can obtain an interference pattern (hologram). From this interference, it is possible to reconstruct a phase image, with magnetic and electrostatic contributions. The latter can be removed by measuring the phase image twice, before and after turning the sample inside the sample holder. Since the magnetic contribution to the phase comes from a vector field, the difference of the phase of the two holograms is twice the magnetic phase. Through the cosine of this magnetic phase, it is possible to visualize isolines that correspond to magnetic flux lines [63, 64].

Phase contours are shown in Figure 4.14 for an in-plane applied field (*a*) and out-of-plane applied field (*b*), for nano-vias with a height of around 40 nm (Results obtained by Dr. Trevor Almeida. Measurements carried out on the *Platform for Characterisation* (PFNC)). It is observed that after an applied in-plane field, there is still a large perpendicular component of the magnetization, although tilted. This tilting can be related to the dipolar coupling, leading to a configuration in which the energy of the system is minimized. For the situation of a field applied perpendicularly, an anti-parallel alignment between magnetic vias is observed. Although this is the situation for this specific measured region of the lamela, it might not be the case in other regions, being dependent on the shape of the via and the strength of the dipolar field. If both situations (in-plane field and out-of-plane field) are compared, it is seen roughly the same magnetization alignment in the vias, although tilted for the in-plane, due to the prior in-plane saturation. This is the case for all of the Co vias

except for a central one. In this case, the magnetization is flipped when comparing the in-plane and perpendicular cases. Indeed, even if we are only seeing a row of vias, there are still some other rows behind these, which stray field interacts with the observed results. These additional sources of dipolar coupling can explain a more complex arrangement of the magnetization in each of the vias.

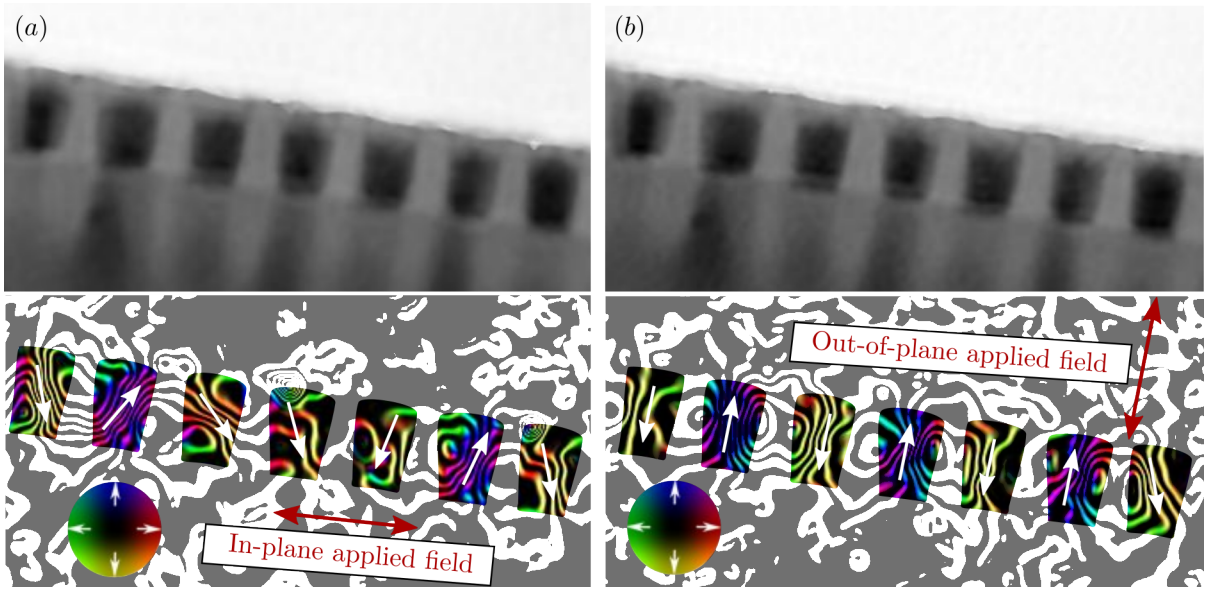


Figure 4.14: Electron holography imagining of magnetic vias with a height of 40 nm. Induction map after (*a*) in-plane applied field and (*b*) out-of-plane applied field. The orientation of the magnetization in the mapping is shown by the color wheel and schematically drawn as a white arrow.

From these initial set of measurements it is shown that, regarding dimensions, this approach would be well suited for high density applications, as the CD of the via is around 20 nm with a pitch of 43 nm. Additionally, we could make use of the first TaN layer to control the diameter and height of the deposited Co, simply by increasing the PVD thickness. This can be interesting to reduce the effective magnetic diameter without reducing excessively the initial CD of the via. Moreover, by keeping the same pitch, but reducing the diameter, it is possible to reduce the stray field between neighbouring vias [177].

The different heights of the magnetic vias can be adapted for different functionalities. As concluded from section 2, for the sample with a 40 nm height, it is challenging to reverse the magnetization of the via with STT, due to its large stability and magnetic volume. However, this can be used as a reference layer. Although the stray field created by this via in the stack would make it difficult to be adapted for practical applications, it can be used as a proof of concept for the integration of Co vias with the MTJ technology. Opposite to the situation of large stability, is the thinner via. The geometry of this via makes its magnetization prefer an in-plane orientation, as confirmed from the VSM hysteresis loops. Thanks to the still considerable surface area on the top of the via (enhanced by the CMP dishing), a surface anisotropy source, such as a FeCo(B)|MgO interface, could be enough to orient this layer perpendicular, acting as a storage layer, albeit with small stability.

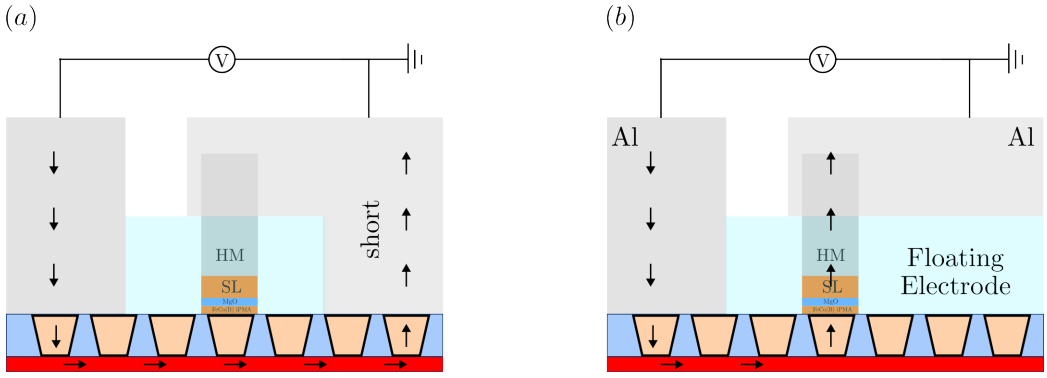


Figure 4.15: Schematics of the process flow with bottom conductive magnetic vias for (*a*) standard MTJ process flow and (*b*) floating electrode approach. The arrows indicate the flow of current.

Before the integration of these vias with the MTJ process flow, there are some constraints that need to be addressed. First, the layer underneath the magnetic vias needs to be conductive (such as W or TiN). In our first batch of wafers this layer is bulk Si, so no electrical measurements can be performed. In the next subsection we will use a new batch of wafers with a W underlayer, which is explored for electrical characterization. Assuming that this layer is conductive, it is necessary to modify the process flow to account for a common bottom electrode. This is shown as a 2D schematic in Figure 4.15. The first situation of this Figure (*a*) follows the usual MTJ process flow, where both electrodes are in contact with the conductive vias. In this case, the current path with least resistance is from electrode to electrode, without crossing the pillar. In our usual MTJ process flow this does not happen because the electrodes are physically separated. To avoid this situation, we make use of a spacer between the conductive vias and the top electrode (commonly referred as floating electrode) (*b*). This avoids shorting, and the current will only flow through the MTJ. In the next section we will then explore this concept of floating electrode and test its viability for the integration of the MTJ with the Co via.

### 4.2.2 Exploring the integration of a MTJ with Co vias using a floating top electrode

In order to perform electrical measurements, a new batch of wafers with a 150 nm W underlayer are fabricated using the DSA approach. This W layer had significant roughness when compared with the bulk Si from the initial study. Thus, prior to the deposition of $SiO_2$, a step of soft CMP is performed, to smooth the W layer. Additionally, before the step of the metalic layer deposition at Fraunhofer, a desoxidation of W with $H_2$ reactive preclean is done, followed by the Ta PVD 3 nm and Co MOCVD 6 nm without air break . The same deposition flow is used for this batch of wafers as for the previous, with the W underlayer being the main change. SEM images after the last CMP step are shown in Figure 4.16 (*a*) for a sample with a height of 36 nm and CD $\approx$ 35 nm and (*b*) for a sample with a height of 16 nm and CD $\approx$ 25 nm. From here we can observe a larger dishing than for the situation of the bulk Si underlayer, as the pitch is still to be around the same 43 nm. Indeed, for

the situation of the thicker vias, these seem to be closer than for the situation of the thinner vias. This will lead to a larger via-to-via magnetic interaction, so that the distribution of the orientation of the magnetization in the magnetic vias can be somewhat complex.

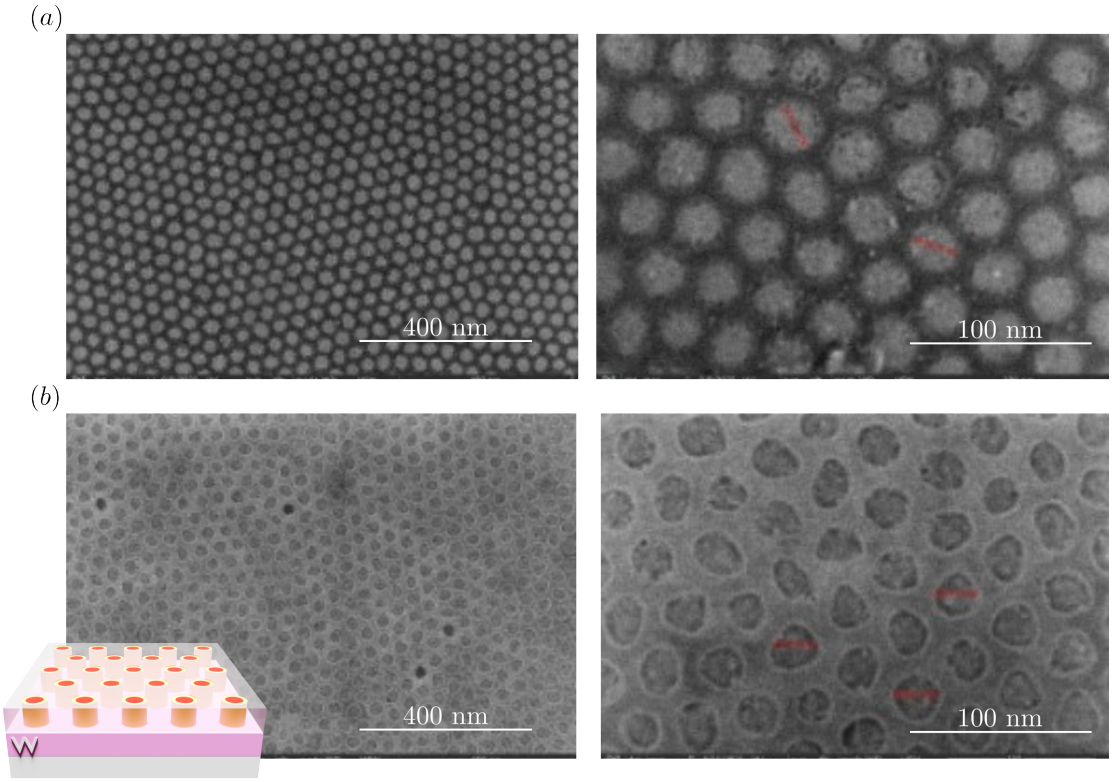


Figure 4.16: SEM images of (*a*) magnetic vias after CMP with a height of 36 nm and CD 35 nm and (*b*) magnetic vias after CMP with a height of 16 nm and CD 25 nm. Schematics show the layers along the height of the wafer: Si (bulk) | W (150 nm | $SiO_2$ with embedded nano-vias.

To study the dipolar coupling present inside our matrix of Co vias we make use of magnetic force microscopy (MFM). These studies are performed at Institute Néel under supervision of Dr. Olivier Fruchart. This technique is similar to AFM but in this situation the tip is coated with a magnetic material. Here the cantilever approaches the surface for a first topographic scan (similar to AFM) and, for a second scan is lifted at a certain lift heigh. It is namelly important to avoid topographic and electrostatic contributions from the surface to the signal. As the tip is scanning the material, stray fields from the material will interact with the tip, applying a force on it. In more detail, the gradient of force along the direction of oscillation of the tip induces a phase shift, which is observed in Figure 4.17 (*a*), for no external applied magnetic field. In this experiment, a tip coated with 20 nm CoCrPt is used. Making use of an electromagnet, it is possible to apply a perpendicular magnetic field to our magnetic material. For convenience, only positive fields are applied. Figure 4.17 shows a $1 \times 1$ $\mu m^2$ scan with a perpendicular field applied up to 400 mT. In the sample without applied field it is observed different domain-like structures. This is the sum of the stray fields from the different magnetic vias which can be antiparallel (bright color) or parallel (dark color) to the magnetization of the tip. As we start increasing the magnitude of the applied field, namely to 154 mT, we observe the appearence of independent small dots. This indicates that some of the moments of the vias

are reversing towards the direction of the applied magnetic field. This effect is clearer at increasing fields, up to 400 mT, where there are still some dots with magnetization antiparallel to the field applied. Due to the hexagonal structure (a central via is surrounded by 6 neighbours) the behaviour of these magnetic moments is strongly affected by inter-via stray field. To understand what is its value and capture variations in coercivity of the vias, we do a minor hysteresis loop, saturating firstly at 650 mT and then starting measuring at 300 mT. This is shown in Figure 4.18. It is seen that,

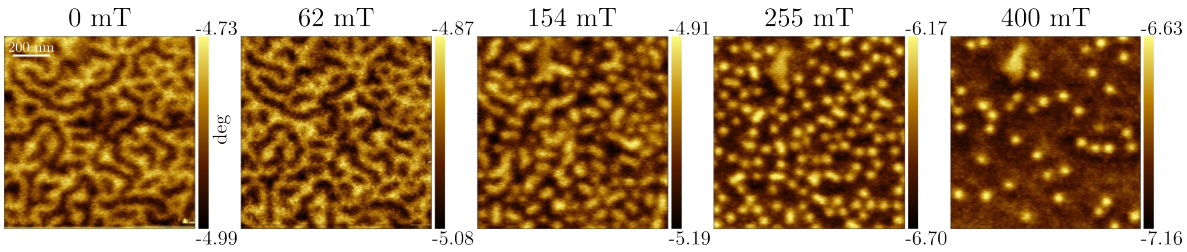


Figure 4.17: MFM images for different applied magnetic fields for a sample with CD 35 nm and height 36 nm. Images obtained from a $1 \times 1 \mu m^2$ sample. Magnetic vias with a magnetization parallel to that of the tip are shown with a black color and those antiparallel to the magnetization of the tip are shown with light color. Measurements realized for a lift height of 15 nm.

at this applied field there is roughly no via with magnetization antiparallel to that of the magnetic tip. By reducing this field with steps of 20 mT we can observe an increase in the number of reversed magnetization of the vias. As the field applied is still positive, this shows that the array prefers an anti-parallel arrangement, as shown in the electron holography experiment. For 160 mT we clearly observe a multitude of magnetic vias with antiparallel magnetization. Although it is not direct from these mappings, the bright dots surrounded by other vias (with opposed orientation, if not observed), within a similar pitch. If we now increase again the field applied towards more positive values, we eventually retrieve a state where most of the magnetization of the vias are aligned in the same direction. The coercivity of each via can be calculated considering the field at which the via switches in both field sweeps. From here it is also possible to extract the offset field (or dipolar field), that 6 neighbours are doing in a single via (assuming only first nearest neighbours). These values are shown in the histograms for the set of 30 vias analyzed. It is observed a somewhat spread values of coercive fields, ranging from 20 to 120 mT, which are promising for high stability. The dipolar field is observed with a maximum at around 270 mT and, considering the 6 nearest neighbours, accounts for a via-via stray field of around 45 mT.

This shows that the interaction between magnetic vias in our very dense array is so strong that it is enough to overcome the self-energy of the via and arrange the array in a somewhat antiparallel pattern. This is the case for the magnetic vias, but it would be a situation for a PSA storage layer with this dimension and pitch. Thus, it is important to find a way to reduce the magnetostatic interaction between magnetic devices with this vertical aspect ratio, which will be explored in the next section. Nevertheless, this interaction field does not pose a limitation to the fabrication of our devices, but rather to understanding the measurement under applied voltage or field.

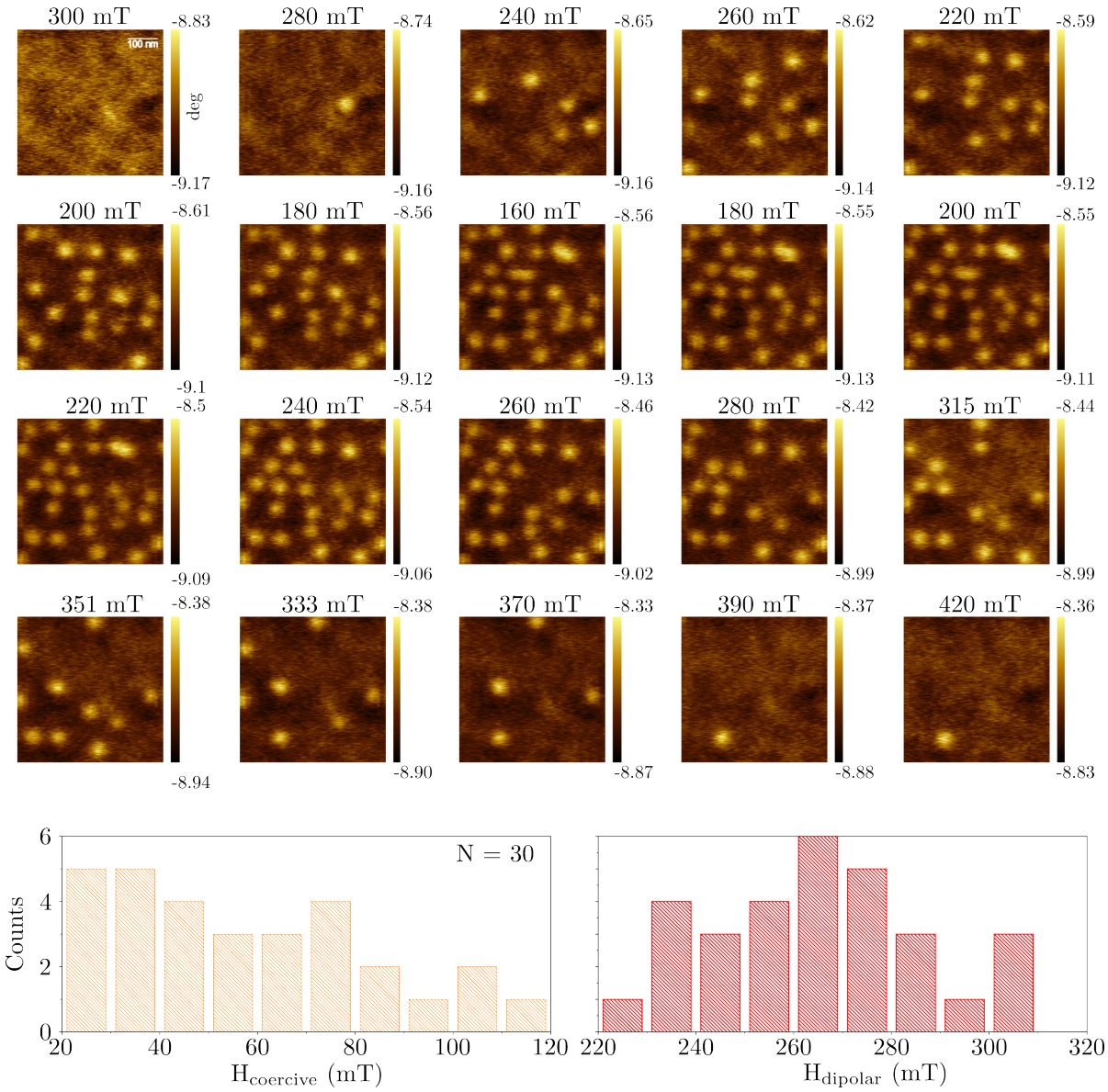


Figure 4.18: MFM images for different applied magnetic fields for a sample with CD 35 nm and height 36 nm. Images obtained from a $1 \times 1 \mu m^2$ sample. Magnetic vias with a magnetization parallel to that of the tip are shown with a black color and those antiparallel to the magnetization of the tip are shown with light color. The values of coercivity and dipolar field for the measured 30 vias are shown in the associated histograms. Measurements realized for a lift height of 10 nm

Now that a preliminary evaluation of the magnetic properties of the Co via array is done, we move to the design of a process flow that accounts for these conductive vias (since each via is conductive and connected to a conductive W layer). As shown in the schematics in Figure 4.15, if we were to use the conventional process flow to fabricate our MTJ, the current would not flow through the device. Thus, it is necessary to modify it slightly and make use of a floating top electrode through a physical separation between the bottom and top electrodes. A schematics of the process flow used for this approach is shown in Figure 4.19 (*a*). Here, we use the example of the MTJ with the usual Ta bottom electrode, rather than the vias, because this process flow has to be compatible with any conductive bottom electrode. At this stage, we would physically separate the electrode through RIE, but instead we now spread ACCUFLO across the entire wafer.

It is now necessary to use lithography to protect part of the ACCUFLO. This is done by using laser lithography instead of the usual UV lithography. This gives us the ability to design the mask we want without the need to physically create a new one. We create a rectangular shape that will protect the ACCUFLO that we want to keep for the floating electrode. If we were to use this mask directly in the laser lithography with a usual AZ1512HS resist, the laser would engrave the pattern in the square we design and, after development, only the squares would come out. This is the opposite of what we want. To fix this issue, we use the reversible resist AZ5214E, the same as for the top electrode definition in our conventional process flow. We then use our designed mask and input the parameters of 15 mW at a pixel pulse duration of 5 % (after optimization) in the laser lithography. After writing, we anneal the wafer at 120° for 2 minutes, this will make the resist reverse. Afterwards we expose the wafer, without any mask, in the usual UV-lithography. After development we are then left with only the squares protecting a part of the ACCUFLO, and we can use the usual RIE step done for the ACCUFLO etching in our process flow. To connect the top electrode to the device, it is necessary to make an opening in the square that we designed. To avoid possible shifts during the writing of the laser lithography, we made it larger than usual. In this case we can use the usual AZ1512HS resist with the engraving parameters of 15 mW at a pixel pulse duration of 45 % (after optimization). The top electrode is constructed using the same approach as for the usual process flow. The schematic of the final step is shown in Figure 4.19 (*b*) for the situation of a Ta bottom electrode.

Before moving to this fabrication in the context of the Co vias, we make preliminary tests using the Ta bottom electrode for a validation of the floating bottom electrode:

1. Deposition of Al contacts on top of a blanket Ta wafer with a non-patterned ACCUFFLO spacer of 500 nm at the center region and around 450 nm at the edge of the wafer. During electrical measurements, the resistance value should be in the MΩ range (open circuit). Knowing that, for electrical contact, the tip scratches the Al pad (to remove some oxidation), this shows that the pressure exerted from the tip is not enough to break the deposited ACCUFLO spacer.

2. Deposition of Al contacts on top of a blanket Ta wafer with the final pattern of the ACCUFLO spacer [schematics of Figure 4.19 (*b*)] without any device. The measured resistance value is still in the MΩ range (open circuit). This shows that there is no current leak through the floating electrode.

After the earlier validation of the floating electrode, we fabricate a usual MTJ with the same stack as the one fabricated for the samples for ECD in PMMA: Ta (220)| FeCo(B) (8) | Pt (80) | (Co (5) / Pt (2.5))$_{\times 6}$ | Co (5) | Ru (9) | (Co (5) / Pt (2.5))$_{\times 3}$ | Co(5) | W (2) | FeCo(B) (10) | Mg (7.5) | (30 s and $3 \times 10^{-2}$ mbar) | Mg (5) | FeCo(B) (15) | W (2) | Ta (20) | Pt (50) (nominal thickness in Angstroms). We observed individual measurement of devices and STT switching, as shown in the phase diagram of Figure 4.19 (*b*.1). Thus, the use of this process flow for a common bottom electrode is validated for conventional MTJ. We can now make use of it for the samples with

the Co vias. This is done in 100 mm wafers diced from the 300 mm initial wafer (where the CMP was performed). It should be noted that now the entire 100 mm wafer does not have a correct CMP, which can affect the electrical measurements (for instance, no connection to the via).

An initial trial makes use of vias with a height of 36 nm. As discussed before, these may be used as a reference layer as we are not expecting them to switch with STT. On top of the vias, before deposition of the magnetic stack, we make an Ar pre-etching of 10 seconds. This will etch some of the CoOx at the interface. Although from the EDX results, shown in Figure 4.12, this oxide seems to be around 5 nm, it is important not to do a strong etching, as this would increase the step height between the $SiO_2$ and the top of the Co via (different etch rates), which can impact the growth of the multilayered stack (principally the MgO). After pre-etching we deposit (stack labeled as P12.01) W (2.3 - 5)| FeCo(B) (8 - 11.6) | Mg (7.5) | (30 s and $3 \times 10^{-2}$ mbar) | Mg (5) | FeCo(B) (14) | W (20) | Ta (20) | Pt (50). Here, we have a wedge in both W and interfacial FeCo(B) to study the influence of its thickness on the rough surface of the Co vias. Devices with nominal CD of 50, 80, 100, 200 and 500 nm are fabricated with the process flow defined beforehand. An illustration of a final device integrated with a single Co via is shown in Figure 4.19 (*c*). Due to the very small pitch of our vias and small CD, a perfect MTJ-via alignment will hardly be the case. In fact, pillars with a CD greater than $\approx$ 60 nm will encompass more than 1 via, to the tens and hundreds for the situation with an increasing CD of 100 and 500 nm. This is an obstacle to the measurement. As each individual via has an associate resistance (increased because of CoOx), a large number of parallel resistances will overshadow the possible TMR value of our device.

To confirm that the magnetic signal remains after the deposition of the multilayered stack, perpendicular VSM measurements are made. These are shown in Figure 4.19 (*c*.1) for the situation of the virgin vias (black circles), and for a stack deposition of (10s Ar etching) | W (3) | FeCo(B) (9) | Mg (7.5) | (30 s and $3 \times 10^{-2}$ mbar) | Mg (5) | FeCo(B) (12) | W (20) | Ta (20) | Pt (50) (nominal thickness in Angstroms) and further annealed at 300° C (red circles). When comparing both, we observe a similar magnetic moment in saturation, as the total magnetic volume of the magnetic layers deposited is quite small compared with the magnetic volume of the vias. Moreover, an increase in coercivity, related with the effect of surface anisotropy, is observed. Electrical measurements are then made on the patterned wafers. Most of the devices did not have a hysteresis signal, showing mainly noise and resistance jumps along the different applied fields [4.19 (*c*.2) and (*c*.3)]. Although this measurement cannot confirm that there is a signal from our device, it is still giving a significant resistance. This can come from the parallel vias but also from the contribution of MgO. In fact, in some loops (not everywhere in the sample and should not be taken as a conclusion), there seems to be a hysteresis behavior [(*c*.4)], with a very small TMR associated. From here we can speculate but also give hints about future work that could be realized. Since some devices worked in the conventional process flow, we can rule out the possibility of leakage current from the floating electrode. However, the quality of the laser lithography fails in the borders of the wafer (thinner resist, and parameters for the laser are optimized for the center region). This can bring about constraints regarding the step of this ACCUFLO spacer, making it a critical step. Furthermore, these samples were diced

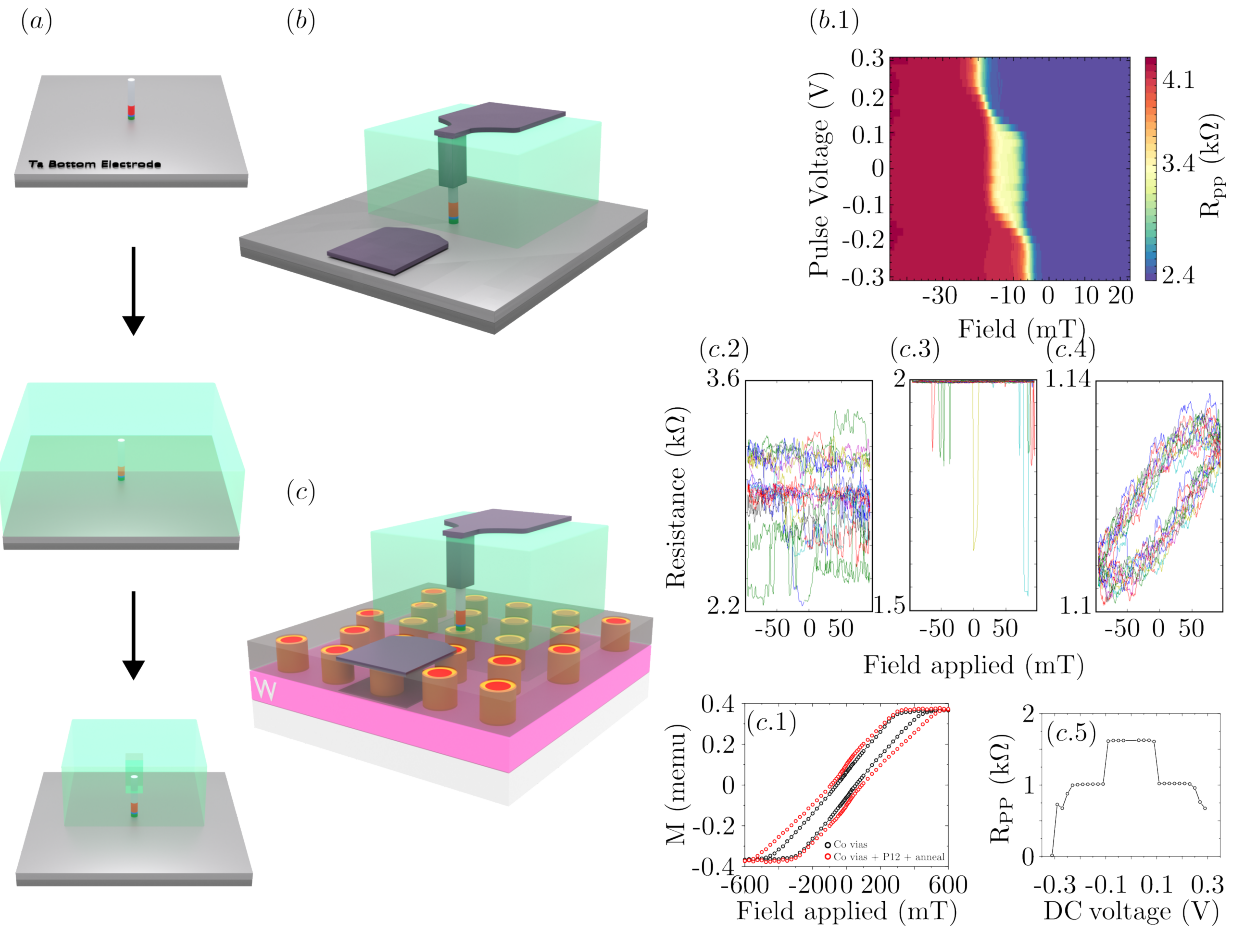


Figure 4.19: (*a*) Schematics of the process flow for the creation of a floating top-electrode, resulting in (*b*) for the case of a Ta bottom electrode or (*c*) for the situation of embedded vias; (*b*.1) Example of a pulsed phase diagram for a device fabricated with Ta bottom electrode, using the floating electrode process flow; (*c*.1) VSM measurements of Co vias with a height of 36 nm before ((in black) and after stack deposition and annealing (in red); (*c*.2 - *c*.3 - *c*.4) RH measurements for devices along the P12.01 wafer showing characteristics loops (*c*.2 and *c*.3), and a rare loop (*c*.4); (*c*.5) Dependency of $R_{PP}$ with applied DC voltage, showing two distict dielectric breakdown.

from the original 300 mm wafer, so what was the best CMP region before, it is not in the center of the fabricated wafer but at the border. Additionally, from the material point of view, the quality of the surface for the MgO growth is believed to be the main contributor for the reduced TMR.

Although it cannot be directly confirmed [loops like the ones in Figure 4.19 (*c*.4) are quite rare], we can still perform some analysis to understand if, qualitatively, there is a current flowing through an oxide. The first prediction is to use a DC voltage and see if we can reduce the resistance of a measured device up to the point where it shorts. This is shown in Figure 4.19 (*c*.5), where we apply a negative and then positive DC voltage (each time increasing in magnitude) for a device measured with an initial $R_{PP} \approx 1.8\,k\Omega$. A first sharp decrease in resistance is observed around $|100\,mV|$, which is not typical of an MgO, as it usually reduces smoothly. A second reduction is observed after a DC voltage of $|\ 200\,mV\ |$, with an eventual dielectric breakdown at $-320\,mV$. Although this value is quite low for the breakdown of a MgO tunnel barrier, we need to consider that, since it is growing on

a rough surface, its quality is poorer than usual. However, we should still refrain from saying that this is the behavior of the MgO, although the breakdown of two insulators is apparent. These can be some $WO_x$ (from the underlayer, although a cleaning was performed before the TaN|Co deposition), $CoO_x$ (from the top of the via), or the MgO.

We can also analyze the dependence of $R_{PP}$ on the CD of the device, but also on R × A of the tunnel barrier. For this purpose, we show in Figure 4.20 the measured $R_{PP}$ as a functional of the EBL CD, for the case of the sample P12.01 (being discussed until now), and a wafer with larger R × A, with stack following W (2.3 - 5)| FeCo(B) (8 - 11.6) | Mg (8.9) | (10 s and 150 mbar) | Mg (8.9) | (10 s and 150 mbar) | Mg (5) | FeCo(B) (12) | W (20) | Ta (20) | Pt (50) (nominal thicknesses in angstroms) (thereafter labeled as P12.03). There are 2 conclusions that we can take

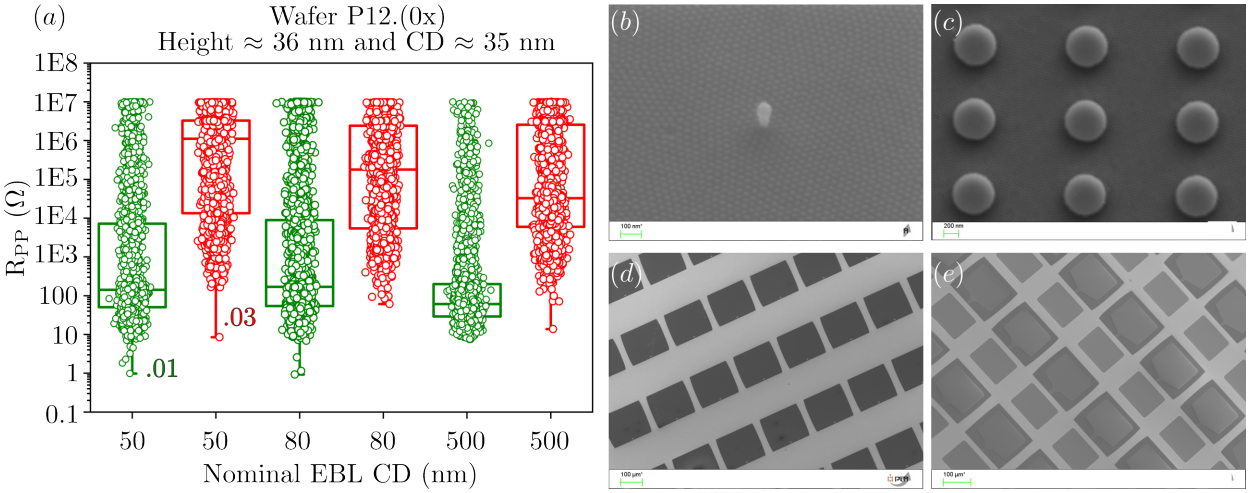


Figure 4.20: (*a*) Minimum resistance mapping for three different EBL nominal CD, for a wafer with low R × A (P12.01) and a wafer with high R × A (P12.03). Different steps along the process flow of the sample P12.03: (*a-b*) definition of the MTJ, (*c*) definition of the floating electrode and (*d*) deposition of the Al contacts.

from the dependency between $R_{PP}$ on the nominal CD from EBL. For the situation of both P12.01 and P12.03, the mean $R_{PP}$ (represented with a box chart) is lower for 500 nm than for 50 nm. This may be representative of the dependence of R × A on the tunnel barrier, which is considered constant throughout the wafer. Furthermore, the resistance value increases significantly for P12.03, which we can associate with the larger R × A of the tunnel barrier (since the contribution from the vias can be assumed to be roughly uniform for the same CD). In both cases, there is still a large distribution of $R_{PP}$ for the same CD. There are several factors that can influence this distribution, and already discussed previously: from the quality of the CMP along the wafer, to the resolution of the writing during laser lithography. These critical steps during fabrication make it difficult to fully identify the step from which the large $R_{PP}$ distribution comes from. Additionally, SEM images along the process of the sample P12.03 show a smooth process, without clear issues during the definition of the pillar (Figure 4.20 (*b*) for a 50 nm nominal CD and Figure 4.20 (*c*) for a 50 nm nominal CD), with the vias clearly defined; definition of the floating electrode (Figure 4.20 (*d*) using laser lithography; and deposition of the electrodes, showing that the top electrode is only atop the floating electrode.

Lastly, to investigate the interface between the Co vias and the MTJ, which can be the main reason for our lack of TMR, we use STEM and EDX (sample preparation and measurement done by Dr. David Copper, from CEA LETI, at PFNC). From Figure 4.21 (*a*) we can observe the connection of the MTJ and its integration with the Co vias. There is observed a straight Ta hard mask, connected to the Al pad. Moreover, the ACCUFLO pad is roughly half-height of the hard-mask. This is important to show that the height of the ACCUFLO thinning is enough for a good contact between the hard-mask and the Al contact (for reference, the ACCUFLO was thinned up to a range of 50 - 70 nm). Below the Ta hard-mask, we can see the MTJ, where the bright color represents the MgO. This is better observed in a close-up EDX mapping of Figure 4.21 (*b*). There, we observe the different layers of the integrated device. The W underlayer (pink), the Ta (cyan) along the via, and the Co via (dark blue) to the multilayered stack, composed of W and interfacial Fe (green), Mg (red), Fe and the capping W, Ta, and Pt (yellow). From here we can see a clear difference between layers, although the first interface between the vias and the W|FeCoB is not clear. Indeed, from the individual color maps shown in Figure 4.21 (*c*), there is no clear Fe signal below the Mg. At this point, it is not clear if this is due to the annealing of the sample, lower FeCo(B) thickness, or W intermixing with FeCo(B). Additionally, there seems to be a thin Co layer on top of all of the vias, which can be indicative of the CMP in this region of the wafer. Nevertheless, the Mg layer seems to be continuous, so its growth should be possible on top of the vias. Several experiments are being conducted, considering larger thicknesses of FeCo(B) and the effect of the annealing at the interface between the vias and the first FeCo(B) interface. The most interesting case would be to use only the center region of the 300 mm wafer, where the CMP is optimized, and to fabricate devices with small nominal CD (emphasis on the single via-contact). Although this reduces the output of wafers, it might be better and more reliable results.

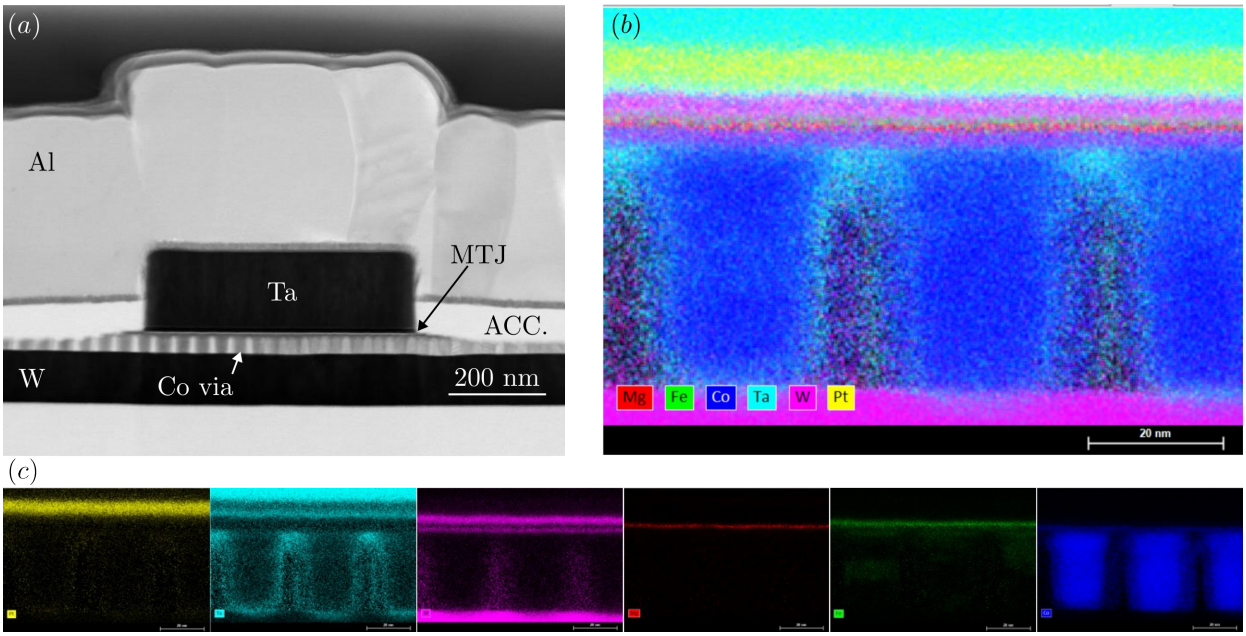


Figure 4.21: (a) STEM imaging of a patterned MTJ device on top of Co vias, (b) associated EDX mapping of a close-up between the magnetic vias and the MTJ and (c) individual element mapping.

Although it is not possible, at this point, to say for sure that we can integrate the MTJ with these vias, we should highlight the progress made with this goal in mind. Co vias were manufactured with small CD ($\approx 25-30\,\text{nm}$) and very small pitch ($43\,\text{nm}$). Moreover, this technique allows different types of material to be deposited, since this is done by ECD.Furthermore, the use of Co makes it viable with a microelectronic roadmap, as it is already common in their process flow. In addition, magnetic characterization is done by electron holography and MFM. Although this is done for the vias, we could expect similar patterns for the situation of the PSA-MTJ at very low pitch. Thus, it is important to mitigate the effect of dipolar interactions between different MTJs with vertical aspect ratio. This is one of the main goals of our next section, where we will explore a different strategy for storage layer, both reducing the magnetic height with increase in stability and reducing the stray field of single pillar devices.

# 5 Dipolar coupled core-shell system for vertical aspect-ratio MTJ

As discussed during this manuscript, high stability can be preserved at low nodes through the use of a layer with vertical aspect-ratio. However, due to the increased aspect-ratio, the issue of stray fields in a dense memory array will be much more pronounced than in usual perpendicular MTJ due to their flat aspect-ratio, as it was discussed in Section 4. In this section we give an alternative approach that reduces both the magnetostatic interaction but also gives an auxiliary enhancement in stability through the use of a tubular structure (magnetic shell) around the vertical aspect-ratio storage layer. Making use of the strong dipolar coupling in this system, it is possible to promote a core-shell synthetic ferrimagnetic state, with an antiparallel storage layer (from now on described as magnetic core) and magnetic shell (schematics shown in Figure 5.1). The gain introduced by this design is twofold. First, the dipolar coupling increases the stability of the device. This allows to reduce the system height, avoiding non-coherent reversals while improving the switching time and switching voltage. Second, the resultant stray field from the composite structure is sharply reduced. This enables a denser array that would not be possible for a single thick magnetic layer.

To describe this unusual system, we make use of both macrospin models and micromagnetic simulations. We demonstrate that, through the use of the magnetic shell, one can achieve faster switching without penalty in the switching voltage, and we outline the parameters for an optimized trade-off of stability versus writability. We then study the stray field for both the situations of the p-MTJ, PSA-MTJ and core-shell PSA-MTJ. We show that through variation in the outer radius of the magnetic shell, it is possible to achieve close to full compensation of the magnetic stray field inside a dense array of core-shell PSA.

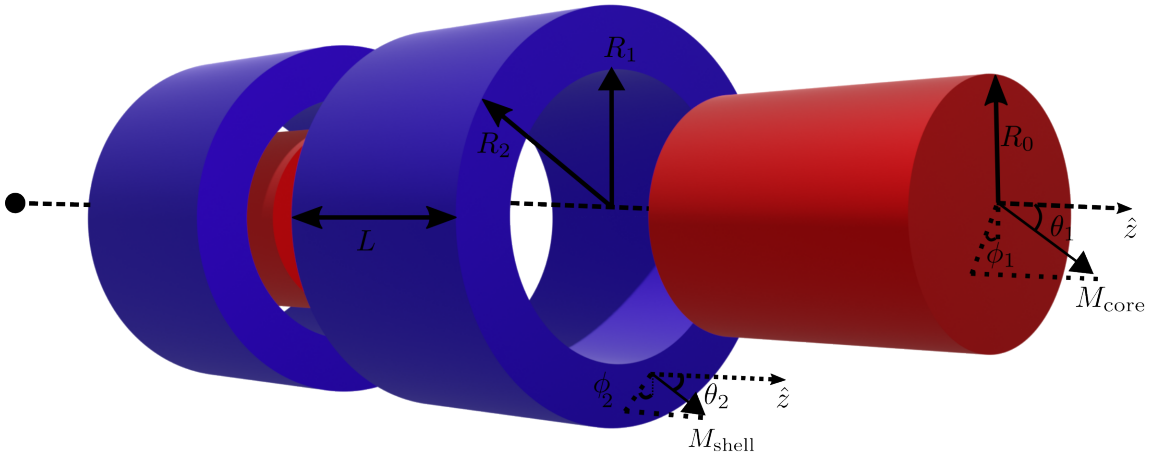


Figure 5.1: Schematics of the core-shell system where $R_0$ is the radius of the magnetic core (shown with red color) with magnetization $M_{\text{core}}$ characterized with the angles $\theta_1, \phi_1$. The magnetic shell (shown with blue color) has inner radius $R_1$ and outer radius $R_2$, magnetization $M_{\text{shell}}$ characterized with the angles $\theta_2, \phi_2$. Both systems have the same height $L$.

## 5.1 Stability of an isolated magnetic shell

Before describing the physics of the coupled core-shell element, it is helpful to describe each of them separately, with a focus here on magnetic anisotropy and thus potential increase in stability. While the situation of the core as a finite-length cylinder has been extensively covered in the context of a single thick layer MTJ [60], the situation of a torus (the magnetic shell) is more unusual. It is the purpose of this section to calculate its demagnetizing factors, which are the relevant parameters as the shape anisotropy is the only source of magnetic anisotropy. To do so, we rely on the already presented approach of phase amplitude $\mathcal{D}$ and Fourier calculation (introduced in Section 2). On practice, the shape amplitude of a shell is simply the subtraction of the shape amplitude of a cylinder with radius $R_1$ from the shape amplitude of a cylinder with radius $R_2$ [178, 179]

$$\mathcal{D}(k_\perp, k_z) = \frac{4\pi}{k_\perp k_z}\left[R_2\mathcal{J}_1(k_\perp R_2) - R_1\mathcal{J}_1(k_\perp R_1)\right]\sin^2\left(dk_z\right) . \tag{66}$$

Following the same reasoning as for the demagnetizing coefficients of a single cylinder, and performing the transformations $q = kR_2$, $\sigma_s = R_1/R_2$, and the shell aspect ratio $\tau^{\text{shell}}$ $(L/2R_2$ )we obtain the integral:

$$\mathcal{N}_{zz}^{\text{shell}}(\sigma_s, \tau^{\text{shell}}) = \frac{1}{\tau^{\text{shell}}(1-\sigma_s^2)}\int_0^{+\infty}\frac{\mathrm{d}q}{q^2}(1-e^{-2q\tau^{\text{shell}}})\left[\mathcal{J}_1(q) - \sigma_s\mathcal{J}_1(\sigma_s q)\right]^2 . \tag{67}$$

The latter can be rewritten in terms of the demagnetising coefficients of full cylinders ($\sigma = 0$) shown in equation (31):

$$\mathcal{N}_{zz}^{\text{shell}}(\sigma_s, \tau^{\text{shell}}) = \frac{1}{1-\sigma_s^2}\left[\mathcal{N}_{zz}^{\text{cylinder}}\left(\tau^{\text{shell}}\right) + \sigma_s^2\mathcal{N}_{zz}^{\text{cylinder}}\left(\frac{\tau^{\text{shell}}}{\sigma_s}\right) - \frac{\sigma_s^2}{\tau^{\text{shell}}}F_0(\sigma_s^2) + \frac{2\sigma_s}{\tau^{\text{shell}}}A_{1,1}^{-1}(2\tau^{\text{shell}}, 1, \sigma_s)\right]. \tag{68}$$

The term $A_{1,1}^{-1}(2\tau^{\text{shell}}, 1, \sigma_s)$ is given as:

$$A_{1,1}^{-1}(2\tau^{\text{shell}}, 1, \sigma_s) = \int_0^{+\infty} q^{-2}e^{2q\tau^{\text{shell}}}\mathcal{J}_1(q)\mathcal{J}_1(\sigma_s q)\mathrm{d}q , \tag{69}$$

which can be solved making use of a combination of elliptical integrals (see, for reference, Equation 10 and Table 1 of [178].

Using Equation 68, it is possible to calculate the preferred orientation of the magnetization in the magnetic shell depending on its geometry ($\tau^{\text{shell}}$, $\sigma_s$). Figure 5.2 (*a*) illustrates the magnetization preferred orientation versus vertical aspect ratio, for several values of $\sigma_s$. The crossing point between $\mathcal{N}_{xx}^{\text{shell}}$ and $\mathcal{N}_{zz}^{\text{shell}}$ highlights the crossover between the perpendicular versus in-plane easy directions. For $\sigma_s \to 0$ the situation is similar to that of a cylinder and the aspect ratio for crossover is consistent,

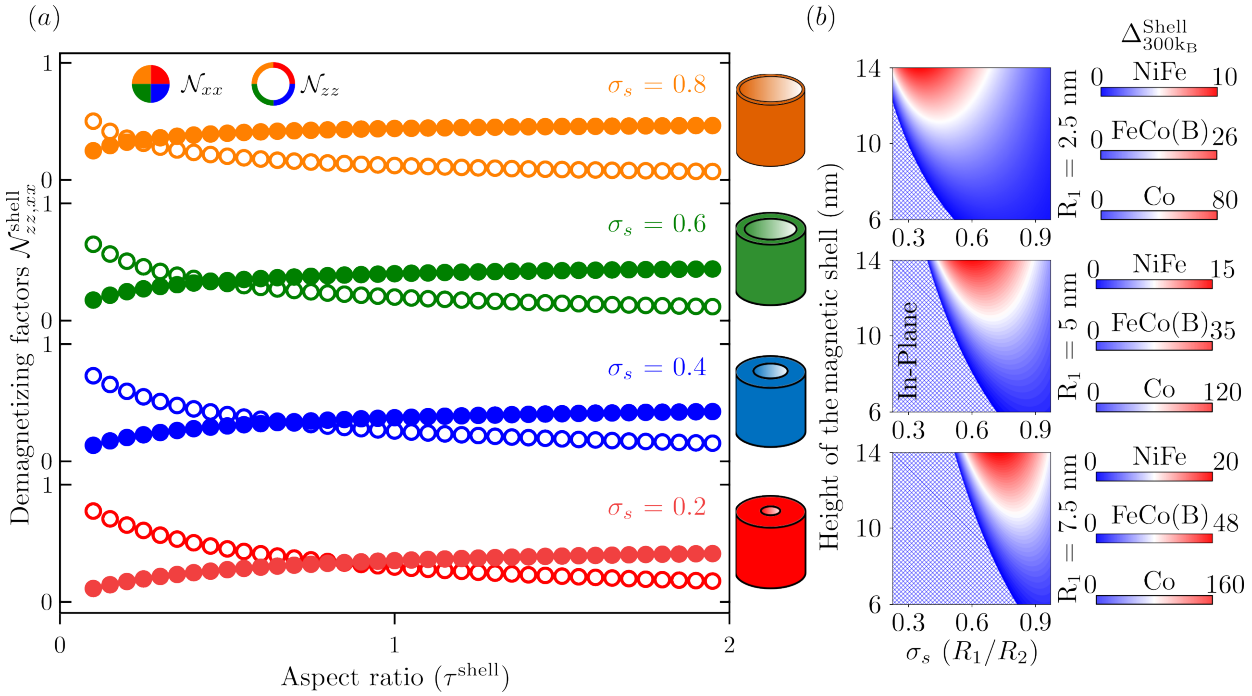


Figure 5.2: ($a$) Demagnetising factors $\mathcal{N}_{xx}$ (filled disks) and $\mathcal{N}_{zz}$ (open disks) for the magnetic shell as a function of the vertical aspect-ratio $\tau^{\text{shell}}$ for different for different values of $\sigma_s$ and ($b$) stability factor of the shell as a function of the shell thickness ratio $\sigma_s$ and aspect-ratio $\tau^{\text{shell}}$ for three different inner radius $R_1$ values for the situation of Ni (0.489 MA/m), NiFe (0.756 MA/m) and Co 1.446 MA/m. The cross-patterned region shows the in-plane orientation of the magnetization.

around $\tau \approx 0.89$. For $\sigma_s \to 1$ the situation is that of a thin shell. The cross-over to a perpendicular easy axis is shifted towards lower vertical aspect ratios. This make sense as asymptotically the situation is that of a rolled thin films, for which the cylinder axis in-the-plane for the film [180]

The thermal stability of a shell with perpendicular easy axis stems from the product of the volume of the shell with the difference of its demagnetizing coefficients $\frac{1}{2}\mu_0 M_s^2 V_s(\mathcal{N}_{xx}^{\text{shell}} - \mathcal{N}_{zz}^{\text{shell}})$. This is shown in Figure 5.2 ($b$) versus the height of the magnetic shell and $\sigma_s$, for different radius of the inner shell. Consistent with Figure 5.2 ($a$), perpendicular anisotropy is promoted by a high aspect ratio and a small thickness of the shell ($\sigma_s \to 1$). In these diagrams, we clearly see that in the case of perpendicular anisotropy, the regions with highest stability are those for a reasonably-thick shell (lower $\sigma$), which comes with a large volume and therefore a large energy barrier. Also, as is the case with standard PSA pillars, the perpendicular stability scales with $\propto M_s^2$, as shown by the color scale for different magnetic materials in the shell, NiFe, FeCo(B) and Co.

## 5.2 Magnetostatic coupling in a core-shell structure and stability increase

We now consider both a core and a shell in dipolar interaction as a composite object, to evaluate how the several geometrical parameters can be best tuned to enhance the stability of this system. In addition to $R_1$, $R_2$ and $L$ already described, we introduce $R_0 < R_1$ as the radius of the core

cylinder, with the shape amplitude function defined in Section 2:

$$\mathcal{D}_{\text{core}}(k_\perp, k_z) = \frac{4\pi}{k_\perp k_z}\left[R_0^2 \mathcal{J}_1^2(k_\perp R_0)\right] \sin^2(dk_z). \tag{70}$$

Similarly to the approach used to calculate the magnetostatic energy of a single magnetic element, the magnetostatic coupling between two different magnetic bodies is given by the interaction between the shape amplitude of the two bodies [178]:

$$E_{\text{dipolar}} = \frac{\mu_0 M_{\text{core}} M_{\text{shell}}}{8\pi^3} \int \frac{\mathrm{d}\mathbf{k}}{k^2} D_{\text{core}}(\mathbf{k}) D_{\text{shell}}(\mathbf{k})(\mathbf{m}_1 \cdot \mathbf{k})(\mathbf{m}_2 \cdot \mathbf{k}), \tag{71}$$

where $D_{\text{core}}$ and $D_{\text{shell}}$ are defined by equations 70 and 66, respectively with $\mathbf{m}_1$ and $\mathbf{m}_2$ the magnetization orientation vector of the core and shell, respectively. Equation 71 can be formally simplified to:

$$E_{\text{dipolar}} \times f(\theta_1, \theta_2, \phi_1, \theta_1) = \pi \mu_0 M_{\text{core}} M_{\text{shell}} R_0 \left[2\cos\theta_1 \cos\theta_2 - \sin\theta_1 \sin\theta_2 \cos(\phi_1 - \phi_2)\right] \mathcal{J}_{cs}\ , \tag{72}$$

where $\mathcal{J}_{cs}$ is a geometrical scaling factor related to the magnetostatic coupling between the core and the shell and $f(\theta_1, \theta_2, \phi_1, \theta_1)$ the associated angular dependence.

Table 4: Angular dependence $f(\theta_1, \theta_2, \phi_1, \phi_2)$ of the dipolar coupling between a core and a shell for selected sets of angles $\theta_1$ and $\theta_2$, with $\phi_1 \equiv \phi_2[\pi]$. For perpendicular magnetization energy maxima are shown with a darker blue background and minima with light blue color. In-plane magnetization energy values are shown with green color (light for minimum and darker for maximum). Crossed situations always have zero energy.

| $\theta_2$ \ $\theta_1$ | $0$ | $\frac{\pi}{2}$ | $\pi$ | $\frac{3\pi}{2}$ | $2\pi$ |
|---|---|---|---|---|---|
| $0$ | 2<br>↑ ↑ ↑ | 0<br>↑ → ↑ | -2<br>↑ ↓ ↑ | 0<br>↑ ← ↑ | 2<br>↑ ↑ ↑ |
| $\frac{\pi}{2}$ | 0<br>→ ↑ → | -1<br>→ → → | 0<br>→ ↓ → | 1<br>→ ← → | 0<br>→ ↑ → |
| $\pi$ | -2<br>↓ ↑ ↓ | 0<br>↓ → ↓ | 2<br>↓ ↓ ↓ | 0<br>↓ ← ↓ | -2<br>↓ ↑ ↓ |
| $\frac{3\pi}{2}$ | 0<br>← ↑ ← | 1<br>← → ← | 0<br>← ↓ ← | -1<br>← ← ← | 0<br>← ↑ ← |
| $2\pi$ | 2<br>↑ ↑ ↑ | 0<br>↑ → ↑ | -2<br>↑ ↓ ↑ | 0<br>↑ ← ↑ | 2<br>↑ ↑ ↑ |

As $(\phi_1, \phi_2)$ are in the range $[0 - \pi]$, any non-zero value of $\phi_1 - \phi_2$ leads to an increase of dipolar energy. Consequently, in the following we assume $\phi_1 = \phi_2 = 0$, *i.e.*, the two macrospins are in the same plane with parallel in-plane components. Table 4 shows the dependence of the angular component ($f(\theta_1, \theta_2, \phi_1, \theta_1)$) of Equation 72 as a function of the magnetic core angle $\theta_1$ and magnetic shell angle $\theta_2$. Here, only 5 different orientations of the angles are examined, giving us a basic understanding of the maximum and minimum of the dipolar coupling. It is observed that maximums of energy are given when both core (central arrows in table 4) and shell (lateral arrows in table 4) are vertically aligned to each other. Indeed, in this situation, the dipolar field from each

magnetic body would be opposite to each other, so that this is the most unfavorable situation, with an energy $2E_{\text{Dipolar}}$. Opposed to this situation is the case when the magnetic layers are vertically antiparallel to each other. In this case, there is a negative energy $-2E_{\text{Dipolar}}$. Situations with mixed perpendicular/in-plane magnetization of the shell and core have zero net coupling energy, as can be seen from equation (72). This stems from the fact that the coupling matrix is diagonal for this high-symmetry case. Finally, in case of in-plane magnetization ($\theta_1 = \theta_2$), alignment of the magnetization vectors are preferred with a negative energy $-E_{\text{Dipolar}}$. Opposite in-plane magnetization (formally, for $\phi_2 = \phi_1 + \pi$) comes with a cost $E_{\text{Dipolar}}$. This legitimates our focusing on the situation $\phi_2 = \phi_1$. In particular, if the two magnetization rotate simultaneously between the two absolute minima of energy $-2E_{Dipolar}$, they would tend to rotate in-phase ($\phi_2 = \phi_1$ and $\theta_2 = \pi - \theta_2$). Note the $2:1$ ratio of dipolar coupling energy between the axial and two transverse directions. This relationship arises from the high symmetry of the situation, however would not be valid for the dipolar coupling of an arbitrary set of two bodies.

Let us now be quantitative, and calculate the numerical value for the dipolar energy written in Equation 72. Compared with earlier work [178], here we expand the modeling to the case in which the core is not in contact with the magnetic shell ($R_0 < R_1$):

$$\mathcal{J}_{sc} = \int_0^{+\infty} \frac{\mathrm{d}k_\perp}{k_\perp^2} \Big[ R_2 \mathcal{J}_1(k_\perp R_2)\mathcal{J}_1(k_\perp R_0) - R_1 \mathcal{J}_1(k_\perp R_1)\mathcal{J}_1(k_\perp R_0) \Big] \left(1 - e^{-k_\perp t}\right) \tag{73}$$

Making use of the notations $q_i = kR_i$, $\sigma_i = R_0/R_i$ and $\tau_i = L/2R_i$ (where $i$ is related to the inner radius $R_1$ and outer radius $R_2$), this can be rewritten as:

$$\frac{\mathcal{J}_{sc}}{R_0^2} = \int_0^{+\infty} \frac{\mathrm{d}q_2}{\sigma_2^2 q_2^2} \mathcal{J}(q_2)\mathcal{J}(\sigma_2 q_2) \left(1 - e^{-2q_2\tau_2}\right) - \int_0^{+\infty} \frac{\mathrm{d}q_1}{\sigma_1^2 q_1^2} \mathcal{J}(q_1)\mathcal{J}(\sigma_1 q_1) \left(1 - e^{-2q_1\tau_1}\right). \tag{74}$$

Making use of the last results from equations 68 and 69, it is possible to write:

$$\frac{\mathcal{J}_{sc}}{R_0^2} = \frac{1}{\sigma_2^2} \Big[ \sigma_2 F_0(\sigma_2^2) + A_{1,1}^{-1}(2\tau_2, 1, \sigma_2) \Big] - \frac{1}{\sigma_1^2} \Big[ \sigma_1 F_0(\sigma_1^2) + A_{1,1}^{-1}(2\tau_1, 1, \sigma_1) \Big]. \tag{75}$$

In addition, these results can be linked to the demagnetizing factors of the shell and core through Equation 68 [replacing the value of $A_{1,1}^{-1}(2\tau_i, 1, \sigma_i)$]. In the end, the the magnetostatic coupling energy depends on the geometry, and it is proportional to the magnetization of both the shell and the core:

$$E_{\text{Dipolar}} \propto R_0^3 M_{\text{core}} M_{\text{shell}} \times \underbrace{\mathcal{J}_{sc}(\tau_0, \tau_1, \tau_2, \sigma_1, \sigma_2)}_{\text{Geometrical Scaling Factor}}. \tag{76}$$

The dependency of the scaling factor ($\mathcal{J}_{sc}$) versus geometry is shown in Figure 5.3 for different values of core radius $R_0$ and constant ratio $\sigma_2 = 0.5$. Thus, the three plots differ in core radius, separation between the inner shell and core, as well as the ratio between the inner and outer radius of the shell $\sigma_s = R_1/R_2$. It is observed an increase in geometrical scaling factor for thinner separations $R_1 \to R_0$ and larger aspect-ratio. The magnetostatic coupling energy can be further increased through an increase in $R_0$ due to the magnetic volume, or through the increase in magnetization of the shell and magnetic core $M_{\text{core}} M_{\text{shell}}$.

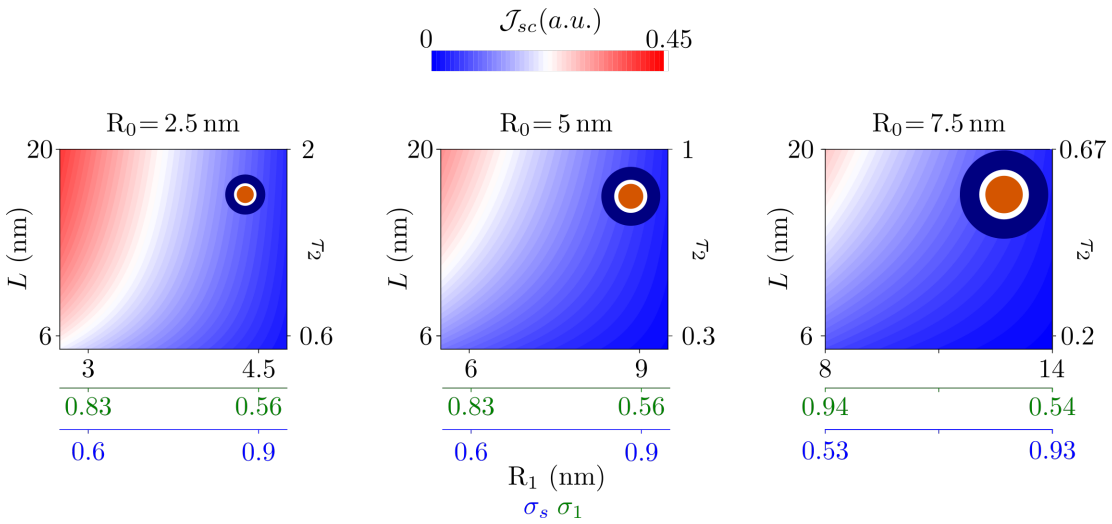


Figure 5.3: Magnitude $\mathcal{J}_{sc}$ of the dipolar coupling between a core and a shell for a fixed value of $\sigma = 0.5$ for different $R_0$, as a function of height $L$ and inner radius $R_1$.

To illustrate a practical case, figure 5.4 shows the dependence of the dipolar coupling energy ($1E_{Dipolar}$) in units of $k_BT$, for a magnetic core with radius $R_0$=5 nm, height of $L = 16$ nm and $R_2 = 13$ nm, with increasing value of the inner radius $R_1$, $M_{\text{core}} = 1$ MA/m and $M_{\text{shell}} = 1.446$ MA/m. As already observed in Figure 5.3, the coupling decreases as the separation between the core and the shell increases. Black open disks stand for the coupling energy calculated with finite-difference micromagnetics, assuming rigid (non-relaxed) magnetization distributions, which validates the analytical model. Note that, if relaxation is allowed, the value of dipolar coupling may be slightly different, however it could not be compared anymore with the macrospin model.

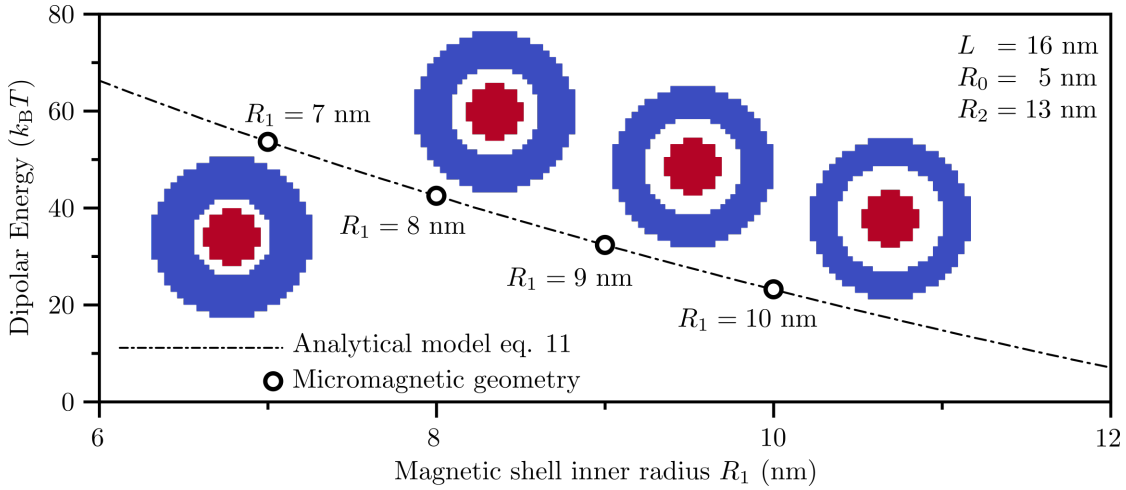


Figure 5.4: Dependence of the dipolar coupling energy (with unit $k_BT$) versus $R_1$ (nm), for a fixed $R_0 = 5$ nm, $R_2 = 13$ nm and $L = 16$ nm with $M_{\text{core}} = 1$ MA/m and $M_{\text{shell}} = 1.446$ MA/m. Micromagnetic results are shown with open black circles and associate micromagnetic geometry displayed, where red represents the magnetic core and blue the magnetic shell.

It is possible to now compute the total energy of the core-shell magnetic system $E_{\text{sys}}$, *i.e.*, considering both the shape self-energy of core and shell, additional anisotropies such as iPMA and their coupling, as calculated in the paragraphs before. The total energy of the system is then

Table 5: (Left) Dependence of the total energy of the system as a function of the the core and shell angles ($\theta_1$, $\theta_2$) without energy shift and (right) with an energy shift of $2\mathcal{C}$.

| $\theta_1$ \ $\theta_2$ | $0$ | $\frac{\pi}{2}$ | $\pi$ |
|---|---|---|---|
| $0$ | $2\mathcal{C}$ | $\mathcal{B}$ | $-2\mathcal{C}$ |
| $\frac{\pi}{2}$ | $\mathcal{A}$ | $\mathcal{A}+\mathcal{B}-\mathcal{C}$ | $\mathcal{A}$ |
| $\pi$ | $-2\mathcal{C}$ | $\mathcal{B}$ | $2\mathcal{C}$ |

| $\theta_1$ \ $\theta_2$ | $0$ | $\frac{\pi}{2}$ | $\pi$ |
|---|---|---|---|
| $0$ | $4\mathcal{C}$ | $\mathcal{B}+2\mathcal{C}$ | $0$ |
| $\frac{\pi}{2}$ | $\mathcal{A}+2\mathcal{C}$ | $\mathcal{A}+\mathcal{B}+\mathcal{C}$ | $\mathcal{A}+2\mathcal{C}$ |
| $\pi$ | $0$ | $\mathcal{B}+2\mathcal{C}$ | $4\mathcal{C}$ |

computed as [178]

$$E_{\text{sys}}(\theta_1,\theta_2) = E_{\text{c}}\sin^2\theta_1 + E_{\text{s}}\sin^2\theta_2 + E_{Dipolar}\left[2\cos\theta_1\cos\theta_2 - \sin\theta_1\sin\theta_2\right] , \tag{77}$$

where $E_{\text{c}}$ is the energy barrier of the isolated magnetic core, $E_{\text{s}}$ is that of the isolated magnetic shell, and $E_{\text{Dipolar}}$ the coupling energy. We can rewrite table 4 considering all these energies. For sake of simplicity and generality, let us introduce the variables $\mathcal{A}$, $\mathcal{B}$, $\mathcal{C}$ and $\mathcal{D}$ for the different angular dependencies on $\theta_1$ and $\theta_2$. This generalization opens the door to consider lower-symmetry cases from the coupling, or other coupling terms, such as RKKY coupling. In this framework we have:

$$\varepsilon_{\text{core-shell}} = \mathcal{A}\sin^2\theta_1 + \mathcal{B}\sin^2\theta_2 - \mathcal{C}\sin\theta_1\sin\theta_2 + \mathcal{D}\cos\theta_1\cos\theta_2 , \tag{78}$$

where $\mathcal{A}$ is the self energy of the magnetic core, $\mathcal{B}$ the self energy of the magnetic shell, $\mathcal{C} = E_{Dipolar}$ and $\mathcal{D} = 2C$ in the present situation. Additional anisotropies, such as iPMA are added in coefficient $\mathcal{A}$. Like previously we restrict the discussion to $\phi_2 = \phi_1$, which yields table 5.

When discussing energy reversal paths, it is convenient to shift all energies by $2\mathcal{C}$, so that the minimum energy state $\varepsilon_{\text{total}}^{[0,\pi]}$ and $\varepsilon_{\text{total}}^{[\pi,0]}$ are zero. Making use of table 5, we can discuss which mechanisms of magnetization reversal to expect in limiting cases, although we consider only a handful of sets of angles. As an example, we compute the coefficients for a system with a magnetic core with $R_0 = 7\,\text{nm}$, iPMA of $1.4\,\text{mJ/m}^2$ and $M_{\text{core}} = 1\,\text{MA/m}$; and magnetic shell with $M_{\text{shell}} = 1.446\,\text{MA/m}$, $R_1 = 8\,\text{nm}$ and $R_2 = 10\,\text{nm}$. The height of the system is increase from 6 nm to 12 nm. These are shown in table 6.

Table 6: Coefficients of the energy of the magnetic system in units of $k_BT$ for different heights and fixed core-shell radius of $R_0 = 7\,\text{nm}$, $R_1 = 8\,\text{nm}$ and $R_2 = 10\,\text{nm}$.

| **Height (nm)** | $\mathcal{A}$ **($k_BT$)** | $\mathcal{B}$ **($k_BT$)** | $\mathcal{C}$ **($k_BT$)** |
|---|---|---|---|
| **6** | 15 | 17 | 19 |
| **8** | 22 | 43 | 25 |
| **10** | 30 | 72 | 32 |
| **12** | 42 | 100 | 35 |

From this table, we can observe that the increase in $\mathcal{B}$ with the increase in height is much larger than for $\mathcal{A}$, showing the high stability of this thin magnetic shell. The coefficient $\mathcal{C}$ seems to increase at a rate similar to that of $\mathcal{A}$, which will increase substantially the stability of the system. For comparison, we now make use of table 5 to predict the preferred energy reversal path of these core-shell system with different height (Figure 5.5 (*a*)). This is done with support from the MEP

calculated through the macrospin model (the micromagnetic simulations give similar results but with a slight different magnitude regarding the dipolar coupling, as expected from the edge effects) which will bring support to our prediction, and shown in figure 5.5 (*b*) as a function of the relative orientation $(\theta_1 - \theta_2)$.

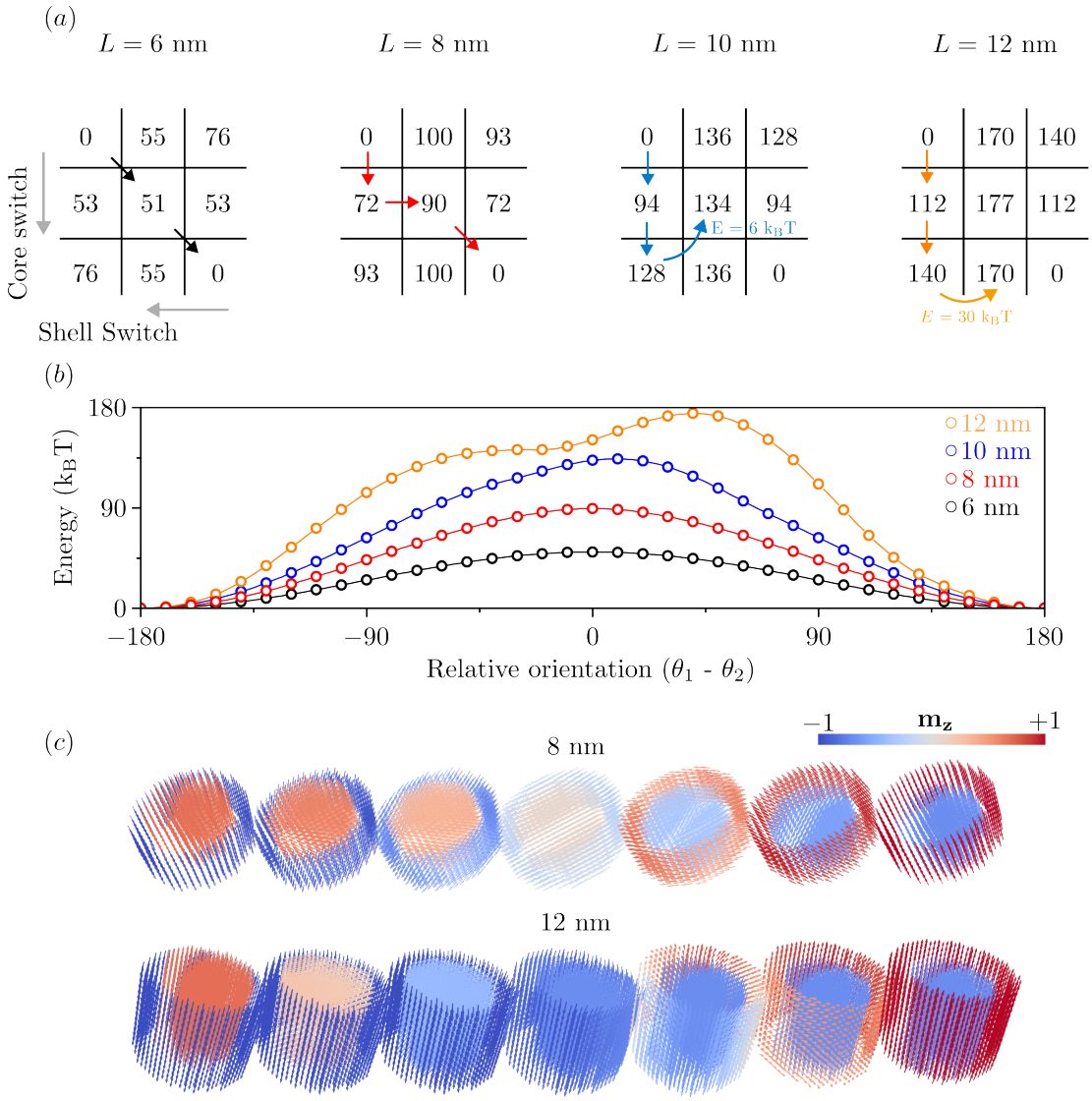


Figure 5.5: (*a*) Reversal path for different heights of the coupled system for the set of angles $\theta_1$ and $\theta_2$. The arrows show the path that brings the minimum energy. (*b*) Macrospin minimum energy path of the system as a function of the relative orientation ($\theta_1$-$\theta_2$) for different heights of the core-shell system and (*c*) associated micromagnetic time frames of the minimum energy path for the heights of 8 nm and 12 nm, magnitude of the magnetization linked with the colorbar.

Starting with lower height, we can see that the least energetic path occurs when the reversal is simultaneous in both layers. This is seen through the matrix but also through the energy barrier. For this to occur, the energy coupling (or $\mathcal{C}$ in this notation) needs to be larger than both energy barriers of the core and magnetic shell (respectively $\mathcal{A}$ and $\mathcal{B}$), $\mathcal{C} > \mathcal{A}\&\mathcal{B}$. By increasing the height of the system to 8 nm we lose the simultaneous reversal as $\mathcal{C} < \mathcal{B}$. Nevertheless, it is not necessary to fully reverse the core for the magnetic shell to reverse. Indeed, it is observed that both core and shell start reversing roughly at the same time, further confirmed by the micromagnetic frames shown in

Figure 5.5 (*c*). For increasing height of 10 nm, we observe that we are already in a two-step reversal situation ($\mathcal{C} < \mathcal{B}$ & $3\mathcal{C} < \mathcal{A} + \mathcal{B}$). In this situation however, the coupling is not strong enough the reverse the magnetic shell ($2\mathcal{C} < \mathcal{B}$). This is observed from the associated matrix reaching a fully parallel alignment. Thus, to further proceed into the reversal, it is necessary to receive an additional 6 $k_BT$ from external sources, such as temperature. This situation is more drastic for a height of 12 nm where an additional energy of 30 $k_BT$ is necessary to fully reverse the magnetic shell, supported by the angular dependence of the MEP and the 3D snapshots of Figure 5.5 (*c*).

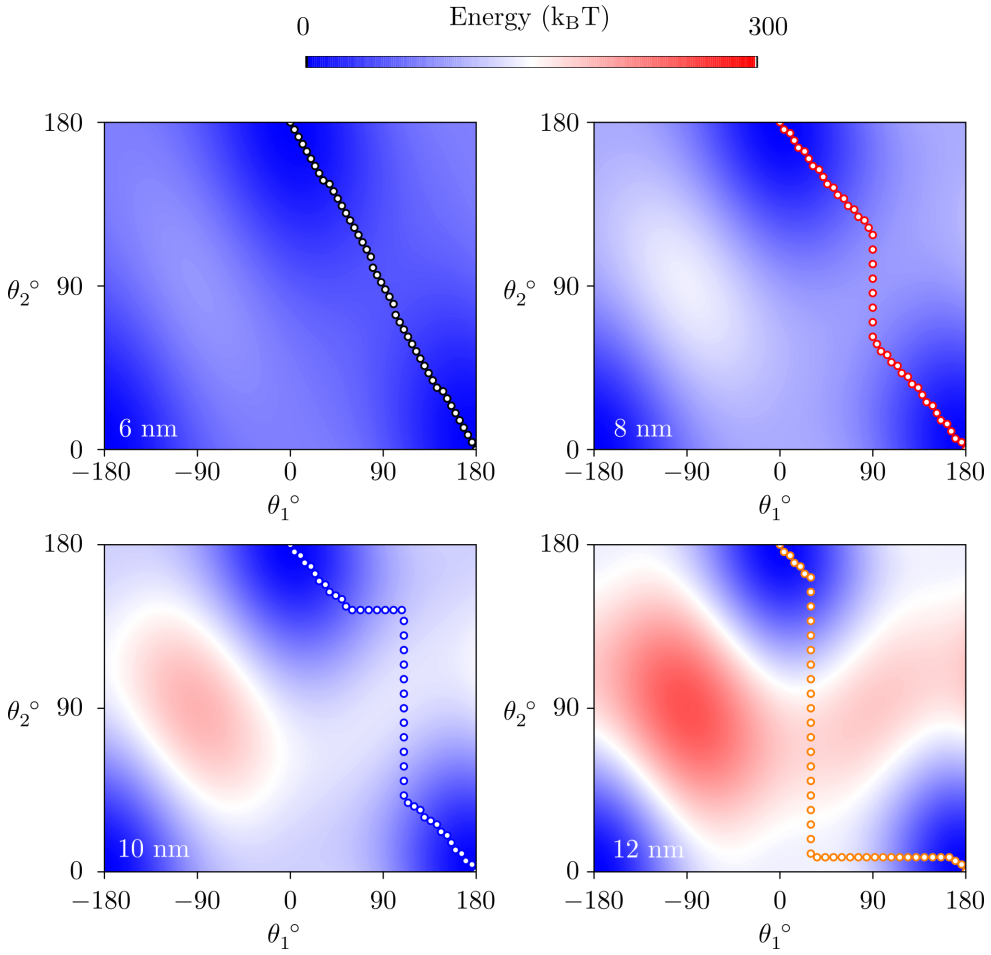


Figure 5.6: Angular dependency of the energy barrier (function of $(\theta_1, \theta_2)$) of the magnetic system for different core-shell height with a fixed core radius of 7 nm, inner shell radius of 8 nm and outer radius 10 nm, $M_{\text{core}} = 1\,\text{MA/m}$ and $M_{\text{shell}} = 1.446\,\text{MA/m}$. The trace of the minimum energy path for each geometry is shown with filled white circles.

At this point, we considered only small angular variations in our matrix. However, the coupling might be large enough for reversal at different angles. For a complete study of the angular dependence and the preferred type of reversal for the magnetic system for different geometries, it is necessary to consider full range of angles, which allows to compute the MEP shown in Figure 5.5. Thus, we consider that the magnetization of the magnetic core can move from $\theta_1 \in [-\pi, \pi]$ and the magnetic shell can move from $\theta_2 \in [0, \pi]$ and plot the total energy values as a colormap, displayed in Figure 5.6. For each vertical aspect ratio, the macrospin minimum energy path is computed [181], and overlapped with the colormap of the angular dependence of the total energy. For all situations, the

state with highest energy is given when both shell and core are in-plane-magnetized and antiparallel to one another. If core and shell have both in-plane magnetization, then the state with lowest energy is when both are aligned parallel, consistent with our consideration that $\phi_2 = \phi_1$. Similarly, the lowest-energy state is given when both shell and core are out-of-plane-magnetized and antiparallel one to one another. The computation for height 6 nm confirm that if the coupling between shell and core is comparable or larger than the shape anisotropy of each element taken separately, both parts rotate simultaneously to minimize the dipolar coupling, highlighted by a line with slope $-1$. On the reverse and again as expected, for weak coupling the two parts reverse sequentially to minimize the maximum energy barrier during reversal. This is clearly the case occurring for the 12 nm-height system. The heights 8 nm and 10 nm illustrate the cross-over situation, with a combination of sequential and coupled paths, as discussed before.

In practice, we identify two criteria to meet in a device, for which one may wish to optimize the set of parameters $\mathcal{A}$, $\mathcal{B}$ and $\mathcal{C}$. The first criteria derives from the fact that the core is electrically connected, but not the magnetic shell. As a consequence, STT would be the driving force to switch the core into the desired final state, while the shell should reverse its magnetization under the sole stimulus of the dipolar coupling with the core. In this context, the situation of weak coupling is not favorable (compared with the anisotropy of the shell considered alone), such as is the case for $L =$ 10 nm and 12 nm. Although for 10 nm, the small energy barrier required the switch the magnetic shell might be provided by thermal fluctuations, the timescale of this event might not be adequate for the purpose of our device. In a general situation and, for the most extreme situation (core switch until parallel alignment), it is necessary that $2\mathcal{C} > \mathcal{B}$, for a reversal of the shell based on dipolar coupling. The second criteria comes along with thermal excitation. In the examples given, the shell has a stability larger than that of the magnetic core, so the preferred path for thermal reversal is similar to the one promoted by STT. However, if the magnetic shell has a stability lower than the core, then it might switch by thermal noise, lowering the stability of the system. It is important to realise that these events also depend on relaxation times. Let us imagine that we have a system in which the magnetic shell has a stability lower than that of the core. If a thermal fluctuation reverses the shell to a fully parallel configuration, we now have a decrease in stability of the system. In this moment, the shell might reverse back to minimize energy, but the core might also reverse the opposite way to minimize energy. The later is dependent on the coupling but also on which one would reverse faster, the magnetic shell, or the magnetic core. Here, we expect the damping to play an important role and, due to this, we study its impact in the reversal dynamics of the system.

## 5.3 Switching time improvement making use of the core-shell geometry

We now proceed to characterizing the switching dynamics of the coupled core-shell system, using the micromagnetic solver introduced in Section 2. We intend to account for current-driven excitation via an MTJ in the core only, processional and possibly non-macrospin effects.

We consider hereafter that the core and thus the interface with MgO is made of a FeCo(B) alloy, with spontaneous magnetization $M_s = 1\,\mathrm{MA/m}$, exchange stiffness $A_{ex} = 15\,\mathrm{pJ/m}$, and a damping value of $\alpha = 0.01$, STT pre-factor $a_0 = 140\,\mathrm{mT/V}$ considering a typical TMR value of 100% and a R×A product of $1.5\,\Omega \cdot \mu\mathrm{m}^2$. The voltage is only applied at one of the flat interfaces of the magnetic core, so that the dynamics of the magnetic shell may only result from its dipolar interaction with the core. Surface anisotropy promoting perpendicular magnetization is considered to be present only at the interface between the core and the tunnel barrier, with a value of $1.4\,\mathrm{mJ/m}^2$.

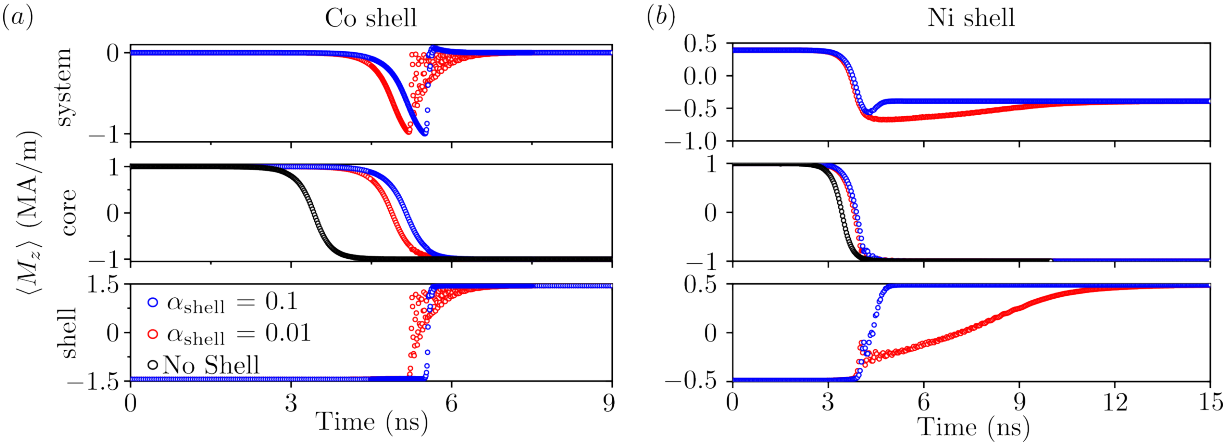


Figure 5.7: Time traces of the total (top row), core (middle row) and shell (bottom row) vertical mean magnetization $\langle m_z \rangle$ for a core-shell system with $R_0 = 7\,\mathrm{nm}$, $R_1 = 8\,\mathrm{nm}$, $R_2 = 10\,\mathrm{nm}$ and a height $L = 8\,\mathrm{nm}$, for a voltage of $-1\,\mathrm{V}$ applied to the core with magnetization saturation of $1\,\mathrm{MA/m}$, and two different damping parameters. Black open circles show the case of the isolated core without shell, blue open circles the situation for a magnetic shell with a damping parameter of 0.1 and red open circles with a damping parameter of 0.01. We consider two materials for the shell: $(a)$ Co with spontaneous magnetization $1.446\,\mathrm{MA/m}$, making a system with $A = 22\,\mathrm{k_BT}$, $B = 43\,\mathrm{k_BT}$ and $C = 25\,\mathrm{k_BT}$ $(b)$ Ni with spontaneous magnetization $0.489\,\mathrm{MA/m}$making a system with$A = 22\,\mathrm{k_BT}$, $B = 5\,\mathrm{k_BT}$ and $C = 9\,\mathrm{k_BT}$. Note the different time scales in the two columns.

We considered first the system presented in Figure 5.5, chosen such that the stability determined from the minimum energy path is around $80\,\mathrm{k_BT}$. It has a length of $8\,\mathrm{nm}$ , $R_0 = 7\,\mathrm{nm}$, $R_1 = 8\,\mathrm{nm}$ and $R_2 = 10\,\mathrm{nm}$. In a first instance we consider a magnetic shell of Co, with damping either $\alpha = 0.01$ or $\alpha = 0.1$. The time traces of the mean perpendicular magnetization components of the core, shell and full system are shown in Figure 5.7. The core clearly switches first, followed later by the shell. The picture for switching is therefore clearly different from simple energetic consideration (figures 5.5 and 5.6), which we understand as the dynamics of the core is driven directly by STT, while that of the shell is driven indirectly by dipolar coupling with the core. The incubation time for switching is somewhat longer with a shell than for an isolated core, which we understand as resulting from the stabilization of the core by the coupling to the shell. The delay is slightly increased for higher damping in the shell, which hints at a coupled dynamics already at the incubation stage, despite the delay for switching the shell. The coupled dynamics is confirmed by a closer inspection of these initial stages, as shown in Figure 5.8 $(a)$. It is observed that the shell starts tilting slightly, during the switching of the core. When considering the full switching of the shell, a striking effect is that

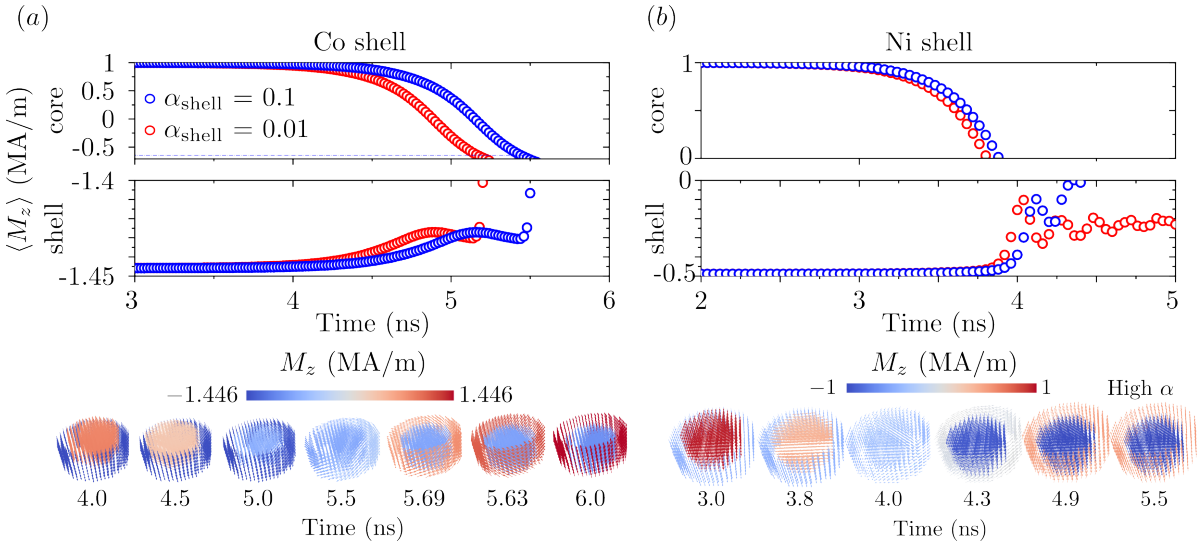


Figure 5.8: (*a*) Zoom of the time traces from Figure 5.7. The top row shows magnetization averaged over the core, while the bottom row shows magnetization of the shell. Note that the time scale is the same in both columns, simply shifted to reflect the different incubation time.

if the damping of the shell is large, then it reaches equilibrium faster although the incubation time is longer. This is explained by the absence of ringing effects, occurring mostly in the low-damping case .

We now consider a shell made of a low magnetization material, considering Ni with spontaneous magnetization of 489 kA/m and exchange stiffness of 8 pJ/m, again for both low and high damping situations (Figure 5.7 (*b*)). As the geometry is unchanged, the moment of the shell no longer compensates the one of the core, resulting in a net moment of the composite element (compare the first row of Figure 5.7). The switching time of the core is shorter than for the Co shell, and it is also barely dependent on the damping parameter of the shell. This is understandable as the lower stray field of the shell has a lower stabilizing effect, and also it is less effective in pumping energy out of the initial oscillations during the incubation time. As concerns the shell, the close examination of the incubation stage also reveals a tilt of magnetization of the shell during the reversal of the core, with a larger angle than for a Co shell. Besides, its full reversal takes longer (Figure 5.7 (*a*)), especially for low damping. Both effects may result from the smaller energy barrier of the magnetic shell (around 5 $k_B T$), so that it is mostly and directly affected by the dipolar coupling with the magnetic core while its own internal field is weak. Micromagnetic snapshots of the switching dynamics for the situations for both magnetic shell compositions are shown for the large damping situation in Figure 5.8. It is observed that, indeed, for the situation of the shell with larger $M_s$, the magnetic core needs to almost fully reverse to have a significant effect in the switching of the magnetic shell. For the situation of low $M_s$, the magnetic shell has already a visible tilt when the magnetic core is in-plane.

This study opens a path to increasing the stability of the vertical aspect-ratio MTJ without additional multilayers along the vertical storage layer. This is accompanied by lower switching voltage and lower switching time of the magnetic core (specially for the situation of a shell with large damping) than it would be situation for isolated magnetic core with larger height. These results

are in accordance with the conclusions obtained in Section 2.4. Indeed, by reducing the height of the system, there is an improvement in the reversal dynamics of the magnetic core. Moreover, these results support the similarity between the nucleation time of the reversal for the magnetic core with and without magnetic shell. As it was already observed, since the height is the same, increase in $\mu_0 H_{eff}^{K}$ of the magnetic core will only play a small role in its nucleation time.

## 5.4 Reduced cross-talk making use of the core-shell concept

We examine here another advantage of the core-shell storage layer, which is the possibility to mitigate the dipolar coupling of neighboring bits in a high dense array. To evaluate the gain quantitatively, we compute the magnetic field emanating from a cylindrical pillar with a formalism based on Fourier Transform, as already described in section II, and implemented in [182]. Knowing that the magnetic field components $H_x, H_y, H_z$ are obtained from the magnetic scalar potential $\varphi_m$ as

$$\overrightarrow{H} = \left( -\frac{\partial \varphi_m}{\partial x}, -\frac{\partial \varphi_m}{\partial y}, -\frac{\partial \varphi_m}{\partial z} \right). \tag{79}$$

The magnetic scalar potential is written as described in section II through

$$\varphi_m = M_s \int_{S1} G(\mathbf{r}_3 - \mathbf{r}_1) d\mathbf{r} - M_s \int_{S2} G(\mathbf{r}_3 - \mathbf{r}_2) d\mathbf{r}, \tag{80}$$

with $S1$ and $S2$ the bottom and top surfaces, respectively, of the magnetic cylinder and, $r$ an arbitrary point in space and $G(\mathbf{r} - \mathbf{r'}) = \frac{1}{4\pi|\mathbf{r}-\mathbf{r'}|}$ is the associated Green's function. It is possible to express this potential in cylindrical coordinates through

$$\varphi_m = M_s \int_0^{R_0} r d\rho \int_0^{2\pi} \rho d\phi \frac{1}{\sqrt{r^2 + (Z-L)^2}} - M \int_0^{R_0} r d\rho \int_0^{2\pi} \rho d\phi \frac{1}{\sqrt{r^2 + (Z)^2}} \tag{81}$$

where $r^2 = R^2 + \rho^2 - 2R\rho\cos(\phi - \Phi)$ is obtained for the cylindrical system, L is the height of the system, $R_0$ the radius of the cylinder and $M_s$ is the spontaneous magnetization. In this representation two different vectors are defined for the subtraction $\mathbf{r} - \mathbf{r'}$, based on $\rho$ and $R$ and the angles $\phi$ and $\Phi$. This integral is calculated for any given value along $Z$ and $r$. Using the Gegenbauer's addition theorem for the Bessel function [182], we can expand the integrand as

$$\frac{\rho}{\sqrt{r^2 + (Z-L)^2}} = \rho \int_0^{\infty} dk e^{-k|Z-L|} \mathcal{J}_0(kr), \tag{82}$$

where $\mathcal{J}_0$ is the first-order Bessel function. Through integration we are then left with

$$\varphi_m = 2\pi R_0 M_s \int_0^{\infty} dk \frac{e^{-k|Z-L|} - e^{-k|Z|}}{k} \mathcal{J}_0(kR) \mathcal{J}_1(kR_0), \tag{83}$$

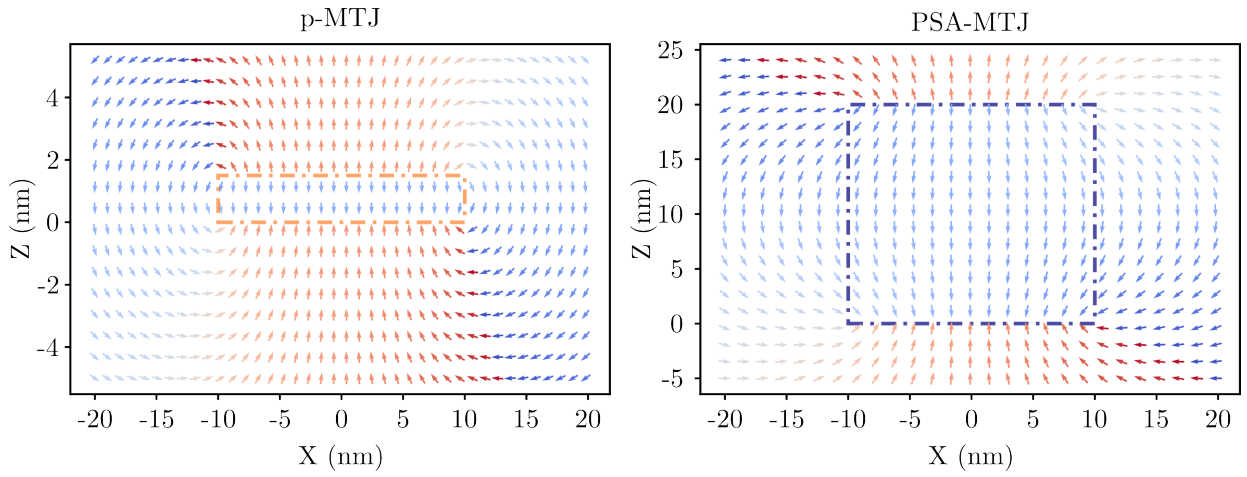


Figure 5.9: 2D orientation of the resulting field from pillars with a base diameter of 20 nm and height of 1.5 nm and 16.5 nm. The color representation of the arrows show the orientation of the magnetic field.

where $R_0$ is the radius of the magnetic cylinder. Using Equation 79, we can then derive the radial ($H_r$) and perpendicular components ($H_z$) of the magnetic field, respectively

$$H_r(r,z) = 2\pi R_0 M_s \int_0^\infty \mathrm{d}k \left[e^{-k|Z-L|} - e^{-k|Z|}\right] \mathcal{J}_1(kr)\mathcal{J}_1(kR_0). \tag{84}$$

and

$$H_z(r,z) = 2\pi R_0 M_s \int_0^\infty \mathrm{d}k \left[\mathrm{sign}(Z-L)e^{-k|Z-L|} - \mathrm{sign}(Z)e^{-k|Z|}\right] \mathcal{J}_0(kr)\mathcal{J}_1(kR_0)\ , \tag{85}$$

where $\mathcal{J}_x$ are the Bessel functions of the order $x$. These equations can be used to calculate both the demagnetizing field (inside the magnetic body $0 < Z < L$ and $r < R_0$ and the stray field outside (for $Z > L$ and $r > |R_0|$). These are displayed in the 2D $xz$ plane in Figure 5.9 for the situation of the perpendicular MTJ with a base diameter of $2R_0 = 20$ nm and height 1.5 nm and for the case of a thick layer with $2R_0 = 20$ nm and height 16.5 nm. The orientation of the resulting field is dependent on $H_x$ and $H_z$. For a perpendicular orientation with magnetization pointing up $+\hat{z}$, we observe that the field in both situations, inside the pillar, is pointing contrary to the orientation of the magnetization, as it is expected of the demagnetizing field. Moreover, we observe that, for the situation of the PSA-MTJ, there is some degree of tilt near the corners of the pillar. This is a known feature at edges and corners in micromagnetic [183, 184], responsible for the flower state observed for thick layers in Section 2. Outside of the magnetic body, for both situations, we observe the typical stray field lines, pointing up from the top surface, parallel to the demagnetizing field at mid height of the pillar and closing at the bottom surface of the pillar.

To study how the magnetic field varies in relation to the geometry of the pillar, we consider a perpendicularly-magnetized cylinder with a fixed base diameter of 10 nm and decreasing the pillar height (for the case of 20, 15 and 10 nm), as shown in Figure 5.10. Here we distinguish the strength and sign of $H_z$ from that of $H_x$. The first striking feature is that, even though the height of the pillar is being substantially reduced, there is no comparatively significant decrease in the stray field. This can be observed for example for the case of $L = 20$ nm and $L = 10$ nm, where the same stray

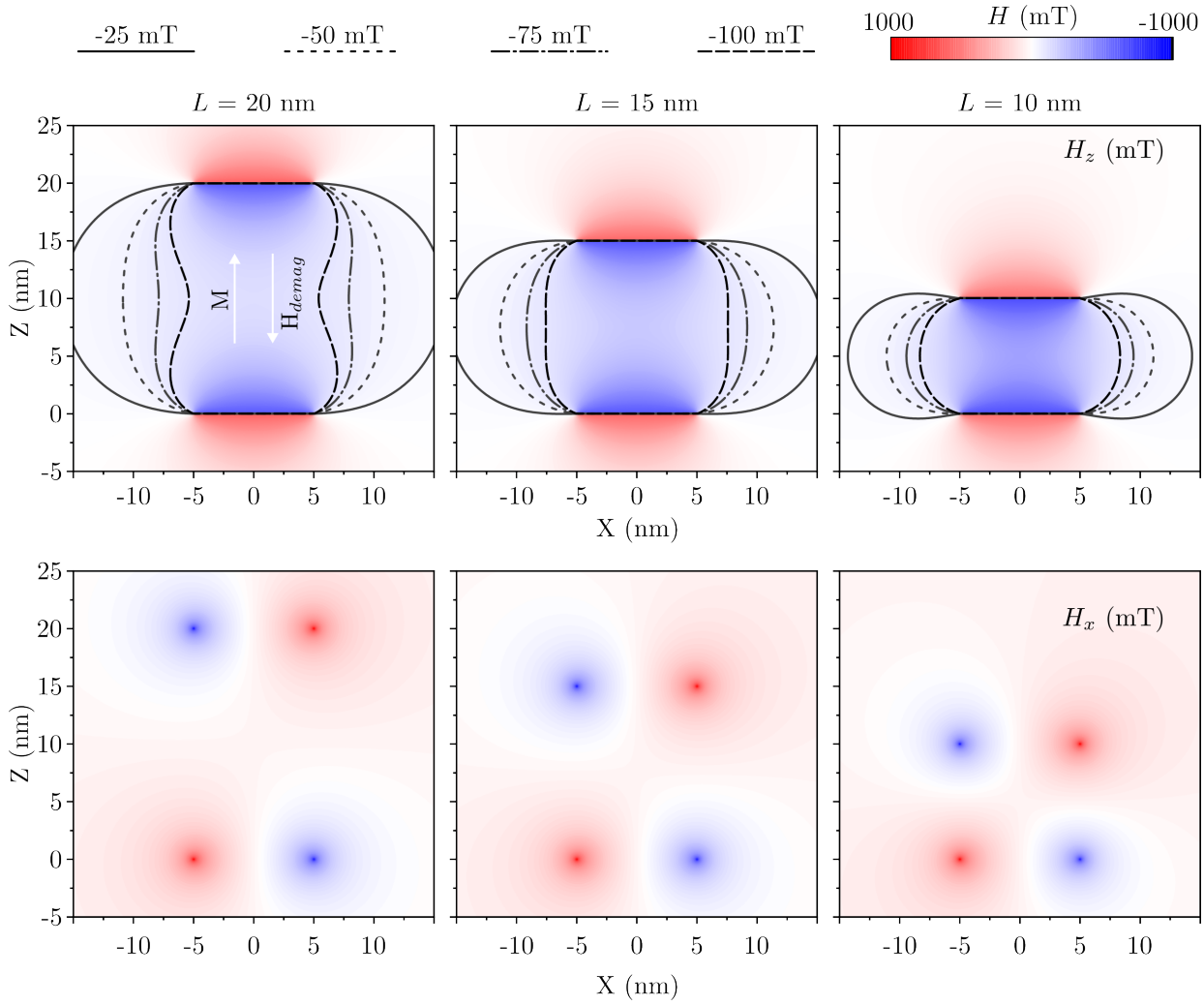


Figure 5.10: Strength of $H_z$ and $H_x$ (mT) for pillars with base diameter 20 nm and different pillar height of 20, 15 and 10 nm for a material with saturation magnetization 1 MA/m.

field magnitude of $-25$ mT has a small shift of 5 nm. Moreover, still from $H_z$, it is observed a larger demagnetizing field for the situation of lower height. Regarding the component of $H_x$, it is observed to be asymmetric along X, which is aligned to the curvature of the stray field lines. Moreover, this values are not varying significantly, as for the situation of $H_z$.

How quantitatively the magnetic stray field is decaying with the distance from the pillar is shown in Figure 5.11 (*b*), displaying the magnetic field strength at mid-height of pillars (for instance, from the example of Figure 5.11 (*a*), for 16.5 nm height) with different aspect ratios, all assumed to have perpendicular magnetization. In the situation of a low aspect ratio (such as the usual p-MTJ with 20 nm diameter and 1.4 nm height), we can observe a thin-film-like demagnetizing field for $r < |R_0|$, with a sharp decay outside the pillar. For thick pillars the demagnetizing field is reduced, but the stray field is greatly enhanced due to the larger volume involved and hence the magnetic moment. Moreover, the decay of this stray field is slower than for the situation of the p-MTJ, being detrimental for dense compact arrays.

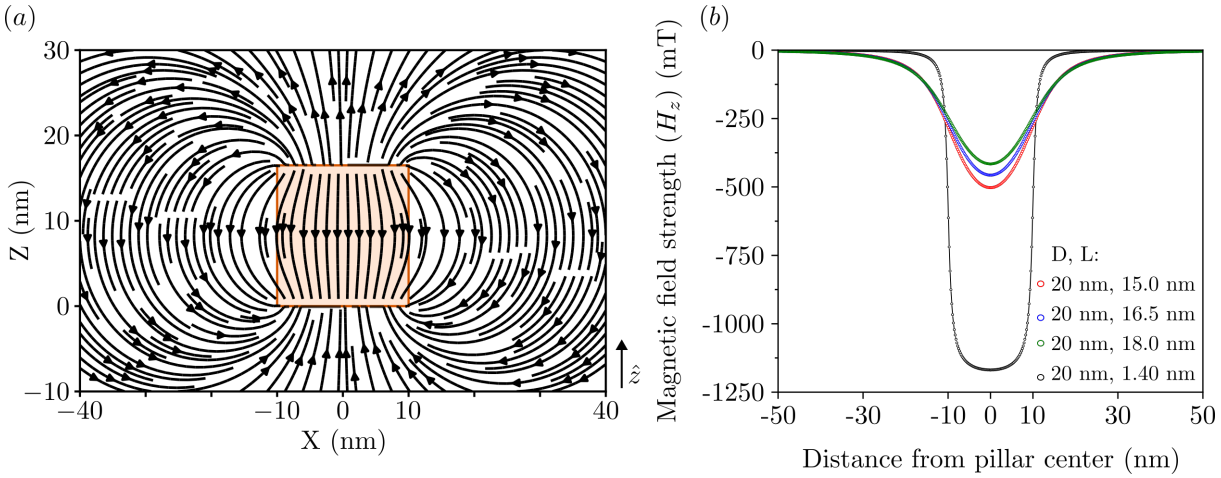


Figure 5.11: ($a$) 2D stray field lines arising from a pillar with high aspect ratio (thickness of 16.5 nm and 20 nm diameter, orange-outlined) with up magnetization along $\hat{z}$. ($b$) magnetic field strength at mid thickness of the magnetic pillar, for 4 different aspect ratios.

Based on the above, we now consider the stray field in a square array of cylinders. As in two dimensions the extension of stray field is short-ranged, typically of the order of the system thickness or so [185], one may evaluate its impact based on a finite-size and $5 \times 5$ array, as depicted in the inset of the Figure 5.12. We define the pitch as the distance between the centers of two adjacent pillars, and thus, when in contact, it equals the pillar diameter. We do not consider the stray field arising from the reference layer below the pillar, as this can be engineered to be negligible. Figure

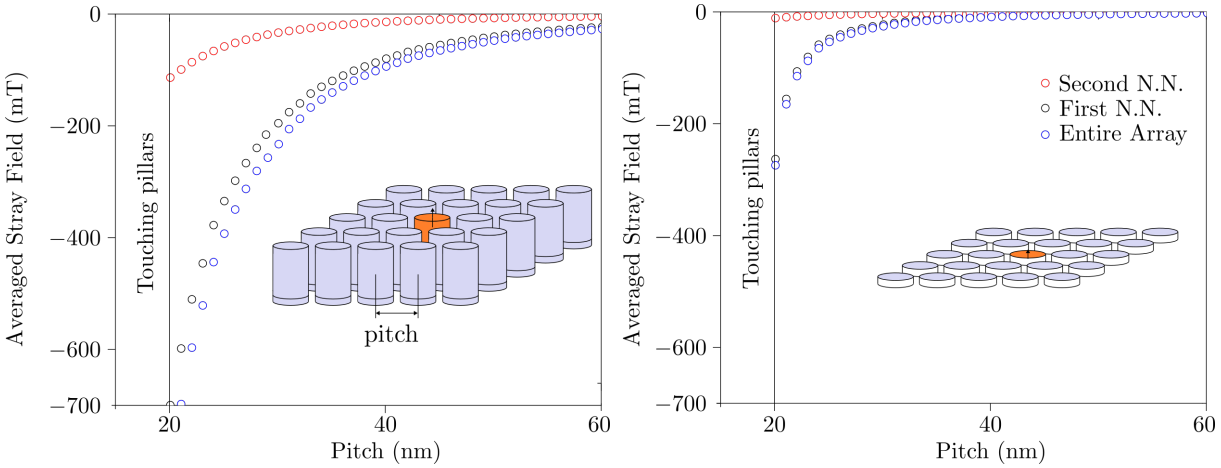


Figure 5.12: Volume-averaged stray field at the central pillar in a $5 \times 5$ array for (left) PSA-MTJs with a diameter of 20 nm and height 16.5 nm and (right) p-MTJs with a diameter of 20 nm and thickness 1.4 nm as a function of the pitch between pillars. The contribution from the first neighbours is shown with black open disks. The contribution of the neighbours is shown with red open disk. The sum of both contributions is shown with open blue disks.

5.12 shows the stray field in an array as a function of its pitch, for pillars of vertical aspect-ratio (14 nm diameter and 8 nm height (left panel), and for cells with a flat aspect ratio (20 nm diameter and 1.4 nm height (right panel), both with spontaneous magnetization of 1 MA/m. These situations correspond, respectively, to PSA-MTJs and p-MTJs. Both panels show the contribution of the first neighbours, the second neighbours, and the total contribution. For p-MTJs, the stray field is

significant for the pillars in contact, but becomes negligible for pitch 50 nm or greater, as standard for usual integration processes [186]. The impact of the second neighbors is insignificant, so considering the impact of the first nearest neighbors is enough [140]. For PSA MTJs, the stray field from the first neighbours is stronger, and that of the second neighbours is non-negligible. The next row of neighbours may be safely ignored thanks to the $1/r^2$ decay of the stray field.

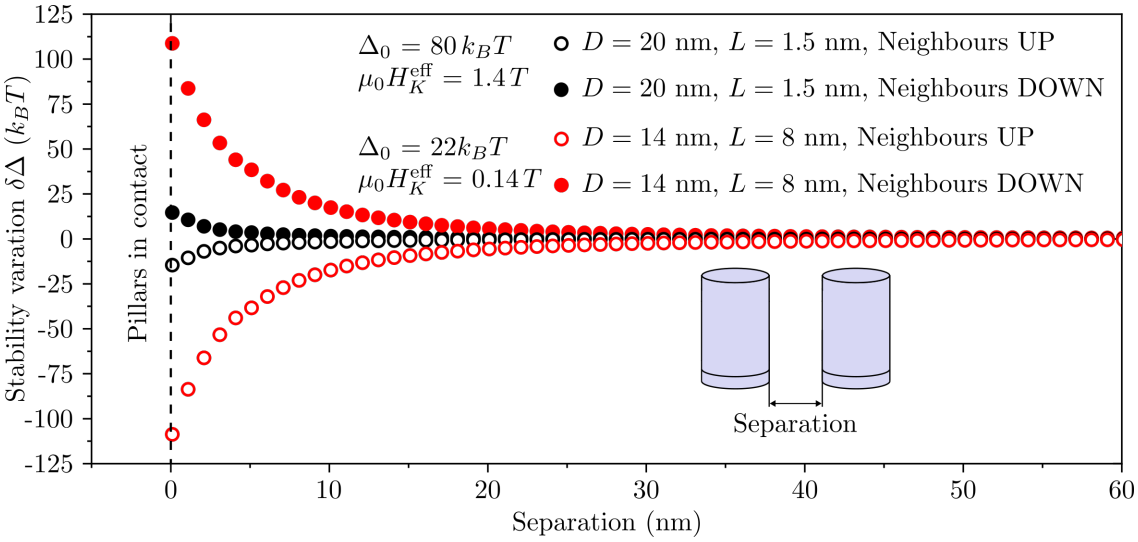


Figure 5.13: Dependency of the variation of the stability factor as a function of the distance between sidewalls of pillars inside a 5x5 array of pillars with (black circles) 20 nm base diameter and 1.5 nm height with an intrinsic stability of 80 $k_BT$ and (red circles) 14 nm base diameter and 8 nm height with an initial stability of 22 $k_BT$. Full circles represent a situation in which all the neighbours have magnetization antiparallel to the main central pillar, and open circles with parallel magnetization to the main central pillar.

The resulting total stray field is significant and is expected to affect the stability factor of the device. It could be increased (reduced) if the average stray field points in the same (opposite) direction as the pillar magnetization [187]:

$$\Delta^{stray}_{k_BT} = \Delta^{0}_{k_BT}\left(1 \pm \frac{H_z^{stray}}{\mu_0 H_{eff}^{K}}\right) , \tag{86}$$

where $\mu_0 H_{eff}^{K}$ is the effective anisotropy field of the magnetic element and $< H_z^{stray} >$ the average perpendicular stray field felt by the pillar. From this equation, one can realize that, through increase of $\mu_0 H_{eff}^{K}$, it is possible to avoid strong relative variations in $\Delta^{stray}_{k_BT}$. For the situation of the PSA-MTJ, in order to reduce its height, it is necessary to increase $\mu_0 H_{eff}^{K}$. This increase will make the device more robust against variations in stability, which are detrimental for the device operation [140]. Nonetheless, as we focus only in the case of a single-layer PSA-MTJ, this increase in $\mu_0 H_{eff}^{K}$ is not straightforward. The variation of the stability ($\delta\Delta = \Delta^{stray}_{k_BT} - \Delta^{0}_{k_BT}$) with the pitch of the array is shown in Figure 5.13, for the situation of the p-MTJ and PSA-MTJ. In the case of an array of p-MTJs it is seen that a pitch around 30 nm (separation plus the device diameter) is sufficient to avoid a significant variation in stability ($\delta\Delta \approx 0$). This is related to the fact that in 2D systems the range of dipolar interactions scales with the height of the system. To the contrary, for PSA-MTJ,

it would be necessary to drastically increase the pitch to 50 nm or more to reach the same level of crosstalk reduction (for instance allowing $\delta\Delta \approx k_B T$). Moreover, it is seen that, for this geometry and stability, for the situation in which the neighbours have magentization parallel to that of the main core, at around a pitch of 25 nm, the stability of the main core is negative, and thus will reverse to an anti-parallel state for a high-enough stray field.

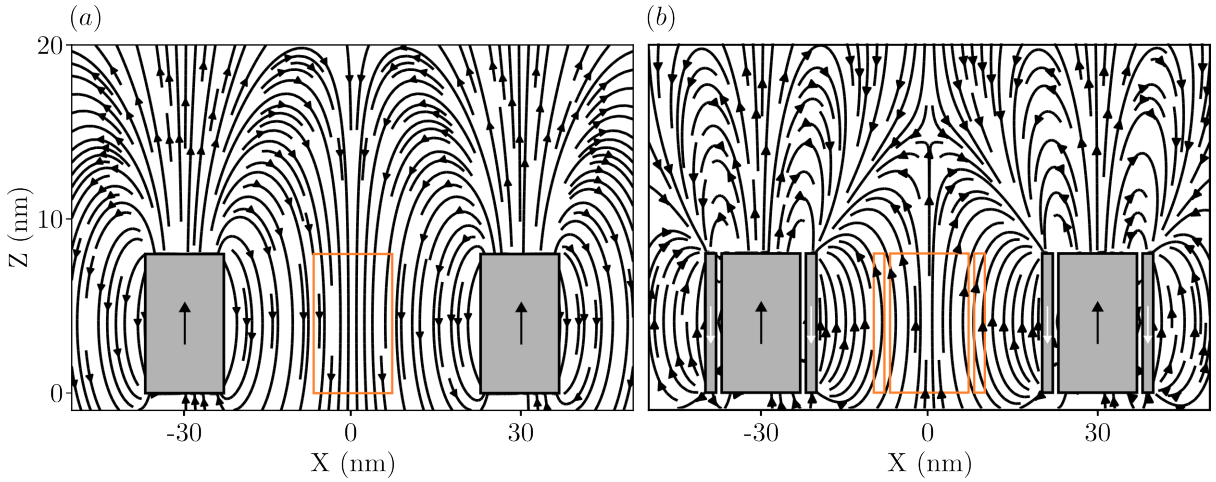


Figure 5.14: 2D stray field lines of ($a$) two magnetic cores with a pitch of 30 nm. Each magnetic core has a diameter of 14 nm and a height of 8 nm and ($b$) two core-shell systems with a pitch of 30 nm. Each system is composed of a magnetic core with a radius of 7 nm, inner radius 8 nm, an outer radius 10 nm, and a height of 8 nm. In both situations, the system is shown with a filled gray color, and the magnetization direction of the core is shown in black, pointing up. For the core-shell situation, the magnetization of the shell is white, pointing down. In both cases, a central element is shown with an orange colour.

We expect that the core-shell design can also contribute to a mitigation of the stray field from the neighboring dots, due to the antiparallel and mostly compensated core and shell magnetic moments. This is illustrated in Figure 5.14, considering the effect of two neighboring cells with center-to-center distance of 30 nm, each with a FeCo(B) core with 14 nm diameter and 8 nm height. The left panel ($a$) shows the case of the simple pillar, while in the right panel ($b$) these are surrounded by a shell of Co with an outer radius of 10 nm The field lines are indeed drastically different in the core-shell system, characteristic of a quadrupolar arrangement, as the core and shell moments are nearly balanced, in contrast with the situation with no magnetic shell, characteristic of a dipolar system.

Figure 5.15 quantitatively shows the volume-averaged dipolar field felt by the core of the central cell in a $5 \times 5$ array, for the case of a core radius of 7 nm with spontaneous magnetization of 1 MA/m, an inner shell radius of 8 nm and a varying outer shell radius from the situation where there is compensation of magnetic volume ($M_c V_c = M_s V_s$, where $V_{c,s}$ is the volume from the core or shell) down to smaller outer radius, with a spontaneous magnetization of 1.446 MA/m. Small variations in the outer radius lead to qualitative variations of the stray field, which, however, always decays much faster with a magnetic shell than without it (open black disks).

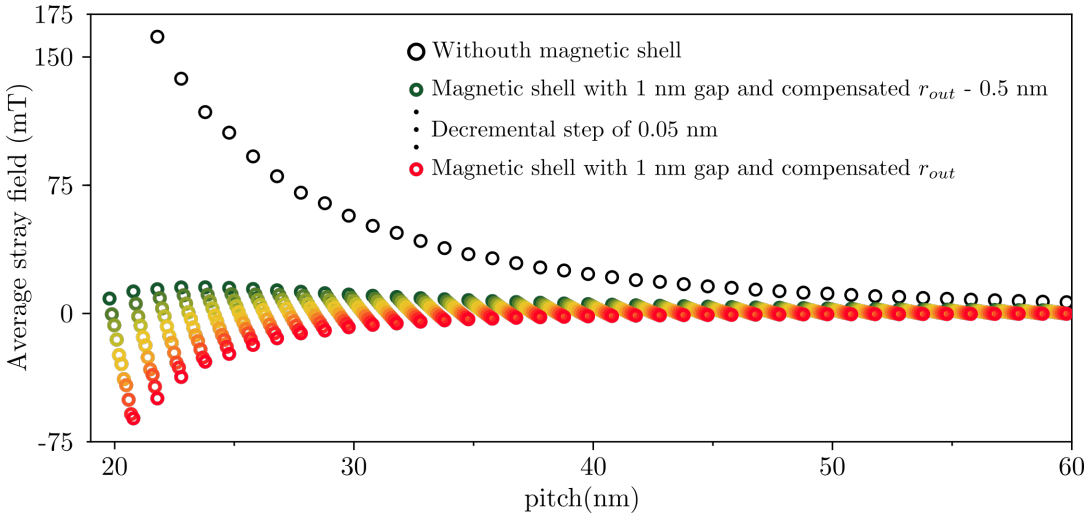


Figure 5.15: Volume averaged stray field felt by a central core in a $5 \times 5$ array. Open back circles is the situation in which none of the pillars with a radius of 7 nm and 8 nm height has a magnetic shell. In red open circles a shell with inner radius of 8 nm is placed. The outer radius is calculated considering compensation of magnetic volume, with a starting value of 9.9 nm (open red circles). Through a decremental reduction of the outer radius (steps of 0.5 nm), a full mitigation can be achieved.

It is observed that, by decreasing the outer radius of the magnetic shell there is a point of full compensation of the resultant stray field. These results show that, through the use of the antiparallel alignment promoted by this core-shell system, we can dramatically reduce the stray field in neighbouring cells, allowing to extend the technology to very dense arrays.

# 6 General Conclusions

The use of a storage layer with vertical aspect-ratio shows promising results for a high stability and high density STT-MRAM at sub-20 nm diameter. However, to be a realistic candidate among all emerging memory technologies, there are still several challenges that need to be addressed, such as the fabrication of low diameter pillars, cross-talk at low pitch and the possible non-uniform reversal at large vertical aspect-ratios. In this dissertation I addressed these obstacles and give proposals on how to solve them.

In **section 2** I make use of a 3D micromagnetic solver, created by Dr. Liliana Buda-Prejbeanu, to study the different mechanism of reversal and switching properties of the PSA-MTJ under applied voltage.

In a first study I analyze the mechanisms of magnetization reversal that can occur depending on the thickness of the magnetic layer. It is observed that, for small vertical aspect ratio $< 1$, a macrospin-like reversal occurs. For larger aspect-ratios, a non-uniform reversal takes place, linked with higher switching voltages and longer switching times. This situation remains when reducing the diameter of the device, as for a practical device the aspect-ratio needs to be continuously increased so that the shape anisotropy maintains a stable perpendicular orientation of the magnetization. Thus, at a certain diameter, to maintain high stability, a non-uniform reversal will occur.

I then compare the switching dynamics of the PSA-MTJ with that of the p-MTJ, for a similar value of stability and diameter. It is observed that the reversal of the p-MTJ is much faster than that of the PSA-MTJ, although the switching voltage appears similar in both cases. Nonetheless, this study is performed for a diameter at which the p-MTJ is still operable. The PSA-MTJ proves itself more important as the diameter is reduced, thanks to its increased stability. Moreover, for DRAM replacement, 20 ns switching times are acceptable, which are in the order of the simulated ones for the PSA-MTJ.

For a given stability factor, the switching time is shown to be improved by reduction of the storage layer height, for instance through the use of a MgO capping for additional iPMA. The switching voltage and the pre-factor $\tau_D$ are also reduced. This indicates that there is another ingredient at play besides the increase in anisotropy field, since the value of the switching voltage should increase with increasing anisotropy field, for a standard macrospin approximation. To discriminate the influence of the anisotropy field I varied the height, anisotropy field and stability. Thus I was able to confirm that the main contributor for the reduction of the switching time is the height of the pillar and not the anisotropy field by itself, as there is less magnetic volume to reverse by STT.

The use of this additional surface anisotropy reaches its limit at around 10 nm diameter and it is necessary to, once again, to increase the height of the pillar, compensating with the perpendicular shape anisotropy. Thus, it is necessary to find alternative ways to further reduce the device height. A possibility is to make use of several MgO laminations, in which the combined effect of the dipolar coupling between layers and the increased iPMA lead to an increase in stability at lower nodes

[87, 106, 120]. However, we would lose the strong tolerance of the stability at increasing operating temperature, as the surface anisotropy has a much stronger dependence with temperature than the magnetization. Additional possibilities rely on the use of alloys with uniaxial anisotropy or materials with larger magnetization saturation. Although there is a large material choice, it is necessary to keep a low damping value for faster STT switching in the storage layer. Thus, at this moment, the choice of MgO laminations is the most direct solution, as the damping remains small. Nonetheless, for automotive applications, the use of the thick layer in the PSA-MTJ seems to be better suited.

In **Section 3** I analyzed, experimentally, the evolution of parameters such as stability and switching current, as a function of the MTJ diameter. I observed that, for a p-MTJ with MgO capping layer, the coercivity is reduced along the reduction in diameter, as had been already shown. An expected result is the transition to a superparamagnetic behaviour of the storage layer. This is of great interest to the emerging field of stochastic computing. I showed, under measurements performed under guidance of Dr. Philippe Talatchian, that it is possible to get a sigmoidal dependence of the dwell times with applied voltage. Although the switching is not particularly fast, it is a first step for a high dense array of stochastic MTJ with an associated very small current needed for reversal. Further studies are necessary to understand how to make this device faster, both fundamentally (understanding of the stochasticity at such small diameters) and through device optimization (for instance, use of lower R×A).

To recover the stability at lower diameters I made use of thicker storage layers, using the concept of PSA-MTJ. It is seen that the coercivity of the layer increases as the diameter is reduced, which is translated to a larger $R_{PP}$. Indeed, such larger resistance brings the switching voltage of our storage layer to values larger than dielectric breakdown of the tunnel barrier. Nonetheless, we were able to switch a device with smaller $R_{PP}$, due to its larger diameter, showing the need to reduce the R×A for the switching of sub-10 nm PSA-MTJ.

In **Section 4** I confront the difficult fabrication of these small diameter devices, aiming at their integration in dense arrays. I suggest two different approaches, both based in the electrodeposition of a metal in pre-patterned nano-vias.

The first study aims to fabricate a device in which the hard-mask is deposited by electrodeposition, performed at Institute Néel (Grenoble, France), under the supervision of Dr. Laurent Cagnon. Here, we replace the need to etch the hard-mask by direct deposition of a metal (in this study, Pt) in pre-patterned vias created by electron beam lithography. After removal of the polymer it is seen that the Pt pillars are standing with a shape that is not easily attained with standard reactive-ion etching. Making use of this initial shape and the fact that the layer is sensitive to ion-beam etching we have a two-fold gain. First I have started with a pillar that already has a very small diameter, so the subsequent trimming is not very agressive, bringing less damage to the MgO and to the shape of the device. Secondly, as the ion-beam etching of the Pt hard-mask happens roughly at the same time as the magnetic multilayers, there is no issue with tilted or fallen pillars (at least in this initial stage) as the entire pillar is etched simultaneously. Although this might bring constraints in the electrical connection to the top electrode, due to the now very small height of the hard-mask, I

was still able to fabricate (at PTA, SPINTEC) 10 nm pillars with relatively high TMR (higher than 100 %) and STT-switching at voltages as low as ± 0.5 V. This demonstrates that electrodeposition, a tool that is rather cheap and can be done at large scale, is a strong contender for high density-MTJ fabrication.

Additional work involves using electrodeposition to deposit part of the thick storage layer, addressed issues with wafer yield. This method allows for creating multilayers within a nano-via (either embedded or written in PMMA), magnetization gradients, and deposition of materials with possible uniaxial anisotropy. Although a direct deposition on the FeCoB|MgO interface is challenging, strategies can be employed to overcome this. One approach involves annealing the MTJ with a metallic capping to prevent oxygen migration that can damage the magnetic properties. Another solution is post-patterning anneal, while the sample is protected by a electrodeposited metallic capping. In both situations, there is an oxidized FeCo(B) layer atop the MTJ, which can prevent STT switching and TMR. To solve this, we can deposit a sacrificial Co layer above the FeCo(B) prior to its oxidation, and further manipulated using electrodeposition. By using a CoPt solution and applied voltage, controlled deposition of individual Co and Pt layers can be achieved, avoiding oxidation of the Co layer. This approach has potential applications for various materials, multilayers, and composition gradients.

In a second study, I make use of the deposition of Co in pre-patterned structures. These differ from the previous study, as I deposit the stack the other way around. This allows us to start with a defined storage layer and avoids the issues of electrodeposition atop of an oxidized layer. Additionally, the shadow effect is smaller in this approach, as a portion of the layer is embedded in what is our substrate. These structures are fabricated in LETI (Grenoble, France) by Dr. Guido Rademaker (BCP deposition), Dr. Khatia Benotmane (Etching of the vias), Dr. Maria Luisa (Co electrodeposition) and Dr. Arnaud Cornélis (CMP after electrodeposition). An intermediate step is done at Fraunhofer (Dresden, Germany), under supervision of Dr. Lukas Gerlich and Dr. Maik Wagner-Reetz. Using these base wafers I performed magnetic and structural characterization. MFM measurements, performed at Institude Néel under assistance of Dr. Olivier Fruchart (SPINTEC), report a strong dipolar coupling between magnetic vias, a result that is supported by electron holography studies done in parallel by Dr. Trevor Almeida and Dr. David Cooper (performed at PFNC). Steps in the full integration of these nano-vias with the MTJ technology are done at PTA, where I validated a different process flow for the use of a common bottom electrode. Although there is no TMR in the measured samples, we hint that it might be an artifact from the CMP process, or possible intermixing at the interface. The latter is a conclusion from EDX characterization performed by Dr. David Cooper on an integrated MTJ device in nano-vias (realised at PFNC).

Further studies are necessary in this study. The most important is to fabricate devices only in the region of the 300 mm with optimal CMP. Moreover, an additional control over the pitch and dimensions of the vias is necessary. By increasing the pitch it is possible to avoid dipolar coupling between vias and, by increasing the diameter, one can be sure to pattern a single top MTJ per via. This would enable us to first validate the integration of a single via with the MTJ and, even though

the diameter might be large, would be a first proof of concept. Additional micromagnetic studies are necessary to understand how the diameter of the FeCo(B) interface, compared to that of the via, plays a role in the stability and STT switching.

Finally, **in Section 5**, to tackle the issue between the limit in stability and the non-uniform reversal for large vertical aspect-ratios, alongside the cross-talk in a high dense array, I make use of analytical and micromagnetic calculations to show that a core-shell structure can achieve a better compromise between stability and switching voltage than usual PSA. I show that by making use of the strong dipolar coupling, we can obtain an antiparallel configuration between core and shell. This increases the stability of the device for a given diameter, allowing to reduce the storage layer height, in turn delaying a non-coherent reversal and reducing the voltage necessary for STT reversal. Moreover, the relaxation of this magnetic shell is faster for increasing damping. Additionally, thanks to the antiparallel configuration, we can mitigate the stray field arising from the thick storage layer. Under certain geometry parameters, I show that the pillars can be as close as the outer radius of the magnetic shell allows, proving it interesting for high density applications.

In practice, a routes for fabrication of this kind of devices, are non non-trivial. Although the concept of core-shell structures is well known, there are no reports of such small features in all of the dimensions. An idea can be the conformal deposition of a magnetic layer after device patterning. However, this needs to be spaced from the MTJ by a very thin dielectric layer. A second approach would be the use of the vias. Here, there is already the deposition of a bilayer, prior to the electrodeposition of our magnetic material, with a shape similar to that of a shell (although with one of the top surfaces covered). For this to work in our device, we would need to be able to clean the bottom of the via, which can be done using, for instance ion beam etching.

In conclusion, the contributions from this dissertation hold promise in advancing high-density STT-MTJ technology across a spectrum of applications. Notably, it gives compelling arguments for the use of a storage layer with vertical aspect-ratio, thanks to its increased stability at reduced nodes and increase tolerance to application temperature. Through the understanding of the micromagnetic reversal dynamics, these devices can be further optimized for faster speed, possibly matching the one of DRAM. Furthermore, the proposal of a core-shell structure is a promising approach for reduced stray fields, a critical aspect for enhanced device performance in high-dense arrays. Beyond memory applications, ultra-small MTJs can extend its application domain to the realms of probabilistic and neuromorphoc computing, driven by their stochastic behaviour. In both high stability and stochastic scenarios, the breakthroughs facilitated by the unconventional deposition techniques brough by electrodeposition, drive the MTJ technology towards ultra-small CDs, necessary for high density arrays.

# References


[1] Steve Lohr. "The Age of Big Data". In: *The New York Times* (2012). URL: https://www.nytimes.com/2012/02/12/sunday-review/big-datas-impact-in-the-world.html.

[2] John Loeffler. *We can't make transistors any smaller, is this the end of Moore's law?* 2022. URL: https://interestingengineering.com/innovation/transistors-moores-law.

[3] Yole Developpment. *Emerging Non-Volatile Memory 2017*. URL: https://pt.slideshare.net/Yole_Developpement/emerging-nonvolatile-memory-2017-report-by-yole-developpement.

[4] Coughlin Associates. *Emerging Memories Ramp Up Report*. Tech. rep. 2019.

[5] Semiconductor Engineering. *Next-Gen Memory Ramping Up*. URL: https://semiengineering.com/next-gen-memory-ramping-up/.

[6] Lam Research. *Tech Brief: Much Ado About Memory*. URL: https://blog.lamresearch.com/tech-brief-much-ado-about-memory/.

[7] Tech Brief: ABCs of New Memory. A Lam Researchl. *Tech Brief: ABCs of New Memory*. URL: https://blog.lamresearch.com/tech-brief-abcs-of-new-memory/.

[8] CYPRESS. *Memories For Embedded Systems - nvSRAM*. URL: https://www.cypress.com/products/nvsram-nonvolatile-sram.

[9] CYPRESS. *F-RAM (Non Volatile Ferroelectric RAM)*. URL: https://www.cypress.com/products/f-ram-nonvolatile-ferroelectric-ram.

[10] M. Trentzsch et al. "A 28nm HKMG super low power embedded NVM technology based on ferroelectric FETs". In: *2016 IEEE International Electron Devices Meeting (IEDM)*. 2016. DOI: 10.1109/iedm.2016.7838397.

[11] N. Xu et al. "A unified physical model of switching behavior in oxide-based RRAM". In: *2008 Symposium on VLSI Technology*. 2008. DOI: 10.1109/vlsit.2008.4588578.

[12] Jeremy Guy. "Evaluation of the performances of scaled CBRAM devices to optimize technological solutions and integration flows". PhD thesis. Université Grenoble Alpes, 2015. URL: https://tel.archives-ouvertes.fr/tel-01325223/document.

[13] Xiangyu Dong, Norman P. Jouppi, and Yuan Xie. "PCRAMsim". In: *Proceedings of the 2009 International Conference on Computer-Aided Design - ICCAD*. 2009. DOI: 10.1145/1687399.1687449.

[14] Wai Cheung Law and Shawn De Wei Wong. "Spin Transfer Torque Magnetoresistive Random Access Memory". In: *Emerging Non-volatile Memory Technologies: Physics, Engineering, and Applications*. Singapore, 2021, pp. 45–102. ISBN: 9789811569128.

[15] Jeongdong Choe. "Recent Technology Insights on STT-MRAM: Structure, Materials, and Process Integration". In: *2023 IEEE International Memory Workshop (IMW)*. 2023, pp. 1–4. DOI: 10.1109/IMW56887.2023.10145822.

[16] Tetsuo Endoh et al. "Recent Progresses in STT-MRAM and SOT-MRAM for Next Generation MRAM". In: 2020, pp. 1–2. DOI: 10.1109/VLSITechnology18217.2020.9265042.

[17] URL: https://www.synopsys.com/designware-ip/technical-bulletin/emram-low-power-advanced-nodes.html.

[18] Karen Heyman. *MRAM Getting More Attention At Smallest Nodes*. 2023. URL: https://semiengineering.com/mram-getting-more-attention-at-smallest-nodes/.

[19] EEWeb. *MRAM Rises in Automotive*. 2023. URL: https://www.eeweb.com/the-rise-of-mram-in-the-automotive-market/.

[20] Tom Coughlin. *$ 20B Emerging Memory Market By 2029*. URL: https://www.forbes.com/sites/tomcoughlin/2019/07/09/20b-emerging-memory-market-by-2029/%5C#795e52f922ef.

[21] i-Micronews. *MRAM: a promising new life after eFlash - An interview with GlobalFoundries*. 2019. URL: https://www.i-micronews.com/mram-a-promising-new-life-after-eflash/.

[22] Igor Žutić, Jaroslav Fabian, and S. Das Sarma. "Spintronics: Fundamentals and applications". In: **76** (2004), pp. 323–410. DOI: 10.1103/RevModPhys.76.323.

[23] Dmytro Apalkov, Bernard Dieny, and J. M. Slaughter. "Magnetoresistive Random Access Memory". In: *Proceedings of the IEEE* **104** (2016), pp. 1796–1830. DOI: 10.1109/jproc.2016.2590142.

[24] M. Julliere. "Tunneling between ferromagnetic films". In: *Physics Letters A* **54** (1975), pp. 225–226. ISSN: 0375-9601. DOI: 10.1016/0375-9601(75)90174-7.

[25] W. H. Butler et al. "Spin-dependent tunneling conductance of Fe|MgO|Fe sandwiches". In: *Physical Review B* **63** (2001), p. 054416. DOI: 10.1103/PhysRevB.63.054416.

[26] J. Mathon and A. Umerski. "Theory of tunneling magnetoresistance of an epitaxial Fe / MgO / Fe(001) junction". In: *Physical Review B* **63** (2001), p. 220403. DOI: 10.1103/PhysRevB.63.220403.

[27] S. Ikeda et al. "Tunnel magnetoresistance of 604% at 300K by suppression of Ta diffusion in CoFeB|MgO|CoFeB pseudo-spin-valves annealed at high temperature". In: *Applied Physics Letters* **93** (2008), p. 082508. DOI: 10.1063/1.2976435.

[28] Bernard Dieny. *Introduction to Magnetic Random-Access Memory*. Wiley-Blackwell, 2017. ISBN: 111900974X.

[29] William Fuller Brown. "Thermal Fluctuations of a Single-Domain Particle". In: *Physical Review* **130** (1963), pp. 1677–1686. DOI: 10.1103/physrev.130.1677.

[30] B.N. Engel et al. "A 4-Mb toggle MRAM based on a novel bit and switching method". In: *IEEE Transactions on Magnetics* **41** (2005), pp. 132–136. DOI: 10.1109/TMAG.2004.840847.

[31] J. J. Sun et al. "Commercialization of 1Gb Standalone Spin-Transfer Torque MRAM". In: *2021 IEEE International Memory Workshop (IMW)*. 2021, pp. 1–4. DOI: 10.1109/IMW51353.2021.9439616.

[32] N. Locatelli, V. Cros, and J. Grollier. "Spin-torque building blocks". In: *Nature Materials* **13** (2013), pp. 11–20. DOI: 10.1038/nmat3823.

[33] N. D. Rizzo et al. "A Fully Functional 64 Mb DDR3 ST-MRAM Built on 90 nm CMOS Technology". In: **49** (2013), pp. 4441–4446. DOI: 10.1109/TMAG.2013.2243133.

[34] S. Ikeda et al. "A perpendicular-anisotropy CoFeB–MgO magnetic tunnel junction". In: *Nature Materials* **9** (2010), pp. 721–724. DOI: 10.1038/nmat2804.

[35] B. Dieny et al. "Opportunities and challenges for spintronics in the microelectronics industry". In: *Nature Electronics* **3** (2020), pp. 446–459. DOI: 10.1038/s41928-020-0461-5.

[36] Viola Krizakova et al. "Spin-orbit torque switching of magnetic tunnel junctions for memory applications". In: *Journal of Magnetism and Magnetic Materials* 562 (2022), p. 169692. DOI: 10.1016/j.jmmm.2022.169692.

[37] Sabpreet Bhatti et al. "Spintronics based random access memory: a review". In: *Materials Today* 20.9 (2017), pp. 530–548. DOI: 10.1016/j.mattod.2017.07.007.

[38] M T Johnson et al. "Magnetic anisotropy in metallic multilayers". In: *Reports on Progress in Physics* **59** (1996), pp. 1409–1458. DOI: 10.1088/0034-4885/59/11/002.

[39] Stephen Blundell. *Magnetism in Condensed Matter*. Oxford University Press, 2001. ISBN: 0198505914.

[40] Bruno Patrick. *Physical origins and theoretical models of magnetic anisotropy*. 1993. URL: http://www1.mpi-halle.mpg.de/~bruno/publis/R_1993_1.pdf.

[41] H. X. Yang et al. "First-principles investigation of the very large perpendicular magnetic anisotropy at Fe|MgO and Co|MgO interfaces". In: *Physical Review B* **84** (2011), p. 054401. DOI: 10.1103/physrevb.84.054401.

[42] S. Baumann et al. "Origin of Perpendicular Magnetic Anisotropy and Large Orbital Moment in Fe Atoms on MgO". In: *Physical Review Letters* **115** (2015), p. 237202. DOI: 10.1103/physrevlett.115.237202.

[43] Amikam Aharoni. *Introduction to the Theory of Ferromagnetism, 2nd edition*. 2001.

[44] D J Craik and R S Tebble. "Magnetic domains". In: *Reports on Progress in Physics* **24** (1961), pp. 116–166. DOI: 10.1088/0034-4885/24/1/304.

[45] J.C. Slonczewski. "Current-driven excitation of magnetic multilayers". In: *Journal of Magnetism and Magnetic Materials* **159** (1996), pp. L1–L7. DOI: 10.1016/0304-8853(96)00062-5.

[46] L. Berger. "Emission of spin waves by a magnetic multilayer traversed by a current". In: *Physical Review B* **54** (1996), pp. 9353–9358. DOI: 10.1103/physrevb.54.9353.

[47] Yiming Huai et al. "Observation of spin-transfer switching in deep submicron-sized and low-resistance magnetic tunnel junctions". In: *Applied Physics Letters* **84** (2004), pp. 3118–3120. DOI: 10.1063/1.1707228.

[48] Amikam Aharoni. "Micromagnetics: past, present and future". In: *Physica B: Condensed Matter* **306** (2001), pp. 1–9. DOI: 10.1016/s0921-4526(01)00954-1.

[49] J. Z. Sun et al. "Spin-torque switching efficiency in CoFeB|MgO based tunnel junctions". In: *Physical Review B* **88** (2013). DOI: 10.1103/physrevb.88.104426.

[50] D. C. Ralph and M. D. Stiles. "Spin transfer torques". In: *Journal of Magnetism and Magnetic Materials* **320** (2008), pp. 1190–1216. DOI: 10.1016/j.jmmm.2007.12.019.

[51] Se-Chung Oh et al. "Bias-voltage dependence of perpendicular spin-transfer torque in asymmetric MgO-based magnetic tunnel junctions". In: *Nature Physics* **5** (2009), pp. 898–902. DOI: 10.1038/nphys1427.

[52] A. A. Timopheev et al. "Respective influence of in-plane and out-of-plane spin-transfer torques in magnetization switching of perpendicular magnetic tunnel junctions". In: *Physical Review B* **92** (2015), p. 104430. DOI: 10.1103/PhysRevB.92.104430.

[53] Z. Li et al. "Perpendicular Spin Torques in Magnetic Tunnel Junctions". In: *Physical Review Letters* **100** (2008), p. 246602. DOI: 10.1103/PhysRevLett.100.246602.

[54] T. Kishi et al. "Lower-current and fast switching of a perpendicular TMR for high speed and high density spin-transfer-torque MRAM". In: *2008 IEEE International Electron Devices Meeting*. 2008. DOI: 10.1109/iedm.2008.4796680.

[55] H. Sato et al. "Perpendicular-anisotropy CoFeB-MgO magnetic tunnel junctions with a MgO / CoFeB / Ta / CoFeB / MgO recording structure". In: *Applied Physics Letters* **101** (2012), p. 022414. DOI: 10.1063/1.4736727.

[56] N. Perrissin et al. "A highly thermally stable sub-20 nm magnetic random-access memory based on perpendicular shape anisotropy". In: *Nanoscale* **10** (2018), pp. 12187–12195. DOI: 10.1039/C8NR01365A.

[57] Nicolas Perrissin et al. "Perpendicular shape anisotropy spin transfer torque-MRAM: Determination of pillar tilt angle from 3D Stoner Wohlfarth astroid analysis". In: *Journal of Physics D: Applied Physics* (2019). DOI: 10.1088/1361-6463/ab4215.

[58] Steven Lequeux et al. "PSA-STT-MRAM solution for extended temperature stability". In: *2021 IEEE International Memory Workshop (IMW)*. 2021, pp. 1–4. DOI: 10.1109/IMW51353.2021.9439609.

[59] S. Lequeux et al. "Thermal robustness of magnetic tunnel junctions with perpendicular shape anisotropy". In: *Nanoscale* **12** (2020), pp. 6378–6384. DOI: 10.1039/C9NR10366J.

[60] N. Caçoilo et al. "Spin-Torque-Triggered Magnetization Reversal in Magnetic Tunnel Junctions with Perpendicular Shape Anisotropy". In: *Physical Review Applied* **16** (2021), p. 024020. DOI: 10.1103/PhysRevApplied.16.024020.

[61] K. Watanabe et al. "Shape anisotropy revisited in single-digit nanometer magnetic tunnel junctions". In: *Nature Communications* **9** (2018), p. 663. DOI: 10.1038/s41467-018-03003-7.

[62] Butsurin Jinnai et al. "Coherent magnetization reversal of a cylindrical nanomagnet in shape-anisotropy magnetic tunnel junctions". In: *Applied Physics Letters* **118** (2021), p. 082404. DOI: 10.1063/5.0043058.

[63] Trevor P. Almeida et al. “Quantitative Visualization of Thermally Enhanced Perpendicular Shape Anisotropy STT-MRAM Nanopillars”. In: *Nano Letters* **22** (2022), pp. 4000–4005. DOI: 10.1021/acs.nanolett.2c00597.

[64] Trevor Almeida et al. “Direct observation of the perpendicular shape anisotropy and thermal stability of STT-MRAM nano-pillars examined by off-axis electron holography”. In: *Microscopy and Microanalysis* **27** (2021), pp. 2170–2172. DOI: 10.1017/S1431927621007819.

[65] Junta Igarashi et al. “Temperature dependence of the energy barrier in X/1X nm shape-anisotropy magnetic tunnel junctions”. In: *Applied Physics Letters* **118** (2021), p. 012409. DOI: 10.1063/5.0029031.

[66] M. Beleggia and M. De Graef. “On the computation of the demagnetization tensor field for an arbitrary particle shape using a Fourier space approach”. In: *Journal of Magnetism and Magnetic Materials* **263** (2003), pp. L1–L9. DOI: 10.1016/S0304-8853(03)00238-5.

[67] Marco Beleggia and Marc De Graef. “General Magnetostatic Shape–Shape Interactions”. In: *Journal of Magnetism and Magnetic Materials* **285** (2005), pp. L1–L10. DOI: 10.1016/j.jmmm.2004.09.004.

[68] S. Tandon et al. “On the computation of the demagnetization tensor for uniformly magnetized particles of arbitrary shape. Part I: Analytical approach”. In: *Journal of Magnetism and Magnetic Materials* **271** (2004), pp. 9–26. DOI: 10.1016/j.jmmm.2003.09.011.

[69] M. Beleggia et al. “Demagnetization factors for elliptic cylinders”. In: *Journal of Physics D: Applied Physics* **38** (2005), p. 3333. DOI: 10.1088/0022-3727/38/18/001.

[70] N. Perrissin et al. “Perpendicular shape anisotropy spin transfer torque-MRAM: determination of pillar tilt angle from 3D Stoner–Wohlfarth astroid analysis”. In: *Journal of Physics D: Applied Physics* **52** (2019), p. 505005. DOI: 10.1088/1361-6463/ab4215.

[71] William Fuller Brown. “Criterion for Uniform Micromagnetization”. In: *Physical Review* **105** (1957), pp. 1479–1482. DOI: 10.1103/PhysRev.105.1479.

[72] Liliana Daniela Buda. “"Developpement d’un code de calcul micromagnétique 2D et 3D : Application à des systèmes réels de types films, plots et fils"”. PhD thesis. 2001. URL: http://www.theses.fr/2001STR13225.

[73] Gavin S. Abo et al. “Definition of Magnetic Exchange Length”. In: *IEEE Transactions on Magnetics* **49** (2013), pp. 4937–4939. DOI: 10.1109/TMAG.2013.2258028.

[74] L. D. Buda et al. “Micromagnetic simulations of magnetisation in circular cobalt dots”. In: *Computational Materials Science* **24** (2002), pp. 181–185. DOI: 10.1016/S0927-0256(02)00184-2.

[75] Michael F. Carilli, Kris T. Delaney, and Glenn H. Fredrickson. “Truncation-based energy weighting string method for efficiently resolving small energy barriers”. In: **143** (2015), p. 054105. DOI: 10.1063/1.4927580.

[76] Gabriel D. Chaves-O’Flynn, A. D. Kent, and D. L. Stein. “Micromagnetic study of magnetization reversal in ferromagnetic nanorings”. In: *Physical Review B* **79** (2009), p. 184421. DOI: 10.1103/PhysRevB.79.184421.

[77] G. D. Chaves-O'Flynn et al. "Stability of $2\pi$ Domain Walls in Ferromagnetic Nanorings". In: *IEEE Transactions on Magnetics* **46** (2010), pp. 2272–2274. DOI: 10.1109/TMAG.2010.2045484.

[78] Gabriel D. Chaves-O'Flynn et al. "Thermal Stability of Magnetic States in Circular Thin-Film Nanomagnets with Large Perpendicular Magnetic Anisotropy". In: *Physical Review Applied* **4** (2015), p. 024010. DOI: 10.1103/PhysRevApplied.4.024010.

[79] Hermann Forster et al. "Energy barrier and effective thermal reversal volume in columnar grains". In: *Journal of Magnetism and Magnetic Materials* **267** (2003), pp. 69–79. DOI: 10.1016/S0304-8853(03)00306-8.

[80] Weinan E, Weiqing Ren, and Eric Vanden-Eijnden. "Energy landscape and thermally activated switching of submicron-sized ferromagnetic elements". In: *Journal of Applied Physics* **93** (2003), pp. 2275–2282. DOI: 10.1063/1.1536737.

[81] M. Chshiev et al. "Analytical description of ballistic spin currents and torques in magnetic tunnel junctions". In: **92** (2015), p. 104422. DOI: 10.1103/PhysRevB.92.104422.

[82] Julie Grollier et al. "Magnetic domain wall motion by spin transfer". In: *Comptes Rendus Physique* **12** (2011), pp. 309–317. DOI: 10.1016/j.crhy.2011.03.007.

[83] Manfred E. Schabes and H. Neal Bertram. "Magnetization processes in ferromagnetic cubes". In: *Journal of Applied Physics* **64** (1988), pp. 1347–1357. DOI: 10.1063/1.341858.

[84] J. J. Kan et al. "Systematic validation of 2x nm diameter perpendicular MTJ arrays and MgO barrier for sub-10 nm embedded STT-MRAM with practically unlimited endurance". In: *2016 IEEE International Electron Devices Meeting (IEDM)*. 2016, pp. 27.4.1–27.4.4. DOI: 10.1109/IEDM.2016.7838493.

[85] D. Apalkov, B. Dieny, and J. M. Slaughter. "Magnetoresistive Random Access Memory". In: *Proceedings of the IEEE* **104** (2016), pp. 1796–1830. DOI: 10.1109/JPROC.2016.2590142.

[86] R. Carboni et al. "Understanding cycling endurance in perpendicular spin-transfer torque (p-STT) magnetic memory". In: *2016 IEEE International Electron Devices Meeting (IEDM)*. 2016, pp. 21.6.1–21.6.4. DOI: 10.1109/IEDM.2016.7838468.

[87] B. Jinnai et al. "High-Performance Shape-Anisotropy Magnetic Tunnel Junctions down to 2.3 nm". In: *2020 IEEE International Electron Devices Meeting (IEDM)*. 2020. DOI: 10.1109/IEDM13553.2020.9371972.

[88] A. Aharoni and S. Shtrikman. "Magnetization Curve of the Infinite Cylinder". In: *Physical Review* **109** (1958), pp. 1522–1528. DOI: 10.1103/PhysRev.109.1522.

[89] Amikam Aharoni. "Magnetization buckling in elongated particles of coated iron oxides". In: *Journal of Applied Physics* **63** (1988), pp. 4605–4608. DOI: 10.1063/1.340138.

[90] Riccardo Hertel and Jürgen Kirschner. "Magnetization reversal dynamics in nickel nanowires". In: *Physica B: Condensed Matter* **343**.11 (2004), pp. 206–210. DOI: 10.1016/j.physb.2003.08.095.

[91] A. Thiaville et al. "Micromagnetic understanding of current-driven domain wall motion in patterned nanowires". In: *EPL (Europhysics Letters)* **69** (2005), p. 990. DOI: 10.1209/epl/i2004-10452-6.

[92] R. H. Koch, J. A. Katine, and J. Z. Sun. "Time-Resolved Reversal of Spin-Transfer Switching in a Nanomagnet". In: *Physical Review Letters* **92**.8 (2004), p. 088302. DOI: 10.1103/PhysRevLett.92.088302.

[93] Kevin Garello et al. "Ultrafast magnetization switching by spin-orbit torques". In: *Applied Physics Letters* **105** (2014), p. 212402. DOI: 10.1063/1.4902443.

[94] Daniel C. Worledge. "Theory of Spin Torque Switching Current for the Double Magnetic Tunnel Junction". In: *IEEE Magnetics Letters* **8** (2017), pp. 1–5. DOI: 10.1109/LMAG.2017.2707331.

[95] J. Z. Sun. "Spin-current interaction with a monodomain magnetic body: A model study". In: *Physical Review B* **62** (2000), pp. 570–578. DOI: 10.1103/PhysRevB.62.570.

[96] Jonathan Z. Sun. "Spin-transfer torque switched magnetic tunnel junction for memory technologies". In: *Journal of Magnetism and Magnetic Materials* **559** (2022), p. 169479. DOI: 10.1016/j.jmmm.2022.169479.

[97] D. Bedau et al. "Spin-transfer pulse switching: From the dynamic to the thermally activated regime". In: *Applied Physics Letters* **97** (2010), p. 262502. DOI: 10.1063/1.3532960.

[98] L. Rehm et al. "Sub-nanosecond spin-torque switching of perpendicular magnetic tunnel junction nanopillars at cryogenic temperatures". In: *Applied Physics Letters* **115** (2019), p. 182404. DOI: 10.1063/1.5128106.

[99] William Fuller Brown. "Thermal Fluctuations of a Single-Domain Particle". In: *Physical Review* **130** (1963), pp. 1677–1686. DOI: 10.1103/PhysRev.130.1677.

[100] Paul Bouquin et al. "Size dependence of spin-torque switching in perpendicular magnetic tunnel junctions". In: *Applied Physics Letters* **113** (2018), p. 222408. DOI: 10.1063/1.5055741.

[101] Shun Kanai et al. "Theory of relaxation time of stochastic nanomagnets". In: *Physical Review B* **103** (2021), p. 094423. DOI: 10.1103/PhysRevB.103.094423.

[102] D. Sanchez Hazen et al. "Real time investigation of double magnetic tunnel junction with a switchable assistance layer for high efficiency STT-MRAM". In: *APL Materials* 10.3 (2022), p. 031104. DOI: 10.1063/5.0080335.

[103] Daniel Sanchez Hazen et al. "Double magnetic tunnel junctions with a switchable assistance layer for improved spin transfer torque magnetic memory performance". In: *Nanoscale* **13** (2021), pp. 14096–14109. DOI: 10.1039/D1NR01656C.

[104] Yutaro Takeuchi et al. "Nanometer-thin L1-MnAl film with B2-CoAl underlayer for high-speed and high-density STT-MRAM: Structure and magnetic properties". In: *Applied Physics Letters* **120** (2022), p. 052404. DOI: 10.1063/5.0077874.

[105] K. Nishioka et al. "Novel Quad-Interface MTJ Technology and its First Demonstration With High Thermal Stability Factor and Switching Efficiency for STT-MRAM Beyond 2X nm". In: *IEEE Transactions on Electron Devices* **67** (2020), pp. 995–1000. DOI: 10.1109/TED.2020.2966731.

[106] B. Jinnai et al. "Fast Switching Down to 3.5 ns in Sub-5-nm Magnetic Tunnel Junctions Achieved by Engineering Relaxation Time". In: *2021 IEEE International Electron Devices Meeting (IEDM)*. 2021. DOI: 10.1109/IEDM19574.2021.9720509.

[107] P. J Kelly and R. D Arnell. "Magnetron sputtering: a review of recent developments and applications". In: *Vacuum* **56** (2000), pp. 159–172. DOI: 10.1016/S0042-207X(99)00189-X.

[108] Michael A. Johnson et al. "Dissociation of Water at the MgO(100)Water Interface: Comparison of Theory with Experiment". In: *The Journal of Physical Chemistry B* **103** (1999), pp. 3391–3398. DOI: 10.1021/jp983729r.

[109] Yoshinori Nagamine et al. "Ultralow resistance-area product of $0.4\Omega\mu m^2$ and high magnetoresistance above 50% in CoFeB|MgO|CoFeB magnetic tunnel junctions". In: *Applied Physics Letters* **89** (2006), p. 162507. DOI: 10.1063/1.2352046.

[110] Koji Tsunekawa et al. "Giant tunneling magnetoresistance effect in low-resistance CoFeB / MgO(001) / CoFeB magnetic tunnel junctions for read-head applications". In: *Applied Physics Letters* **87** (2005), p. 072503. DOI: 10.1063/1.2012525.

[111] Lavinia Elena Nistor et al. "Correlation Between Perpendicular Anisotropy and Magnetoresistance in Magnetic Tunnel Junctions". In: *IEEE Transactions on Magnetics* **46** (2010), pp. 1412–1415. DOI: 10.1109/TMAG.2010.2045641.

[112] M. A. Ruderman and C. Kittel. "Indirect Exchange Coupling of Nuclear Magnetic Moments by Conduction Electrons". In: *Physical Review* **96** (1954), pp. 99–102. DOI: 10.1103/PhysRev.96.99.

[113] S. S. P. Parkin and D. Mauri. "Spin engineering: Direct determination of the Ruderman-Kittel-Kasuya-Yosida far-field range function in ruthenium". In: *Physical Review B* **44** (1991), pp. 7131–7134. DOI: 10.1103/PhysRevB.44.7131.

[114] T. Liu et al. "Thermally robust Mo / CoFeB / MgO trilayers with strong perpendicular magnetic anisotropy". In: *Scientific Reports* **4** (2014), p. 5895. DOI: 10.1038/srep05895.

[115] H. Honjo et al. "Impact of Tungsten Sputtering Condition on Magnetic and Transport Properties of Double-MgO Magnetic Tunneling Junction With CoFeB|W|CoFeB Free Layer". In: *IEEE Transactions on Magnetics* **53** (2017), pp. 1–4. DOI: 10.1109/TMAG.2017.2701838.

[116] Y. S. Choi et al. "Effect of Ta getter on the quality of MgO tunnel barrier in the polycrystalline CoFeB|MgO|CoFeB magnetic tunnel junction". In: *Applied Physics Letters* **90** (2007), p. 012505. DOI: 10.1063/1.2426902.

[117] B. D. Schrag et al. "Néel "orange-peel" coupling in magnetic tunneling junction devices". In: *Applied Physics Letters* **77** (2000), pp. 2373–2375. DOI: 10.1063/1.1315633.

[118] J. Moritz et al. "Orange peel coupling in multilayers with perpendicular magnetic anisotropy: Application to (Co/Pt)-based exchange-biased spin-valves". In: *Europhysics Letters* **65** (2004), p. 123.

[119] Lavinia E. Nistor et al. "Oscillatory interlayer exchange coupling in MgO tunnel junctions with perpendicular magnetic anisotropy". In: *Physical Review B* **81** (2010), p. 220407.

[120] Sadahiko Miura et al. "Scalability of Quad Interface p-MTJ for 1X nm STT-MRAM With 10-ns Low Power Write Operation, 10 Years Retention and Endurance $> 10^{11}$". In: *IEEE Transactions on Electron Devices* **67** (2020), pp. 5368–5373. DOI: 10.1109/TED.2020.3025749.

[121] F. Yaghmaie et al. "Improvement of PMMA electron-beam lithography performance in metal liftoff through a poly-imide bi-layer system". In: *Microelectronic Engineering* **87** (2010), pp. 2629–2632. DOI: 10.1016/j.mee.2010.07.030.

[122] Alvaro Palomino. "Scalable spintronics devices with reduced Pt and Ru content". PhD thesis. 2022. URL: https://theses.hal.science/tel-03889377.

[123] M.P. Sharrock. "Measurement and interpretation of magnetic time effects in recording media". In: *IEEE Transactions on Magnetics* **35** (1999), pp. 4414–4422.

[124] L. Tillie et al. "Data retention extraction methodology for perpendicular STT-MRAM". In: *2016 IEEE International Electron Devices Meeting (IEDM)*. 2016, pp. 27.3.1–27.3.4. DOI: 10.1109/IEDM.2016.7838492.

[125] N. Strelkov et al. "Stability phase diagram of a perpendicular magnetic tunnel junction in noncollinear geometry". In: *Physical Review B* **95** (2017), p. 184409.

[126] Julie Grollier et al. "Neuromorphic spintronics". In: *Nature electronics* **3** (2020), pp. 360–370. DOI: https://DOI.org/10.1038/s41928-019-0360-9.

[127] Alice Mizrahi et al. "Neural-like computing with populations of superparamagnetic basis functions". In: *Nature Communications* **9** (2018), p. 1533. DOI: 10.1038/s41467-018-03963-w.

[128] Kerem Yunus Camsari, Sayeef Salahuddin, and Supriyo Datta. "Implementing p-bits With Embedded MTJ". In: *IEEE Electron Device Letters* **38** (2017), pp. 1767–1770. DOI: 10.1109/LED.2017.2768321.

[129] William A. Borders et al. "Integer factorization using stochastic magnetic tunnel junctions". In: *Nature* **573** (2019), pp. 390–393. DOI: 10.1038/s41586-019-1557-9.

[130] Matthew W. Daniels et al. "Energy-Efficient Stochastic Computing with Superparamagnetic Tunnel Junctions". In: *Physical Review Applied* **13** (2020), p. 034016. DOI: 10.1103/PhysRevApplied.13.034016.

[131] Navid Anjum Aadit et al. "Massively parallel probabilistic computing with sparse Ising machines". In: *Nature Electronics* **5** (2022), pp. 460–468. DOI: 10.1038/s41928-022-00774-2.

[132] Giovanni Finocchio et al. “The promise of spintronics for unconventional computing”. In: *Journal of Magnetism and Magnetic Materials* **521** (2021), p. 167506. DOI: 10.1016/j.jmmm.2020.167506.

[133] Keito Kobayashi et al. “Sigmoidal curves of stochastic magnetic tunnel junctions with perpendicular easy axis”. In: *Applied Physics Letters* **119** (2021), p. 132406. DOI: 10.1063/5.0065919.

[134] K. Hayakawa et al. “Nanosecond Random Telegraph Noise in In-Plane Magnetic Tunnel Junctions”. In: *Physical Review Letters* **126** (2021), p. 117202. DOI: 10.1103/PhysRevLett.126.117202.

[135] C. Safranski et al. “Reliable Sub-nanosecond MRAM with Double Spin-torque Magnetic Tunnel Junctions”. In: 2022, pp. 288–289. DOI: 10.1109/VLSITechnologyandCir46769.2022.9830306.

[136] Takuya Funatsu et al. “Local bifurcation with spin-transfer torque in superparamagnetic tunnel junctions”. In: *Nature Communications* **13** (2022), p. 4079. DOI: 10.1038/s41467-022-31788-1.

[137] Leo Schnitzspan, Mathias Kläui, and Gerhard Jakob. “Nanosecond True-Random-Number Generation with Superparamagnetic Tunnel Junctions: Identification of Joule Heating and Spin-Transfer-Torque Effects”. In: *Phys. Rev. Appl.* **20** (2023), p. 024002. DOI: 10.1103/PhysRevApplied.20.024002.

[138] Christopher Safranski et al. “Demonstration of Nanosecond Operation in Stochastic Magnetic Tunnel Junctions”. In: *Nano Letters* **21** (2021), pp. 2040–2045. DOI: 10.1021/acs.nanolett.0c04652.

[139] Shinji Yuasa et al. “Giant room-temperature magnetoresistance in single-crystal Fe|MgO|Fe magnetic tunnel junctions”. In: *Nature Materials* **3** (2004), pp. 868–871.

[140] Lizhou Wu et al. “Impact of Magnetic Coupling and Density on STT-MRAM Performance”. In: *2020 Design, Automation & Test in Europe Conference & Exhibition (DATE)*. 2020, pp. 1211–1216.

[141] Y. Kim et al. “Integration of 28nm MJT for 816Gb level MRAM with full investigation of thermal stability”. In: *2011 Symposium on VLSI Technology - Digest of Technical Papers*. 2011, pp. 210–211.

[142] Hideo Sato et al. “1T-1MTJ Type Embedded STT-MRAM with Advanced Low-Damage and Short-Failure-Free RIE Technology down to 32 nm MTJ Patterning”. In: *2018 IEEE International Memory Workshop (IMW)*. 2018, pp. 1–4.

[143] V. D. Nguyen et al. “Novel approach for nano-patterning magnetic tunnel junctions stacks at narrow pitch: A route towards high density STT-MRAM applications”. In: *2017 IEEE International Electron Devices Meeting (IEDM)*. 2017, pp. 38.5.1–38.5.4.

[144] Zihui Wang et al. “STT-MRAM for Embedded Memory Applications”. In: *2020 IEEE International Memory Workshop (IMW)*. 2020, pp. 1–3.

[145] D. Edelstein et al. “Full copper wiring in a sub-0.25 /spl mu/m CMOS ULSI technology”. In: *International Electron Devices Meeting. IEDM Technical Digest.* 1997, pp. 773–776.

[146] Henry H. Radamson et al. “Miniaturization of CMOS”. In: *Micromachines* **10** (2019), p. 293. DOI: 10.3390/mi10050293.

[147] Igor L. Markov. “Limits on fundamental limits to computation”. In: *Nature* **512** (2014), pp. 147–154. DOI: 10.1038/nature13570.

[148] Liang Gong Wen et al. “Ruthenium metallization for advanced interconnects”. In: *2016 IEEE International Interconnect Technology Conference / Advanced Metallization Conference (IITC/AMC)*. 2016, pp. 34–36. DOI: 10.1109/IITC-AMC.2016.7507651.

[149] Shibesh Dutta et al. “Highly Scaled Ruthenium Interconnects”. In: *IEEE Electron Device Letters* **38** (2017), pp. 949–951. DOI: 10.1109/LED.2017.2709248.

[150] Ruth Brain. “Interconnect scaling: Challenges and opportunities”. In: *2016 IEEE International Electron Devices Meeting (IEDM)*. 2016, pp. 9.3.1–9.3.4. DOI: 10.1109/IEDM.2016.7838381.

[151] Mehul Naik. “Interconnect Trend for Single Digit Nodes”. In: *2018 IEEE International Electron Devices Meeting (IEDM)*. 2018, pp. 5.6.1–5.6.4. DOI: 10.1109/IEDM.2018.8614541.

[152] “Cobalt bottom-up contact and via prefill enabling advanced logic and DRAM technologies”. In: 2015, pp. 25–28. DOI: 10.1109/IITC-MAM.2015.7325605.

[153] Yu Jiang et al. “Development of electroless Co via-prefill to enable advanced BEOL metallization and via resistance reduction”. In: *2016 IEEE International Interconnect Technology Conference / Advanced Metallization Conference (IITC/AMC)*. 2016, pp. 111–113. DOI: 10.1109/IITC-AMC.2016.7507700.

[154] Ivan Ciofi et al. “Modeling of Via Resistance for Advanced Technology Nodes”. In: *IEEE Transactions on Electron Devices* **64** (2017), pp. 2306–2313. DOI: 10.1109/TED.2017.2687524.

[155] “Selective co growth on Cu for void-free via fill”. In: 2015, pp. 265–268. DOI: 10.1109/IITC-MAM.2015.7325663.

[156] “Damascene Benchmark of Ru, Co and Cu in Scaled Dimensions”. In: 2018, pp. 172–174. DOI: 10.1109/IITC.2018.8430407.

[157] Sandra Ruiz-Gómez, Claudia Fernández-González, and Lucas Perez. “Electrodeposition as a Tool for Nanostructuring Magnetic Materials”. In: **13** (2022), p. 1223. DOI: 10.3390/mi13081223.

[158] Claudia Fernández-González et al. “Scaling Up the Production of Electrodeposited Nanowires: A Roadmap towards Applications”. In: *Nanomaterials* **11** (2021), p. 1657. DOI: 10.3390/nano11071657.

[159] Michal Stano and Olivier Fruchart. “Magnetic nanowires and nanotubes”. In: vol. 27. 2018, pp. 155–267. DOI: 10.1016/bs.hmm.2018.08.002.

[160] Adele Pacquette, Eugene O'Sullivan, and Mahadevaiyer Krishnan. "Electrodeposition of Platinum Group Metals for Interconnects Beyond 5nm Technology Node". In: *ECS Meeting Abstracts* MA2021-01 (2021), pp. 934–934. DOI: 10.1149/MA2021-0124934mtgabs.

[161] Yukimi Jyoko. "Preparation of Perpendicular Magnetization Co/Pt Nanostructures by Electrodeposition". In: *Electrochemical and Solid-State Letters* **2** (1999), p. 67. DOI: 10.1149/1.1390736.

[162] Philippe Allongue and Fouad Maroun. "Self-ordered electrochemical growth on single-crystal electrode surfaces". In: *Journal of Physics: Condensed Matter* **18** (2006), S97. DOI: 10.1088/0953-8984/18/13/S07.

[163] D. R. Gabe. "The role of hydrogen in metal electrodeposition processes". In: *Journal of Applied Electrochemistry* **27** (1997), pp. 908–915. DOI: 10.1023/A:1018497401365.

[164] Song-Zhu Chu et al. "Fabrication and Structural Characteristics of Nanocrystalline FePt Thin Films and FePt Nanowire Arrays Embedded in Alumina Films on ITO/Glass". In: **108** (2004), pp. 5582–5587. DOI: 10.1021/jp0378642.

[165] Yukimi Jyoko. "Characterization of Electrodeposited Magnetic Co/Pt and CoNi/Pt Nanostructures". In: *Electrochemical and Solid-State Letters* **3** (1999), p. 377. DOI: 10.1149/1.1391153.

[166] Yukimi Jyoko and Walther Schwarzacher. "Characterization of electrodeposited magnetic Co/Pt multilayered nanostructures". In: *Electrochimica Acta* **47** (2001), pp. 371–378. DOI: 10.1016/S0013-4686(01)00589-8.

[167] Yukimi Jyoko, Satoshi Kashiwabara, and Yasunori Hayashi. "Preparation of Giant Magnetoresistance Co/Cu Multilayers by Electrodeposition". In: *Journal of The Electrochemical Society* **144** (1997), pp. L5–L8. DOI: 10.1149/1.1837354.

[168] S. Kashiwabara, Y. Jyoko, and Y. Hayashi. "Structure and Magnetic Properties of Electrodeposited Cobalt/Platinum Multilayers". In: *MRS Online Proceedings Library* **451** (1996), pp. 407–412. DOI: 10.1557/PROC-451-407.

[169] V. Georgescu, V. Mazur, and B. Pushcashu. "Microstructural characterisation of electrodeposited Co/Pt multilayers". In: *Materials Science and Engineering: B* **68** (2000), pp. 131–137. DOI: 10.1016/S0921-5107(99)00599-1.

[170] "Perpendicular anisotropy in electrodeposited, Co-rich Co–Pt films by use of Ru underlayers". In: **89** (2006), p. 112506. DOI: 10.1063/1.2339070.

[171] Ho-Cheol Kim, Sang-Min Park, and William D. Hinsberg. "Block Copolymer Based Nanostructures: Materials, Processes, and Applications to Electronics". In: *Chemical Reviews* **110** (2010), pp. 146–177. DOI: 10.1021/cr900159v.

[172] Austin P. Lane et al. "Directed Self-Assembly and Pattern Transfer of Five Nanometer Block Copolymer Lamellae". In: *ACS Nano* **11** (2017), pp. 7656–7665. DOI: 10.1021/acsnano.7b02698.

[173] Antoine Legrain et al. “Straightforward Integration Flow of a Silicon-Containing Block Copolymer for Line–Space Patterning”. In: *ACS Applied Materials  Interfaces* **9** (2017), pp. 43043–43050. DOI: 10.1021/acsami.7b12217.

[174] Amine Lakhdari. “Control of nanometric Copper and Cobalt layers by electrodeposition for the metallization used in microelectronic interconnections”. PhD thesis. 2021. URL: https://theses.hal.science/tel-03274619.

[175] C. A. Ross et al. “Micromagnetic behavior of electrodeposited cylinder arrays”. In: *Physical Review B* **65** (2002), p. 144417. DOI: 10.1103/PhysRevB.65.144417.

[176] C. A Ross et al. “Magnetic properties of arrays of electrodeposited nanowires”. In: *Journal of Magnetism and Magnetic Materials* **249** (2002), pp. 200–207. DOI: 10.1016/S0304-8853(02)00531-0.

[177] Sandrine Da Col et al. “Reduction of magnetostatic interactions in self-organized arrays of nickel nanowires using atomic layer deposition”. In: *Applied Physics Letters* **98** (2011), p. 112501. DOI: 10.1063/1.3562963.

[178] M. Beleggia, D. Vokoun, and M. De Graef. “Demagnetization factors for cylindrical shells and related shapes”. In: *Journal of Magnetism and Magnetic Materials* **321**.9 (2009), pp. 1306–1315. DOI: 10.1016/j.jmmm.2008.11.046.

[179] M. Beleggia et al. “Phase diagram for magnetic nano-rings”. In: *Journal of Magnetism and Magnetic Materials* **301** (2006), pp. 131–146. DOI: 10.1016/j.jmmm.2005.06.024.

[180] J. Escrig et al. “Phase diagrams of magnetic nanotubes”. In: *Journal of Magnetism and Magnetic Materials* **308** (2007), pp. 233–237. DOI: 10.1016/j.jmmm.2006.05.019.

[181] Iñigo Marcos-Alcalde et al. “MEPSA: minimum energy pathway analysis for energy landscapes”. In: *Bioinformatics* **31** (2015), pp. 3853–3855. DOI: 10.1093/bioinformatics/btv453.

[182] Tomohiro Taniguchi. “An analytical computation of magnetic field generated from a cylinder ferromagnet”. In: *Journal of Magnetism and Magnetic Materials* **452** (2018), pp. 464–472. DOI: 10.1016/j.jmmm.2017.11.078.

[183] W. Rave, K. Ramstöck, and A. Hubert. “Corners and nucleation in micromagnetics”. In: *Journal of magnetism and magnetic materials* **183** (1998), pp. 329–333. DOI: 10.1016/S0304-8853(97)01086-X.

[184] A. Thiaville, D. Tomáš, and J. Miltat. “On Corner Singularities in Micromagnetics”. In: *physica status solidi (a)* **170** (1998), pp. 125–135. DOI: 10.1002/(SICI)1521-396X(199811)170:1<125::AID-PSSA125>3.0.CO;2-8.

[185] O. Fruchart et al. “High coercivity in ultrathin epitaxial micrometer-sized particles with in-plane magnetization: Experiment and numerical simulation”. In: *Phys. Rev. B* **57** (1998), pp. 2596–2606. DOI: 10.1103/PhysRevB.57.2596.

[186] Lei Wan et al. “Fabrication and Individual Addressing of STT-MRAM Bit Array With 50 nm Full Pitch”. In: *IEEE Transactions on Magnetics* **58** (2022), pp. 1–6. DOI: 10.1109/TMAG.2022.3147729.

[187] A. V. Khvalkovskiy et al. “Basic principles of STT-MRAM cell operation in memory arrays”. In: *J. Phys. D: Appl. Phys.* **46**.7 (2013), p. 074001. DOI: 10.1088/0022-3727/46/7/074001.